Christoph Schluckner, MSc

Carbon Formation and Effective Removal Strategies in High Temperature Solid Oxide Fuel Cell Anodes Fuelled with Diesel Reformates

Doctoral Thesis

In fulfilment of the requirements
for the degree
Doctor of Technical Sciences

submitted to
Graz University of Technology

Faculty of Mechanical Engineering and Economical Sciences

Supervisor
Univ.-Prof. Dipl.-Ing. Dr. techn. Christoph Hochenauer

Second Supervisor
Univ.-Prof. Dipl.-Phys. Dr. rer. nat. Jürgen Fleig

Graz, March 2017

Affidavit

I hereby declare that I am the sole author or this thesis, that I have not used any sources other those cited, and that I have made explicit reference to the sources of all material that was quoted, whether directly or indirectly. The document uploaded to the TUGraz online platform is identical to this text.

Graz,

Date   Signature

Abstract

Their high level of fuel flexibility makes it possible for solid oxide fuel cells (SOFCs) to utilize hydrocarbons as fuel. This type of fuel supply carries with it the risk of carbon formation within the cell, which results in deteriorating cell performance. This deterioration is generally known as degradation. The topic of this thesis is the detailed modelling of high temperature SOFCs. In particular, it focuses on identifying the sources of degradation and developing effective strategies for performance regeneration.

The first aim of this thesis is to develop a simulation model that predicts carbon formation. The ability to accurately predict the local and time-dependent occurrence of these formations would make it possible to identify the operating conditions that lead to major degradation, as well as the regions particularly at risk of degradation.

The second aim of this thesis is to develop and analyse efficient and effective carbon removal strategies. In addition to removing carbon deposits, such strategies must fulfil a second equally important task: the regeneration of the initial cell performance. If this regeneration is possible, the lifetime of SOFCs can be prolonged and SOFC technology will be closer commercialization.

This thesis is divided into four major parts: (1) the creation of a simulation base model, (2) the identification of the main carbon precursors, (3) the internal reforming of synthetic reformates, and (4) effective carbon removal strategies. The commercial software ANSYS Fluent was used with a SOFC sub-module to simulate the performance of a planar $100 \times 100 \, mm^2$ cell. These simulations were supported by experiments, which were performed at a high temperature SOFC test bench at the Institute of Thermal Engineering (IWT) at the Graz University of Technology. All relevant aspects of fuel cell simulation, such as the solver settings, sub-models, boundary conditions and material data were scrutinized, and their impact on the solution's accuracy was investigated. The results were used to refine the numerical model and led to a thoroughly validated and highly accurate simulation model.

The generated $3D$ base model is a detailed reproduction of the above mentioned test bench. One highlight of these results is the accurate prediction of a single cell's electrochemical performance for conventional and alternative fuels, such as hydrogen and diesel reformate, in the temperature range of $750 - 850\,^{\circ}C$. The model makes it possible to simulate local and time-dependent temperature profiles and specific fuel cell characteristics, such as current density or activation overpotential distribution. The internal reforming of light hydrocarbons is

described by a detailed elementary heterogeneous reaction mechanism. This mechanism makes it possible to simulate the spatial and temporal distribution of surface adsorbed species in the porous electrode structures, including elementary carbon. Its local adsorption profile identified the inlet region of a cell as particularly susceptible to degradation.

In a further step, the model was used to investigate the origin of carbon formations. Methane was identified as the main carbon precursor in the typical SOFC temperature region ($600 - 1,000\,^\circ C$) for different gas mixtures, including diesel reformates. The model showed that the largest amount of carbon deposits occur when using synthetic reformates with a high methane to carbon monoxide ratio. These findings represent the significant contribution of this thesis. The surface carbon profiles of the detailed numerical model were connected with thermodynamic equilibrium results which delivered carbon formation rates. These rates can be assigned to the performance degradation of the cell. Furthermore, detailed analysis revealed that steady-state carbon adsorption profiles differ greatly from results obtained at the beginning of operation. Moreover, the detailed model made it possible to identify another potential performance degradation source: nickel re-oxidation. The simulation model provided information about the position, time and extent of the oxygen adsorbed to the surface.

Finally, four fundamentally diverse carbon removal strategies to restore cell performance were developed and scrutinized in the temperature range of $400 - 800\,^\circ C$. They were applied after permanent performance degradation resulting from carbon deposits was detected. Both CO_2 and a mixture of CO_2 and O_2 showed high carbon removal rates. However, an extraordinarily high nickel re-oxidation potential was identified, which makes them unsuitable as cell-protecting methods for industrial applications.

Two further major findings of this thesis are the following successful carbon removal strategies: first, the use of humidified hydrogen, and second, the novel approach of carrying out carbon removal during cell polarization. Both of these enabled a safe, cell-protecting and efficient process. Deposited carbon was removed and the initial cell performance was repeatedly and effectively restored. Both of these methods are reliable and can therefore extend the lifetime of SOFCs. They are both promising new approaches that move SOFC technology closer to commercialization.

Kurzfassung

Ein Alleinstellungsmerkmal von SOFCs (engl. Solid Oxide Fuel Cells) ist ihre Brennstoffflexibilität und die damit einhergehende Möglichkeit Kohlenwasserstoffe direkt umzusetzen. Der Kohlenwasserstoffbetrieb birgt jedoch das Risiko der Kohlenstoffbildung und folglich einer Leistungseinbuße. Diese Leistungseinbuße wird generell als Degradation bezeichnet. Die vorliegende Arbeit behandelt die Modellierung und Simulation von Hochtemperaturbrennstoffzellen. Die Kerninhalte bilden dabei die Identifikation von Degradationsmechanismen aufgrund von Kohlenstoffablagerungen und die Entwicklung und Erprobung effektiver Regenerationsstrategien.

Das erste Ziel dieser Arbeit ist die Erstellung eines Simulationsmodells, das diese Kohlenstoffablagerungen während des Betriebs einer Zelle abbilden kann. Eine genaue Voraussage der zeitlich zu erwartenden Ablagerungen ermöglicht es, solch kritische Betriebspunkte zu identifizieren und deren genaue Lage zu lokalisieren.

Die Entwicklung und Analyse effizienter und effektiver Strategien zur Entfernung der gebildeten Kohlenstoffablagerungen sind weitere Ziele dieser Arbeit. Solche Strategien werden als Regenerationsstrategien bezeichnet. Neben deren Grundvoraussetzung, der schonenden Entfernung, gibt es eine weitere, gleich wichtige Anforderung an diese Strategien: Die Wiederherstellung der ursprünglichen Zellleistung. Dadurch soll die Lebensdauer der Zellen verlängert und die gesamte SOFC-Technologie einen Schritt näher zur Kommerzialisierung gebracht werden.

Diese Arbeit umfasst vier große Themenbereiche: (1) Erstellung eines Simulationsgrundmodells, (2) Identifikation der Hauptkohlenstoffbildungspfade, (3) Interne Reformierung synthetischer Reformate und (4) Effektive Regenerationsstrategien. Als Simulationssoftware kam in dieser Arbeit das kommerzielle Produkt ANSYS Fluent mit einem zusätzlichen SOFC-Modul zur Anwendung. Damit wurde die Funktion und Leistung einer planaren $100 \times 100\,mm^2$ Einzelzelle beschrieben. Alle Simulationsergebnisse wurden durch experimentelle Daten validiert, die am Hochtemperaturbrennstoffzellenprüfstand des Instituts für Wärmetechnik an der Technischen Universität Graz gewonnen wurden. Alle relevanten Aspekte der Brennstoffzellensimulation wurden umfangreich untersucht und deren Einfluss auf die Lösung analysiert. Die Ergebnisse dieser Untersuchungen wurden zur Erstellung eines optimierten und gründlich validierten Simulationsmodells verwendet.

Das $3D$ Simulationsgrundmodell stellt eine detaillierte Abbildung des SOFC Prüfstandes dar. Dieses Modell ermöglicht die Berechnung der elektrochemischen Leistung von elektrolyt- (electrolyte supported cell (ESC)) und anodengestützten (anode supported cell (ASC)) Einzelzellen in einem Temperaturbereich von $750 - 850\,°C$ während des Betriebs mit konventionellen und alternativen Brenngasen. Spezieller Fokus wurde in dieser Arbeit auf die Verwendung von Dieselreformat gelegt. Die Temperatur-, Spezies-, Stromdichte- oder die Aktivierungsüberpotentialverteilung sind nur wenige charakteristische Beispiele die mit diesem Modell berechenbar sind. Ein detaillierter auf Elementarreaktionen basierender heterogener Reaktionsmechanismus wurde zur Beschreibung der internen Reformierung kurzkettiger Kohlenwasserstoffe verwendet. Dadurch konnte die räumliche und zeitliche Verteilung der auftretenden Oberflächenspezies in den porösen Elektrodenstrukturen simuliert werden. Zu diesen Spezies zählt auch elementarer Kohlenstoff. Mithilfe des erstellten Simulationsmodells wurde der Einlassbereich einer Zelle als besonders für Degradation anfällig identifiziert.

In einem weiteren Schritt wurde das Modell verwendet um Hauptkohlenstoffbildungspfade zu identifizieren. Methan wurde in einem für SOFCs typischen Temperaturbereich ($600 - 1,000\,°C$) für unterschiedliche Gasgemische eindeutig als Hauptkohlenstoffbildner identifiziert. Weiters wurde das Verhältnis von Methan und Kohlenmonoxid in Reformaten als wichtiger Faktor isoliert. Hohe Werte dieses Verhältnisses führten zu hohen Kohlenstoff-Oberflächenbesetzungen. Diese Oberflächenbesetzungen wurden mit thermodynamischen Gleichgewichtsberechnungen in Verbindung gesetzt. Dadurch konnten auftretende Kohlenstoffbildungsraten und folglich die Zelldegradation bestimmt werden. Eine Analyse des zeitlichen Verlaufs der Kohlenstoff-Oberflächenbesetzungen zeigte große Unterschiede zwischen Start und Dauerbetrieb der Zelle. Neben Kohlenstoff kann eine weitere Degradationsart im Brennstoffzellenbetrieb auftreten: Nickel re-oxidation. Diese Art der Degradation konnte ebenfalls mithilfe des Simulationsmodells adressiert werden.

Abschließend wurden vier grundsätzlich verschiedene Regenerationsstrategien entwickelt und im Temperaturbereich zwischen 400 und $800\,°C$ eingehend untersucht. Sie wurden angewendet, nachdem eindeutig eine permanente Verringerung der Zellleistung festgestellt wurde. CO_2 und ein Gasgemisch, bestehend aus CO_2 und O_2, ermöglichten eine sehr schnelle Entfernung der Kohlenstoffablagerungen. Nichtsdestotrotz sind diese beiden Strategien für einen Einsatz in technischen Anwendungen ungeeignet, da bei deren Verwendung ein außerordentlich hohes Potential der Nickel Re-oxidation auftritt.
Wesentliche Ergebnisse dieser Arbeit sind die beiden erfolgreichen, zukunftsträchtigen Regenerationsstrategien: Ein Wasserstoff-Wasserdampfgemisch sowie ein neuartiger Ansatz zur Entfernung von Ablagerungen während des Betriebs der Zelle unter Last. Mithilfe dieser Verfahren konnte ein sicherer, zellschonender und effizienter Entfernungsprozess realisiert werden. Diese beiden Methoden sind zuverlässig und können daher die Lebensdauer einer SOFC Zelle verlängern. Sie stellen somit vielversprechende Strategien dar, um die SOFC-Technologie einen Schritt näher der Kommerzialisierung zu bringen.

Acknowledgments

To my parents

Contents

List of Figures

List of Tables

Acronyms

μCHP	micro combined heat and power
AFC	alkaline fuel cell
APU	auxiliary power unit
ASC	anode supported cell
BOP	balance of plant
C(gr)	graphite
CAD	computer aided design
CFD	computational fluid dynamics
CNF	carbon nano fibers
d.b.	dry base
DGM	dusty-gas model
EL	electrolyte-anode interface
ESC	electrolyte supported cell
FVM	finite volume method
GDC	Gadolinium doped Ceria
IWT	Institute of Thermal Engineering
LSCF	Lanthanum Strontium Colbat Ferrite
LSM	Lanthanum Strontium Manganese Oxide
MCFC	molten carbonate fuel cell
MFC	mass flow controller
MSR	methane-steam reforming
OCV	open circuit voltage

PAFC	phosphoric acid fuel cell
PAH	polycyclic aromatic hydrocarbons
PEMFC	proton exchange membrane fuel cell
S/C	steam-to-carbon ratio
SEM	scanning electron microscopy
SIMPLE	Semi-Implicit Method for Pressure-Linked Equations
SLPM	standard liter per minute
SMM	Stefan-Maxwell model
SOFC	solid oxide fuel cell
SURF	anode-flow channel interface
TPB	three phase boundary
TPO	temperature programmed oxidation
w.b.	wet base
WGSR	water-gas shift reaction
YSZ	yttria-stabilized zirconia

Symbols

Symbol	Description	Unit
A	Frequency factor	dependent on reaction order
α_a	Anodic charge transfer coefficient	-
α_c	Cathodic charge transfer coefficient	-
$\alpha_{(i)}$	Carbon formation activity of reaction i	-
α_L	Average ratio pore size and contact length	-
α_s	H_2/CO electrochemistry split factor	-
B_g	Permeability	m^2
β	Temperature exponent	-
$C_{mp,i}$	Specific molar heat capacity of species i	$\mathrm{J\,mol^{-1}K^{-1}}$
c_i	Molar concentration of gaseous species i	$\mathrm{mol\,m^{-3}}$
$c_{g,i}$	Molar concentration of gaseous species i in adsorbed state	$\mathrm{mol\,m^{-2}}$
$c_{s,j}$	Molar concentration of site species j in adsorbed state	$\mathrm{mol\,m^{-2}}$
$D_{i,j}^e$	Effective binary diffusion coefficient	$\mathrm{m^2\,s^{-1}}$
D^e	Overall effective diffusion coefficient	$\mathrm{m^2\,s^{-1}}$
D_k^e	Effective Knudsen diffusion coefficient	$\mathrm{m^2\,s^{-1}}$
D_p	Average pore size	m
D_s	Average particle size	m
$\Delta_R G_m(T,p)$	Molar Gibb's free energy of reaction	$\mathrm{J\,mol^{-1}}$
$\Delta_R S_m(T,p)$	Molar entropy of reaction	$\mathrm{J\,mol^{-1}\,K^{-1}}$
$\Delta_R H_m^0(T^0,p^0)$	Standard molar enthalpy of reaction	$\mathrm{J\,mol^{-1}}$
$\Delta_R H_m(T,p)$	Molar enthalpy of reaction	$\mathrm{J\,mol^{-1}}$
ΔU	Local voltage jump	V
e	Elementary charge of an electron	C
E_A	Activation energy of reaction	$\mathrm{J\,mol^{-1}}$
E_{el}	Activation energy for the ionic transport	$\mathrm{J\,mol^{-1}}$

Symbol	Description	Unit
E	Total energy	J
$E_{Act,a}$	Anodic activation energy	$J\,mol^{-1}$
$E_{Act,c}$	Cathodic activation energy	$J\,mol^{-1}$
ε	Porosity	-
η	Dynamic viscosity	$kg\,m^{-1}\,s^{-1}$
η_i'	Rate coefficient of gaseous reactant species i	-
η_{Act}	Activation overpotential	V
η_i''	Rate coefficient of gaseous product species i	-
η_{Conc}	Concentration overpotential	V
η_{Ω}	Ohmic overpotential	V
$\vec{F}$	External body forces	$kg\,m\,s^{-2}$
F	Faraday constant	$C\,mol^{-1}$
γ_a	Anodic exchange current density pre-coefficient	$A\,m^{-2}$
γ_c	Cathodic exchange current density pre-coefficient	$A\,m^{-2}$
$\vec{g}$	Gravitational vector	$m\,s^{-2}$
$\dot{H}_i$	Enthalpy fluxes of species i	W
$H_{m,i}(T)$	Molar enthalpy of species i	$J\,mol^{-1}$
I	Electrical current	A
i	Current density	$A\,m^{-2}$
$i_{0,i}$	Reference exchange current density	$A\,m^{-2}$
i_{lim}	Limiting current density	$A\,m^{-2}$
$\vec{J}_i$	Diffusive flux of species i	$kg\,m^{-2}\,s^{-1}$
K	Equilibrium constant	dependent on reaction order
k_b	Rate coefficient of backward reaction	dependent on reaction order
k_e	Effective thermal conductivity	$W\,m^{-1}\,K^{-1}$
k_f	Rate coefficient of forward reaction	dependent on reaction order
L_{TPB}	Three-phase boundary length	m

Symbol	Description	Unit
L_a	Anode thickness	m
L_c	Cathode thickness	m
L_{el}	Electrolyte thickness	m
λ	Thermal conductivity	$\mathrm{W\,m^{-1}K^{-1}}$
λ_p	Mean free path length before molecule collision	m
M_i	Molecular weight of species i	$\mathrm{kg\,mol^{-1}}$
μ	Mass fraction	$\mathrm{kg\,kg^{-1}}$
N_A	Avogadro constant	$\mathrm{mol^{-1}}$
$\dot{n}_{el}$	Molar flow of electrons	$\mathrm{mol\,s^{-1}}$
$\dot{n}_{fuel}$	Molar fuel flow	$\mathrm{mol\,s^{-1}}$
N_g	Total number of gaseous species	-
N_s	Total number of surface site species	-
N_i	Molar flux of species i	$\mathrm{mol\,s^{-1}}$
n^{el}	Electron ratio	-
ν	Mol fraction	$\mathrm{mol\,mol^{-1}}$
$\nu_{st,i}$	Stoichiometric coefficient	-
$\nu'_{st,i}$	Stoichiometric coefficient of reactant R	-
$\nu''_{st,i}$	Stoichiometric coefficient of product P	-
$\nu'_{st,s,i}$	Stoichiometric coefficient of surface reactant R	-
$\nu''_{st,s,i}$	Stoichiometric coefficient of surface product P	-
$\eta'_{s,j}$	Rate coefficient of reactant surface site species j	-
$\eta''_{s,j}$	Rate coefficient of product surface site species j	-
ϕ	Electrical potential	V
P_{rev}	Reversible power	W
p_i	Partial pressure of species i	Pa
p	Operating pressure	Pa
p^0	Standard pressure	Pa
$\dot{Q}_{H_2}$	Excess heat flux of hydrogen oxidation reaction	W
R_{ed}	Area-specific electronic electrode resistance	$\Omega\,\mathrm{m^2}$
R_{el}	Area-specific ionic electrolyte resistance	$\Omega\,\mathrm{m^2}$
R_Ω	Area-specific ohmic resistance	$\Omega\,\mathrm{m^2}$
r	Reaction rate	$\mathrm{mol\,m^{-2}\,s^{-1}}$
Re	Reynolds number	-
ρ	Density	$\mathrm{kg\,m^{-3}}$
ρ_i	Surface site density of active centers	$\mathrm{mol\,m^{-2}}$

Symbol	Description	Unit
R_m	Molar gas constant	$J\,mol^{-1}K^{-1}$
$S_{O^{2-}}$	Ionic O^{2-} molar flux	$mol\,m^{-2}\,s^{-1}$
σ	Electrical or ionic conductivity	$\Omega^{-1}\,m^{-1}$
σ_0	Ionic conductivity pre-factor	$\Omega^{-1}\,m^{-1}$
σ_{el}	Ionic conductivity of the electrolyte	$\Omega^{-1}\,m^{-1}$
Ω_D	Temperature dependent collision integral	-
$\sigma_{i,j}$	Average collision diameter	Å
S^{CO_2}	Carbon dioxide mass flux	$mol\,s^{-1}$
S^{CO}	Carbon monoxide mass flux	$mol\,s^{-1}$
S^h	Heat source term	$W\,m^{-3}$
S^{H_2}	Hydrogen mass flux	$mol\,s^{-1}$
S^m	Mass source term	$kg\,m^{-3}$
$S^{O^{2-}}$	Oxygen ion mass flux	$mol\,s^{-1}$
S^{H_2O}	Water vapor mass flux	$mol\,s^{-1}$
τ	Tortuosity	-
$\overline{\overline{\tau}}$	Stress tensor	$N\,m^{-2}$
T	Temperature	K
ϑ	Surface coverage	-
t	Time	s
U_{cell}	Cell voltage	V
U_{Nernst}	Nernst voltage	V
U_{rev}	Reversible cell voltage	V
$\vec{v}$	Velocity vector	$m\,s^{-1}$
V	Volume	m^3
$\dot{V}$	Volumetric flow	SLPM, standard liters per minute
W_{rev}	Reversible work	$J\,mol^{-1}$
X_i	Conversion rate	-

1

Introduction

This section is intended to provide a brief introduction to fuel cells, to highlight the motivation and goals of this thesis, and to convey the benefits and possibilities of fuel cell simulation. A deeper understanding of the theory behind solid oxide fuel cells, as well as a review of research activities in the field of high temperature solid oxide fuel cells are provided in chapters dedicated to those topics, respectively.

1.1. Fuel Cells: Their Potential and Their Limitations

Fuel cells are electrochemical devices that directly convert the chemical energy of a fuel into electrical energy. Thus, fuel cell technology holds the promise of power generation with high efficiency and low environmental impact. Fuel cells are not limited by the thermodynamic limitations of heat engines, such as the Carnot efficiency. Moreover, fuel cells produce power with minimal pollutants by avoiding 'classic' combustion. In contrast to batteries, fuel cells require an uninterrupted feed of both reductant and oxidant for their continuous operation. Generally, fuel cell systems comprise a number of components [1]:

- Unit cells, in which the electrochemical reactions occur
- Modularly combined arrangements of unit cells called 'stacks', which form units with the desired electrical output capacity
- Balance of plant (BOP), which includes feed stream conditioning, thermal management, electric power conditioning and other secondary functions

Fuel cells can be categorized in several ways, one of which is the type of electrolyte they contain. The most prominent and most widely used types of cells are: proton exchange membrane fuel cells (PEMFCs), alkaline fuel cells (AFCs), phosphoric acid fuel cells (PAFCs), molten carbonate fuel cells (MCFCs), and solid oxide fuel cells (SOFCs). In this thesis, the focus is on SOFCs. The basic physical structure of these high temperature fuel cells is shown in Figure 1.1 [1].

In a typical SOFC unit cell, the anode (negative electrode) is continuously fed with fuel and the cathode (positive electrode) is continuously fed with an oxidant (most often oxygen from
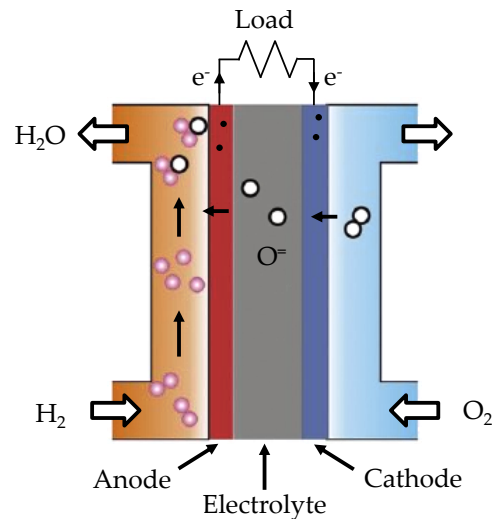
Figure 1.1.: Functional principle of a SOFC [2]

air). The direct conversion of constituents is called electrochemical conversion. It takes place at the so-called three phase boundary (TPB), i.e. close to the electrode-electrolyte interface. This reaction produces an ionic current through the electrolyte, which electrically isolates and spatially separates both electrodes. An electric current is thus driven through an external circuit to perform work on the load [1].

A major benefit of SOFCs is their great fuel flexibility. This is made possible by operating temperatures in the range of 600 to $1,000\,°C$. The direct electrochemical oxidation of hydrogen and carbon monoxide is a unique feature of SOFCs, and one that makes them superior to other low temperature fuel cells. Using SOFCs, hydrocarbons can be internally reformed on the catalytically active surfaces of the fuel electrode. Nevertheless, their internal reformation includes the risk of permanent and irreversible performance degradation. Carbon deposits can form and block the chemically- and electrochemically-active sites. This leads to increased charge-transfer resistances, and the cell performance deteriorates. Steam can be added to prevent carbon deposit formation. However, this dilutes the fuel which lowers the cell's achievable output [2, 3].

Nonetheless, despite extensive scientific research in the field of SOFC technology, SOFCs face major lifetime limitations due to reversible and irreversible degradation phenomena, such as the aforementioned carbon formation, nickel re-oxidation, and particle sintering.

1.2. A Short Outline of the Structure of This Thesis

To get past the proof-of-concept and prototype stage, up-and-coming technologies have to be capable of continuous and stable long-term operation. Performance deterioration as a result of carbon formation in the porous anode structure is still a major issue that has prevented SOFCs from breaking into commercial production. Numerical simulations can be used to model

these processes in an effective and time-efficient manner, and to gain information about this topic. Consequently, the research questions behind this dissertation were: (1) Is a commercial computational fluid dynamics (CFD) software able to predict the chemical and electrochemical performance of a single SOFC? And (2): Is it possible to model performance degradation effects?

In order to speed up the commercialization process of SOFCs, this thesis provides:

1. A detailed dynamic numerical model to describe the electrochemical performance of a SOFC single cell fuelled with conventional and hydrocarbon fuels
2. Scrutiny of major gaseous precursors to carbon formation as well as the operating conditions that provoke it and initiate performance deterioration
3. A detailed catalyst surface site occupation analysis that identifies the most frequent and most important surface site species that appear during internal reforming of hydrocarbon mixtures
4. Effective carbon removal strategies that restore cell performance, substantiated by a temporal analysis of the surface site occupation process

The spatially resolved simulation results were validated by means of experimental polarization curve measurements, gas analysis, and an assessment of the cell's microstructure before, during and after performance deterioration occurred.

1.3. Impact of This Work in the Scientific Community

Numerical simulation is a powerful tool for the description and analysis of the spatial and temporal occurrence of thermal, chemical and electrochemical processes that are carried out during short- and long-term operation of single SOFCs and stacks. A large number of different simulation approaches exist in the literature. These cover a broad range of applications, from micro-models that describe electrode kinetics [4] and ion diffusion in materials [5] to macro-models that match the global flow field [6–8] and BOP models for entire SOFC systems [9].

This thesis presents a flexible and dynamic numerical model for $3D$ and $2D$ simulations in order to predict the transient and steady state electrochemical performance of various types of single SOFCs fuelled with hydrogen and hydrocarbon mixtures. Particular attention was paid to the utilization of diesel reformates. Moreover, a detailed heterogeneous reaction mechanism for the internal reforming of light hydrocarbons is implemented in the model. This makes it possible to predict and scrutinize the surface occupation state during the reformation of diesel reformates, which contain methane and other carbonaceous species. In addition to oxidizing atmospheres, operating temperatures in the range of $600 - 1,000\,°C$ render experimental investigations in SOFCs almost impossible. Thus, the temporal and spatial surface site occupation profiles calculated with this model make it possible to identify regions that are particularly susceptible

to performance degradation, brought about by carbon formation and nickel re-oxidation for example. The model was further used to develop novel strategies to remove carbon deposits from the cell and, to restore the initial cell performance. The strengths and weaknesses of a multitude of promising carbon removal strategies and approaches proposed in the literature were identified with the model developed in this thesis. Detailed numerical analyses revealed their impact on the surface without the need to run expensive and time-consuming experiments. Thus, valuable time and money were saved.

The model developed and the findings presented in this thesis are new to the scientific community. This model will help researchers gain deep and thorough insight into processes that are impossible to detect via in-operando experimental investigations of high temperature SOFCs. The model was used to investigate different types of cells (various mechanical support designs) and thus will aid in the development of a broad range of strategies and procedures to prolong the lifetime of single SOFCs and stacks. These advancements will promote fuel cell development and accelerate the commercialization process of this particular technology.

1.4. Methods and Future Fields of Application

The simulation model presented in this thesis is an exact geometric reproduction of the experimental test rig at the Institute of Thermal Engineering at the Graz University of Technology. Therein, single planar $100 \times 100\,mm^2$ SOFCs can be tested for their performance on pure fuels and any synthetic mixture. The simulation model developed is based on the commercially available CFD ANSYS Fluent, with customized code for the reaction kinetics of internal reformation, and an additional module to describe the electrochemical performance of SOFCs.

For the purpose of this investigation, both numerical and experimental research was conducted in the field of high temperature fuel cell science. In this thesis, diesel reformates and conventional gases were used to cover a broad range of fuels and to open the field of solid oxide fuel cells to potential markets. Possible future applications for SOFC technology include stationary power plants, micro combined heat and power (μCHP) units for domestic homes, and mobile devices such as auxiliary power units (APUs), for mobile homes, refrigerated trucks, and other small scale applications. These applications use conventional diesel as fuel, which can be utilized in SOFCs when it is reformed. As mentioned above, the simulation model is extremely versatile and can thus be applied to a multitude of applications.

2

Modelling Solid Oxide Fuel Cells

This chapter provides a short introduction to the theoretical background of solid oxide fuel cells as well as approaches to modelling them. The sections below provide information about the basics of fuel cells, the loss mechanisms that occur during operation, and the advantages of high temperature fuel cells over other types of fuel cells. State-of-the art numerical approaches to describe the cell performance are presented along with methods for addressing and identifying sources of degradation. Short and precise introductions to specific topics are provided at the beginning of the relevant chapters.

2.1. Electrochemical Reactions of a SOFC

As stated in the introduction, a fuel cell converts the chemical energy of a gaseous fuel directly into electrical energy. The electrical effects can be explained by thermodynamics. The fuel and the oxidant are fed to two spatially-separated electrodes in order to inhibit direct oxidation [10]. Oxygen is fed to the oxygen electrode (cathode), where it is reduced to oxygen ions (O^{2-}) by electrons, according to Eq. (2.1) [11].

$$O_2 + 4e^- \rightharpoonup 2O^{2-} \tag{2.1}$$

At the anodic TPB the transported oxygen ions react with an adsorbed fuel to form water vapour H_2O and carbon monoxide CO_2, according to Eq. (2.2) and (2.3) [2, 11].

$$H_2 + O^{2-} \rightharpoonup H_2O + 2e^- \tag{2.2}$$

$$CO + O^{2-} \rightharpoonup CO_2 + 2e^- \tag{2.3}$$
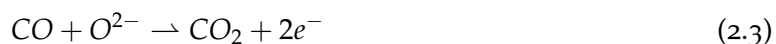
The released electrons are then conveyed to the cathode via an external electrical load. Hydrogen would seem to be an ideal fuel for SOFCs, but is in fact preferred for low temperature fuel cells (e.g. PEMFC) due to their higher efficiencies at room temperature. SOFCs provide the

exceptional opportunity to electrochemically convert carbon monoxide, which is a catalyst poison to every low temperature fuel cell.

The dense, gas-tight, oxygen-ion conducting electrolyte is the central element of the fuel cell, and separates the two electrodes. It prevents the electrons from passing through it but allows the oxygen ions to be conducted to the anode. The electrolyte is generally ceramic, and made from materials such as yttria-stabilized zirconia (YSZ), which conducts these oxygen ions at temperatures from 500 to $1,500\,^{\circ}C$ [10, 11].

Since they can be utilized with a preceding reforming step, gaseous hydrocarbons (e.g. methane or propane derived from pipelines or liquid stores) or fuels from biomass gasification are far more attractive for SOFCs than pure hydrogen feeds. The internal reforming of light hydrocarbons will be discussed in further detail below.

According to Eqs. (2.2) and (2.3), the released electrons represent an electric current from the anode to the cathode side. This current I is a linear function of the flow of electrons, as given by Eq. (2.4):

$$I = \dot{n}^{el}\left(-e\right)N_A = -\dot{n}^{el}\,F = -2\dot{n}_{H_2}\,F = -2\dot{n}_{CO}\,F \tag{2.4}$$

In Eq. (2.4), $\dot{n}_{el}$ is the molar flow of electrons in $mol\,s^{-1}$, e is the elementary charge of a single electron ($e = (1.60217733 \pm 0.00000049) \times 10^{-19}\,C$), N_A is the Avogadro constant ($6.022169 \times 10^{23}\,mol^{-1}$), and F is the Faraday constant ($96,485.309 \pm 0.029\,C\,mol^{-1}$) [11].

2.2. The Nernst Voltage

A SOFC can be treated thermodynamically in terms of the free enthalpy of the reactions that occur therein, as described above. This allows the calculation of the reversible work for the reversible reactions. The maximum electrical work of a SOFC at constant temperature and pressure is given by the negative of the Gibb's free enthalpy of the occurring reaction. This reversible work W_{rev} of a SOFC can thus be found by [2, 11]

$$W_{rev} = \Delta_R G_m(T,p) = \Delta_R H_m(T,p) - T\,\Delta_R S_m(T,p). \tag{2.5}$$

The thermodynamic efficiency of a cell can be found by relating the Gibb's free enthalpy to the reaction enthalpy of a system, as shown in Eq. (2.6).

$$\eta_{th} = \frac{\Delta_R G_m(T,p)}{\Delta_R H_m(T,p)} = \frac{\Delta_R H_m(T,p) - T\Delta_R S_m(T,p)}{\Delta_R H_m(T,p)} = 1 - \frac{T\Delta_R S_m(T,p)}{\Delta_R H_m(T,p)} \tag{2.6}$$

Fuel cells are thus not Carnot-limited, which is the reason behind their high efficiencies even at ambient temperatures.

Assuming ideal gas behaviour (reaction enthalpy $\Delta_R H_m$ is independent from the operating pressure), the molar Gibb's free enthalpy $\Delta_R G_m(T, p)$ simplifies to [11]:

$$\Delta_R G_m(T, p) = \Delta_R H_m(T) - T \Delta_R S_m(T, p) \tag{2.7}$$

The molar reaction enthalpy $\Delta_R H_m(T)$ is calculated using the stoichiometric coefficients of reactants and products $\nu_{st,i}$ [1]:

$$\Delta_R H_m(T) = \sum_i \nu_{st,i} H_{m,i}(T)\bigg|_{Products} - \sum_i \nu_{st,i} H_{m,i}(T)\bigg|_{Reactants} \tag{2.8}$$

with the particular species' enthalpy $H_{m,i}(T)$:

$$H_{m,i}(T) = H_{m,i}(T_0) + \int_{T_0}^{T} C_{mp,i}(T) dT \tag{2.9}$$

wherein $C_{mp,i}(T)$ is the temperature dependent specific molar heat capacity of species i. Due to the ideal gas assumption, the pressure dependence is neglected. The molar entropy of reaction $\Delta_R S_m(T, p)$ is calculated by [11]:

$$\Delta_R S_m(T, p) = \Delta_R S_m^0(T, p^0) - R_m \ln \prod_i \left(\frac{p_i}{p^0}\right)^{\nu_{st,i}} \tag{2.10}$$

R_m is the universal molar gas constant ($8.3144598\,J\,mol^{-1}\,K^{-1}$), p_i is the partial pressure of species i, and p^0 is the standard pressure. Equations (2.7) to (2.10) result in the final form of the Gibb's free energy [11]

$$\Delta_R G_m(T, p) = \Delta_R G_m^0(T, p^0) + R_m T \ln \prod_i \left(\frac{p_i}{p^0}\right)^{\nu_{st,i}}. \tag{2.11}$$

The connection between thermodynamic and electrical quantities can be found by the power of a SOFC. The reversible electrical power P_{rev} of a SOFC is the product of the reversible cell voltage U_{rev} and the current I. Moreover, this equals the product of molar fuel flow and the Gibb's free enthalpy of the occurring reaction [11]:

$$P_{rev} = U_{rev}\, I = \dot{n}_{fuel}\, W_{rev} = \dot{n}_{fuel}\, \Delta_R G_m(T, p) \tag{2.12}$$

$$U_{rev} = -\frac{\dot{n}_{fuel}\, \Delta_R G_m(T, p)}{I} = -\frac{\dot{n}_{fuel}\, \Delta_R G_m(T, p)}{\dot{n}_{el}\, F} = -\frac{\Delta_R G_m(T, p)}{n^{el}\, F} \tag{2.13}$$

Herein, the product of molar electron flow $\dot{n}_{el}$ and the Faraday constant F equals the electric current I. The molar fuel flow $\dot{n}_{fuel}$ only accounts for the gaseous species that take part in the oxidation reaction and thus differ from the overall fuel inlet flow. The electrochemical oxidation of hydrogen or carbon monoxide results in [11]:

$$\frac{\dot{n}_{fuel}}{\dot{n}_{el}} = \frac{1}{n^{el}} = \frac{1}{2}, \tag{2.14}$$

which can be derived from the half-cell reactions Eqs. (2.2) and (2.3). In Eq. (2.14), n^{el} is the electron ratio, which is the number of electrons that are released during the ionization process of one fuel molecule (e.g. H_2 or CO).

Finally, the Nernst voltage U_{Nernst} for a fuel cell can be found by combining Eqs. (2.11) and (2.13) [11]. The Nernst equation outlines how reversible electrochemical cell voltages vary as a function of species concentration, gas pressure, and so on. This equation is the centrepiece of fuel cell thermodynamics.

$$U_{Nernst} = -\frac{\Delta_R G_m^0(T, p^0)}{n^{el} F} - \frac{R_m T}{n^{el} F} \ln \prod_i \left(\frac{p_i}{p^0} \right)^{\nu_{st,i}} \tag{2.15}$$

This voltage should be equivalent to the open circuit voltage (OCV), which can be measured when no electrical current is drawn from the cell, unless there is leakage across the electrolyte. The Nernst voltage of a SOFC fuelled with hydrogen can be calculated with [11]

$$U_{Nernst} = -\frac{\Delta_R G_m^0(T, p^0)}{2 F} - \frac{R_m T}{2 F} \ln \left(\frac{p_{H_2O} \, p^{0 \, 1/2}}{p_{H_2} \, p_{O_2}^{1/2}} \right). \tag{2.16}$$

When a fuel mixture of different electrochemically convertible constituents is used, the Nernst equation can be calculated for any combustible species in the mixture. The Gibb's free enthalpy changes with the different reactions that are taken into account. Thus, independent of the fuel considered (whether hydrogen, carbon monoxide, or even methane), the resulting Nernst voltage remains the same [11].

2.3. The Polarization Curve

The Nernst voltage in Eq. (2.15) represents the ideal cell voltage that can be reached under the given boundary conditions (T, p). Unfortunately, when a finite current is drawn from the cell, further irreversibilities occur. The reversible operation of fuel cells is technically impossible, due to the mixing effects of the products along the anode. The gaseous products that emerge in the anodic porosity during cell operation dilute the fuel mixture, and thus induce irreversibilities. All processes within a SOFC require energy, which reduces the total available energy of the

system. The transport limitations of gaseous products can cause diffusional losses. Moreover, the materials in SOFCs have a finite conductivity, which causes ohmic losses under load operation. The main losses, also referred to as polarization overpotentials, include activation overpotentials η_{Act}, concentration overpotentials η_{Conc}, and ohmic overpotentials η_{Ω}. The cell voltage U_{cell} under load operation is significantly reduced in comparison to the theoretical maximum Nernst voltage. The real voltage output of a SOFC can be found using Eq. (2.17) [2].

$$U_{cell} = U_{Nernst} - \eta_{\Omega} - \eta_{Act} - \eta_{Conc} \qquad (2.17)$$

In Eq. (2.17), all of the parasitic losses that occur are taken into account, and thus decrease the maximum realizable voltage output U_{cell} of a cell.
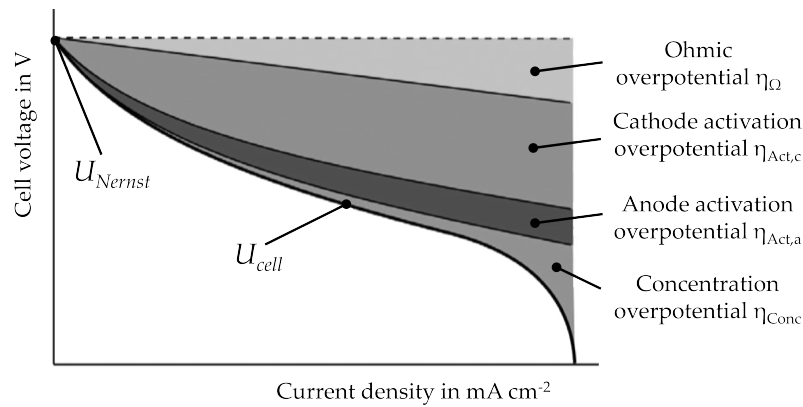
Figure 2.1.: Illustration of a SOFC single-cell polarization curve [12]

Figure 2.1 summarizes all of the overpotentials that occur, and depicts the characteristic polarization curve of fuel cells as a result thereof. This figure provides a good illustration of the losses that occur and further indicates the load regions in which each particular loss is most dominant. These losses are discussed in further detail below.

2.3.1. Ohmic Overpotential η_{Ω}

Ohmic overpotentials arise in a fuel cell as a result of resistance to the ion flow in the electrolyte and the electron flow in the electrodes. SOFC electrodes typically have a high metal loading with high electric conductivity, which limits their ohmic losses. Thus, ohmic losses in a SOFC are typically dominated by the oxygen ion resistance through the electrolyte. A decrease in the electrolyte thickness therefore effectively decreases ohmic overpotentials η_{Ω}. The ionic flow in the electrolyte obeys Ohm's law, according to Eq. (2.18) [12–14]:

$$\eta_{\Omega} = i \, R_{\Omega} = i \, (R_{ed} + R_{el}) \qquad (2.18)$$

wherein R_Ω is the sum of area-specific ionic and electronic resistances of the fuel cell. R_Ω includes electronic resistances in the electrodes, R_{ed}, and ionic resistances in the solid electrolyte, R_{el}. The specific ionic resistance of the electrolyte can be expressed as:

$$R_{el} = L_{el}\,\sigma_{el} = L_{el} \left[\sigma_0\, T^{-1}\, exp\left(-\frac{E_{el}}{R_m T}\right)\right]^{-1} \tag{2.19}$$

where E_{el} denotes the activation energy for the ionic transport and σ_{el} is the ionic conductivity of the electrolyte. σ_0 is a pre-factor and L_{el} is the electrolyte thickness [13].

2.3.2. Activation Overpotential η_{Act}

Electrochemical reactions, like every chemical reaction, involve energy barriers that have to be overcome. This barrier is the reaction's activation energy, which results in an activation or charge-transfer overpotential. It is brought about by the transfer of charges between the electronic and ionic conductors. Thus, a fraction of the cell voltage is lost to drive this charge transfer reaction. When only one rate-controlling step is assumed, the Butler-Volmer equation Eq. (2.20) provides a correlation between the activation overpotential η_{Act} and the current density i [13, 14]:

$$i = i_{0,i} \left[\exp\left(\alpha_a \frac{n^{el} F \eta_{Act,i}}{R_m T}\right) - \exp\left(-\alpha_c \frac{n^{el} F \eta_{Act,i}}{R_m T}\right)\right] \tag{2.20}$$

In Eq. (2.20), i describes the current density and $i_{0,i}$ is the exchange current density of each electrode. $i_{0,i}$ describes the forward and reverse electrode reaction rate at equilibrium voltage. A high $i_{0,i}$ denotes high electrochemical reaction rates, which mean that good fuel cell performance can be expected. When identifying η_{Act}, $i_{0,i}$ is a crucial value. It is a measure of the catalytic activity and depends on the operating conditions (partial pressures p_i of reacting species and temperature T), material properties, the microstructure of the electrode and the length of the three-phase boundary. α_a and α_c are the anodic and cathodic charge transfer coefficients, respectively. They depend on the electrocatalytic reaction mechanism and typically take values between 0 and 1. They are further constrained by $\alpha_a + \alpha_c = 1$. In SOFCs, both reactions are assumed to be symmetrical; thus, α_a and α_c are generally set to equal 0.5. Solving the Butler-Volmer equation and thus evaluating η_{Act} requires an iterative scheme, such as Newton's method [13, 14].

It is possible to describe the exchange current densities for the anode $i_{0,a}$ and cathode $i_{0,c}$, based on the experimental findings of [15], as so:

$$i_{0,a} = \gamma_a L_{TPB,a} \left(\frac{p_{H_2}}{p^0}\right)\left(\frac{p_{H_2O}}{p^0}\right) \exp\left(-\frac{E_{Act,a}}{R_m T}\right) \tag{2.21}$$

$$i_{0,c} = \gamma_c L_{TPB,c} \left(\frac{p_{O_2}}{p^0} \right)^{0.25} \exp \left(-\frac{E_{Act,c}}{R_m T} \right) \tag{2.22}$$

where $E_{Act,a}$ and $E_{Act,c}$ are the anodic and cathodic activation energies, respectively. γ_a and γ_c are anodic and cathodic pre-exponential factors for the exchange current density. There is an exchange current density for each electrode (anode and cathode), which means that there are also diverse activation overpotentials for both the anode $\eta_{Act,a}$ and cathode $\eta_{Act,c}$. The exchange current densities for the numerical simulations in Chapter 3 were determined based on Eqs. (2.21) and (2.22), respectively. Deng and Petric [16] proposed a method to evaluate the TPB length, as given by Eq. (2.23).

$$L_{TPB} = \frac{72\alpha_L [D_p - \varepsilon(D_p + D_s)]\varepsilon}{D_s^2 D_p^2 (1 - \sqrt{1 - \alpha_L^2})} \tag{2.23}$$

Based on geometrical considerations, L_{TPB} can be found for the anode and cathode, respectively, as a function of particle size D_s, pore size D_p, porosity ε, and an average ratio α_L of particle size and contact length between the grains. The Butler-Volmer equation can then be simplified to:

$$i = 2i_0 \sinh \left(\frac{n^{el} F \eta_{act}}{2 R_m T} \right) \tag{2.24}$$

Using Eq. (2.24), an analytical solution to the Butler-Volmer correlation can be found.

2.3.3. Concentration Overpotential η_{Conc}

Concentration overpotentials η_{Conc} occur as the result of mass-transfer limitations when the fuel is depleted at the TPB. They become a significant loss at high current densities and, similarly, at high fuel utilizations ($\geq 80\%$). The diffusion of gases through the porous electrodes, the depletion of reactants and the formation of products are the main factors that contribute to the concentration overpotential.

Concentration overpotential can be understood as the difference between the ideal and real cell voltage (when ohmic and activation losses have already been corrected). The real cell voltage is determined at the TPB, whereas the ideal voltage is calculated in terms of bulk species partial pressures [17]. The concentration overpotentials for a binary $H_2 - H_2O$ system at the anode and $O_2 - N_2$ at the cathode, respectively, can be found using [15]:

$$\eta_{Conc,a} = -\frac{R_m T}{n^{el} F} \ln \left(\frac{p'_{H_2} p_{H_2O}}{p_{H_2} p'_{H_2O}} \right) \tag{2.25}$$

$$\eta_{Conc,c} = -\frac{R_m T}{n^{el} F} \ln \left[\left(\frac{p'_{O_2}}{p_{O_2}} \right)^{\frac{1}{2}} \right] \tag{2.26}$$

where p'_{H_2}, p'_{H_2O} and p'_{O_2} are equal to the species partial pressures at the three-phase boundary. p_{H_2}, p_{H_2O} and p_{O_2} are the partial pressures in the flow channel. The partial pressures at the TPB are generally unknown and cannot be measured during SOFC operation. Thus, in determining the concentration overpotentials, the main goal is to develop suitable models that predict these partial pressures.

Generally, two different mass transport phenomena can be distinguished in porous electrode structures: (1) a diffusive flux, driven by species concentration gradients, and (2) a viscous flow, driven by pressure gradients. Gas transport in the porous electrode structure occurs mainly in the form of diffusion. Darcy's viscous flow can thus be neglected [17].
Different diffusion mechanisms and their corresponding modelling approaches are thus discussed below.

Diffusion Mechanisms

Both molecular (ordinary) and Knudsen diffusion can be used to describe the diffusive transport of species through the electrodes. The relative importance of the individual diffusion mechanisms depends on the occurrence of molecular-molecular collisions (ordinary diffusion) and molecular-wall collisions (Knudsen diffusion). Thus, the governing diffusion mechanism depends on the microstructure of the porous electrodes (porosity ε, tortuosity τ, pore size D_p, and permeability B_g) [13].
Molecular diffusion is dominant in porous structures with large pores. In contrast, Knudsen diffusion dominates when pore size is small compared to the mean free path length in the gas compartment [18]. This is characterized by the Knudsen number, $K_n = \lambda_p / D_p$, where λ_p is defined as the mean free path length of a molecule until collision with a pore wall and D_p is the pore diameter. In typical SOFC electrodes, $Kn \approx 1$, so that both molecular diffusion and Knudsen diffusion have to be taken into account [13, 14].

The Knudsen diffusion coefficient D_k^e can be determined for round pores by means of the kinetic theory of gases. In order to account for the tortuous paths in the porous electrodes, the coefficient has to be modified in terms of an effective coefficient [17, 19]

$$D_k^e = \frac{\varepsilon}{\tau} \frac{2D_p}{3} \sqrt{\frac{8R_m T}{\pi M_i}} \tag{2.27}$$

where M_i is the molecular weight of the diffusing gas. The effective diffusion coefficient for binary diffusion $D_{i,j}^e$ can be calculated using the Chapman-Enskog model [14]:

$$D_{i,j}^e = 0.0018583 \frac{\varepsilon}{\tau} \left(\frac{1}{M_i} + \frac{1}{M_j} \right)^{\frac{1}{2}} \frac{T^{\frac{3}{2}}}{p^0 \, \sigma_{i,j}^2 \, \Omega_D} \tag{2.28}$$

In Eq. (2.28), $\sigma_{i,j}$ is the average collision diameter and Ω_D is the temperature-dependent collision integral. $\sigma_{i,j}$ and Ω_D can be calculated by means of tabulated data.

Diffusive gas transport in fuel cells is often described by Fick's model, the Stefan-Maxwell model (SMM) or the dusty-gas model (DGM), which is an extension of the SMM that incorporates Knudsen diffusion effects. Depending on the model used to describe the diffusion, varied levels of detail can be achieved to describe the diffusion process. Thus, these models provide different levels of accuracy in predicting concentration overpotentials. The dusty-gas model predictions are more accurate for multicomponent mixtures than those of Fick's model [18]. This can be attributed to the method by which the overall effective diffusion coefficients are determined in both models.

Fick's Model

Fick's law is the simplest diffusion model and is often applied in polarization curve models using binary systems. Fick's model makes it possible to find analytical solutions, and is thus easier to implement than the Stefan-Maxwell or dusty-gas model.
For a one-dimensional process at steady state and electrochemical reactions occurring at the TPB, Fick's model for the molar flux N_i of species i is given by Eq. (2.29) [20]

$$N_i = -\frac{p^0 D_i^e}{R_m T} \frac{d\nu_i}{dx} \tag{2.29}$$

where x is the length and D_i^e is the overall effective diffusion coefficient, which is defined as $\left(D_i^e\right)^{-1} = \left(D_k^e\right)^{-1} + \left(D_{i,j}^e\right)^{-1}$.
For a binary $H_2 - H_2O$ system at the anode, assuming equi-molar counter diffusion, and $N_{H_2} = N_{H_2O} = -(i/2F)$, and oxygen at the cathode, assuming $N_{O_2} = -i/4F$, partial pressures p'_{H_2}, p'_{H_2O} and p'_{O_2} at the anodic TPB thus result from Eq. (2.29) to [14]:

$$p'_{H_2} = p_{H_2} - \frac{R_m T L_a}{2F D_{H_2}^e} i, \quad p'_{H_2O} = p_{H_2O} + \frac{R_m T L_a}{2F D_{H_2O}^e} i \tag{2.30}$$

$$p'_{O_2} = p_{O_2} - \frac{R_m T L_c}{4F D_c^e} i \tag{2.31}$$

for the anodic (H_2 and H_2O) and cathodic (O_2) species. Here, L_a and L_c are the anode and cathode thickness, respectively.
Eq. (2.25), makes it possible to find an analytical solution for the particular concentration overpotentials $\eta_{Conc,a}$ and $\eta_{Conc,c}$ by means of Eqs. (2.30) and (2.31).

$$\eta_{Conc,a} = -\frac{R_m T}{2F} \ln\left(1 - \frac{i}{i_{lim,a}}\right) + \frac{R_m T}{2F} \ln\left(1 + \frac{p_{H_2} i}{p_{H_2O} i_{lim,a}}\right) \tag{2.32}$$

$$\eta_{Conc,c} = -\frac{R_m T}{4F} \ln \left(1 - \frac{i}{i_{lim,c}} \right). \tag{2.33}$$

By means of Eqs. (2.32) and (2.33) it is possible to find an analytical solution for the concentration overpotentials using Fick's first law of diffusion. In Eqs. (2.32) and (2.33), $i_{lim,i}$ is the limiting current density of the particular electrode. It denotes the maximum achievable current density, at which complete fuel utilization occurs. It can be deduced from Eqs. (2.30) and (2.31) by solving for i and subsequently setting the fuel partial pressures at the TPB to zero. i_{lim} for the anode and cathode results in [21]:

$$i_{lim,a} = \frac{2F p_{H_2} D_{H_2}^e}{R_m T L_a}, \quad i_{lim,c} = \frac{4F p_{O_2} D_c^e}{R_m T L_c} \tag{2.34}$$

Stefan-Maxwell Model

The Stefan-Maxwell model is often used in multi-component systems because it includes molecular collisions among the different types of gas species. This is represented by the more sophisticated left hand side of Eq. (2.35) for a one dimensional problem [20].

$$\sum_{j=1, j \neq i}^{n} \frac{\nu_j N_i - \nu_i N_j}{D_{i,j}^e} = -\frac{p^0}{R_m T} \frac{d\nu_i}{dx} \tag{2.35}$$

An analytical solution for the concentration overpotential η_{Conc} of a binary system can be found in a similar way to the methodology described for Fick's model. The solution follows from Eq. (2.25) for the anodic electrode to [18]:

$$\eta_{Conc,a} = -\frac{R_m T}{2F} \ln \left(\frac{\left(\nu_i - \frac{i R_m T}{2FD_{i,j}^e p^0} L_a \right) (1 - \nu_i)}{\nu_i \left(1 + \frac{i R_m T}{2FD_{i,j}^e p^0} L_a - \nu_i \right)} \right). \tag{2.36}$$

Here, ν_i represents the mole fraction of species i in the bulk of the gas channel. It is plain to see that this model is more complex than Fick's model, but it also provides a more detailed reproduction of the diffusion process and thus better describes the diffusional losses. However, it is noted that only molecular diffusion is taken into account, as can be seen by the diffusion coefficient $D_{i,j}^e$.

Dusty-gas Model

The dusty-gas model is an extension of the Stefan-Maxwell model and takes both Knudsen and molecular diffusion into account. Thus, gas-wall interactions are also incorporated in the dusty-gas model. The model assumes that the pore walls are large pseudo molecules (dust),

which are uniformly distributed in the domain. The flux ratio is determined using Graham's law of diffusion in gaseous mixtures. The DGM is more accurate than Fick's model, when $Kn \approx 1$, because, at these conditions, the assumption of equimolar counter diffusion is no longer valid. Molar flux transport according to the DGM is seen in [18]:

$$\frac{N_i}{D_{k,i}^e} + \sum_{j=1, j \neq i}^{n} \frac{\nu_j N_i - \nu_i N_j}{D_{i,j}^e} = -\frac{p^0}{R_m T} \frac{d\nu_i}{dx} - \frac{\nu_i}{R_m T} \left(1 + \frac{1}{D_{k,i}^e} \frac{B_0 p^0}{\mu} \right) \frac{dp^0}{dx} \qquad (2.37)$$

The second term on the right hand side in Eq. (2.37) is the permeation flux. It takes into account the effect of the total pressure gradient on mass transport. It is possible to assume the total pressure is uniform over the entire thickness of the porous electrode. Thus, this term can be neglected. Only the diffusion flux needs to be taken into account here. Eq. (2.37) can thus be reduced to [18]

$$\frac{N_i}{D_{k,i}^e} + \sum_{j=1, j \neq i}^{n} \frac{\nu_j N_i - \nu_i N_j}{D_{i,j}^e} = -\frac{p^0}{R_m T} \frac{d\nu_i}{dx} \qquad (2.38)$$

It is difficult to find an analytical solution for the species mole fraction at the TPB. Thus, numerical methods are normally applied to solve for the unknown variable. The concentration polarizations η_{Conc} for the anode and cathode (using Eqs. (2.25) and (2.26)), respectively can then be calculated using these molar amounts.

Diffusion Model Used in This Thesis to Predict Concentration Overpotentials η_{Conc}

As a conclusion to this section, different applicable diffusion models are briefly discussed and their usage in the CFD software is analysed. Fick's model is the simplest and there are analytical solutions for it. Nevertheless, molecular transport processes are only described in a simple way and multicomponent systems cannot be described correctly. Since this thesis deals with synthetic diesel reformates, which are composed of six species, Fick's model cannot be used. ANSYS Fluent does not offer the option of modelling Knudsen diffusion, which means that the DGM cannot be used. Thus, in order to describe multi-component diffusional mass transport and to predict concentration overpotentials η_{Conc} during cell operation, the SMM was applied. The tortuous nature of the porous structure was accounted for by using an effective diffusion coefficient (correction by ε/τ), as shown in Eq. (2.28).

2.4. Chemical Reactions and Internal Reforming of Light Hydrocarbons

This section provides a brief overview of the chemical reactions that are catalysed in SOFCs. It will also present and examine drawbacks of such reactions, in terms of their possible sources of performance degradation. The mechanisms that can occur during internal reforming of hydrocarbon fuels are presented in detail in Section 3.4.

Generally, it is possible to distinguish between two kinds of chemical reactions. There are:

- **Global reactions**, which describe the overall behaviour of a chemical reaction. They summarize several elementary reactions, but are not able to describe intermediate species formation. Eqs. (2.40) - (2.44) are examples of such global reactions.
- **Elementary reactions** proceed exactly as described by the reaction equation on an atomic or molecular basis. New species are formed through the collision of molecules and atoms. An example of an elementary reaction is given in Eq. (2.39) for the oxidation of hydrogen.

$$H + O_2 \rightharpoonup OH + O \tag{2.39}$$

In the course of the research for this thesis, different reaction mechanisms for the internal reforming of light hydrocarbons were investigated. They differed in their complexity and in their underlying modelling approaches. Thus, their principles are briefly sketched out below. Generally, a distinction is made between homogeneous and heterogeneous reactions:

- In **homogeneous reactions**, all of the participating constituents are present in one phase, e.g. gas or liquid phase.
- A **heterogeneous reaction** occurs, when the participating constituents are in both the fluid and solid phases. This is true for catalysed processes, such as catalytic combustion, as well as reforming or electrochemical reactions at the three-phase boundary.

As indicated above, the internal reforming of light hydrocarbons is a heterogeneous process as is the particular case of diesel reformates in SOFCs. Gaseous constituents, including methane, react on the catalytic surface (nickel is the state-of-the-art chemical and electrochemical catalyst) of the porous anode structure to form reaction products. Other long-chain hydrocarbons need to be pre-reformed prior to using them as fuel feed. These heterogeneous reactions can be described by global gas phase reactions, such as the methane-steam reforming (MSR) reaction, Eq. (2.40), the water-gas shift reaction (WGSR), Eq. (2.41), and by the following equations [22, 23]:

$$CH_4 + H_2O \rightleftharpoons CO + 3H_2\,, \quad \Delta_R H_m^0 = 205,885\,J\,mol^{-1} \tag{2.40}$$

$$CO + H_2O \rightleftharpoons CO_2 + H_2\,, \quad \Delta_R H_m^0 = -41,146\,J\,mol^{-1} \tag{2.41}$$

$$CH_4 + 2H_2O \rightleftharpoons CO_2 + 4H_2, \quad \Delta_R H_m^0 = 164,747 \, J \, mol^{-1} \tag{2.42}$$

$$CH_4 + CO_2 \rightleftharpoons 2CO + 2H_2, \quad \Delta_R H_m^0 = 247,023 \, J \, mol^{-1} \tag{2.43}$$

$$CH_4 + 3CO_2 \rightleftharpoons 4CO + 2H_2O, \quad \Delta_R H_m^0 = 329,299 \, J \, mol^{-1} \tag{2.44}$$
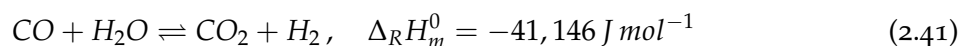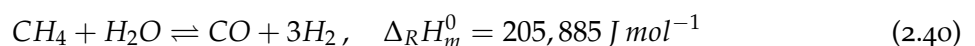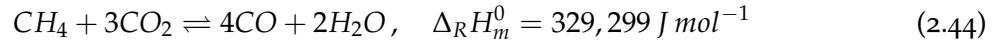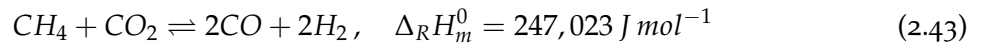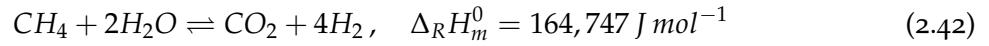
The above mentioned reactions are catalysed by the incorporated metallic catalyst in the anodic electrode of SOFCs. In state-of-the-art solid oxide fuel cells, nickel is used as a catalyst for both the chemical and the electrochemical reactions.

Besides the before mentioned reactions, also dry reforming (Eqs. (2.43) and (2.44)) is possible. The dry reforming reactions, Eqs. (2.43) and (2.44), are often neglected in modelling approaches in literature since they are quite slow in terms of kinetics. Eq. (2.42) is a linear combination of Eqs. (2.40) and (2.41) and thus provides no additional useful information. Therefore, it is also often neglected in simulation models found in literature [23].

The sign of the standard reaction enthalpies $\Delta_R H_m^0$ indicates whether the reaction is endothermic or exothermic. Eqs. (2.40) and (2.42) - (2.44) are increasingly endothermic, thus requiring energy to occur. Their spatial occurrence can be qualitatively detected by a temperature decrease in the region of the reaction. The water-gas shift reaction Eq. (2.41) is slightly exothermic, which indicates the release of energy at its occurrence. This can generally be measured by a temperature increase.

2.4.1. Homogeneous Reaction Kinetics

Chemical reaction kinetics have to be taken into account when physical and chemical transport processes show comparable time scales. Reaction kinetics describe the rate at which a reaction occurs, and consider both the temporal progress and reaction pathway of a chemical process from its initial condition until chemical equilibrium. The reaction kinetics of elementary reactions can be determined by measurements [24].

Homogeneous reaction kinetics can be used as a simplified approach to describing the catalysed reforming reactions. This simplification reduces the computational costs, but also significantly reduces the level of detail in reaction modelling, which thus limits the ability to conduct a detailed investigation of the processes that occur.

A bimolecular, gaseous elementary reaction can be expressed, as in Eq. (2.45) [24]:

$$\nu'_{st,A} A + \nu'_{st,B} B \underset{k_b}{\overset{k_f}{\rightleftharpoons}} \nu''_{st,C} C + \nu''_{st,D} D \tag{2.45}$$
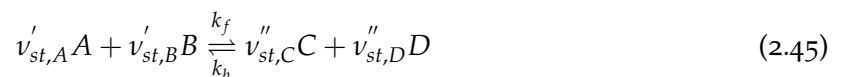
where $\nu'_{st,i}$ is the stoichiometric coefficient of reactant R, and $\nu''_{st,i}$ is the stoichiometric coefficient of product P. k_f and k_b are the reaction rate coefficients for the forward and backward reactions, respectively. In general, the reaction rate of a chemical reaction is given by Eq. (2.46) [24]

$$r = k_f \prod_i c_i^{v'_{st,i}} - k_b \prod_i c_i^{v''_{st,i}}. \tag{2.46}$$

In Eq. (2.46), c_i is the molar species concentration. The forward and backward reaction rate coefficients, k_f and k_b, are temperature dependent and can be deducted from molecular collision theory. This temperature dependence can be described by the Arrhenius equation, as for the forward rate coefficient in Eq. (2.47) [24]:

$$k_f = A\, T^\beta \exp\left(-\frac{E_A}{R_m\, T}\right) \tag{2.47}$$

where T^β represents the temperature dependency of the frequency factor A and E_A is the activation energy for the reaction. In order to describe a chemical reaction as it occurs, a number of elementary reactions are required. A collection of such elementary reactions, for the purpose of describing a process, e.g. the internal reforming of methane, is called a reaction mechanism (see Table 3.4 for a simple global reaction mechanism) [24].
The backward reaction rate coefficient k_b is calculated by the equilibrium constant K, as given by Eq. (2.48):

$$k_b = \frac{k_f}{K} = k_f \exp\left(-\frac{\Delta_R G_m^0(T, p^0)}{R_m\, T}\right)^{-1} \tag{2.48}$$

The forward and backward reaction rate constants are connected via the equilibrium constant K. The equilibrium constant K is defined by the standard Gibb's free energy of reaction $\Delta_R G_m^0(T, p^0)$, the gas constant R_m, and the temperature T. Thus, the equilibrium constant can be determined by thermodynamics and is independent of reaction kinetics.
Global homogeneous reaction kinetic mechanisms are frequently applied in numerical models for the internal reforming of methane in SOFCs. These are often simplified approaches that describe the overall process and are mainly used to calculate conversion rates and identify endothermic and exothermic regions within a cell. In Sections 3.3 and 3.4, different global reaction mechanisms are scrutinized for their usability in SOFC modelling applications.

2.4.2. Heterogeneous Reaction Kinetics

Heterogeneous reactions are of particular importance when it comes to modelling catalysed processes, such as the internal reforming of methane over nickel in SOFC anodes. A catalyst accelerates the rate of reaction by reducing the activation energy of the catalysed reaction compared to the same homogeneous reaction. The final equilibrium composition of the system is not disturbed by the catalyst. In contrast to homogeneous systems, heterogeneous systems are dependent of the gas phase, the mass flux to and from the catalyst surface and the surface

reaction chemistry. The reactions take place at the catalytically active centres. In a Langmuir-Hinshelwood mechanism, heterogeneous reactions in porous structures can be divided into four steps [24]:

- **Film and pore diffusion** of reactants and products: Reactive species diffuse through the outer film (see the diffusion models in Section 2.3) to and from the active centre in a pore
- **Adsorption** of reactants at the solid active centre from the gas phase
- **Surface reaction** of two adsorbed species
- **Desorption** of products into the gas phase by clearing the active centre

This reaction pathway is shown schematically in Figure 2.2 [24].
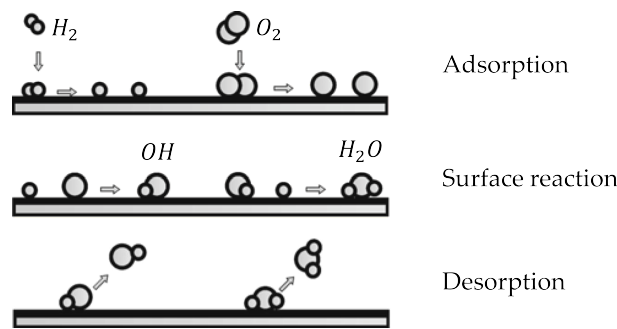
Figure 2.2.: Scheme of a catalysed hydrogen oxidation reaction [24]

In numerical models of heterogeneous systems, the rate of production and consumption of chemical species based on the above mechanism needs to be found. The rate of adsorption and desorption is governed by chemical kinetics, in addition to diffusion to and from the catalytically active centres. Thus, heterogeneous reactions create sources and sinks of chemical species in the gas phase, as well as on the reacting surface. The reaction rate of a surface reaction is given by Eq. (2.49) [25].

$$r = k_f \left(\prod_i^{N_g} c_{g,i}^{\eta_i'} \right) \left(\prod_j^{N_s} c_{s,j}^{\eta_{s,j}'} \right) - k_b \left(\prod_i^{N_g} c_{g,i}^{\eta_i''} \right) \left(\prod_j^{N_s} c_{s,j}^{\eta_{s,j}''} \right). \tag{2.49}$$

Here, $c_{g,i}$ and $c_{s,j}$ represent concentrations of gaseous and surface species, respectively, in their adsorbed states. For gaseous reactant and product species, η_i' and η_i'' are the corresponding rate exponents. $\eta_{s,j}'$ and $\eta_{s,j}''$ are the reaction rate coefficients of reactant and product site species. Based on this, the net molar rate of production or consumption of each species i is determined by [25]

$$r_{i,g} = \sum_{n=1}^{N_{nxm}} \left(v_{st,i,n}'' - v_{st,i,n}' \right) r_n \quad i = 1, 2, 3, \ldots, N_g \tag{2.50}$$

$$r_{i,s} = \sum_{n=1}^{N_{nxm}} \left(v_{st,s,i,n}'' - v_{st,s,i,n}' \right) r_n \quad i = 1, 2, 3, \ldots, N_s \tag{2.51}$$

where N_g and N_s are the total numbers of gaseous and surface species, respectively. $v'_{st,s,i}$ and $v''_{st,s,i}$ are the stoichiometric coefficients of surface reactant and product species. The surface site coverage $X(s)$ is defined as [25]

$$X(s) = c_{s,j}\, \rho_s^{-1} \tag{2.52}$$

where ρ_i is the surface site density, which describes the maximum number of adsorbed moles per area. The surface coverage of all adsorbed species adds up to unity. This surface site coverage will be used to discuss the processes that occur within the porosity of an SOFC anode [25].

In Section 3.4 (Table 3.8), a detailed heterogeneous reaction mechanism for the internal reforming of methane in high-temperature SOFC anodes is presented. This mechanism was implemented in the numerical code and was used to investigate and scrutinize the gas-surface interactions that occur during internal reforming. The production and consumption rates of all of the species involved were calculated based on the approach presented above.

2.5. Governing Transport Equations

This section provides a brief overview of the governing transport equations of the finite volume method (FVM) for usage in CFD. Basic aspects of the FVM and spatial discretization are not addressed in this thesis. The interested reader is referred to Ref. [26] for a detailed and comprehensive review of the topics of CFD and FVM. All of the transport equations are given their in differential form. The flow inside a SOFC single-cell housing is, in general, three dimensional. Thus, it requires a $3D$-simulation by solving the full Navier-Stokes equations. The flow inside SOFC flow structures is governed by the following conservation laws:

$$\frac{\partial \rho}{\partial t} + \nabla \cdot (\rho \vec{v}) = S^m \tag{2.53}$$

Eq. (2.53) is the general form of the mass conservation equation, where ρ is the density, t is time, $\vec{v}$ is the fluid velocity vector and S^m is a source term for mass added to the continuous phase (e.g. species production through chemical reactions).
The conservation of momentum is described by Eq. (2.54), whereby p is the static pressure, $\bar{\bar{\tau}}$ is the stress tensor, and $\rho \vec{g}$ is the gravitational body force. $\vec{F}$ are the external body forces, and also contain other model-dependent source terms, such as porous media or user-defined sources [27].

$$\frac{\partial}{\partial t}(\rho \vec{v}) + \nabla \cdot (\rho \vec{v}\vec{v}) = -\nabla p + \nabla \cdot (\bar{\bar{\tau}}) + \rho \vec{g} + \vec{F} \tag{2.54}$$

The simulations account for the conservation of energy with Eq. (2.55). Here, E is the total energy per unit mass, k_e is the effective thermal conductivity (defined according to the flow regime; either laminar or turbulent), $H_{m,i}(T)$ is the enthalpy of species i and $\vec{J}_i$ is the diffusive mass flux of species i [27].

$$\frac{\partial}{\partial t}(\rho E) + \nabla \cdot (\vec{v}(\rho E + p)) = -\nabla \left(k_e \nabla T - \sum_i H_{m,i}(T)\vec{J}_i + (\overline{\overline{\tau}} \cdot \vec{v}) \right) + Sh \qquad (2.55)$$

The terms on the right hand side of Eq. (2.55) are listed according to their rank: first the energy transfer due to conduction, then species diffusion, and then viscous dissipation. The source term S^h on the far right includes the heat of chemical reactions and any other volumetric heat sources within a fuel cell, such as ohmic heat generation. In all electrically conducting zones (e.g. current collectors or electrodes), ohmic heating is added to the energy equation as a source term. Additionally, the energy equation requires treatment at the electrode-electrolyte interface to account for the heat lost or generated as the result of overpotentials and electrochemistry (i.e. ohmic loss through the electrolyte and activation overpotential). Computation of the total energy balance on the electrolyte interface is done by means of the enumeration of all species' enthalpy flux, including the heat of formation (sources of chemical energy entering the system) and subtraction of the work done (leaving the system), which is the local voltage multiplied by the local current density. What remains is the heat due to irreversibilities.

Finally, the conservation of species needs to be fulfilled when a species conversion, such as a chemical reaction, occurs. The local mass fraction μ of a species i is calculated by Eq. (2.56)

$$\frac{\partial}{\partial t}(\rho \mu_i) + \nabla \cdot (\rho \vec{v} \mu_i) = -\nabla \cdot \vec{J}_i + r_i \qquad (2.56)$$

In Eq. (2.56), $\vec{J}_i$ is the diffusive mass flux of species i and r_i is the net rate of production of species i by a chemical reaction. $N-1$ transport equations are solved by the CFD code for N chemical species in the reaction system. The diffusive mass flux $\vec{J}_i$ of species i is solved according to the applied diffusion model, as presented earlier in Section 2.3.3. For the simulations involving diesel reformate, the Stefan-Maxwell model was used. For binary ($H_2 - H_2O$) and ternary ($H_2 - H_2O - N_2$) systems, Fick's model was applied.

For laminar flows, no chemistry-turbulence interaction is applied as they can generally be expected in high temperature SOFC fuel channels. The reaction rates r_i that appear as source terms in Eq. (2.56) are computed using the general reaction-rate expressions. This finite rate kinetics approach is recommended for laminar flows, where the formulation is exact. The effect of turbulent fluctuations on kinetics rates are neglected, and reaction rates are determined directly by general finite-rate chemistry. These net rates of production or depletion are calculated using either Eq. (2.46) for homogeneous reactions or Eq. (2.49) for heterogeneous reactions. Thus, no additional models are used for the reaction modelling.

Simple one- or two-step homogeneous reaction mechanisms to describe the internal reforming of methane (as given by Eqs. (2.40) and (2.41)) in a numerical model can be implemented and applied at low additional computational cost.

However, the implementation of a detailed heterogeneous reaction mechanism (as was used in this thesis, see Table 3.8), based on elementary reactions and solved by a laminar-finite rate approach in a transient time scale, results in a significant additional computational load. Additionally, the sub-model used to describe the performance of the SOFC (as described in the next section) introduces further species and energy source terms that require further computational power.

The simulation model generated is thus capable of describing the detailed chemical reaction steps that take place during internal reforming and load operation on both a transient and steady-state time scale, which results in the need for a distinct amount of computational power.

2.6. The Numerical Representation of a SOFC

There exists a range of either open source or proprietary numerical modelling software for three-dimensional flows. The simulations performed for this research project were carried out with the commercially-available CFD modelling program, ANSYS Fluent [25]. An additional electrochemistry sub-module, referred to as 'SOFC Fuel Cell With Unresolved Electrolyte' was used to cover the electrochemical reactions of a SOFC [27]. As indicated by its name, in the sub-module, the electrolyte is treated as a thin surface which separates the two electrodes. The electrolyte was thus only resolved in two dimensions ($x-$ and $y-$direction) as an infinitesimally thin plane, but its thickness was not geometrically discretized.
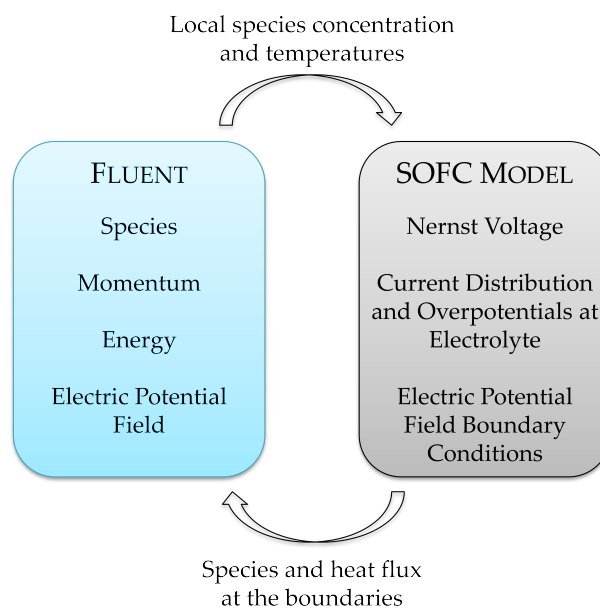
Figure 2.3.: Scheme of Fluent solver and SOFC sub-module interaction [27]

Figure 2.3 provides a schematic of the sub-module's integration in Fluent. The sub-module's task is to couple the electric field with the mass, momentum, species, and energy transport that come about as a result of the local electrochemical reactions. The electric field is used as a boundary condition for solving all transport equations, and is solved for all solid parts (current collectors and porous electrodes). Furthermore, the sub-module also accounts for the entropy losses and heating effects brought about by chemical reactions. The sub-module performs the following tasks:

- Balances of mass and heat in the flow channels and in the porous electrodes.
- Transport of electric current and the electric potential field in solid conductors and porous zones.
- Modelling of the electrochemical reactions that occur at the electrode-electrolyte interface (TPB).

The three-dimensional electrical conduction is solved in a similar way to the calculation of heat transfer. The calculation of the potential field in the conductive regions is based on the conservation of charge. The governing equation for the electric field is the Laplace equation:

$$\nabla \cdot (\sigma_{el} \nabla \phi) = 0 \qquad (2.57)$$

In Eq. (2.57), σ_{el} is the electrical conductivity and ϕ is the electrical potential. The electric field calculation combines ohmic losses in all conducting materials (electrodes, electrolytes and current collectors), contact resistances at the relevant interfaces, ohmic heating brought about by ohmic losses in the conductors, and the current density throughout the domain. The sub-module assumes uniform contact between the electrodes and the current collectors.

The electrochemistry and the electric field interact only at the electrolyte interface. The CFD code treats this interface as an impermeable wall. To account for the effect of electrochemistry, a 'jump' condition is applied to the two sides of the electrolyte (wall and shadow-wall), so that the potential field can be solved. In order to couple the electrochemical behaviour with the potential field, all of the electrochemical effects that occur have to be included in this jump condition and therefore equal the actual cell voltage U_{cell}. Thus, all loss mechanisms, as described in Section 2.3, are accounted for, including the Nernst voltage U_{Nernst}, activation overpotentials η_{Act} on both the anode and cathode, ohmic electrolyte losses, and ohmic losses in solid conductors η_{Ω}. This correlation (Eq. (2.58)) describes the voltage difference on the anode and the cathode side of the electrolyte, as was presented in a more general form in Eq. (2.17).

$$U_{cell} = U_{Nernst} - \eta_{\Omega} - \eta_{Act,a} - \eta_{Act,c} \qquad (2.58)$$

η_{Ω} represents the sum of all ohmic overpotentials of the electrolyte and ohmic losses in the conducting regions (current collectors and porous electrodes), as shown in Section 2.3.1. The

activation overpotentials η_{Act} at the anode and cathode are calculated using Newton's method to solve the full version of the Butler-Volmer equation, as given by Eq. (2.20). Additionally, the energy equation needs to be modified at the electrode-electrolyte interface in order to account for all of the losses that occur (activation and ohmic losses through the electrolyte). The overall energy balance on the electrolyte surface is determined by the enthalpy flux of all species, including the heat of formation of electrochemical reactions. The excess heat $\dot{Q}_{H_2}$ due to irreversibilities can thus be calculated for the hydrogen reaction as seen in Eq. (2.59).

$$\dot{Q}_{H_2} = \dot{H}_{H_2} + \dot{H}_{O_2} - \dot{H}_{H_2O} - i\Delta U \tag{2.59}$$

In Eq. (2.59), $\dot{H}_i$ are the enthalpy fluxes for the participating constituents and ΔU is the local voltage jump. The irreversibilities are then put as a source term S^h $\left(S^h = \dot{Q}_{H_2}/V_{zone}\right)$ in equal amounts into both electrodes. V_{zone} is the volume of the corresponding cell zone.

The fuel cell module also accounts for CO electrochemistry, as given in Eq. (2.3). Carbon monoxide oxidation is modelled by an H_2/CO split factor α_s, if CO is available in the anodic fuel channel:

$$\alpha_s = \frac{\nu_{H_2}}{\nu_{H_2} + \nu_{CO}} \tag{2.60}$$

In Eq. (2.60), ν_{H_2} and ν_{CO} are hydrogen and carbon monoxide mole fractions, respectively. The electrochemistry is modelled to occur at the electrode-electrolyte-interface. By using the information of the local current density, the species molar flux to the electrode boundaries is computed according to Eq. (2.61) for the cathode, and according to Eqs. (2.62) and (2.63) for the anode side.

$$S^{O^{2-}} = -\frac{i}{2F} \tag{2.61}$$

$$S^{H_2} = -\frac{\alpha_s i}{2F}, \quad S^{H_2O} = \frac{\alpha_s i}{2F} \tag{2.62}$$

$$S^{CO} = -\frac{(1-\alpha_s)\,i}{2F}, \quad S^{CO_2} = \frac{(1-\alpha_s)\,i}{2F} \tag{2.63}$$

Here, $S^{O^{2-}}$ is the cathodic oxygen ion molar flux, whereas S^{H_2}, S^{H_2O}, S^{CO}, and S^{CO_2} are the anodic molar fluxes of electrochemical reactants and products. These fluxes in Eqs. (2.61) - (2.63) are calculated by the split factor α_s, the current density i, and the Faraday constant F. The fluxes are put in Eq. (2.53) as mass source terms S^m [27].

3

Creation of a Flexible Simulation Base Model

Numerical modelling is a highly useful tool for understanding the variety of superimposed transport phenomena in SOFCs. There are two major different approaches to modelling that are investigated in literature: these are (1) micro-modelling and (2) macro-modelling approaches. Micro-models consider the functional or electrochemically active layer of the electrode to be a discrete volume, comprising a randomly-packed electrocatalyst and electrode materials. In many cases, these correspond to the atomic or molecular level. The representative length scales of micro-models are $10^{-9}\,m$ and those of time scales are $10^{-12}\,s$. Macro-models deal with the macroscopic or overall operational behaviours of SOFCs. Macro-modelling is mostly done by means of the finite-volume-discretization method, using commercially available CFD codes, such as ANSYS Fluent, STAR-CD, COMSOL Multiphysics or FLOW3D. These codes make it possible to locally and temporally predict and visualize flow and temperature profiles, species distributions within the porous anodic structure, and the flow channels that are brought about by internal reforming reactions and electrochemical reactions [28–31].

The increasing computational power of commercial workstations affects electrochemical devices' ability to run numerical simulations. This means that large planar single cells, short stacks, and entire stacks can be investigated with decreasing computing time. In [32–36], various simulation approaches were used to scrutinize both the electrochemical and thermal performance of different high temperature fuel cell designs and layouts. CFD applications are powerful tools to carry out in-detail investigations of chemical and electrochemical reactions, thanks to their versatility in terms of code customization and reaction modelling. The numerical model of any kind of high temperature fuel cell makes it possible to study all of the processes that occur therein, and to identify their impact when superimposed. The coupling of all the physical, chemical and electrochemical transport processes that occur inside a fuel cell system results in a simulation model close to reality. Thus, locally-resolved temperature, species, or current density distribution can be calculated and visualized, as shown in [37–39]. The experimental measurement of spatial temperature, species, and current density distribution inside a high temperature reducing/oxidizing environment is an extraordinarily demanding task. Thus,

numerical models can be effectively used as an economic alternative. A numerical simulation model facilitates both understanding and visualization of the reactions and processes that occur within its validated limits.

In this chapter, a simulation model of a $100 \times 100\,mm^2$ SOFC is created and investigated in terms of its performance on different fuels, at varying temperature levels, and its eligibility to be used as a base model for the simulation of degradation phenomena. This chapter is divided into four main sections: (3.1) a detailed description of the experimental test bench and all of its parts, (3.2) the creation of a simulation base model for an entire planar cell fed with hydrogen, (3.3) the use of hydrocarbon-containing fuel mixtures to investigate internal reforming in a different cell type, and (3.4) the scrutiny of methods to describe the performance degradation that is brought about by carbon deposition during the internal reforming of hydrocarbon-containing fuel mixtures. The model is then validated with experimental data on electrochemical, chemical, and thermal performance so as to ensure correctness of the model.

3.1. The SOFC Test Bench at the Institute of Thermal Engineering[1]

Figure 3.1 shows a scheme of the SOFC test bench. This experimental test bench is composed of a gas control system with calibrated mass flow controllers (MFCs) (M+W Instruments D5100) for gaseous species (Hydrogen ($H2$), carbon monoxide (CO), methane ($CH4$), carbon dioxide ($CO2$) and nitrogen ($N2$)), a humidifier system (bubbler), and a furnace, in which a ceramic cell housing was installed.
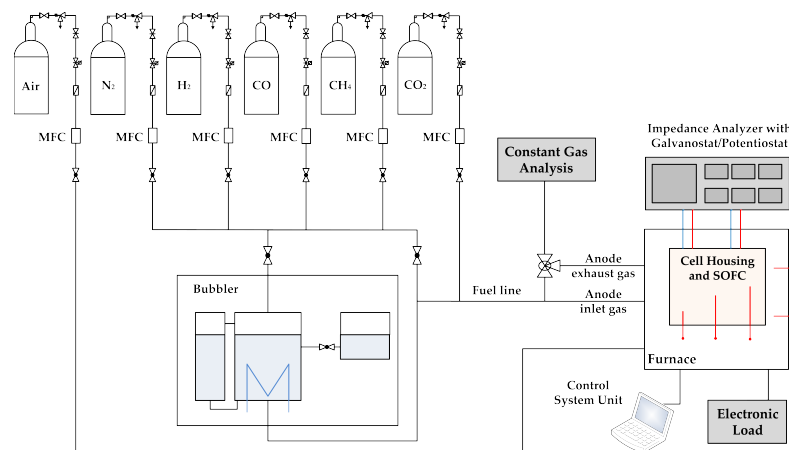
Figure 3.1.: Test bench scheme [42]

Furthermore, it contains a gas analyser (ABB Advance Optima Uras 14 + Caldos 17) for continuous gas species measurement of (CH_4, CO, CO_2 and H_2) at the fuel cell's anode inlet and outlet; thermocouples within the furnace and the fuel line; and a control system unit. Heating of the testing apparatus was controlled by the measurement readings of thermocouples

---

[1]Segments of this section were published in the *International Journal of Hydrogen Energy* under the title "Three-dimensional numerical and experimental investigation of an industrial-sized SOFC fueled by diesel reformat": Part I [40], Part II [41].

placed inside the testing chamber. The water temperature within the bubbler, or rather, the corresponding partial pressure, controlled the humidification of the fuel. Complete saturation was presupposed and validated by comparative measurements. The humidity of the gas was verified and calibrated by condensing the water vapour in the fuel stream. All of the required fuel species, with the exception of CO_2, were mixed before entering the humidifier, based on their required compositions. Carbon dioxide was excluded due to its solubility in water. The fuel cell itself was placed inside the ceramic cell housing. A schematic diagram of the housing is shown in Figure 3.2(a).

The ceramic Al_2O_3 single cell housing consists of a multitude of parts, which can be assigned to two assembly groups: (1) the anodic parts; and (2) the cathodic parts. Their main requirement is to feed the particular flows to the anode and cathode side. Furthermore, the parts were designed to prevent mixing of the flows in order to impede uncontrolled oxidation of the fuel. Fuel was fed to the anode side, whereas the oxidant was fed to the cathode side of the housing (cf. Figure 3.2(a)).

(a) Entire cell housing [40]   **(b)** Main parts [41]
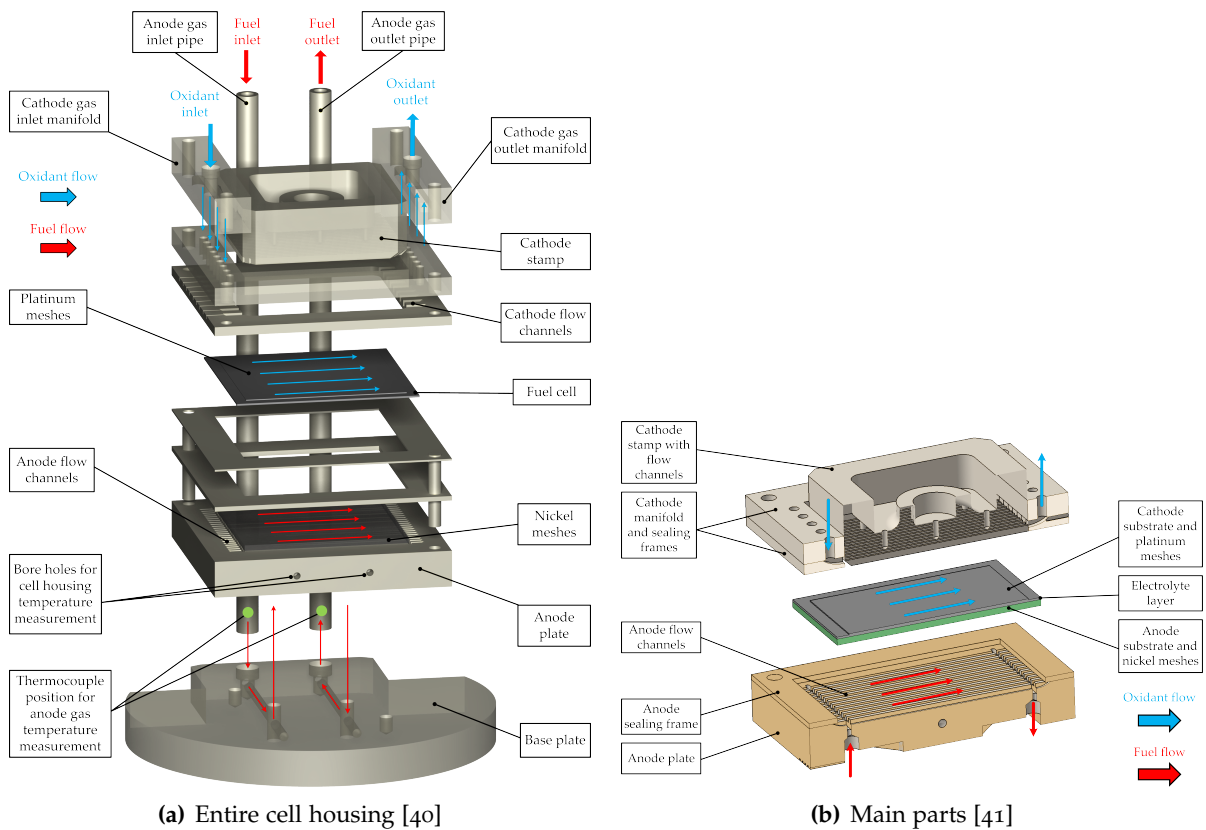
Figure 3.2.: Exploded views of the ceramic cell housing

All of the parts necessary to position and seal the $100 \times 100\,mm^2$ SOFC single cell are shown and identified in Figure 3.2(b). The oxidant flow is indicated by blue arrows. Red arrows indicate the fuel flow path. As can be seen from the direction of the arrows, the gases are supplied in co-flow condition. Thus, both fluids flow in the same direction. Ceramic sealing frames of different sizes and thicknesses were used to seal the two fluid flows. In addition to this surface seal, which is achieved by means of the planar frames, a glass sealing material was

used between the electrolyte and cathode frame to establish a high-quality seal. In order to ensure a clear and thorough understanding of their complex geometry, both flow fields will be discussed in detail below.

3.1.1. Anode Flow Field

The SOFC test bench can be used to supply the single cell housing with both dry and hu-midified fuels. These fuels can be any gaseous fuel eligible for use in SOFCs. The fuel was led through the vertical anode gas inlet pipe into the base plate. It was guided to the anodic plate through internal bore holes. The gas was then distributed across the whole cell width to thirty-four flow channels. The quality of the distribution was investigated numerically and is scrutinized in Section 3.2. Within these channels, the fuel streamed along the fuel cell's anode, where it was electrochemically oxidized. Finally, the gas was led through the anodic plate and the base plate to the anode outlet pipe. The anode fuel flow is schematically represented by solid red arrows in Figs. 3.2(a) and 3.3. Thermocouples for temperature measurement were installed inside the anode plate and the inlet and outlet pipes in order to verify the temperature distribution along the cell (see Figure 3.2(a)). In order to conduct the electrical current, metallic current collectors (nickel meshes of different aperture sizes) were applied between the anode plate and the fuel cell.

Type N thermocouples (shielded against radiation effects and calibrated) were placed inside the anodic fuel pipe (see green dots in Figure 3.2(a)) to measure the fuel's inlet and outlet tem-peratures. Experimentally determined outlet temperatures were used as validation parameters, in addition to anode outlet species concentrations and the electrical performance of the cell. A comparison of the simulations and experiments carried out is shown in Section 3.3.3. In Figure 3.2(b), a simplified and magnified exploded view of the cell housing is shown to provide a better view of the complex inner geometry of the cell housing.

3.1.2. Cathode Flow Field

The cathodic gas was applied at the cathode inlet manifold. Depending on the requirements, the SOFC test bench can provide the cathode flow field with ambient air, compressed air, synthetic air, or pure oxygen, O_2. Similar to the anode side, the stream on the cathode side was directed through bore holes to the fuel cell's cathode. It was also uniformly distributed across the cell's width by means of several thin flow channels. The exhaust air was led out of the cathode flow side at the outlet manifold. Solid blue arrows depict the air flow through the cathode side of the cell housing (see Figure 3.2(a) and 3.2(b)). Electrical contacting of the cathode was accomplished using both fine and coarse platinum meshes.

3.1.3. Fuel Cell Properties

The assembled cell housing is depicted in Figure 3.3(a). Therein, it can be seen that the cell housing was designed to form a high-quality seal around the two flow fields. The housing is placed in this assembled state is heated up to the desired operating temperature (800 °C for an anode supported cell) in an electric furnace. A specific heating procedure is applied to ensure a high-quality seal, enable complete reduction of the anodic catalyst, and avoid the induction of unwanted thermal stresses.

(a) Assembly and flow explanation   **(b)** Scheme of cell layers and flow configuration
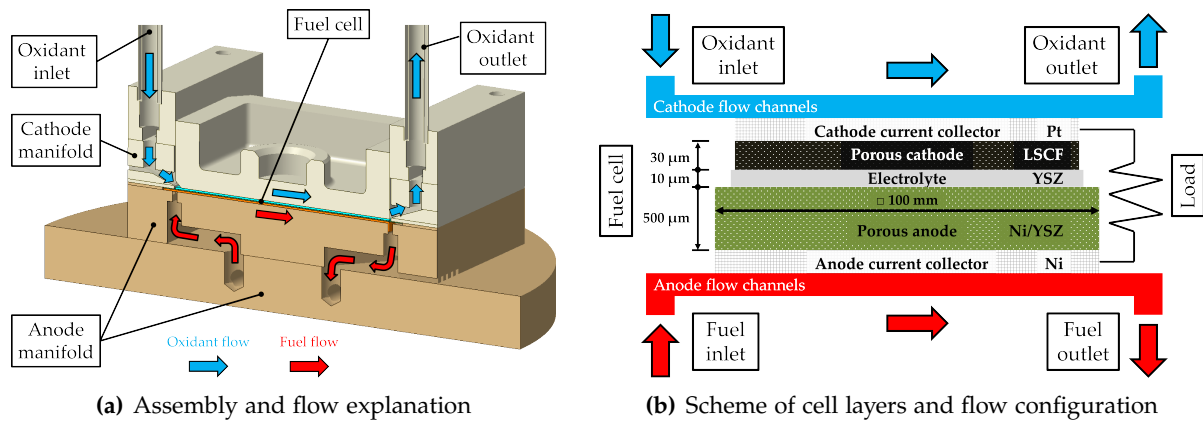
Figure 3.3.: Cell housing assembly and scheme of fuel cell setup

In Figure 3.3(b) a simplified schematic of the cell's cross-section is shown. As described above, the anode and cathode are supplied with fuel and oxidant, respectively. Metallic current collectors are inserted on top of the anodic and cathodic substrates to close the electric circuit. These current collectors are nickel and platinum meshes on the anode and cathode sides, respectively. Furthermore, these meshes are used to evenly distribute the gases across the cell and to provide uniform mechanical and electrical contact on the cell. The cell dimensions are also given in Figure 3.3(b). As can be seen from the schematic, a 500 μm thick porous Ni-YSZ anode layer ensures the mechanical stability of the cell. A dense 10 μm YSZ electrolyte is layered upon the anode. A 5 μm CeO_2 barrier layer (not shown in the schematic) was put on top of the electrolyte to prevent unwanted nickel-ion diffusion from the anode through the electrolyte to the cathode [43]. A mixed-ionic-electronic conducting Lanthanum Strontium Colbat Ferrite (LSCF) cathode, with a thickness of 30 μm was used as the oxidant electrode. All materials and important dimensions are provided in Figure 3.3(b). Based on the given information, it is possible to create a numerical model to predict and calculate cell performance.

3.2. Performance of an Anode Supported SOFC Fuelled with Hydrogen

As described above, a three-dimensional CFD model of the complete anode-supported SOFC, fed with mixtures of hydrogen and water vapour, was generated in order to investigate the

flow conditions inside the cell housing and to validate the performance of the electrochemistry module. The overall dimensions of the planar SOFC were $100 \times 100\,mm^2$ for the anode and $90 \times 90\,mm^2$ for the electrolyte and cathode. The cells thus had a catalytically active area $90 \times 90\,mm^2$. Many studies use planar or button cells with a much lower active area [44–47]. These types of cells are easier to handle, since the establishment of a high-quality gas seal is simpler. The use of large planar cells requires a central and uniform application of force, which is a demanding task at such high operating temperatures. Meaningful experimental results are thus harder to obtain and denote a valid experimental procedure, if reproducibility can be established. The cells examined in this thesis are more likely to be used in future technical applications due to their large active area, which results in a reasonable power output. The simulations and experiments in this dissertation therefore provide representative results for cells that are suitable for commercial use.

(a) $3D$-Model of the entire cell with anodic and cathodic flow channels

(b) Detail of the computational grid
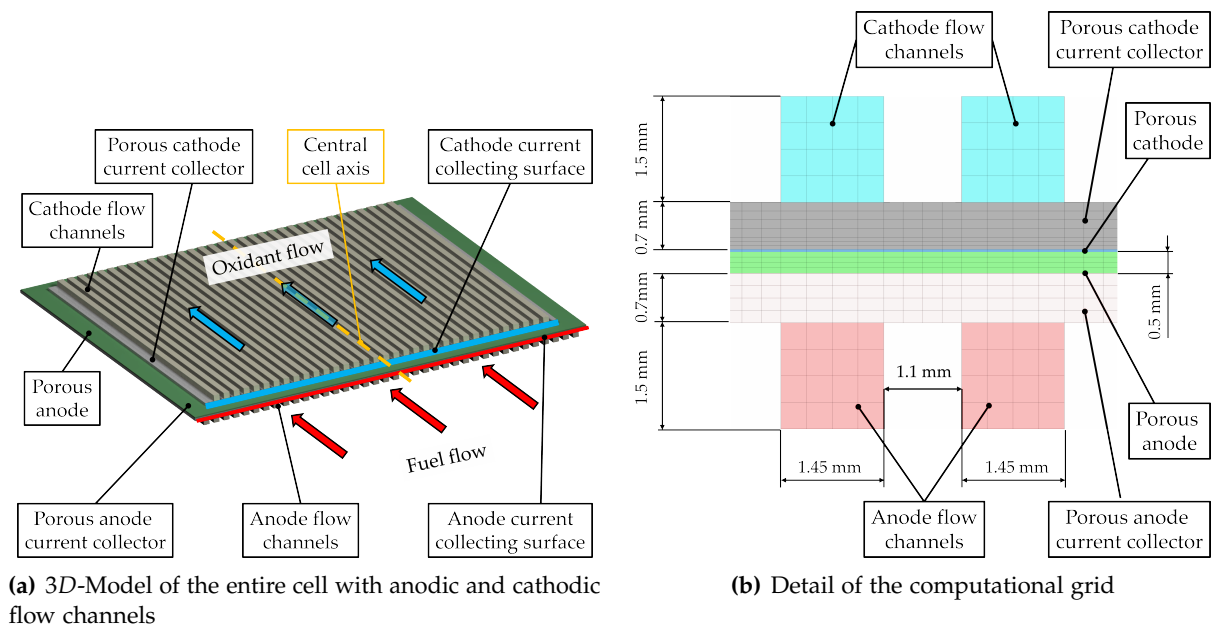
Figure 3.4.: Geometric model and detail of the spatial discretization

In Figure 3.4, a schematic of the $3D$-model of the entire cell (Figure 3.4(a)) alongside a magnified detail of two channel ribs with the relevant dimensions and spatial discretization (Figure 3.4(b)) is shown. The model of the entire cell only consists of the anodic and cathodic flow channels, the porous current collectors, and the porous electrodes. The $10\,\mu m$ thin electrolyte makes it possible to use a numerical approach that does not make it necessary to geometrically discretize this thin layer. Thus, it was modelled as a thin, existing layer, but was not geometrically-discretized. The numerical domain was discretized with hexahedral cells, as can be seen in Figure 3.4(b). Due to the geometrical boundary conditions, the entire model was discretized by a conformal mesh of only 9.5×10^5 cells, with a maximum skewness of 0.1 and a maximum aspect ratio of 40. The SOFC sub-module requires a conformal mesh in order to correctly predict the electrochemical performance of the cell, such as the Nernst voltage, as well as the ohmic and activation overpotentials.

3.2.1. Boundary Conditions

The fuel and oxidant were fed to the anode and cathode flow channels in a co-flow condition. The flow conditions of the two inlet manifolds were evaluated in separate simulations, and the mass flow profile was set as boundary conditions for the flow channel inlets. The outlets were defined as pressure outlets. The current collection point for the model was set at the outer surfaces of the nickel (anode) and platinum (cathode) meshes. These current collecting surfaces are schematically indicated in Figure 3.4(a) as red and blue surfaces. As initially stated, dry and humidified (0, 0.03 and 0.11 $mol_{H_2O}\, mol^{-1}$) hydrogen ($0.45\, mol\, mol^{-1}\, H_2$) in nitrogen were used as fuels for the experiments and simulations. Synthetic air ($0.21\, mol\, mol^{-1}\, O_2$ in N_2) was used as an oxidant. The operating temperature was set to $800\,°C$, which is a typical value for ASCs. A volumetric anodic flow rate of 2.4 standard liter per minute (SLPM) was used for all of the cases investigated. The synthetic air flow rate was set to 4 SLPM. These volumetric flow rates were converted according to mass flow rates, and applied to the relevant inlets.

Both the fuel mixture and air were modelled as incompressible ideal gases. The density was therefore assumed to be dependent only on the temperature. This seems to be a good assumption, due to marginal pressure changes within the flow field. The determination of the specific heat capacity c_p of both the gas mixture and the air was taken into account by the composition-dependent mixing law. The mixture's specific heat capacity was calculated as a mass fraction μ_i average of the pure species heat capacities $c_{p,i}(T)$:

$$c_{p,mixture}(T) = \sum_i \mu_i\, c_{p,i}(T). \tag{3.1}$$

Thermal conductivity λ as well as the dynamic viscosity η were both calculated by the ideal gas mixing law. The particular heat capacities $c_{p,i}(T)$, thermal conductivities λ_i and viscosities η_i were calculated by polynomials of the fifth or sixth order, depending on the species [48].

The fuel cell's anode was electrically contacted by layers of fine and coarse nickel meshes of different aperture sizes. On the cathode side of the cell, platinum meshes were applied in order to conduct the electrical current. Porosity of the different mesh types and layers were calculated based on geometrical considerations of the mesh aperture and the wire diameters. A simplified mesh unit was considered to ensure the porosity of the entire mesh. The material properties of the fuel cell's anode and, cathode as well as the corresponding current collector materials can be found in Table 3.2.

The ANSYS SOFC sub-module offers the possibility to define a reference boundary condition with corresponding anodic and cathodic reference exchange current densities. These exchange current densities represent the corresponding electrochemical reaction rates of the anode or cathode. The reference anode and cathode exchange current densities were calculated based on a $0D$-polarization curve model, and are dependent on the boundary conditions applied, including, among others, temperature, species partial pressures, and the TPB length. The

reference condition was thus set to $0.45\ mol\ mol^{-1}\ H_2$, $0.11\ mol\ mol^{-1}\ H_2O$, and supplementary N_2. The reference exchange current densities were calculated to be $i_{0,A} = 21,589\ A\ m^{-2}$ and $i_{0,C} = 2,053\ A\ m^{-2}$ for the anode and cathode, respectively. The actual current densities and activation losses were determined, based on the Butler-Volmer equation (2.20). The fuel composition and reference exchange current densities are shown in Table 3.1.

Table 3.1.: Fuel compositions, w.b. (N_2 supplementary)

ν_{H_2} in $mol\ mol^{-1}$	ν_{H_2O} in $mol\ mol^{-1}$	$i_{0,A}$ in $A\ m^{-2}$	$i_{0,C}$ in $A\ m^{-2}$
0.45	0		
0.45	0.03		
0.45	0.11	$21,589$	$2,053$

Table 3.2 contains the material parameters that were used for the simulation, including porosity, tortuosity, thermal conductivity, heat capacity, electrical conductivity, and density of all incorporated cell layers, materials and model properties.

Table 3.2.: Material parameters used for simulations on hydrogen feeds

Parameter	Value	Unit
Cathode current collectors		
Porosity ε	0.856	$-$
Tortuosity τ	1.5	$-$
Electrical conductivity σ	$2.66 \cdot 10^6$	$\Omega^{-1} m^{-1}$
Density ρ	$21,200$	$kg\ m^{-3}$
Cathode LSCF		
Porosity ε	0.35 [49]	$-$
Tortuosity τ	4.5 [50]	$-$
Thermal conductivity λ	11 [51]	$W\ m^{-1} K^{-1}$
Specific heat capacity $C_{mp,i}$	900 [49]	$J\ kg^{-1} K^{-1}$
Electrical conductivity σ	$4.2 \cdot 10^7 T^{-1} exp^{-\frac{1200}{T}}$ [52]	$\Omega^{-1} m^{-1}$
Density ρ	$6,000$ [49]	$kg\ m^{-3}$
Electrolyte		
Thermal conductivity λ	2 [51]	$W\ m^{-1} K^{-1}$
Specific heat capacity $C_{mp,i}$	300 [49]	$J\ kg^{-1} K^{-1}$
Ionic conductivity σ	$100(0.3685 + 0.002838 \exp^{\frac{10,300}{T}})^{-1}$ [27]	$\Omega^{-1} m^{-1}$
Density ρ	$5,560$ [49]	$kg\ m^{-3}$
Anode Ni-YSZ		
Porosity ε	0.45 [49]	$-$
Tortuosity τ	4.5 [50]	$-$
Thermal conductivity λ	10 [51]	$W\ m^{-1} K^{-1}$
Specific heat capacity $C_{mp,i}$	650 [49]	$J\ kg^{-1} K^{-1}$
Electrical conductivity σ	$9.5 \cdot 10^7 T^{-1} \exp^{-\frac{1,150}{T}}$ [52]	$\Omega^{-1} m^{-1}$
Density ρ	$6,200$ [49]	$kg\ m^{-3}$
Anode current collectors		
Porosity ε	0.4	$-$
Tortuosity τ	1.5	$-$
Electrical conductivity σ	$2.282 \cdot 10^6$	$\Omega^{-1} m^{-1}$
Density ρ	$8,900$	$kg\ m^{-3}$

In Table 3.2, all of the required material and model parameters are listed, except for the contact resistance between the current collectors and their respective electrode layers. This resistance

is dependent on the mechanical force applied to the cell to ensure a gas-tight seal and adds linearly to the ohmic losses of the cell, as shown in Eq. (2.58). This value cannot be estimated experimentally. Thus, the decision was made to adapt the ohmic losses of the numerical model to the experimental results. Thereby, the contact resistance was found to equal $0.02\,m\Omega\,m^2$.

3.2.2. Numerical Setup for All Simulations in This Chapter

Steady state simulations were conducted to predict the cell performance, overpotentials, flow profile, species and temperature distributions. A double precision pressure-based (segregated) solver was used. Due to a very low averaged Reynolds number, in both the anode and cathode flow channels, a laminar flow regime was assumed. This was deduced using a standard correlation for flows inside a rectangular channel [53]. For laminar flows, Darcy's law is used to model flow in the porosity. Radiative impacts were neglected because this single cell housing is within an electrically-heated furnace and is therefore operated at a constant temperature.

Furthermore, thermal boundary conditions for all walls were set to be adiabatic. An adiabatic boundary condition is an arguable approximation, due to the experimental setup: the ceramic cell housing is put inside an oven that is held at a constant temperature by several heating coils. The temperature increase during the operation of the single fuel cell was experimentally determined to be small. This will be validated in the simulation. Pressure-velocity coupling was done by means of a Semi-Implicit Method for Pressure-Linked Equations (SIMPLE) scheme. Momentum, species, energy and the electrochemical (SOFC) sub-module equations were discretized by second-order upwind schemes. For pressure, the standard discretization scheme was applied. Fluid flow-chemistry interaction was modelled with a laminar finite rate approach. Stop criteria that indicated a converged solution were set when the residuals of continuity and (x, y and z)-velocity fell below 10^{-5} and when the residuals of species, energy, and SOFC equations were below 10^{-7}. In addition, monitors on several features, such as cell voltage, species molar fractions at the outlets, and the temperature at the anode outlet were monitored and analysed. When their values remained stable, the simulation was considered to be converged and was aborted. The calculation time varied for different simulations, such as when differing Arrhenius-type reaction paths were investigated. To give an approximate guiding value, convergence was reached after $10,000$ iterations, which, on the workstations in use (Intel Core-i7-3930 6 x 3.20 GHz, 32 GB RAM), corresponds to a calculation time of about twenty hours.

3.2.3. Performance Validation of The Electrochemistry Model

The performance of a fuel cell is best described by its characteristic curve, the polarization curve. Therein, cell voltage is plotted over current or current density. The polarization curves for the three fuel feeds described in Table 3.1, with varying water vapour content, are shown in Figure 3.5.
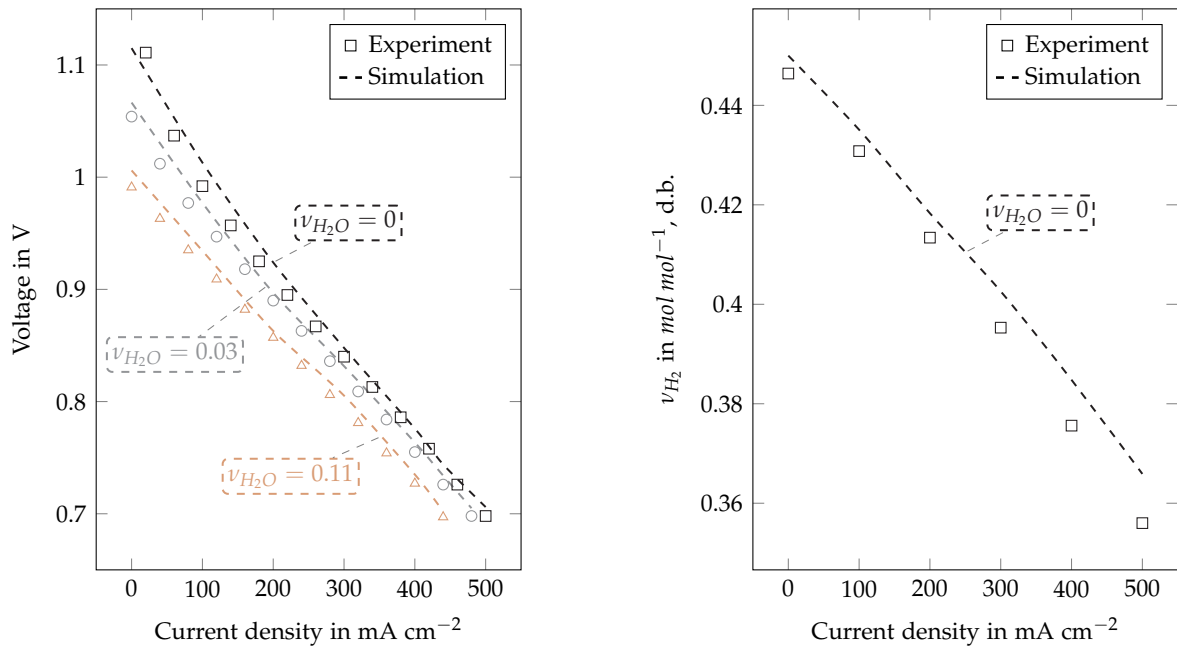
(a) Polarization curves of dry and humidified hydrogen mixtures at $800\,°C$

(b) Outlet composition for dry hydrogen fuel, d.b.

Figure 3.5.: Validation of the SOFC sub-module at $800\,°C$

As can be seen from Figure 3.5(a), high power outputs were achieved for the cells fuelled with dry and humidified hydrogen (markers represent experimental values). The lower voltage limit was set to $0.7\,V$, since this is the threshold value for nickel oxidation at $800\,°C$ [54]. Thus, every polarization curve measurement was stopped at $0.7\,V$. The highest power output was measured with a dry hydrogen fuel ($500\,mA\,cm^{-2}$). According to the Nernst-equation (Eq. (2.15)), the OCV decreases with increasing water vapour partial pressure. The performance and validity of the numerical SOFC model created can be seen by the dashed lines. The model predicted the electrochemical performance of the three investigated fuel compositions over the entire load range with high accuracy. The highest relative deviations between the numerical and experimental results occurred for the fuel mixture with $0.11\,mol\,mol^{-1}$ water vapour, and amounted to $+1.17\,\%$. Deflections for the other gas mixtures were lower. The simulation model slightly overestimates the electrochemical performance of all gas mixtures. The deviation mentioned above is by far the greatest deviation that occurred and thus reflects the high accuracy and validity of the simulations.

A comparison between the experimental and numerical outlet gas composition for the dry hydrogen fuel is shown in Figure 3.5(b). The plotted molar amounts refer to a dry base. The experimental and numerical results are also in very good agreement. Relative deviations between the numerical and the experimental data are in the range of $+0.8$ and $+2.7\,\%$, with an average deviation of $+1.68\,\%$. These results further underline the validity and accuracy of the numerical model.

The results presented above make it possible to state that the simulation model created predicts the chemical and electrochemical performance of an ASC with marked accuracy. This means

that the numerical results have been validated, and the model can therefore be used to further scrutinize the processes that occur within cells, and to investigate local and temporal effects occurring within the anodic substrate. These effects, including current density distribution, local species inhomogeneities, velocity and temperature distributions, and locally varying activation losses can be investigated with the generated model. Selected simulation results are displayed hereafter.

3.2.4. Simulation Results for Selected Operating Points

This section will display and discuss the simulation results of $0.03\,mol\,mol^{-1}$ humidified hydrogen at various cell loads. First, a cross-section of the anodic and cathodic flow channels is investigated. This cross-section is located at the centre of the fuel cell. Its position is shown schematically in Figure 3.4(a).

(a) Contours of O_2 molar fractions at $100\,mA\,cm^{-2}$

(b) Contours of H_2O molar fractions at $100\,mA\,cm^{-2}$, w.b.

(c) Contours of O_2 molar fractions at $480\,mA\,cm^{-2}$

(d) Contours of H_2O molar fractions at $480\,mA\,cm^{-2}$, w.b.
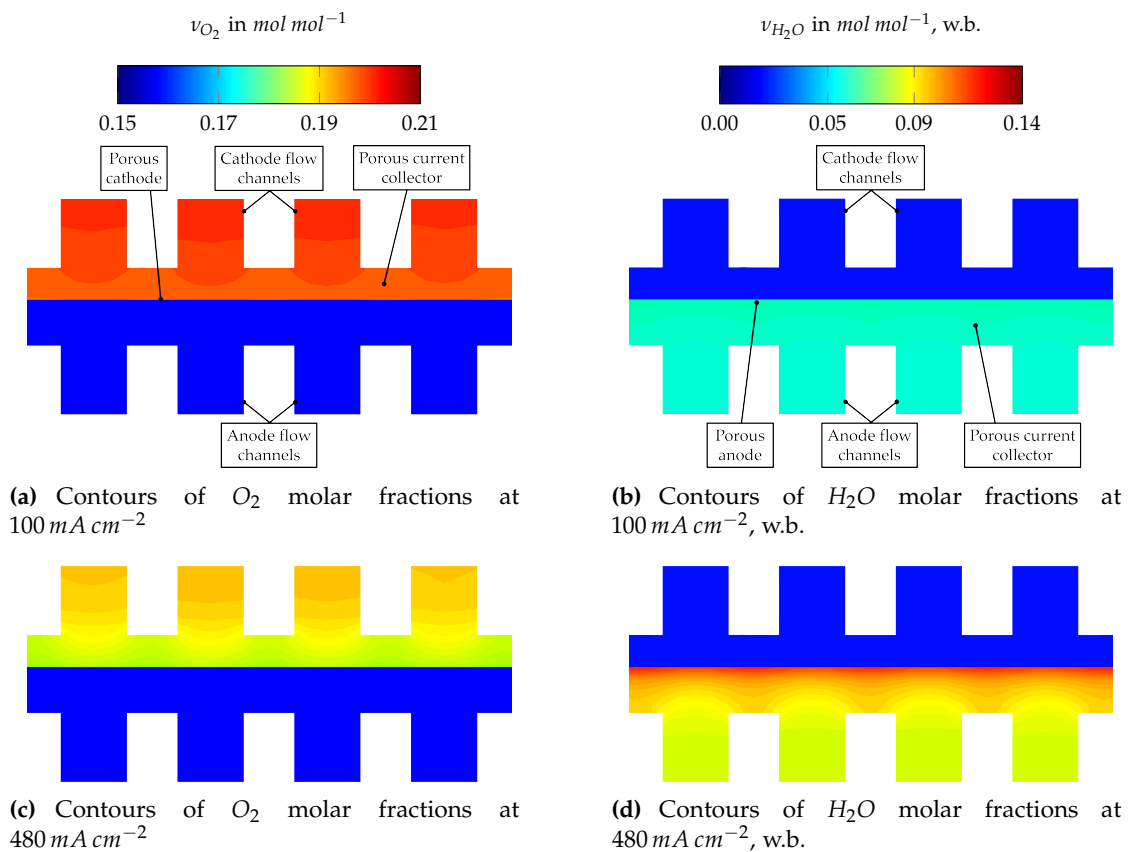
Figure 3.6.: Contours of O_2 and H_2O in the flow channels at $800\,^{\circ}C$ at various cell loads

Figures 3.6(a) and 3.6(c) show the contours of the oxygen molar fractions within the cathodic flow channels, the porous current collectors, and the porous cathode. At $100\,mA\,cm^{-2}$ (cf. Figure 3.6(a)) oxygen utilization is low, and only marginal spatial species inhomogeneities can be seen. Increasing the cell load to $480\,mA\,cm^{-2}$ $(0.7\,V)$ raises the oxygen ion molar flux from the cathode to the anode. Oxygen is consumed and is thus being depleted. This can be seen in Figure 3.6(c). Diffusive mass transport within the porous current collector region, and

especially in the cathode catalyst layer, in combination with the O^{2-} flux through the electrolyte provoke noticeable species gradients. Since oxygen is electrochemically reduced to O^{2-} at the TPB in the porous cathode, and then conducted through the electrolyte to the anode, oxygen molar fractions decrease within the porosity and the flow channel. A further increase in the cell load would eventually lead to 100 % oxygen utilization; this would put the cell in a critical state, causing the cell voltage to sharply decline. Other than the species gradients between the flow channels and the porous structures, further inhomogeneities can be seen (outer vs. inner ribs). These are caused by the asymmetrical inlet manifolds of the ceramic cell housing (see Figure3.2(a), and the existent flow profile within the flow channels, respectively. This indicates that the fuel is not being provided uniformly to the cell. The impact of this inhomogeneity will be described and discussed below.

In Figures 3.6(b) and 3.6(d), contours of water vapour molar fractions are shown at $100\,mA\,cm^{-2}$ and $480\,mA\,cm^{-2}$, respectively. Water vapour is formed within the porous anode structure, or, to be more precise, at the three phase boundaries. The numerical model assumes that these three phase boundaries are located in the vicinity of the electrolyte. Thus, water vapour is formed at the anode-electrolyte interface. This is clearly shown in Figure 3.6(d). Inverse species profiles occur in the same way as described for the cathode side. These are again caused by the diffusive species transport limitation within the porous anode and the current collector porosity. Product water will always be formed in a gaseous state, due to the high operating temperature of $800\,^{\circ}C$.

(a) H_2

(b) H_2O
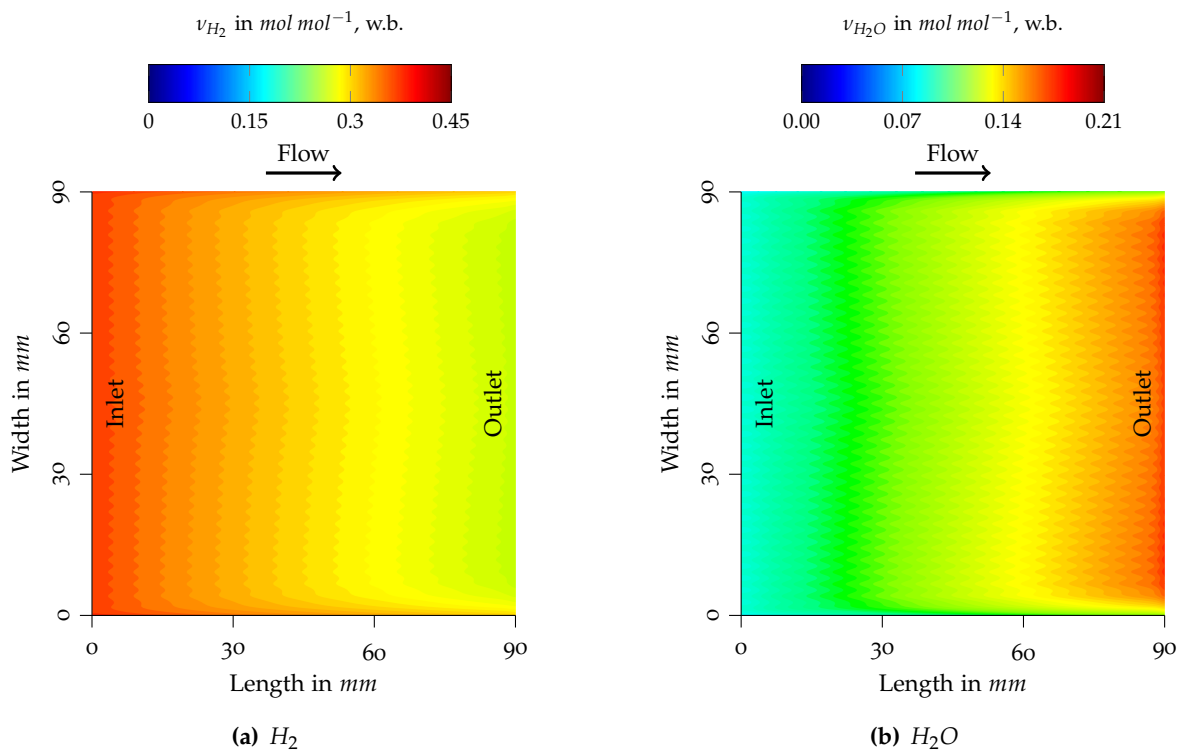
Figure 3.7.: Species contours at the anode-electrolyte interface at $800\,^{\circ}C$ and $480\,mA\,cm^{-2}$, w.b.

Local species trends are also investigated at the anode-electrolyte interface. Here, it is possible to scrutinize a view normal to the electrolyte surface. In Figure 3.7, the depletion and formation

of product water is shown. The flow profile across the entire cell is shown, and the fuel flow direction is indicated by the arrow at the top of the figure. The species profiles on the outer walls come about as a result of its no-slip condition and due to the fact that, in this position, the housing has no flow channels (cf. Figure 3.4(a)) on the cathode side. This means that oxygen can only diffuse into this layer, and therefore, convective mass transport to the porous layer is hindered. Electrochemical reactions are thereby impeded, causing these species profiles to appear on the anode side. In the centre of the cell, slightly higher species mole fractions occur as a result of the underlying velocity flow profile.

(a) Contours of O_2 molar fractions

(b) Contours of H_2 molar fractions

(c) Contours of H_2O molar fractions
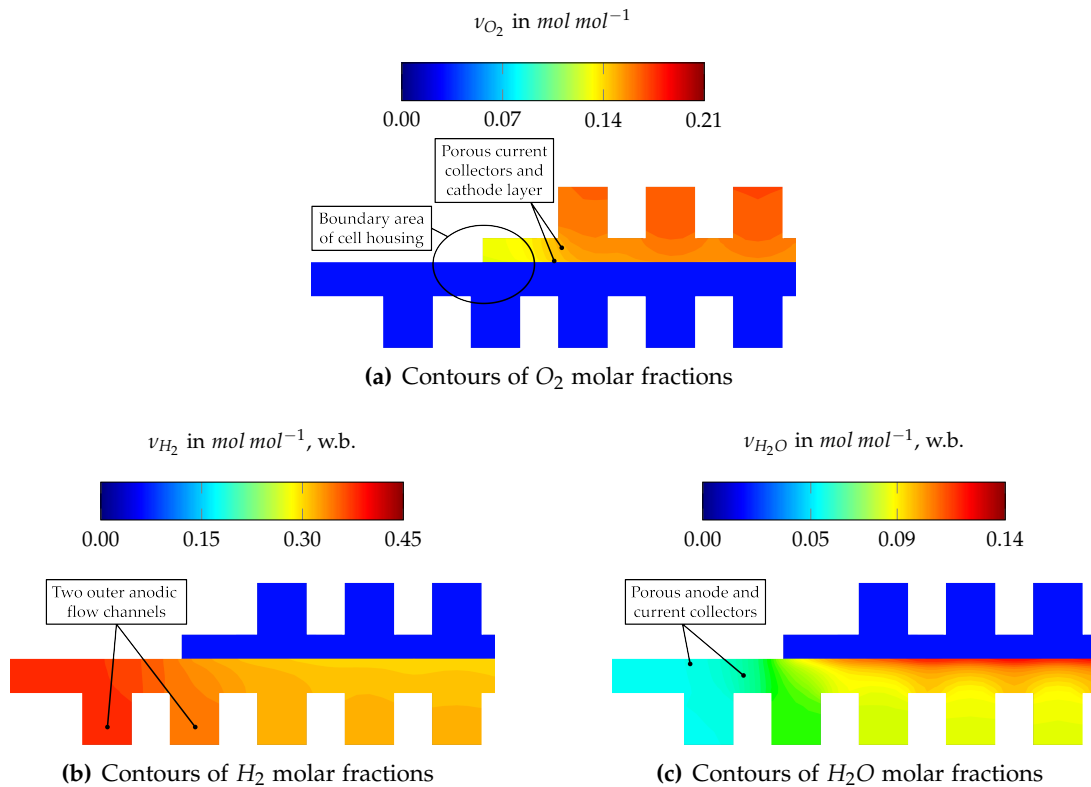
Figure 3.8.: Detail analysis: Species distribution at the outer walls of the housing. Operating temperature $800\,°C$ at $480\,mA\,cm^{-2}$

As described at the beginning of Section 3.2, the overall dimensions of the cathode are smaller $(90 \times 90\,mm^2)$ compared to the anode $(100 \times 100\,mm^2)$. Thus, the cathode is $5\,mm$ smaller at each side than the anode. This discrepancy is shown in Figure 3.8 (left parts of all sub-figures), where the anode flow channels overlap with the cathode flow channels. In the near-wall region and at the boundary area of the cell housing, the cell is asymmetrically equipped with flow channels. The cathode side thus offers two flow channels less on each side compared to the anode side. As can be seen in Figure 3.8(a), depletion of oxygen occurs due to diffusive transport limitations in the porous cathode substrate and current collector region. The outer parts of the cathode are under-supplied with oxygen due to these transport limitations. The hydrogen and water vapour contours in Figures 3.8(b) and 3.8(c) clarify the flow and species profile in Figures 3.7(a) and 3.7(b). Hydrogen and water vapour mix through the outer two channels with already partly depleted fuel or produced water vapour, resulting in this non-trivial flow profile. This

is an interesting finding, and, due to the complex experimental arrangement and boundary conditions, this problem could not have been identified without the aid of this numerical model.

The current density distribution across the cell can be used to identify regions in danger of degradation caused by fuel depletion, thus leading to nickel re-oxidation. Further, local hot spots caused by local high current densities can be addressed. $3D$ numerical modelling makes it possible to efficiently determine these locally diverse current distributions, which represent the oxygen molar flux through the electrolyte. Locally resolved current density measurements in large planar cells are complex tasks for which numerical simulation demonstrates its strengths in spatially-resolved and time-dependent investigations. The simulations thus offer an economic alternative to investigate these local parameters.

(a) Contours of current density i in $mA\,cm^{-2}$ **(b)** Contours of anode activation overpotential in mV
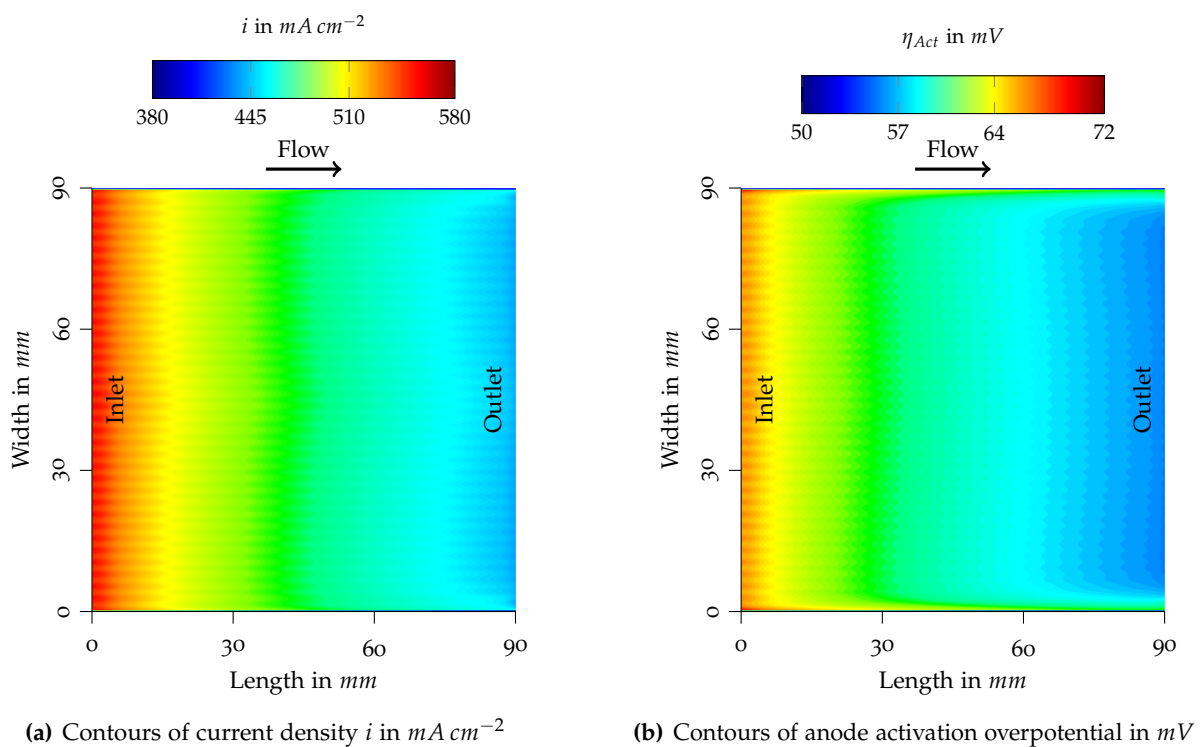
Figure 3.9.: Current density distribution and anode activation overpotential at $800\,°C$ and $480\,mA\,cm^{-2}$

Figure 3.9(a) shows contours of the current density distribution across the electrolyte for an average cell load of $480\,mA\,cm^{-2}$. The highest loads occur at the beginning of the cell, and steadily decrease towards the outlet. The calculated profile occurs mainly due to the co-flow conditions of the fuel and oxidant flow. Counterflow conditions would cause a more homogeneous profile, while crossflow conditions would cause the profile to be distorted by 90° distorted. Since the highest current densities occur at the cell inlet, electrochemical reaction rates are highest here. This leads to an increase in the cell temperature. Exaggerated cell loads can thus induce thermal stresses that lead to cracks. These cracks can cause the mechanical destruction of the cell. The current density distribution follows the same trend, as shown in Figure 3.7. The current density profile normal to the main flow direction can best be described as having a wide 'W'-shape. The maximum current density profile occurs

at a height of $45\,mm$ in the centre of the cell. The 'W'-shape then flattens to both sides of the cell. The inhomogeneities at the outer parts are brought about by the mixing effects, as described above, which also influences the oxygen ion molar flux across the electrolyte. Thus, this inhomogeneous current density profile occurs. This is a further important outcome of these simulations. The single cell housing used in this thesis provides an almost uniform flow profile across the cell. The inner active area ($\pm 40\,mm$ normal to the flow direction from the centreline) is free from wall-boundary and mixing effects. This area can thus be further scrutinized in subsequent investigations.

The cell performance is also determined by the local and overall losses, such as the activation overpotentials. Figure 3.9(b) shows the contours of the anodic overpotential distribution at an average cell load of $480\,mA\,cm^{-2}$. The activation overpotentials are dependent on the local partial pressures of hydrogen and water vapour, as shown in equations (2.21) and (2.20). They are at their highest when only low amounts of reaction products (water vapour) are available. Thus, local overpotentials peak at the cell inlet and decline towards the outlet, at which H_2O partial pressures are already higher, and hydrogen has been partially utilized (see Figures 3.7(a) and 3.7(b)). The local profile is similar to that of hydrogen and water vapour, since they are directly dependent on each other. Further, local and distorted activation overpotentials occur at the outer parts of the cell, where the mixing effects of the anode reflect those of the cathode side. This lowers the total voltage and, eventually, the cell's power output. A possible improvement to cell performance would require an optimized cell housing within which these mixing effects cannot occur. This would require an equal number of flow channels on each side of the electrode and an identical catalytically-active area.

3.2.5. Summary: Hydrogen Fuelled Base Model

Within this section, the numerical model of an entire anode-supported SOFC single cell, fuelled with both dry and humidified hydrogen mixtures, was presented. A detailed numerical representation of the experimental setup was generated, including the flow profile as induced by the inlet manifold design, as well as every single flow channel, the current collectors (metallic meshes of different aperture sizes), and the porous electrodes of the single cell. The chemical and electrochemical performance of the model was validated with experimental data by means of polarization curves and an analysis of the gaseous outlet composition. The simulation and the experimental results were found to be in very high accordance, which emphasizes the validity of the simulation results. Based on this validation, local phenomena were investigated that are difficult to determine experimentally. These were the local current density distribution, species distribution within the flow channels, and the porous substrate across the active area, in addition to the determination of local overpotentials. The model also showed that the cell housing had weaknesses and room for improvement, which is caused by the anode and cathode sides' differing number of flow channels. These flaws to the cell housing notwithstanding, the model described in this chapter is perfectly suitable for the detailed investigation of local and temporal phenomena, including performance deterioration caused by degradation effects. The

centre of the cell is exposed to an almost-uniform fuel distribution, and this area will thus be investigated in further detail. Degradation causes, possible modelling approaches, and their effects will be scrutinized in the following sections.

3.3. Performance of an Electrolyte-Supported SOFC Fuelled with Hydrocarbon Fuel Mixtures[2]

As stated in Chapter 2, SOFCs have two major advantages over low temperature PEMFCs: (1) their electrochemical conversion of carbon monoxide and (2) the direct internal utilization of hydrocarbons. Thus, in a further step, the numerical model created in this dissertation was extended to describe the internal reformation of hydrocarbon fuel mixtures, and an additional cell type (ESC) was used to highlight its versatility.

SOFCs eliminate the need to remove the carbon monoxide (CO) in gaseous fuel mixtures prepared from liquid fossil fuels. Their high operating temperatures inhibit the poisoning of the anode catalyst by CO, and, on top of that, the CO can be directly electrochemically converted [55]. The direct supply of hydrogen to SOFC systems can be replaced by hydrogen-rich fuel mixtures (reformates) generated by hydrocarbon reformers. This substitution does not require the hydrogen infrastructure, which is necessary for PEMFCs, making SOFCs much more practical systems than PEMFCs at the present time [56]. Using liquid hydrocarbon fuels, energy can be saved and emissions reduced, in addition to providing reformers with a mobile on-board power supply and decentralizing energy supplies [57].

3.3.1. Boundary Conditions and Geometrical Setup

To demonstrate the flexibility of the numerical model, a further cell type was investigated. An electrolyte-supported single cell was used, with electrodes (Ni-Gadolinium doped Ceria (GDC) anode and a Lanthanum Strontium Manganese Oxide (LSM) cathode) of a $50\,\mu m$ thickness. The ion-conducting electrolyte layer was thicker ($100\,\mu m$) due to its mechanical-support function. Fuel and oxidant were fed to the anode and cathode flow channels, respectively, both in co-flow condition, as described in Section 3.1. One advantage of SOFCs is their ability to internally reform light hydrocarbons, such as methane. For numerical and experimental fuel cell analysis, three different hydrocarbon-containing fuel mixtures were investigated - in order to determine the effect of methane on the cell performance. These mixtures represent any kind of hydrocarbon reformate, including diesel reformate. First, a mixture was used with an elevated amount of methane and without carbon monoxide. Secondly, the amount of methane was lowered to a moderate level, and the carbon monoxide content was increased. Thirdly,

---

[2]Segments of this section were published in the *International Journal of Hydrogen Energy* under the title "Three-dimensional numerical and experimental investigation of an industrial-sized SOFC fueled by diesel reformat - Part I: Creation of a base model for further carbon deposition modeling" [40].

Table 3.3.: Hydrocarbon fuel mixture compositions

Species	Mixture 1	Mixture 2	Mixture 3	Unit
N_2	0.4586	0.4712	0.4946	$mol\,mol^{-1}$
H_2	0.1806	0.16	0.157	$mol\,mol^{-1}$
CO	0	0.126	0.1397	$mol\,mol^{-1}$
H_2O	0.11	0.11	0.11	$mol\,mol^{-1}$
CO_2	0.1199	0.1103	0.0987	$mol\,mol^{-1}$
CH_4	0.1309	0.0225	0	$mol\,mol^{-1}$

methane was completely replaced by carbon monoxide. This variety of mixtures represents the various gas mixtures of a hydrocarbon reformer at different operating conditions. Table 3.3 shows the species' molar amounts of the three fuel mixtures.

Synthetic air ($0.21\,mol\,mol^{-1}\,O_2$ in N_2) was used as oxidant. In addition to the different fuel compositions, the cell performance at three temperature levels was investigated. These levels are 750, 800 and 850 °C. The flow rates were again set to 2.4 SLPM for the fuel mixtures, and to 4 SLPM for the synthetic air.

Two different global homogeneous reaction mechanisms for the internal reformation of methane within the porous anode were used. First, data from Vakouftsi et al. [44] for activation energy E_A, and frequency factor A was used for the methane-steam reforming reaction MSR and the water- gas shift reaction WGSR. Second, values from Achenbach and Riensche [58] and Bustamante et al. [59] were investigated. The humidified fuel was preheated to the necessary temperature and fed to the anode. It was then internally reformed through the linearly-independent reactions of MSR (see Eq. (2.40)) and WGSR (see Eq. (2.41)). In order to determine whether or not there is a predominant condition of equilibrium either on the educt or product side of the reactions, several simulations were analysed that only took the forward reaction (unidirectional) or forward and backward reaction (bidirectional) into account. Activation energies E_A and frequency factors A of the respective cases can be seen in Table 3.4.

Table 3.4.: Activation energies E_A and frequency factors A

Source	MSR		WGSR	
	Variant 1	Variant 2	Variant 1	Variant 2
	[44]	[58]	[44]	[59]
Activation energy E_A in $10^5\,kJ\,kmol^{-1}$	2.25	0.82	1.04	3.19
Frequency factor A in 10^8	1.91	4.274	$1.199 \cdot 10^{-5}$	2.2

The modelling and simulation of internal reforming within the porous anodic structure requires higher computational time. Thus, in order to keep these times as low as possible and to simultaneously increase the level of detail of the model, the simulation domain was minimized. Only one flow channel was geometrically discretized. Furthermore, the current collectors (several wires of the meshes) were geometrically discretized in order to identify local peaks in the current density distribution brought about by the local contact of the wires. A schematic cross-section of the fuel cell and the surrounding ceramic housing is shown in

Figure 3.10(a). A simplified abstraction of the 34 flow channel-containing single cell housing was created. The flow channel investigated is situated in the middle of the cell.

(a) Schematic of the periodically repeating flow channel structure in the single cell housing

(b) Isometric view of the single flow channel used for these simulations

(c) Detail of the computational grid
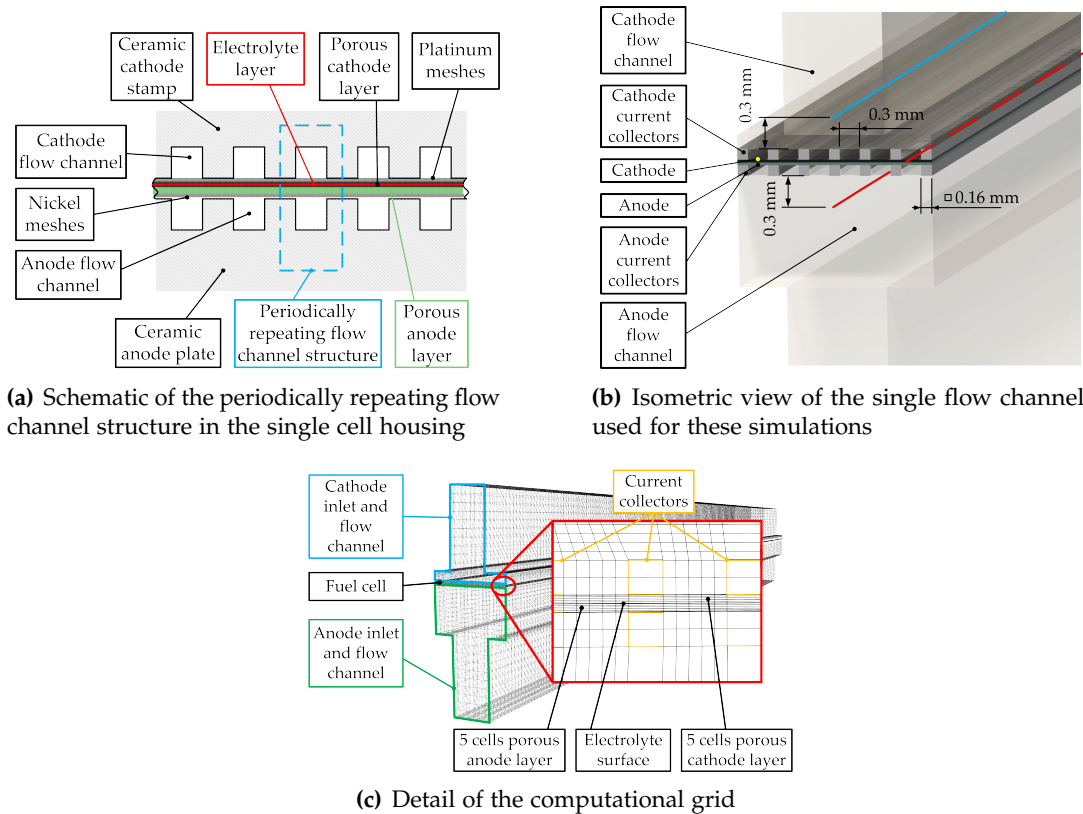
Figure 3.10.: Scheme of the flow channels, a detailed view of the numerically examined single channel and the computational grid [40]

With good accordance, the flow profile is symmetrical from the central axis of the cell (see Figure 3.4(a) for the position of this central axis). This simplification is representative of the cell's average characteristics, and is thus reasonable. It provides results which can be applied to the whole cell, except for the near-wall regions, where inhomogeneities occur due to mixing effects and the unequal cell geometry.

A schematic diagram of the periodically-repeating flow channel structure as well as a detailed view of a single channel, can be seen in Figures 3.10(a) and 3.10(b). In the latter image, the structure of the anodic (nickel) and cathodic (platinum) current collectors are shown. These current collectors are in direct contact with the anode and cathode, respectively. In contrast to conventional stack designs, where the electrical current is conducted by bi-polar plates, at the SOFC test bench at the IWT, the electrical current was conducted by these thin current collectors. The material properties of the fuel cell's anode, cathode and the corresponding current collector materials can be found in Table 3.5. The current density distribution will be different than that of an industrial stack due to the applied current collector meshes. The thin current collector wires have a diameter of $0.16\,mm$ and a $0.3\,mm$ mesh size. One simplification was to transform the cylindrical wires into prismatic wires. This was done to allow for a hexahedral computational grid structure. Furthermore the anode (represented by green nickel oxide) and the black cathode are displayed in Figure 3.10(a) and 3.10(b). The remaining space

on the top and bottom in this figure are the flow channels for both cathode and anode. The dimensions of the model are $w \times h \times l = 2.92 \times 8.97 \times 90\,mm$. The electrolyte was modelled as an infinitely thin layer. This means that only the cell's anode and cathode needed to be geometrically designed. Both the anode and cathode are numerically discretized as ordinary three-dimensional domains, with the appropriate viscous resistance in every particular spatial direction, so as to describe the general behaviour of such a porous zone. These domains were resolved by five cells normal to the main flow direction. The generated mesh consisted of approximately $600,000$ hexahedral cells with a maximum aspect ratio of 40 within the anode and cathode porous zones. Lawlor et al. [60] showed that the aspect ratio chosen is sufficient for this application. Due to the relatively simple geometrical conditions, only hexahedrons with negligible skewness could be used. Figure 3.10(c) shows the computational grid used for simulations with the cell layers for each electrode, the cells in-between the nickel and platinum current collectors, as well as the discretization of the current collectors.

Table 3.5.: Material parameters used for simulations on hydrocarbon fuel mixtures

Parameter	Value	Unit
Cathode current collectors		
Electrical conductivity σ	$1.5 \cdot 10^7$	$\Omega^{-1}m^{-1}$
Density ρ	$21,200$	$kg\,m^{-3}$
Cathode contact resistance	10^{-8}	$\Omega\,m^2$
Specific heat capacity $C_{mp,i}$	140	$J\,kg^{-1}K^{-1}$
Thermal conductivity λ	72	$W\,m^{-1}K^{-1}$
Cathode LSM		
Porosity ε	0.3	−
Tortuosity τ	3	−
Thermal conductivity λ	1.15	$W\,m^{-1}K^{-1}$
Specific heat capacity $C_{mp,i}$	565	$J\,kg^{-1}K^{-1}$
Electrical conductivity σ	7937	$\Omega^{-1}m^{-1}$
Density ρ	$4,375$	$kg\,m^{-3}$
Anode Ni-GDC		
Porosity ε	0.3	−
Tortuosity τ	3	−
Thermal conductivity λ	6.23	$W\,m^{-1}K^{-1}$
Specific heat capacity $C_{mp,i}$	595.1	$J\,kg^{-1}K^{-1}$
Electrical conductivity σ	$3.33 \cdot 10^5$	$\Omega^{-1}m^{-1}$
Density ρ	$3,030$	$kg\,m^{-3}$
Anode current collectors		
Electrical conductivity σ	$1.5 \cdot 10^7$	$\Omega^{-1}m^{-1}$
Density ρ	$8,900$	$kg\,m^{-3}$
Anode contact resistance	10^{-7}	$\Omega\,m^2$
Specific heat capacity $C_{mp,i}$	446	$J\,kg^{-1}K^{-1}$
Thermal conductivity λ	91	$W\,m^{-1}K^{-1}$

3.3.2. Numerical Setup

The numerical setup for the electrolyte-supported cell simulations was similar to that of the previous simulations, described in Section 3.2.2. The solver settings, discretization approaches, and models used were kept the same. For the simulations, the co-flow condition of the cathodic

and anodic gas streams was applied as described in the experimental setup (see Figure 3.2). Both the anode and cathode inlet were modelled as mass flow inlets. Similarly, both outlets were defined as pressure outlets. Chemical species diffusion is modelled using the Stefan-Maxwell model to simulate the details of molecular transport processes. Exterior walls (interface of periodically repeating geometry) were defined as stationary walls with a specified shear stress of zero. This assured that the flow regime of the single channel correlated with that of the entire, real geometry.

3.3.3. Simulation Results for Hydrocarbon Fuel Mixtures

Both fuel cell performance and temperature distribution depend on transport phenomena such as mass and heat transfer, as well as charge transport. Numerous simulations were conducted with the aim of creating a validated, reliable, basic simulation model that is able to predict flow, temperature and species profiles during the internal reforming of light hydrocarbons. As described above, different temperature levels, fuel mixtures, and various kinetic approaches for the internal reforming of methane were scrutinized in order to describe both the gas phase reactions and electrochemical interactions that occur.

(a) $750\,°C$

(b) $800\,°C$

(c) $850\,°C$
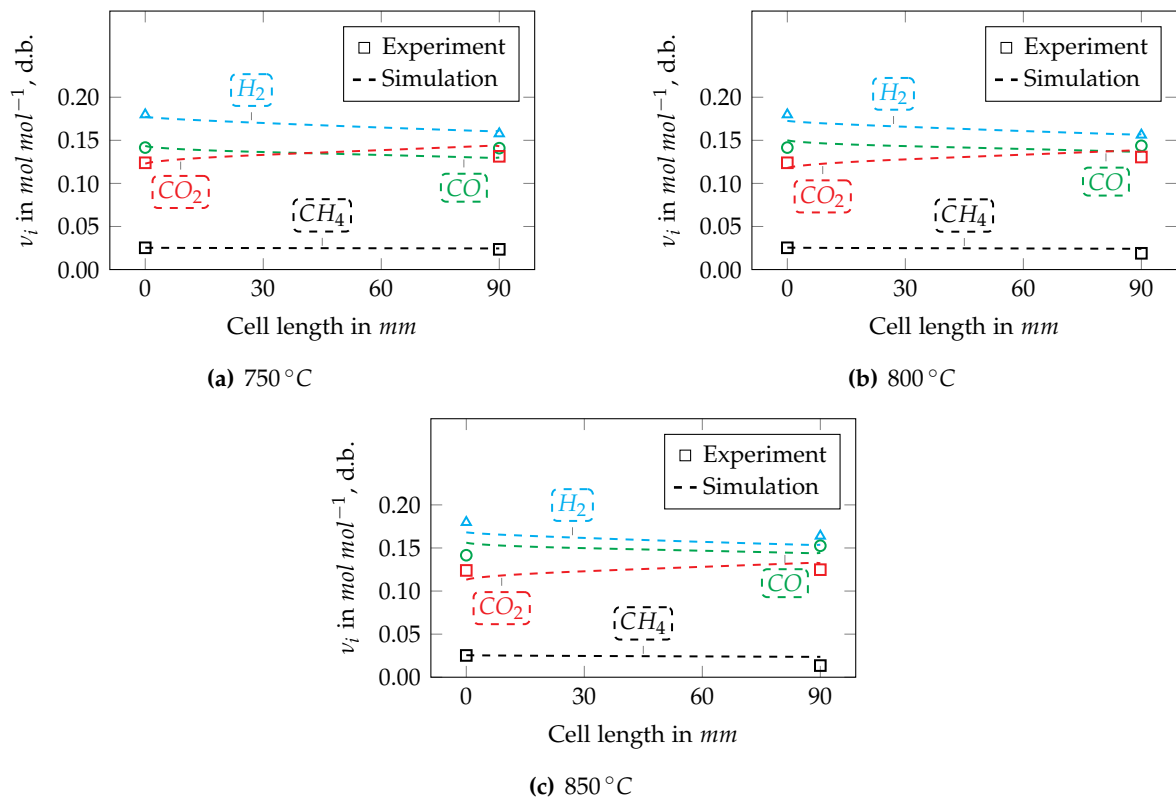
Figure 3.11.: Species distribution (d.b.) along the anode flow channel for gas mixture 2 (cf. Table 3.3), current density $120\,mA\,cm^{-2}$ and Arrhenius factors of Variant 2 (cf. Table 3.4) [40]

The first set of problems mentioned was examined using two different kinetic approaches for methane reforming at the anode. Furthermore, the reactions' equilibria were investigated by changing the reaction direction. The approaches taken into account were chosen from Refs. [59],

[58], and [44], as described in Table 3.4. It is desirable to reduce the cell's operating temperature, thus, simulations at low ($750\,°C$, medium $800\,°C$) and high ($850\,°C$) operating temperatures were carried out.

Figure 3.11 depicts the synthetic fuel mixture species distribution at the examined temperatures and current density of $120\,mA\,cm^{-2}$, and the kinetic approach of Variant 2 (cf. Table 3.4) for mixture 2 (see Table 3.3) along the anode flow channel. All of the assessed values were determined on a horizontally-centred line, elevated $0.3\,mm$ above the current collector surface, in order to represent different parameters at a specific position in the flow channel. To evaluate the cathodic gas compositions, a line similar to the aforementioned approach was created within the cathode flow channel. The positioning of these lines can be seen in Figure 3.10(b), and is indicated by the red (anode flow channel) and blue (cathode flow channel) lines.

In Figure 3.11, solid lines indicate the simulated values for the species fractions. Experimental data, that was monitored online during the execution of the tests, is depicted as markers. Due to the experimental test setup, the operating temperature, and the geometry, it was not possible to measure local species fractions within the anode or cathode flow channels. The anode gas species composition was determined at two fixed positions. First, species concentration was measured in the gas line before entering the anode gas inlet pipe. The exhaust anode gas composition was determined at the anode gas pipe outlet. Gas analysis and the according measurement points are schematically illustrated in Figure 3.1 and 3.2(a). Experimental data for the gas phase reactions is therefore only available for two specific points, which are situated at a short distance from the fuel cell housing inlet and outlet. The experimental data, however, is situated at the beginning (active cell length $0\,mm$) and end of the fuel cell's active cell length (active cell length $90\,mm$) in the diagrams (Figures 3.11(a) - 3.11(c)). The measured data thus represents averaged values of all of the local reactions that occur. The species distribution shown in Figure 3.11(a) represents the fuel cell behaviour at $750\,°C$.

The methane species trend is plotted as a dark blue, almost-horizontal line. The chemical equilibrium of the MSR reaction for a temperature of $750\,°C$ should be on the product side of this reaction [61, 62]. Experimental data shows that internal reforming reaction rates of methane in the applied cell are low in this particular application. The theoretical equilibrium shows that the cell's anode material, that is the incorporated nickel, has an almost negligible effect on the reaction's kinetics. The kinetics are therefore too slow to catalyse the reforming reaction. Deflections between the simulated and experimental methane trends can be noticed as the temperatures rise. This indicates that the reaction kinetics parameters garnered from literature underestimate the reforming process. Nevertheless, both the numerical and experimental methane data are in an acceptable range, suggesting that the kinetic parameters chosen are suitable for this specific application. The experimental data also shows that the water-gas shift reaction takes place in combination with the electrochemical carbon monoxide oxidation. This can be seen by the green and red cross-marks. The CO_2 species molar fractions don't change to a significant degree between the fuel cell's inlet and outlet. The gas phase reaction's equilibrium

is more likely to be on the reactant side than on the product side at the applied temperature, as can be seen in the results of [63–66].

The simulated *CO* trend does not match that of the experiment. Possible causes for this are the fact that other chemical reactions take place in the gas phase, which are not taken into account by the simulation. These reactions are likely to be the dry-reforming reaction of methane or methane decomposition. Furthermore, in the numerical simulations, carbon monoxide is used as fuel for the electrochemical reactions. It is electrochemically oxidized according to Eq. (2.3), which contributes to the simulated CO trend. The simulated molar species trend of carbon monoxide deviates by approx. $-1\,vol\%$ from the experiment, while carbon dioxide emissions are overestimated by about $0.5\,vol\%$. The solid purple and blue lines indicate the hydrogen and water vapour trends, respectively, along the active cell length. These trends indicate the cell's hydrogen electrochemistry. It can clearly be seen that hydrogen is consumed as it flows along the cell. Its molar amount decreases from $0.16\,mol\,mol^{-1}$ at the flow channel inlet to $0.14\,mol\,mol^{-1}$ at the outlet. Water vapour generation shows the opposite behaviour. Contour plots of the simulation results of gas mixture 2, the reaction kinetics of Variant 2, and a current density of $120\,mA\,cm^{-2}$ are shown in Figure 3.12.

(a) Hydrogen

(b) Water vapor

(c) Carbon monoxide

(d) Carbon dioxide
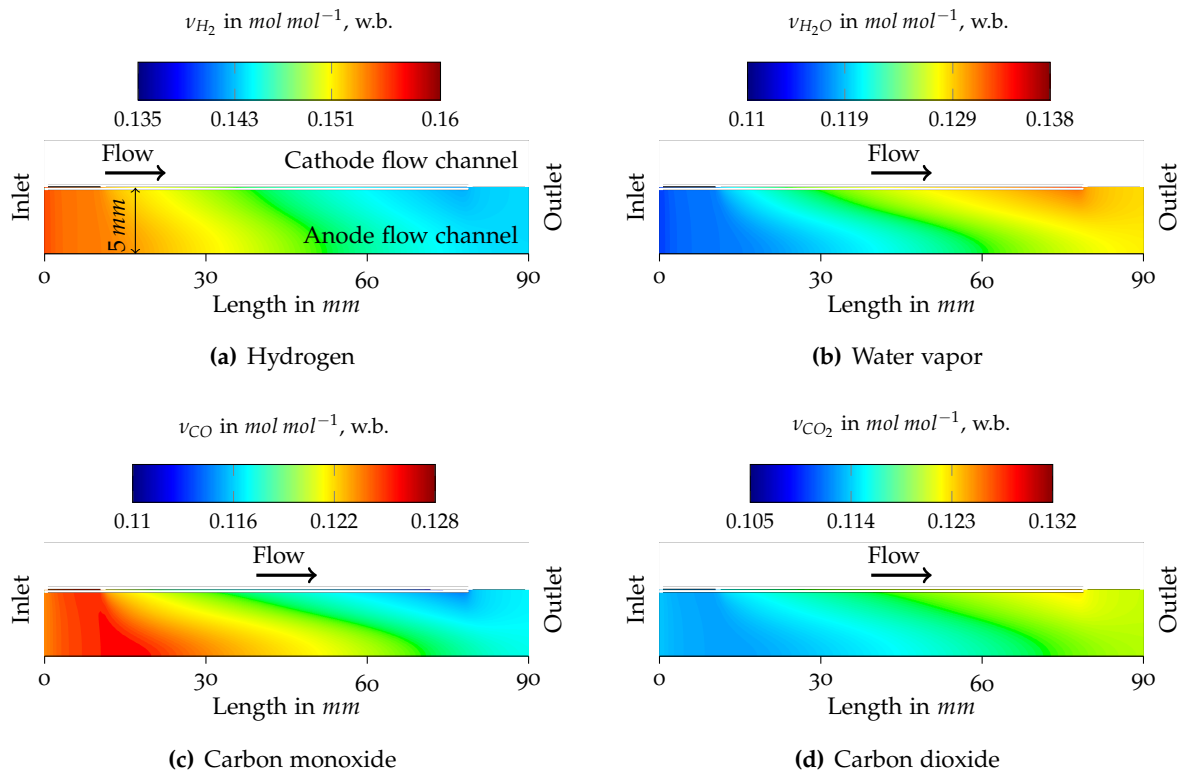
Figure 3.12.: Species contours in $mol\,mol^{-1}$ (wet base) for gas mixture 2 and reaction kinetics of Variant 2 along a longitudinal cutting plane through the simulated flow channel at $750\,°C$ and $120\,mA\,cm^{-2}$ for the ESC cell [40] (dimensions not to scale)

With these contours, it's possible to better understand the diagrams shown in Figure 3.11, as well as the general reactions and species trends within the anode flow channel. The flow direction and general information on inlet-, outlet- and cell-positioning is provided in Figure

3.12(a). The flow direction and the remaining boundary conditions for Figures 3.12(b) - 3.12(d) are similar to those in the hydrogen contour plot. This particular point of operation, of $120\,mA\,cm^{-2}$, represents a low cell load. Therefore, the fuel utilization, water vapour, and carbon dioxide production as a result of the electrochemical reactions are also low. Due to the ionic oxygen flux from the cathode, through the electrolyte, and to the anode, the fuel is diluted and there has to be a change in the molar species fractions.

Figures 3.11(b) and 3.11(c) show the species distribution along the anodic flow channel for $800\,°C$ and $850\,°C$, respectively. In these figures, it is possible to see that the general trend of the reactions, as previously described, matches the results of the experiment. The molar species amounts at the cell's outlet of both the experiment and the simulation show high correlation, as seen in Figure 3.11(b). The conversion rate of the electrochemical oxidation of hydrogen and carbon monoxide can also be seen to increase with rising temperature. The concurrence of the simulated values and experimentally determined parameters decreases when the operating temperature is increased to $850\,°C$. Both carbon monoxide and hydrogen species fractions at the outlet rise in comparison to Figures 3.11(b) and 3.11(a). This indicates that the methane reforming reaction shifts its equilibrium to the product side as temperatures increase. The experimental data further suggests that the water-gas shift reaction's equilibrium moves to the reactant side with these boundary conditions. At the chosen operating point of $120\,mA\,cm^{-2}$, it is not possible for the electrochemical reaction to fully convert the hydrogen and carbon monoxide into water vapour and carbon dioxide. The simulated values show a slight but constant deviation from the experimental data.

(a) $100\,mA\,cm^{-2}$

(b) $120\,mA\,cm^{-2}$
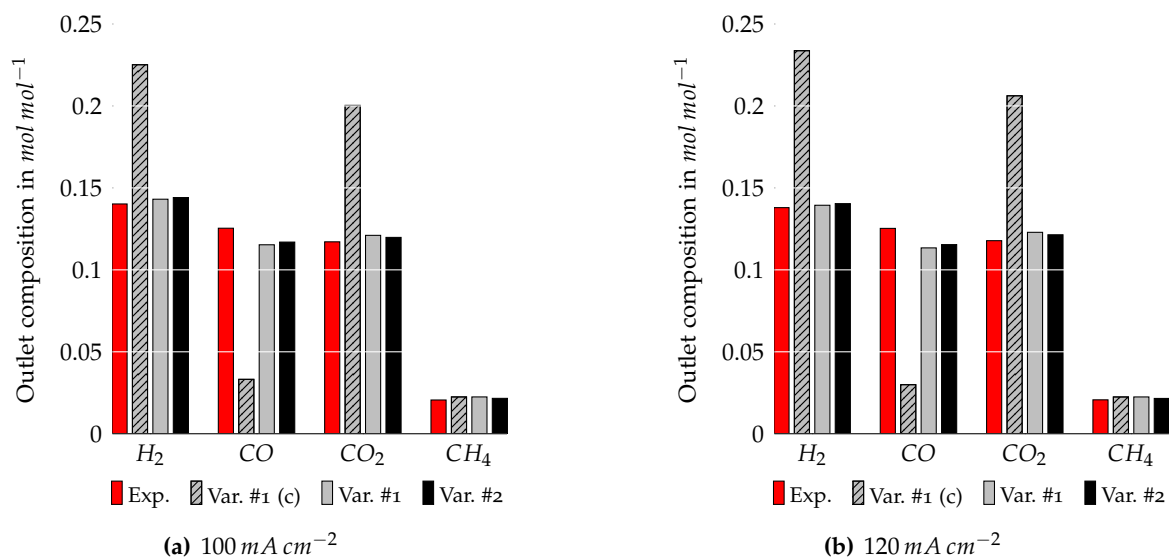
Figure 3.13.: Mass weighted averaged molar amounts at the anode flow channel outlet for different kinetic approaches at $750\,°C$ and gas mixture 2 [40]

Figure 3.13 shows a comparison of different kinetic approaches and experimental data for gas mixture 2 at $750\,°C$. The molar species amounts are plotted as averaged values across the anode flow channel outlet area. The fuel inlet composition for gas mixture 2 can be revisited in Table 3.3. Figure 3.13(a) shows the results for $100\,mA\,cm^{-2}$ and in Figure 3.13(b), the results for

$120\,mA\,cm^{-2}$ are depicted.

The diagrams are divided into four sections, which correlate to the fuel species. Red bars show the experimentally determined molar species fractions. Different gas phase reaction directions (complete stoichiometric conversion or dynamic equilibrium) and different reaction kinetics were examined in order to identify appropriate reaction rates for the present application of this electrolyte-supported solid oxide fuel cell. These differing approaches are illustrated by the grey and black bars. The grey, hatched bars depict the results for the kinetic approach of Variant 1 (cf. Table 3.4) in which complete stoichiometric conversion was assumed (i.e. only the forward reaction path of Eqs. 2.40 and 2.41 were taken into account). This approach is additionally marked with an index 'c' for complete stoichiometric conversion. The plain grey bars (not hatched) are the simulation results of the same kinetic approach (Variant 1), but in dynamic equilibrium (both forward and backward reaction path were simulated). This indicates that the reaction's equilibrium is dependent on the prevalent temperature. The simulation results for the kinetic approach of Variant 2 are plotted as black bars. The different reaction approaches and their accuracy were evaluated by means of the reaction product molar amounts. The experiment showed that the hydrogen molar amount slightly decreased. This demonstrates that hydrogen is converted to an average amount. Molar amounts of this species at the cell's inlet and outlet change from 0.16 to 0.14. Both methane and carbon monoxide are only marginally reformed. It seems that at this particular point of operation, no specific gas phase reaction takes place. Figure 3.14(a) shows that, at a temperature of $850\,°C$ and a cell voltage of $0.775\,V$, a current density of $120\,mA\,cm^{-2}$ was drawn from the cell. A slight decrease in the amount of methane and carbon monoxide thus results in the production of marginal amounts of hydrogen. Hydrogen species decrease due to the electrochemical oxidation of oxygen.

Figure 3.13 shows another interesting simulation result. The grey bar depicts the calculation results for Variant 1 with complete stoichiometric conversion. This approach solely models the forward reaction path of the gas phase reactions that occur. With this approach, the reaction equilibrium of the water-gas shift reaction was keenly overestimated. This can best be seen by the molar species amounts of both carbon monoxide and carbon dioxide. The reactants (CO and H_2O, respectively) decrease considerably from 0.126 and 0.11 at the inlet to 0.03 and 0.046 for both current density simulations. Simultaneously, the reaction products' species amounts (CO_2 and H_2) rise. As can be seen from the experimentally-determined values, this modelling approach delivers unsatisfactory results.

The dynamic equilibrium for kinetics Variant 1 results in acceptable ranges. The two different kinetic approaches (Variant 1 and 2, see Table 3.4) deliver nearly identical values. Marginal species molar amounts were calculated. To decide which kinetic approach fits best for this current application, numerous simulations were conducted for a variety of temperatures, fuel compositions, and current densities. It was found that the kinetics approach of Variant 2 was most suitable for the entire simulation matrix. The simulated spatial species distribution of this particular kinetics approach were shown in Figure 3.12. This kinetics approach was thus used for all further simulations in this section.

In Figure 3.14, the polarization curves for two different gas mixtures (mixtures 2 and 3) and

kinetics Variant 2 are shown. Figure 3.14(a) displays the cell response for gas mixture 2 while Figure 3.14(b) shows the characteristic curves for mixture 3. In each diagram the experimentally and numerically determined cell voltages for temperatures of $750\,^{\circ}C$, $800\,^{\circ}C$ and $850\,^{\circ}C$ are plotted.

(a) Gas mixture 2   **(b)** Gas mixture 3
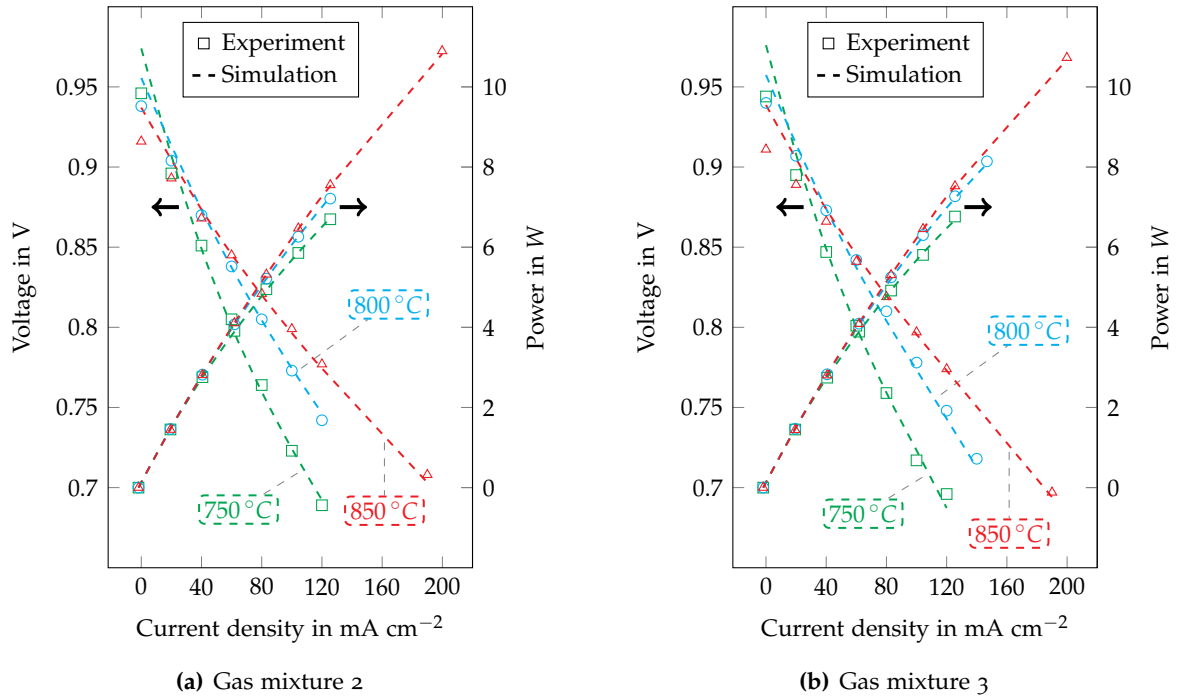
Figure 3.14.: Polarization curves for two different gas mixtures at 750, 800 and 850 $^{\circ}C$ for kinetics Variant 2 [40]

It is possible to see that there is a strong correlation between the simulation and experiment for different gas compositions. Slight deflections can be noticed at OCV. As described in Eq. (2.58), the cell voltage is calculated by evaluating of the theoretical Nernst voltage and the losses that occur, such as overpotentials. These overpotentials were determined by solving the Butler-Volmer equation (Eq. (2.20)). The simulated open circuit voltage is equal to the theoretical Nernst voltage. Sealing the fuel cell is difficult due to present cell dimensions and the cell housing used. Marginal leakages can explain this slight deviation at OCV. This difference is most notable in a range of $\Delta U = 2\,mV$. The polarization curves show that a cell voltage decrease as operating temperatures increase. This is caused by the decrease in Gibbs free energy with rising temperatures. OCV lowers from $0.946\,V$ at $750\,^{\circ}C$ to $0.916\,V$ at $850\,^{\circ}C$. Furthermore, the voltage gradient can also be seen to decrease with increasing temperatures. This means that as the operating temperatures rise, a higher cell voltage is achievable at constant current density (compare cell voltages at $120\,mA\,cm^{-2}$). This can be attributed to the increasing oxygen ion conductivity of the thick, solid electrolyte. An increase in the conductivity equals a decrease in the ohmic resistance, which can be seen in the slope of the polarization curves. On the second axis of ordinates in Figure 3.14, data for the cell's power output is plotted. The maximum cell power output rises with increasing operating temperatures (approx. $11\,W$ at maximum current density). Comparing the two different gas compositions, it is possible to see slight differences in the cell voltage. This is caused by the different partial pressures of the gas mixture species.

On the second axis of ordinates in Figure 3.14, data for the cell's power output is plotted. Maximum cell power output rises with increasing operating temperature (approx. 11 W at maximum current density). Comparison of the two different gas compositions shows slight differences in the cell voltage. This is caused by different partial pressures of the gas mixture species.

Figure 3.15 shows an overlay plot of the current densities i at the anode surface and the molar species amounts of methane along a longitudinal cut of the anodic flow channel. In this case, gas mixture 1 with kinetic Variant 2 at 850 °C and an average system current density of 120 $mA\,cm^{-2}$ were set as boundary conditions.
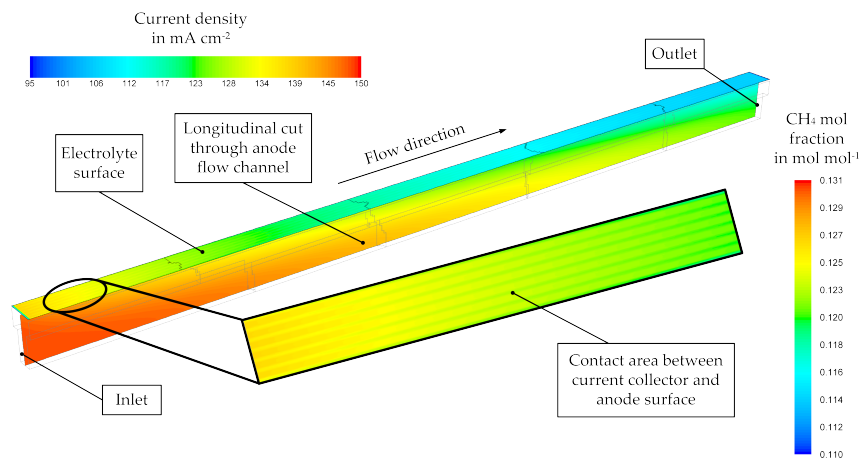
Figure 3.15.: Current density i and molar CH_4 species concentration along the anode surface and anode flow channel for gas mixture 1, reforming kinetics of Variant 2 at 850 °C and a total current density of 120 $mA\,cm^{-2}$ [40]

Current density distribution is shown for the anode surface, where the current collectors are in direct contact with the anode. These junctions can clearly be seen in the contour plot. Peak current densities occur where the current collector wires are connected to the surface. Current densities are lower between these wires, and can be seen to decrease along the cell length. This is due to decreasing molar species amounts of the electrochemically reacting species. Although a total system current density of 120 $mA\,cm^{-2}$ was set as a boundary condition, locally higher values do occur. This is due to the local partial pressures of reactants, and the position of the current collection. Similar simulation results were shown in Refs. [60] and [67]. The contour plot of methane molar fractions along the flow channel is displayed as a longitudinal cut through the centre of the channel. The contours show that methane is reformed as the fuel flows along the fuel cell. According to the MSR reaction, carbon monoxide and hydrogen are produced when methane is utilized. These products are further used for electrochemical oxidation with oxygen ions. Molar CH_4 amounts decrease from 0.131 at the anode inlet to about 0.12 at the outlet.

3.3.4. Summary of the ESC Simulations

In this section, the numerical model generated to describe the behaviour and performance of solid electrolyte fuel cells was extended to address an electrolyte-supported cell type. Further, the internal reforming of light hydrocarbons within the porous anode structure was introduced in order to represent the full capabilities of SOFCs. This represents the flexibility of the simulation model. To do so, only the cell-specific parameters, such as conductivities, layer thicknesses, and material properties had to be adapted so as to achieve a good fit between the model and the experiment. The geometrical model was simplified in order to keep the computational costs within a reasonable amount. A single flow channel was numerically cut out of the entire cell housing, with adequate boundary conditions to represent a broad area of the cell.

The electrochemical and gas phase reactions occurred simultaneously, and therefore their reactions are superimposed. An analytical locally-resolved simulation can be done by means of chemical kinetics software solvers. CFD is perfectly suited for simulating complex chemical/electrochemical superposed reacting systems, like the high-temperature solid oxide fuel cell. The model predicted the electrochemical performance of the cell with acceptable accordance to the experiment. Three different gas mixtures, representing any kind of hydrocarbon reformate, such as diesel reformate, were used as fuels. The internal reforming reactions were difficult to model due to the overall complexity of the application. Both gas phase and electrochemical reactions (hydrogen as well as carbon monoxide) occur simultaneously. The calculation of the correct reaction equilibrium was investigated and solved to an acceptable degree of precision. With the generated numerical model of an electrolyte-supported SOFC, reliable calculations were carried out for different fuel compositions and a wide temperature range. The simulation was validated with experimental data, indicating that the calculation results are trustworthy. High accordance was also achieved between the predicted and measured polarization curves. The modelling of electrochemical reactions and both the performance and experimental data are all in strong agreement. Small SOFC cells have been widely investigated in literature. Here, a large planar fuel cell with dimensions of $100 \times 100 \, mm^2$ and with an active cell area of $90 \times 90 \, mm^2$ was analysed in detail. In the next section, the simulation model generated will be used to calculate carbon deposition on the anode surface. When using hydrocarbon fuels, such as reformates, as fuels for solid oxide fuel cells, it is possible that carbon will form and be deposited on the anode surface. Thus, it is necessary to find a way to model carbon formation within the porous anodic structure and to identify the critical operating conditions leading to this degradation.

3.4. Scrutiny of Internal Reforming Kinetics and Carbon Formation Modelling Approaches[3]

The previous sections presented the creation of a base model to describe the electrochemical performance of solid oxide fuel cells. This model was shown to predict the polarization curves of diverse fuels (hydrogen and hydrocarbon mixtures). Furthermore, the model was demonstrated to be highly flexible through the investigation of two different types of cells (anode-supported and electrolyte-supported cells). The reaction kinetics to describe the reforming of methane within the porous anode for electrolyte supported cells were also investigated. This inquiry showed that internal reforming of methane can be described with global homogeneous kinetics approaches. Nevertheless, further scrutiny is necessary to identify a kinetics-based reaction scheme that predicts reforming rates suitable for anode-supported cells, and which can be used as a basis to describe carbon formation within the porous anodic structure.

3.4.1. Internal Reforming Mechanisms of Light Hydrocarbons

The internal reforming of methane in SOFCs, directly within the porous anode, is made possible by the catalytically-active nickel within the substrate. Problems associated with SOFC internal reforming include carbon formation, anode particle sintering, anode leeching, delamination, and intrinsic endothermic disposition, during steam reforming. Furthermore, channel blocking, which is caused by deposited carbon and its subsequent re-oxidation, is a critical failure since the electrolyte can be cracked, leading to a mechanical destruction of the cell [68].

Providing SOFCs with fuels containing hydrocarbons carries the inherent risk of carbon depositions on the anode. Performance degradation is a likely consequence thereof [69, 70]. Carbon deposition can occur in concert with a corrosion reaction known as metal dusting, which is the carbon-assisted disintegration of bulk metal into metal powder. Metal dusting implies the diffusion of carbon into the interior of the metal, followed by the deposition of graphite within the metal, causing the metal to mechanically break up [71].

Methane reforming (steam reforming, dry reforming, as well as autothermal oxidation) and the water-gas shift reaction on Ni-YSZ catalysts have long been studied by different research groups, and many kinetic approaches have been proposed [7, 8, 22, 23, 72–74]. These studies have developed various homogeneous global reaction expressions [7, 22, 23, 72, 73] as well as very detailed heterogeneous catalytic reaction mechanisms. Global homogeneous reactions are primarily modelled by two- or three-step mechanisms, in which steam reforming and shift reactions are incorporated. These global reactions take only gas-phase species reactions into account. Thus, detailed reaction paths and precipitation of elementary carbon are not described.

---

[3]Segments of this section were published in the *International Journal of Hydrogen Energy* under the title "Three-dimensional numerical and experimental investigation of an industrial-sized SOFC fueled by diesel reformat - Part II: Detailed reforming chemistry and carbon deposition analysis" [41].

Hecht et al. [74], Zhu et al. [8] and Maier et al. [75] have developed a detailed heterogeneous reaction mechanism for methane reforming on nickel-based catalysts. This mechanism involves water-gas shift and oxidation reactions, the formation of carbon monolayers, and methanation reactions. The mechanism consists of pairs of twenty-one irreversible elementary reactions. With this mechanism, it is possible to predict chemisorbed carbon on the catalytically active areas of the anode. The precise representation of the reforming process within the porous anode structure is a basic requirement for reliable numerical fuel-cell simulations. The detailed analysis of different reaction steps is made possible with this detailed wall-surface reaction mechanism.

3.4.2. Carbon Formation as Caused by Different Fuels

Cimenti and Hill [76] studied the fuelling of SOFCs with liquid fuels, including liquefied petroleum gas, dimethyl ether, ethanol, methanol, and carbon-free liquid fuels. They reported that methanol could be an optimal liquid fuel because of its low carbon-formation propensity. With regard to anode design for hydrocarbon fuels in SOFCs, it was found that sufficient electrochemical activity and low carbon formation can be balanced.

Kendall, Slinn, and Preece [77] used micro-tubular SOFCs to study the theory that anodic damage due to deposition is mainly caused by the bonds between two carbon atoms in the fuel. Numerous different molecules were tested as fuels for SOFCs, and it was found that ethers without such bonds can be run without substantial carbon formation. When operating the SOFC with glycerol and N-methyl methanamide, a tremendous decrease in short- and long-term cell performance was observed. When the cell was supplied with other molecules, such as methanoic acid, almost constant cell performance was reached over a long time period, similar to hydrogen operation.

Carbon deposition on Ni-YSZ anodes, as well as their deactivation due to feeding with pure methane and methane/steam, has been investigated in a number of studies [44, 78–84].

Finnerty et al. [78] studied the steam reforming activity and surface chemistry of different anode material combinations. The authors were able to show that three different kinds of carbon can be formed on anodes when fuelling SOFCs with methane. The carbon types (I-III) were classified by the temperature required for their removal by oxidation. It was found that the amount and type of deposited carbon strongly depends on the exposure time. With increasing load, more methane was converted, at the same time as less carbon was deposited. Changes in the anode material composition (doping with small quantities of molybdenum) showed a clear reduction in carbon deposition rates. It was stated that carbon deposition occurs on the surface of the porous anode structure. The deposition takes place through dissociative catalytic adsorption of C_xH_{2x+2} - molecules, as shown in Eq. (3.2).

$$C_xH_{2x+2} \rightleftharpoons xC + (x+1)H_2 \qquad\qquad (3.2)$$

More specifically, carbon can precipitate from methane through reaction (3.3).

$$CH_4 \rightleftharpoons C + 2H_2 \tag{3.3}$$

Steam can be added to the gas stream to chemically remove the adsorbed carbon from the surface, as shown in reaction (3.4).

$$C + H_2O \rightleftharpoons CO + H_2 \tag{3.4}$$

Bartholomew [85] found that large amounts of steam increase the system complexity, reduce the overall process efficiency, and increase the risk of anode re-oxidation.

Alzate-Restrepo and Hill [79] showed that carbon formation depends on the load at which the cell is operated. Carbon deposited on a polarized cell was hydrogenated and was easier to remove by temperature programmed oxidation (TPO) than carbon built at OCV. With rising current density, carbon deposition rates decreased, but the properties of the carbon remained unchanged. Removal of the deposited carbon became more difficult with increasing operational time and/or anode thickness, since TPO measurements showed that most of the carbon was dehydrogenated, and thus less reactive.

Girona et al. [80] performed experiments and simulations of circular anode-supported SOFCs fed either with synthetic biogas or humidified hydrogen. Simulations were conducted to assess the risk of coking as dependent on the CH_4 concentration in the gaseous fuel and on the cell voltage. It was shown that, with elevated methane molar fractions and low current densities, the risk of carbon formation is high for the given operating conditions. Carbon formation was avoided at high cell loads (current density $i \approx 200 \, mA \, cm^{-2}$) and with low methane amounts.

Koh et al. [81] experimentally investigated a $4 \times 4 \, cm^2$ anode-supported planar SOFC, made from LSM, YSZ and Ni-YSZ, and fed with methane. Carbon deposition on the anode was analysed via electrochemical impedance spectroscopy. They found that open-circuit condition is favourable for carbon deposition, even for humidified methane fuel. Furthermore, both reversible and irreversible carbon deposition were found to be possible. Carbon formed during SOFC operation can be oxidized by O^{2-} ions supplied by the electrochemical reaction; on the contrary, irreversible carbon formation occurs where carbon particulate are formed. In terms of location, reversible carbon depositions occur at the vicinity of the TPB (adsorbed gas molecules combine with oxygen ions), while irreversible carbon deposition occurs mostly on the metallic nickel surface and/or in case of excess methane. The authors showed that carbon deposited by CH_4/H_2O gas mixtures is reversible when it is oxidized at a finite current load and a thermodynamically carbon-free condition. Cell performance is not affected by this reversible carbon deposition.

The authors of Refs. [82] and [83] conducted both experimental and numerical investigations of planar anode-supported SOFCs fed with methane and syngas, respectively. The internal reforming of methane over Ni-based catalysts was described by a generalized Langmuir-Hinshelwood type kinetic model, that had been previously developed by Xu and Froment [22]. Carbon deposition reactions were taken into account for methane cracking, Boudouard, and the water-gas shift reaction. Possible carbon formations were calculated by means of the thermodynamic carbon formation activities of the reactions mentioned beforehand. Different S/C ratios, as well as the influence of different syngas components, were investigated. The authors demonstrated that for global S/C ratios greater than unity, at and temperatures ranging from 600 to 900 °C, carbon formation is thermodynamically possible within the porous anode structure.

Klein et al. [84] and Vakouftsi et al. [44] numerically studied possible carbon deposition on solid oxide fuel cells' anodes (tubular [84] and planar [44]) by calculating the thermodynamic activity of the methane cracking and Boudouard reaction. Furthermore, they combined both activities in order to assess the influence of both reactions at the same time. The calculated formation activity only denotes a thermodynamic possibility of forming elementary carbon. At different temperature levels and fuel compositions, carbon formation was shown to be possible at the anode inlet zone.

A simple numerical carbon deposition analysis was conducted by Nikooyeh, Jeje, and Hill [86] by investigating the steam/carbon ratio inside planar anodes. This approach made qualitative predictions of carbon formation and deposition regions.

Since many studies have simulated and evaluated the impact of methane and/or methane/steam mixtures on cell behaviour and cell degradation, in the future, it will be interesting to investigate the use of hydrogen-rich fuels with high volumetric energy density for SOFCs. Liquid hydrocarbon fuels are of special interest. Liquid fuels offer a higher volumetric energy density than gaseous fuels, which means that they have a huge potential for for future applications.

The aim of this section is to assess the possibility of carbon deposition on an anode-supported planar SOFC fed with a hydrocarbon fuel mixture. The base model is utilized and extended by further reaction mechanisms. For the future of SOFC applications and their eventual commercialization, it is of great importance to determine the location and amount of carbon deposited within the porosity of the anode. It will be of future interest to identify the critical operating conditions and locations within the fuel cells' anodes in order to improve stack designs. Furthermore, with better knowledge of carbon formation pathways, accelerated damage testing can be conducted.

Thus, in addition to previously-investigated internal reforming kinetic approaches, scrutiny of further steam reforming reaction mechanisms over nickel catalysts available in the literature is done in this section to determine more accurate reaction and methane conversion rates. Below, both homogeneous global reaction mechanisms and a detailed heterogeneous reaction mechanism are investigated in detail. Kinetic and thermodynamic data will be interpreted in

the CFD base model so as to highlight any possible sources of error in the numerical prediction of methane conversion rates. Many different kinetic approaches to methane steam reforming are available in literature, and it is thus important to analyse their different behaviour and to visualize their kinetics. Again, the simulated data is validated by experimental data in order to derive reliable simulation results for the prediction of carbon deposition on the cell's anode.

3.4.3. Numerical Setup

The overall numerical setup of the simulations in this section is the same that presented in Section 3.2.2. Chemical species diffusion is predicted by the Stefan-Maxwell model to simulate the details of molecular transport processes. The SOFC sub-module was used again to predict the electrochemical performance of the cell and all of the electrochemical losses that occur.

3.4.4. Chemical Reaction Mechanisms

In Section 3.3, different kinetic reaction mechanisms were investigated for the simulation of electrolyte-supported SOFCs. These types of cells have an anodic layer, which is thin due to the mechanical support of the electrolyte. Thus, catalytic Ni sites accompanied by reforming rates are lower compared to anode-supported cells. Below, reforming kinetics are scrutinized in order to determine appropriate mechanisms to describe the reactions that occur in anode-supported cells. This section thus examines global homogeneous reaction mechanisms as well as a detailed heterogeneous reaction mechanism.

Global Chemical Kinetics

In this section, global chemical kinetics for the two most prominent reforming reactions (MSR, Eq. (2.40) and WGSR, Eq. (2.41), see Section 2.4) are investigated in detail. The following Arrhenius-type factors (see Table 3.6) were applied to model global homogeneous methane steam reforming MSR and water-gas shift reactions WGSR. The following factors were determined by Arrhenius-curve fits:

Table 3.6.: Applied Arrhenius-type factors for homogeneous reaction kinetics approaches

Approach #	Frequency factor A $kmol\,m^{-3}\,s^{-1}$		Activation Energy E_A $J\,kmol^{-1}$		Source
	MSR	WGSR	MSR	WGSR	
H1	$1.49 \cdot 10^{17}$	$1.16 \cdot 10^5$	$2.21 \cdot 10^8$	$2.56 \cdot 10^7$	Hou and Hughes [23]
H2	$1.38 \cdot 10^{12}$	$1.17 \cdot 10^{12}$	$2.44 \cdot 10^8$	$1.22 \cdot 10^8$	Lehnert, Meusinger, and Thom [72]
H3	$2.55 \cdot 10^6$	–	$9.5 \cdot 10^7$	–	Ahmed and Foger [7], Anode A
H4	$8.44 \cdot 10^{10}$	–	$2.08 \cdot 10^8$	–	Ahmed and Foger [7], Anode B

The approach abbreviation **'Hx'** indicates that homogeneous reaction kinetics were used. The reaction orders of approach **H1** (Source: Hou and Hughes [23]) are described in their study. The remaining reaction orders applied in this section are listed in Table 3.7.

Table 3.7.: Corresponding reaction orders

Approach #	Reaction order		
	CH_4	CO	H_2O
H2	1	1	1
H3	0.85	-	−0.35
H4	1.4	-	−0.8

The catalytic conversion of methane into carbon monoxide and hydrogen within the porous anodic structure was modelled by the global reactions described above, and the related kinetic reaction approaches.

Detailed Heterogeneous Chemical Reaction Mechanism

Hecht et al. [74], Zhu et al. [8] and Maier et al. [75] developed a detailed heterogeneous chemical reaction mechanism for methane reforming over nickel catalysts. This mechanism consists of twenty-one pairs of irreversible surface reactions among six gas phase species and thirteen surface adsorbed species. This mechanism includes methanation reactions, oxidation reactions, water-gas shift reactions, as well as reactions for the formation of carbon monolayers on the catalyst surface (e.g. nickel in the porous anode substrate). These reactions are modelled as gas-surface and surface-surface interactions, which create sinks and sources both in the gas phase and on the reactive surfaces within the porous substrate. This increased level of detail in reaction modelling is distinctly different from simple homogeneous reaction mechanisms, and enables a more detailed interpretation of all of the processes that occur. The reaction rates are represented in Arrhenius form. Kinetic and thermodynamic data used from the papers mentioned above were interpreted in the CFD model and converted to an appropriate unit system. The sticking coefficients were transferred into an Arrhenius-type form. The reaction mechanism can be seen in Table 3.8.

Table 3.8.: Heterogeneous reaction mechanism for methane reforming on nickel catalysts taken from Refs. [8, 74, 75]. The parameters are: Frequency factor A, Arrhenius-type activation energy E_A, additional temperature exponent β ($k = A\,T^\beta \exp\left(-E_A\,R_m^{-1}\,T^{-1}\right)$). $Ni(s)$ denotes a free surface site on the catalytic active Ni surface.

No.	Elementary Reaction	A in $kmol\,m^{-2}\,s^{-1}$	E_A in $J\,kmol^{-1}$	β
1.	$H_2 + 2Ni(s) \rightharpoonup 2H(s)$	$3.62 \cdot 10^{14}$	0	0.5
2.	$2H(s) \rightharpoonup H_2 + 2Ni(s)$	$2.55 \cdot 10^{18}$	$8.12 \cdot 10^7$	0
3.	$O_2 + 2Ni(s) \rightharpoonup 2O(s)$	$9.09 \cdot 10^{13}$	0	0.5
4.	$2O(s) \rightharpoonup O_2 + 2Ni(s)$	$4.28 \cdot 10^{22}$	$4.75 \cdot 10^8$	0
5.	$CH_4 + Ni(s) \rightharpoonup CH_4(s)$	$2.73 \cdot 10^6$	0	0.5
6.	$CH_4(s) \rightharpoonup CH_4 + Ni(s)$	$8.71 \cdot 10^{15}$	$3.75 \cdot 10^7$	0
7.	$H_2O + Ni(s) \rightharpoonup H_2O(s)$	$3.22 \cdot 10^7$	0	0.5

8.	$H_2O(s) \rightharpoonup H_2O + Ni(s)$	$3.73 \cdot 10^{12}$	$6.08 \cdot 10^7$	0
9.	$CO_2 + Ni(s) \rightharpoonup CO_2(s)$	2061.43	0	0.5
10.	$CO_2(s) \rightharpoonup CO_2 + Ni(s)$	$6.48 \cdot 10^7$	$2.6 \cdot 10^7$	0
11.	$CO + Ni(s) \rightharpoonup CO(s)$	$1.29 \cdot 10^8$	0	0.5
12.	$CO(s) \rightharpoonup CO + Ni(s)$	$3.56 \cdot 10^{11}$	$1.11 \cdot 10^8$	0
13.	$H(s) + O(s) \rightharpoonup Ni(s) + OH(s)$	$5 \cdot 10^{21}$	$9.79 \cdot 10^7$	0
14.	$OH(s) + Ni(s) \rightharpoonup H(s) + O(s)$	$1.78 \cdot 10^{20}$	$3.61 \cdot 10^7$	0
15.	$H(s) + OH(s) \rightharpoonup Ni(s) + H_2O(s)$	$3.0 \cdot 10^{19}$	$4.27 \cdot 10^7$	0
16.	$Ni(s) + H_2O(s) \rightharpoonup H(s) + OH(s)$	$2.27 \cdot 10^{20}$	$9.18 \cdot 10^7$	0
17.	$2OH(s) \rightharpoonup H_2O(s) + O(s)$	$3 \cdot 10^{20}$	$1 \cdot 10^8$	0
18.	$H_2O(s) + O(s) \rightharpoonup 2OH(s)$	$6.73 \cdot 10^{22}$	$2.11 \cdot 108$	0
19.	$C(s) + O(s) \rightharpoonup Ni(s) + CO(s)$	$5.2 \cdot 10^{22}$	$1.48 \cdot 10^8$	0
20.	$Ni(s) + CO(s) \rightharpoonup C(s) + O(s)$	$1.35 \cdot 10^{21}$	$1.61 \cdot 10^8 - 5 \cdot 10^7 \, \theta_{CO(s)}$	-3
21.	$CO(s) + O(s) \rightharpoonup Ni(s) + CO_2(s)$	$2 \cdot 10^{18}$	$1.24 \cdot 10^8 - 5 \cdot 10^7 \, \theta_{CO(s)}$	0
22.	$Ni(s) + CO_2(s) \rightharpoonup CO(s) + O(s)$	$4.65 \cdot 10^{22}$	$8.93 \cdot 10^7$	-1
23.	$Ni(s) + HCO(s) \rightharpoonup H(s) + CO(s)$	$3.1 \cdot 10^{20}$	$0 + 5 \cdot 10^7 \, \theta_{CO(s)}$	0
24.	$H(s) + CO(s) \rightharpoonup Ni(s) + HCO(s)$	$4.02 \cdot 10^{19}$	$1.32 \cdot 10^8$	-1
25.	$Ni(s) + HCO(s) \rightharpoonup CH(s) + O(s)$	$3.7 \cdot 10^{23}$	$9.58 \cdot 10^7$	-3
26.	$CH(s) + O(s) \rightharpoonup Ni(s) + HCO(s)$	$4.60 \cdot 10^{19}$	$1.1 \cdot 10^8$	0
27.	$Ni(s) + CH_4(s) \rightharpoonup H(s) + CH_3(s)$	$3.7 \cdot 10^{20}$	$5.77 \cdot 10^7$	0
28.	$H(s) + CH_3(s) \rightharpoonup Ni(s) + CH_4(s)$	$6.03 \cdot 10^{20}$	$6.16 \cdot 10^7$	0
29.	$Ni(s) + CH_3(s) \rightharpoonup H(s) + CH_2(s)$	$3.7 \cdot 10^{23}$	$1 \cdot 10^8$	0
30.	$H(s) + CH_2(s) \rightharpoonup Ni(s) + CH_3(s)$	$1.29 \cdot 10^{22}$	$5.53 \cdot 10^7$	0
31.	$Ni(s) + CH_2(s) \rightharpoonup H(s) + CH(s)$	$3.7 \cdot 10^{23}$	$9.71 \cdot 10^7$	0
32.	$H(s) + CH(s) \rightharpoonup Ni(s) + CH_2(s)$	$4.09 \cdot 10^{23}$	$7.92 \cdot 10^7$	0
33.	$Ni(s) + CH(s) \rightharpoonup H(s) + C(s)$	$3.7 \cdot 10^{20}$	$1.88 \cdot 10^7$	0
34.	$H(s) + C(s) \rightharpoonup Ni(s) + CH(s)$	$4.56 \cdot 10^{21}$	$1.61 \cdot 10^8$	0
35.	$CH_4(s) + O(s) \rightharpoonup OH(s) + CH_3(s)$	$1.7 \cdot 10^{23}$	$8.83 \cdot 10^7$	0
36.	$OH(s) + CH_3(s) \rightharpoonup CH_4(s) + O(s)$	$9.88 \cdot 10^{21}$	$3.04 \cdot 10^7$	0
37.	$CH_3(s) + O(s) \rightharpoonup OH(s) + CH_2(s)$	$3.7 \cdot 10^{23}$	$1.30 \cdot 10^8$	0
38.	$OH(s) + CH_2(s) \rightharpoonup CH_3(s) + O(s)$	$4.61 \cdot 10^{20}$	$2.36 \cdot 10^7$	0
39.	$CH_2(s) + O(s) \rightharpoonup OH(s) + CH(s)$	$3.7 \cdot 10^{23}$	$1.27 \cdot 10^8$	0
40.	$OH(s) + CH(s) \rightharpoonup CH_2(s) + O(s)$	$1.46 \cdot 10^{22}$	$4.71 \cdot 10^7$	0
41.	$CH(s) + O(s) \rightharpoonup OH(s) + C(s)$	$3.7 \cdot 10^{20}$	$4.81 \cdot 10^7$	0
42.	$OH(s) + C(s) \rightharpoonup CH(s) + O(s)$	$1.63 \cdot 10^{20}$	$1.29 \cdot 10^8$	0

3.4.5. Carbon Formation

Besides the investigation of different reforming kinetics approaches, this section's objective is to analyse carbon formation in the catalytic active regions of a high temperature fuel cell. Different global carbon formation paths are known in literature. Reaction (3.3) and (3.5) - (3.9) are well known for causing the coking of the anode.

$$2CO \rightleftharpoons C + CO_2 \tag{3.5}$$

$$CO + H_2 \rightleftharpoons C + H_2O \tag{3.6}$$

$$CO_2 + 2H_2 \rightleftharpoons C + 2H_2O \tag{3.7}$$

$$CH_4 + 2CO \rightleftharpoons 3C + 2H_2O \tag{3.8}$$

$$CH_4 + CO_2 \rightleftharpoons 2C + 2H_2O \tag{3.9}$$

Methane cracking (Eq. (3.3)), the Boudouard reaction (Eq. (3.5)), and the carbon monoxide reduction reaction, Eq. (3.6), are the most likely paths for carbon formation and gasification. Hou and Hughes [23] found no perceptible carbon deposits on the catalyst surface during their experiments which investigated the reverse water-gas shift reaction. Hence, Eqs. (3.7) - (3.9) are neglected in the simulations. The methane cracking reaction is favoured for carbon deposition at high operating temperatures. With rising temperatures, the amount of CO becomes significant due to the exothermic water-gas shift reaction (cf. Eq. (2.41)). Hence, the Boudouard reaction has to be taken into account. Possible carbon formation is evaluated by means of two different approaches [22, 23, 74, 75, 82].

First, the thermodynamic carbon formation activity $\alpha_{(i)}$ is scrutinized. The carbon formation activities for Eqs. (3.3), (3.5) and (3.6) are determined by Eqs. (3.10) - (3.12) [22, 23, 82].

Table 3.9.: Chemical reaction and reaction equilibrium constant

Reaction i	$K_{eq,i}$	Carbon activity α_i	
(3.3)	$4.161 \cdot 10^7 \, exp(-10,614 \, T^{-1})$ [22, 23, 82]	$\alpha_{(3.3)} = K_{eq,(3.3)} \, p_{CH_4} \, p_{H_2}^{-2}$	(3.10)
(3.5)	$5.744 \cdot 10^{-12} \, exp(20,634 \, T^{-1})$ [22, 23, 82]	$\alpha_{(3.5)} = K_{eq,(3.5)} \, p_{CO}^2 \, p_{CO_2}^{-1}$	(3.11)
(3.6)	$3.173 \cdot 10^{-10} \, exp(16,318 \, T^{-1})$ [22, 23, 82]	$\alpha_{(3.6)} = K_{eq,(3.6)} \, p_{CO} \, p_{H_2} \, p_{H_2O}^{-1}$	(3.12)

In these equations, $K_{eq,i}$ represents the equilibrium constants of the corresponding reaction i, which can be seen in Table 3.9 and p_j represents the partial pressures of species j involved in reaction i. If $\alpha_i = 1$, the system is in thermodynamic equilibrium. Carbon formation is possible when $\alpha_i > 1$, which indicates that the system is in disequilibrium. For $\alpha_i < 1$ carbon formation reactions are inhibited. Thanks to the profile of carbon activities, it is possible to observe the location of potential carbon formation [22, 23, 82].

The second approach is when carbon monolayers - formed during the dissociative reactions of methane over the nickel catalyst - are taken into account. This is done by means of the detailed heterogeneous reaction mechanism presented in Table 3.8 of Refs. [8, 74, 75].

3.4.6. Boundary Conditions for the Simulations

No changes were made to the experimental setup thoroughly described in Section 3.1. Hydrocarbon reformates can be represented by their main components: CH_4, CO, CO_2, H_2, H_2O and

N_2. The reformate composition mainly depends on the operational mode of the reformer used. The diesel reformate composition applied for the experiments and simulations can be seen in Table 3.10. All fuel species, based on the given composition, were mixed in the fuel line and were fed to the anode side of the fuel cell. Synthetic air ($0.21\, mol\, mol^{-1}\, O_2$ in N_2) was fed to the cathode.

The numerical model of an ASC single cell was used, as in Section 3.2. The anode substrate thickness was $0.5\, mm$, due to its mechanical support function. The electrolyte and cathode functional layers were $10\, \mu m$ and $30\, \mu m$ thick, respectively. As in previous sections, the thoroughly validated fuel cell model with an unresolved electrolyte [27] was chosen, in order to correctly represent the physical cell. Experiments were conducted for a temperature of $800\, °C$. The simulations were validated with data gained from appropriate experiments. Based on these validated simulations, further numerical investigations were carried out for temperatures of 750 and $850\, °C$. Fuel and air flow rate were set to values typical of SOFC systems, and are also given in Table 3.10.

Gas mixture properties, such as thermal conductivity λ, dynamic viscosity η, and specific heat capacity $C_{mp,i}$ were modelled, as shown in Section 3.2.1. The material properties of the fuel cell's anode, cathode, and electrical current collectors, as well as the model parameters of the fuel cell module [27] and supplementary geometrical data can be seen in Table 3.10. The electrochemical and electrical property estimations are based on data given in [27, 44]. The anode and cathode current collectors were made of alloys of nickel and platinum, respectively, the properties of which were considered to be similar to their pure elements.

Table 3.10.: Material and numerical properties used for the simulations. Reference: ^{e} estimate, ^{a} assumed, ^{f} fitted, ^{m} measured

Parameter	Value	Unit
Electrochemical properties		
Anode exchange current density $i_{0,A}$	$10750^{\,f}$	$A\, m^{-2}$
Cathode exchange current density $i_{0,C}$	$512^{\,f}$	$A\, m^{-2}$
Electrolyte resistivity	$0.1^{\,e}$	Ωm
Cathode current collectors		
Electrical conductivity σ	$1.5 \cdot 10^{7\,e}$	$\Omega^{-1} m^{-1}$
Density ρ	$21,200$	$kg\, m^{-3}$
Cathode contact resistance	$10^{-8\,e}$	$\Omega\, m^2$
Specific heat capacity $C_{mp,i}$	140	$J\, kg^{-1} K^{-1}$
Thermal conductivity λ	72	$W\, m^{-1} K^{-1}$
Cathode LSCF		
Porosity ε	$0.3^{\,a}$	–
Tortuosity τ	$3^{\,a}$	–
Thermal conductivity λ	1.15	$W\, m^{-1} K^{-1}$
Specific heat capacity $C_{mp,i}$	565 [27]	$J\, kg^{-1} K^{-1}$
Electrical conductivity σ	7937 [27]	$\Omega^{-1} m^{-1}$
Density ρ	$4,375$ [27]	$kg\, m^{-3}$
Thickness	$30^{\,m}$	μm

Anode Ni-YSZ		
Porosity ε	$0.3^{\,a}$	–
Tortuosity τ	$3^{\,a}$	–
Thermal conductivity λ	6.23	$W\,m^{-1}K^{-1}$
Specific heat capacity $C_{mp,i}$	595.1 [27]	$J\,kg^{-1}K^{-1}$
Electrical conductivity σ	$3.33 \cdot 10^{5}$ [27]	$\Omega^{-1}m^{-1}$
Density ρ	$3,030$ [27]	$kg\,m^{-3}$
Thickness	$500^{\,m}$	μm
Anode current collectors		
Electrical conductivity σ	$1.5 \cdot 10^{7}$	$\Omega^{-1}m^{-1}$
Density ρ	$8,900$	$kg\,m^{-3}$
Anode contact resistance	$10^{-7\,e}$	$\Omega\,m^{2}$
Specific heat capacity $C_{mp,i}$	446	$J\,kg^{-1}K^{-1}$
Thermal conductivity λ	91	$W\,m^{-1}K^{-1}$
Geometry parameters		
Length	$0.09^{\,m}$	m
Width	$0.0025^{\,m}$	m
Height	$0.002^{\,m}$	m
Experimental conditions		
Temperature	800	$^{\circ}C$
Pressure	$1.013 \cdot 10^{5}$	Pa
Fuel compositions		
Flow rate	2.4	$SLPM$
Hydrogen / Nitrogen mixture		
H_2	0.456	$mol\,mol^{-1}$
H_2O	0.113	$mol\,mol^{-1}$
N_2	0.431	$mol\,mol^{-1}$
Hydrocarbon fuel mixture (diesel reformate)		
CH_4	0.0225	$mol\,mol^{-1}$
CO_2	0.098	$mol\,mol^{-1}$
CO	0.137	$mol\,mol^{-1}$
H_2	0.154	$mol\,mol^{-1}$
H_2O	0.113	$mol\,mol^{-1}$
N_2	0.4755	$mol\,mol^{-1}$
Oxidant composition		
Flow rate	4	$SLPM$
O_2	0.21	$mol\,mol^{-1}$
N_2	0.79	$mol\,mol^{-1}$

The electrochemical performance of the numerical model was evaluated by fitting the anode and cathode exchange current density to experimental measurements. The modelled exchange current densities i_0 were altered to fit the simulated and measured polarization curve at a cell current density of $300\,mA\,cm^{-2}$ and the corresponding cell voltages ($0.75\,V$ for the dry hydrogen/nitrogen mixture). In order to determine these parameters, dry and humidified hydrogen/nitrogen mixtures were used (see Table 3.10). The hydrogen molar fraction was kept constant; in case of a humidified mixture, the nitrogen molar fraction was reduced and water

vapour was added.

In order to keep the computational cost of these simulations in an acceptable range, the investigated domain was simplified further. Figure 3.16 shows the process of simplifying the numerical simulation model. The procedure was similar to the one described in Section 3.3, but a further symmetry plane was used inside the flow channel (cf. Figure 3.16(b)) to keep the number of grid cells needed for geometrical discretization low. For the mesh, $225,000$ hexahedrons were used, with a maximum aspect ratio of 30 and a maximum skewness of 0.36. As shown by Lawlor et al. [60], the aspect ratio and skewness are in a sufficient range for this application. The mesh is displayed in Figure 3.16(c).

(a) Periodically repeating flow channel structure

(b) Isometric view of the flow channel used for simulations

(c) Hexahedral mesh with 225,000 cells
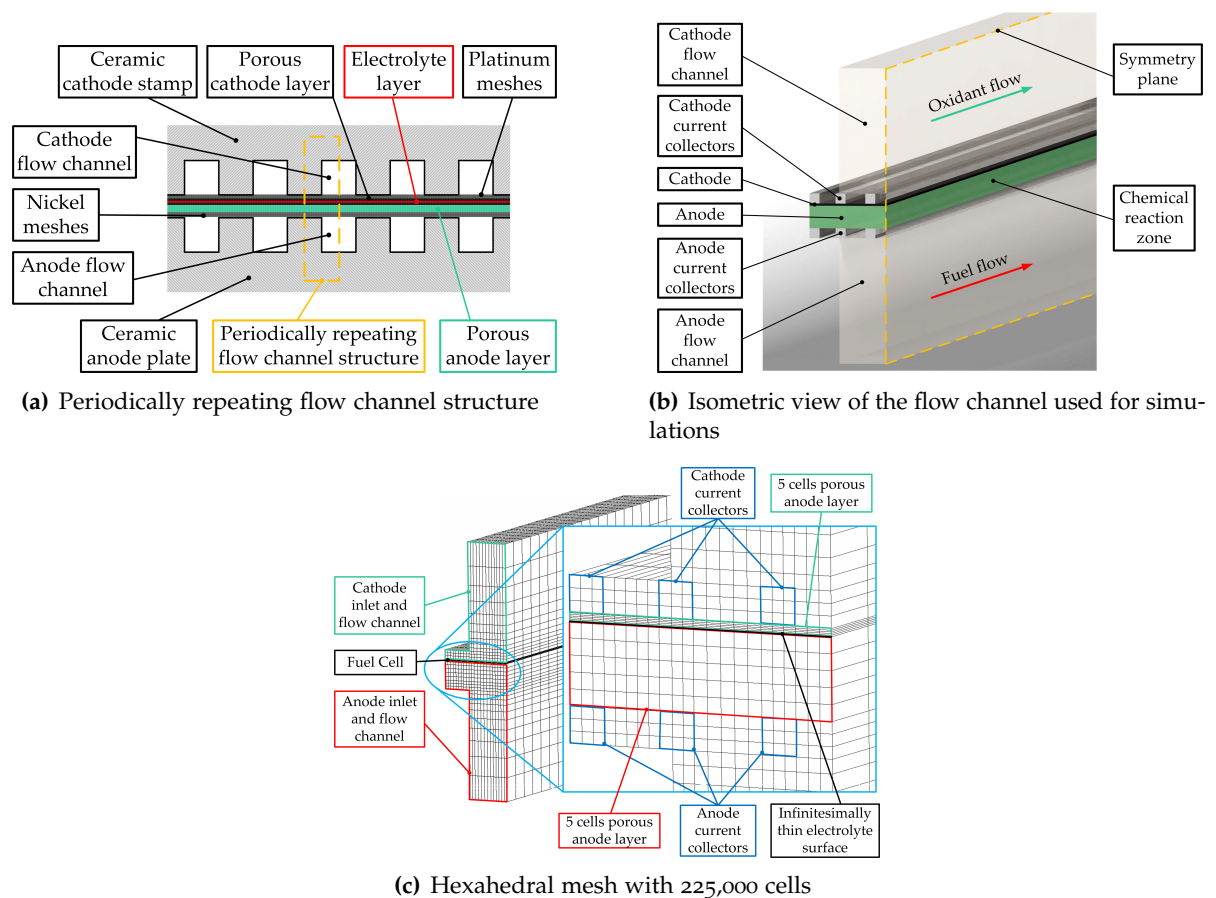
Figure 3.16.: Scheme of the flow channel arrangement, channel rendering and the mesh used for simulations [41]

Anodic and cathodic inlets were defined as mass flow inlets. In order to correctly describe a fully-developed laminar flow profile, inlet and outlet channels were added before and after the cell. These channels were included in the simulations, but were suppressed in Figures 3.16(b) and 3.16(c) in order to place the focus on the display of the fuel cell discretization. The outlets were defined as pressure outlets, and the corresponding wall boundary conditions were set to correctly represent the flow channel modelled as a simplification of an entire cell. Isothermal boundary conditions were set for the ceramic walls.

3.4.7. Polarization Curves for Different Reforming Kinetics

Figure 3.17 shows the calculated and experimentally-determined polarization curves for the investigated anode-supported cell at $800\,^{\circ}C$. Sampling points for the simulations were set for OCV, 40, 100, 200 and $260\,mA\,cm^{-2}$.
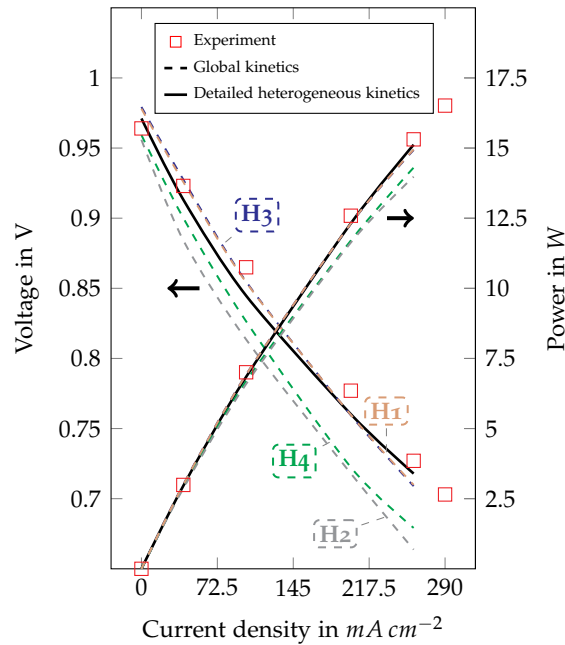
Figure 3.17.: Polarization curves operated on diesel reformate (cf. Table 3.10) for different reforming approaches (cf. Table 3.6 for homogeneous kinetics and Table 3.8 for heterogeneous kinetics) at $800\,^{\circ}C$ [41]

It is possible to see that due to different global and detailed kinetic reaction mechanisms, various cell performances were calculated. This is due to unequal methane reforming characteristics, which deliver variable amounts of electrochemically oxidizable fuel species, such as hydrogen or carbon monoxide. Experimental data is depicted by the red markers. An open circuit voltage of $U_{OCV} = 0.964\,V$ was measured for the diesel reformate composition used (cf. Table 3.10). As can be seen in the graph, the performances that were achieved are acceptable for cells of this type ($100 \times 100\,mm^2$) and for this fuel composition ($i_{max} = 290\,mA\,cm^{-2}$). The electrical contacting of button or unit cells is easier than for the type of cells used in these experiments, which leads to increased current densities in smaller sized cells. Simulation results for global reaction mechanisms are depicted as dashed lines. It can clearly be seen that there were notable differences in the cell performance prediction as a result of the diversified kinetic approaches. Global kinetic approaches **H1** and **H3** (dashed yellow and blue lines, see Table 3.6 for kinetics approach) show the best correlation throughout the whole load range. Kinetics approaches **H2** and **H4** (dashed grey and green lines) show greater deflections from the experiment. The simulation results for the detailed heterogeneous reaction mechanism are represented by the black solid line. OCV is slightly overestimated. Voltage deflections between experiment and simulation were calculated in a range of $10\,mV$. Cell power output is plotted on the second axis of ordinates. A maximum cell load of $290\,mA\,cm^{-2}$ at $0.703\,V$ was measured, providing $16.5\,W$ of cell power output.

3.4.8. Gas-phase Reaction Validation of Numerical Simulations

The reforming characteristics of SOFCs are of particular interest, since the internal reforming of methane in the anode-supported structure is made possible by the catalytically active nickel. Nickel is used as both a catalyst and an electrical conductor. In order to correctly predict the regions where carbon formation and deposition may occur, it is necessary to have a reliable representation of carbon formation processes. As shown in global reactions (3.3), (3.5) and (3.6), different carbon formation paths exist. Global reforming reaction mechanisms model a simplified reaction path of complex elementary reactions. Methane reforming is catalytically activated, and thus a heterogeneous reaction. In order to validate the quality of different global reforming kinetics, the conversion of methane into hydrogen and carbon monoxide was monitored.

(a) Hydrogen

(b) Carbon monoxide

(c) Carbon dioxide

(d) Methane
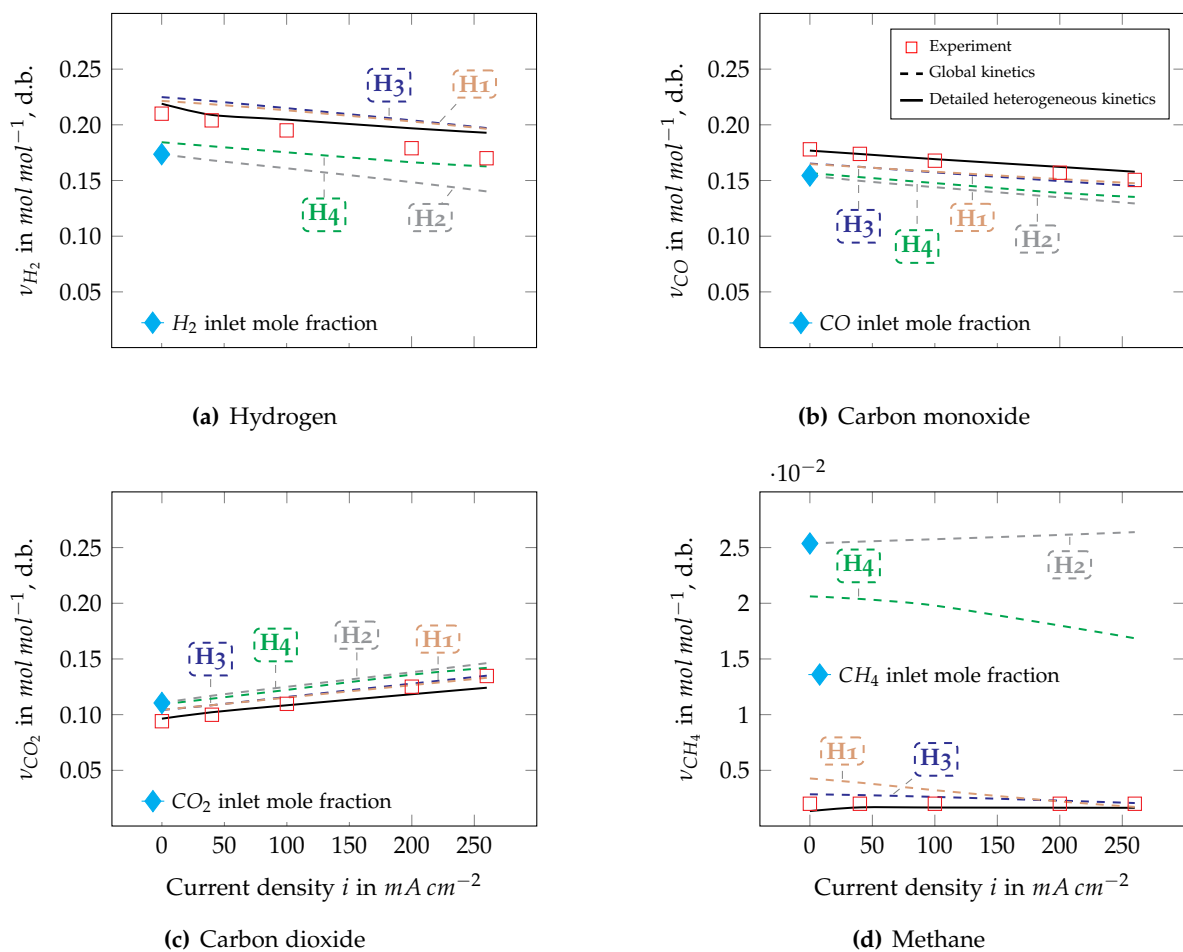
Figure 3.18.: Anode outlet composition and species reaction rates over the entire load range [41]

Figure 3.18 shows the measured and simulated species molar fraction distribution at the anode's outlet over varied cell loads. For a better understanding of the conversion rates, the reformate inlet composition is drawn as a single diamond marker within these plots. Dashed lines represent the global reforming kinetics simulations, while a solid line indicates the data of the detailed heterogeneous reaction mechanism. Reforming properties can best be seen at

the open circuit voltage (OCV) since, at this point of operation, only chemical reactions take place; electrochemical reactions do not occur as no current is drawn; no extra water is formed nor is heat added to the system. Figures 3.18(a) and 3.18(b) show the hydrogen and carbon monoxide molar fraction trends, respectively. Due to the internal reforming of methane, the H_2 and CO molar fractions rise from 0.174 to 0.21 and 0.154 to 0.178, respectively, as determined in the experiment. The carbon dioxide molar fraction (see Figure 3.18(c)) decreases at OCV since the reaction's equilibrium shifts toward reactants at this temperature level. The reforming rate can be represented by relative conversion rates. Relative conversion is defined as

$$X_i = \frac{N_{i,feed} - N_{i,out}}{N_{i,feed}}. \tag{3.13}$$

where X_i is the relative conversion, $N_{i,feed}$ are moles of species i fed to the system and $N_{i,out}$ are moles of species i leaving the system. The cells and nickel meshes used for these experiments show very high methane conversion rates of $X_{CH_4} = 92\,\%$, which can be calculated from data in Figure 3.18(d). The reforming kinetics of homogeneous approach **H2** and **H4** (dashed grey and green lines) show low or almost no conversion of methane at OCV. Thus, the simulated fuel composition at the anode outlet differs greatly from the experimental data. Global reaction mechanisms **H1** and **H3** (dashed yellow and blue lines) deliver higher methane conversion rates, whereas the calculated values of **H3** (dashed blue line) best fit the experimental results with $X_{CH_4} = 88.8\,\%$.

The simulation results of the numerically expensive detailed heterogeneous reforming mechanism (solid black line) deliver methane conversion rates of $X_{CH_4} = 94.7\,\%$, which is a slight overestimation of the experiment. Carbon monoxide and carbon dioxide trends of the heterogeneous approach are in almost perfect agreement for the whole load range. However, there are slight deflections in the hydrogen molar fractions between the experiment and simulations. The gradient of the detailed reaction mechanism is still marginally different from that of the experiment. This could be a result of the different reaction mechanisms used for the chemical reforming reactions and the electrochemical reactions. Heterogeneous reactions were used to calculate reforming performances, whereas the electrochemical reactions based on homogeneous reactions, e.g. the Nernst equation, were solved using partial pressures of the electrochemically active species.

In Figure 3.19, reaction rates r_i on a dry base (related to the geometric surface of the anode) for the involved gas phase species are shown as a function of the ionic molar flux $S_{O^{2-}}$ ($S_{O^{2-}} = i/2F$). Here, F is the Faraday constant and i the current density. The graph shows the calculated rates for experimental data (red markers), the detailed heterogeneous reaction mechanism (solid black lines), and the best fitting global reaction mechanisms of **H3** (dashed blue lines).

The reaction rates for hydrogen and carbon monoxide are shown in Figure 3.19(a). The internal reforming performance of the catalyst can best be seen at OCV ($S_{O^{2-}} = 0$). As shown

and discussed in Figure reffig:reforming-characteristics, both numerical kinetics approaches slightly overestimate the internal reforming performance of methane. Thus, simulated hydrogen reaction rates exceed the experimental values, although both the methane and carbon monoxide conversion and the corresponding reaction rates are in good accordance with the experiment and simulation. Nonetheless, a satisfactory fit was achieved with the detailed heterogeneous reaction mechanism. The global kinetics approach **H3** further overestimates the hydrogen reaction rate, when compared to the detailed mechanism. An increment of the oxygen ion flux $S_{O^{2-}}$ results in a decrease of the hydrogen reaction rate, since it is consumed and product water is formed.

(a) Hydrogen and carbon monoxide   **(b)** Carbon dioxide and methane
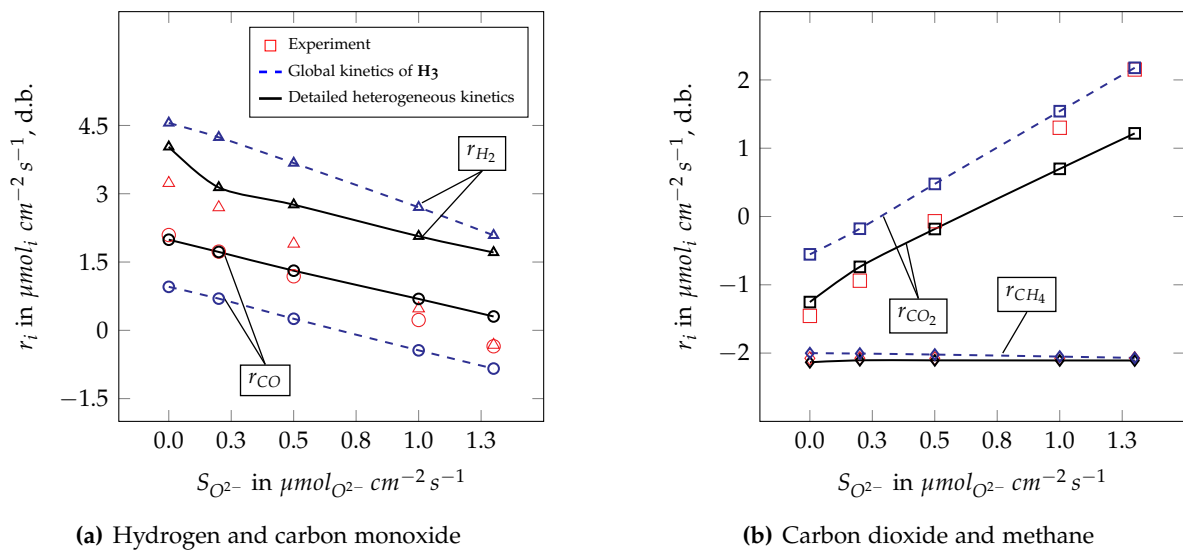
Figure 3.19.: Reaction rates r of reacting species: experimental data, global kinetics approach **H3** and the detailed heterogeneous approach [41]

Figure 3.19(b) shows the reaction rates for carbon dioxide and methane. Methane conversion is independent of cell load. Thus, this is a pure chemical reaction and not influenced by electrochemical reactions. These minimal discrepancies between the experimental and simulated reaction rates at OCV result in the differences for hydrogen shown in Figure 3.19(a). This reflects the difficulty in modelling the correct reaction rates for the methane steam reforming reaction, due to the reaction's stoichiometry.

The carbon monoxide data at OCV for the detailed heterogeneous mechanism shows that all of the reactions involved predict the reaction rates to a satisfactory extent. The global kinetics approach, **H3**, underrates this reaction. Trends for carbon dioxide production and carbon monoxide consumption fit the experimental data in a good way, both qualitatively and quantitatively. Differences occurred at high cell loads, indicating that the electrochemical conversion of H_2 and CO is slightly underrated. This indicates that the reference exchange current density $i_{0,i}$ is marginally too low. The initial fit was done for a hydrogen-water vapour mixture. The reaction rates for this mixture, containing only one electrochemically convertible constituent, were correctly predicted by the model. However, the presence of a second electrochemically convertible species (CO) can be seen to have an influence on the electrochemical activity. Nonetheless, the chemical and electrochemical performance prediction of the simulation model were

deemed to be satisfactory, however, the fact that there is room for improvement in predicting the H_2/CO electrochemistry interaction was noted.

3.4.9. Reforming Characteristics of Different Kinetic Approaches

Figure 3.20 shows gas phase species distribution along the cell. Figures 3.20(a), 3.20(c), 3.20(e) and 3.20(g) show the averaged molar species fractions along the cell for OCV. The measured values are shown as single diamond markers at 0 and 90 mm, and represent the gas composition at the anode inlet and outlet, respectively. The simulated data is depicted as either dashed lines (global reforming kinetic mechanisms) or as a solid line (detailed heterogeneous kinetic mechanism).

Similar to the results shown in Figure 3.18, the best agreement between the experiment and the simulation was reached with the detailed heterogeneous reaction mechanism (black solid line). This mechanism incorporates not only reforming and shift reactions, but also partial and total oxidation in addition to methanation reactions. As indicated by the axis of ordinates scale, the simulation results are of very high quality, since the peak deflections are $0.01\,mol\,mol^{-1}$. As can be seen by the dashed lines for carbon monoxide and carbon dioxide, the water-gas shift reaction is slightly underestimated. The reforming mechanisms of the global kinetic approach **H2** and **H4** fail to correctly predict the chemical reactions that occur. Approaches **H1** and **H3** resulted in trends for hydrogen (cf. Figure 3.20(a)) and methane (cf. Figure 3.20(g)) similar to those of the detailed heterogeneous mechanism. Thus, the MSR reaction is modelled correctly for these approaches. A weakness of these approaches was found for the WGSR reaction. None of the investigated global kinetics approaches managed to correctly predict the reaction rates, and thus the outlet carbon monoxide (cf. Figure 3.20(c)) and carbon dioxide (cf. Figure 3.20(e)) composition were also incorrect.

Figures 3.20(b), 3.20(d), 3.20(f) and 3.20(h) show contour plots of molar species fractions calculated by the detailed heterogeneous mechanism along a cross-section of the anode flow channel (cf. Figure 3.16(b) for the description of the evaluation plane). Axes of ordinates and abscissae are scaled differently in order to make it easier to interpret the data (different scaling factors for the cell length and the channel height). The fuel cell is positioned at the top of the channel (at channel height 2 mm). Chemical reactions were modelled to occur solely within the porous anode structure, which is 0.5 mm thick, and situated above the channel. It is possible to see that the reaction products diffuse from this layer into the flow channel. These contour plots clearly show that species are unequally distributed within the flow channels since chemical reactions can only occur in the presence of a catalyst, which, in this case, is nickel. Figure 3.20(h) shows that the reforming reaction is quite fast, and that methane is almost entirely converted after two thirds of the cell length. The species conversion rates can also be interpreted by the inclination of the corresponding diagrams.

In conclusion, the detailed heterogeneous mechanism was the only approach that correctly predicted the outlet composition. Very high accordance was achieved between the experimentally-

(a) Hydrogen

(b) Contours of hydrogen

(c) Carbon monoxide

(d) Contours of carbon monoxide

(e) Carbon dioxide

(f) Contours of carbon dioxide

(g) Methane

(h) Contours of methane
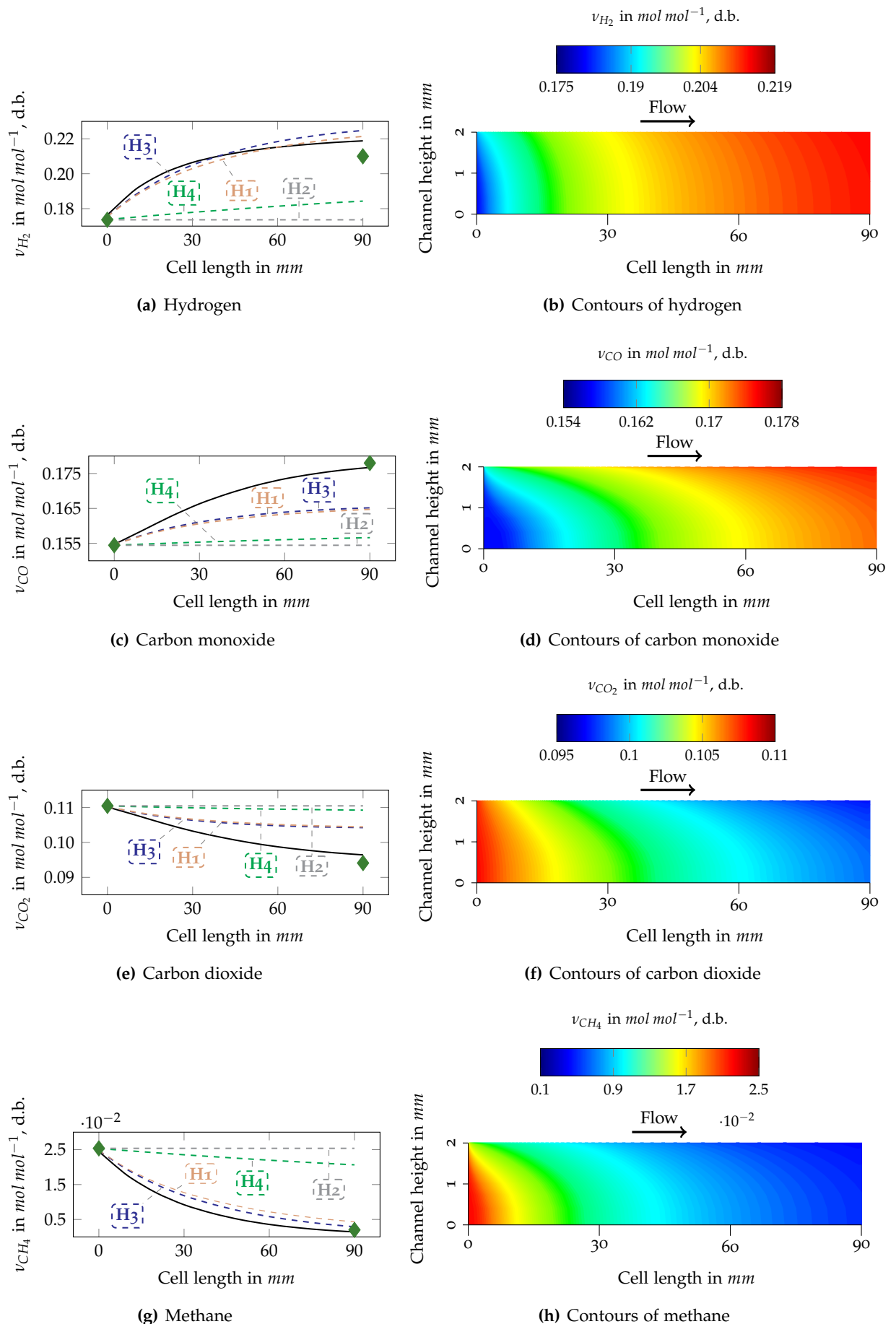
Figure 3.20.: Species distribution (dry base) for different kinetic approaches along the cell (cf. Table 3.6) in 3.20(a), 3.20(c), 3.20(e), 3.20(g), and contours of species molar fraction (dry base) for the detailed heterogeneous mechanism (see Table 3.8) in 3.20(b), 3.20(d), 3.20(f) and 3.20(h) [41]

determined outlet composition and the simulated data. The CFD model thus correctly predicts the chemical and electrochemical performance of the investigated ASC cell. Thus, a validated simulation base was generated for the investigation of other processes that occur during fuel cell operation.

3.4.10. Carbon Formation Activity

With the above results for gas phase species, reliable data is available to scrutinize further reactions, such as the formation and deposition of carbon on and within the porous anode structure. When global kinetics approaches for the simulation of internal reforming reactions are used, the only possibility to numerically describe carbon formation is to determine carbon formation activities. The precipitation of a solid carbon phase is very difficult to describe numerically, and there is not yet a satisfactory modelling approach in literature.

As shown in Table 3.9, carbon formation activities can be simulated based on the equilibrium of gas phase species. These activities indicate whether the dissociation reaction in question is in equilibrium or in disequilibrium. Thus, carbon formation activities indicate whether or not carbon forms due to a certain reaction, for example, the methane-cracking reaction (Eq. (3.3)), the Boudouard reaction (Eq. (3.5)) or the carbon monoxide reduction reaction (Eq. 3.6).

Carbon formation and deposition is thermodynamically possible if a carbon formation activity is bigger than unity. According to Refs. [22] and [23], reactions (3.3), (3.5) and (3.6) are the most probable elementary carbon sources in SOFC applications. Thus, carbon formation activities $\alpha_{(3.3)}$, $\alpha_{(3.5)}$ and $\alpha_{(3.6)}$ were implemented in the CFD-code by means of user-defined functions. The magnitude and position of the activities indicate regions that are vulnerable to carbon deposition within the porous anode structure.

The formation activities of carbon during the internal reforming of diesel reformate (cf. Table 3.10), depicted in Figures 3.21 and 3.22, was analysed at three different positions within the porous anode structure. The anode surface (dashed lines), anode centre (solid lines) and the three-phase boundary (dotted lines) were examined (see schematic of evaluation lines shown in Figure 3.21(a) for a better visualization of the different positions). Furthermore, different cell load cases (OCV: black lines, $100\,mA\,cm^{-2}$: blue lines and $260\,mA\,cm^{-2}$: orange lines) were investigated, since Finnerty et al. [78] and Alzate-Restrepo and Hill [79] showed that elementary carbon formed under open circuit conditions and under load conditions exhibited different characteristics; that is, carbon formed at higher cell loads was more reactive than that formed under open circuit conditions since it was hydrogenated. Thus, carbon formation activities were evaluated at OCV, at a medium cell load of $100\,mA\,cm^{-2}$ and a maximum load of $260\,mA\,cm^{-2}$ at $0.7\,V$.

In Figure 3.21(a), the carbon formation activities $\alpha_{(3.3)}$ (brought about by the methane cracking reaction (3.3)) are shown for the global reforming mechanism **H3**. With a rising cell load (indicated by different colours), formation activity magnitude decreases significantly. However,

the simulated activities still remain significantly below unity for the entire cell length, which indicates carbon does not form as a result of the methane cracking reaction for this particular fuel mixture. The highest values were calculated for the three-phase-boundary TPB at OCV.

(a) $\alpha_{(3.3)}$ for global kinetics of approach **H3**

(b) $\alpha_{(3.3)}$ for the detailed heterogeneous reaction mechanism
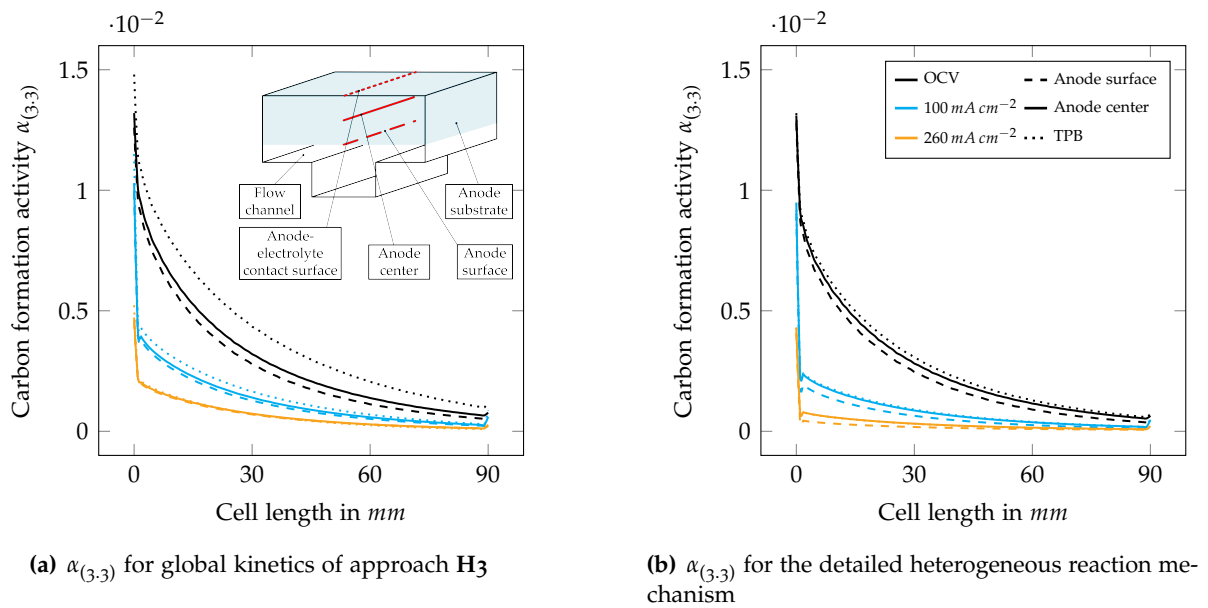
Figure 3.21.: Carbon formation activity $\alpha_{(3.3)}$ along the cell at different positions within the porous anode and at various cell loads at $800\,^\circ C$ for the global reaction kinetics **H3** and the detailed heterogeneous mechanism [41]

Values for $\alpha_{(3.5)}$ and $\alpha_{(3.6)}$ are well above unity. Thus, only the data for $\alpha_{(3.5)}$ is plotted in Figure 3.22. It is possible to see that, throughout the anode thickness, carbon formation activity decreases significantly. Carbon formation caused by the Boudouard reaction is thus most likely to occur on the anode surface. Diverse cell loads result in marginally different activities. According to this thermodynamic analysis, carbon formation is most likely to occur on the anode surface due to the Boudouard reaction (3.5) and reaction (3.6). Carbon formation caused by methane cracking (reaction (3.3)) is unlikely to occur, due to the marginal methane partial pressures of the applied gas mixture.

Looking at the carbon activities $\alpha_{(3.3)}$ of the methane cracking reaction for the detailed heterogeneous reaction mechanism (see Figure 3.21(b)), it is possible to see that the global reaction mechanism **H3** produced an analogous shape and magnitude. Minimal activity was calculated during maximum cell load. Carbon formation activity due to methane cracking resides below unity for the entire cell length. Again, this indicates that carbon formation due to methane cracking is not possible. In Figure 3.22(b), $\alpha_{(3.5)}$ is distinctly different than the simulation results of the global reaction mechanism **H3**. The maximum values at the anode surface (dashed lines) are reduced to about 50 % in comparison to values calculated with the global mechanism **H3**. Carbon activity is also decreased at the anode centre (solid lines), whereas activities increased slightly (dotted lines) at the anode-electrolyte contact surface. The carbon activities are well above unity, again indicating that carbon forms as a result of the dissociative Boudouard reaction.

Experiments were conducted with the diesel reformate composition described (cf. Table 3.10), and with either elevated carbon monoxide or elevated methane mole fractions, in order to evaluate the simulation results of carbon formation activity. The cell performance (voltage and anode exhaust composition) was monitored in order to identify major carbon precursors.

(a) $\alpha_{(3.5)}$ for global kinetics of approach **H3**

(b) $\alpha_{(3.5)}$ for the detailed heterogeneous reaction mechanism
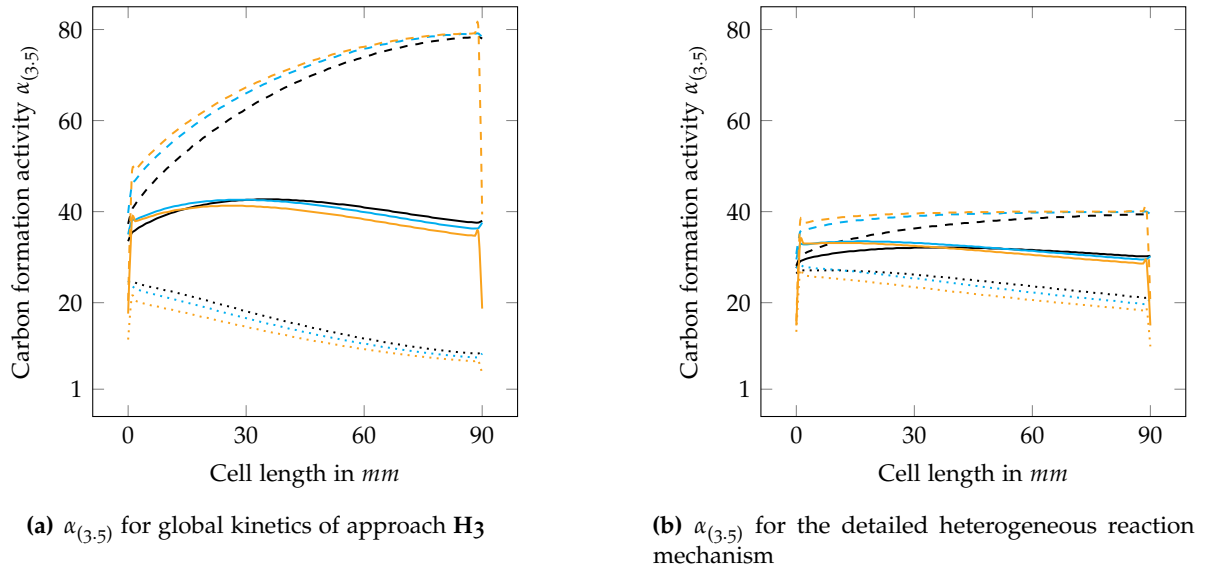
Figure 3.22.: Carbon formation activity $\alpha_{(3.5)}$ along the cell at different positions within the porous anode and at various cell loads at $800\,°C$ for the global reaction kinetics **H3** and the detailed heterogeneous mechanism [41]

Increased methane mole fractions led to a rapid performance decrease within several minutes. An increase of carbon monoxide in the fuel supply did not result in cell performance deterioration, even after several hours. Thus, it showed that methane is a major carbon formation pathway in this application. Carbon did not form due to the Boudouard reaction, and the cell performance did not decrease. The simulated carbon formation activities only describe the thermodynamic equilibrium of the reactions considered. The reaction kinetics of the dissociative reactions mentioned were not modelled. Based on these experiments, the notion of coking resulting from the dissociation of carbon monoxide has to be questioned. The kinetics of this reaction were slow, and led to no detectable performance degradation. Carbon formation is more likely to occur as the result of methane cracking, which led to a rapid deterioration in the performance of the cell. The carbon formation activities that were simulated describe the thermodynamic possibilities, but do not account for reaction kinetics.

The carbon formation activities described above are the only ways to simulate carbon formation when global reaction approaches for internal reforming are applied. Since they only represent a deviation from the thermodynamic equilibrium of a reaction, they do not provide the option of describing the local formation of carbon deposits as a solid species. This is a major drawback of using this approach for future investigations of carbon formation. Moreover, this approach cannot be used for subsequent carbon removal simulations, since no locally fixed (deposited) carbon is existent. Because of its increased relevance to the present study, the detailed heterogeneous reaction mechanism that makes it possible to directly predict the

amount of adsorbed elementary carbon on the catalytic active surface was scrutinized. This mechanism allows the spatial and temporal analysis of surface-adsorbed species, which is a decisive advantage over global reforming mechanisms. A detailed analysis of this mechanism was carried out, and is presented in the following section.

3.4.11. Analysis of Detailed Wall-Surface Chemistry

It is possible to gain considerable insight into carbon depositions through detailed heterogeneous reactions. As seen in Table 3.8, the detailed reaction mechanism incorporates the decomposition reactions of methane, lower hydrocarbons, and carbon-containing fuel species, such as carbon monoxide and carbon dioxide. Thus, it is possible simulate and scrutinize the amount and position of surface-adsorbed elementary carbon and its corresponding precursors within the spatially-resolved anode structure.

Figures 3.23 and 3.24 show contour plots of surface-adsorbed species on the anode surface at OCV, 100 and $260\,mA\,cm^{-2}$ at $800\,°C$ (see schematic for position as depicted in Figure 3.21(a)) while using diesel reformate (cf. Table 3.10). The plots show different scaling factors (length and width have varying scaling factors to provide a better view, due to the dimensions of the geometry, which can be reviewed in Table 3.10).

(a) Contours of surface adsorbed C(s)   **(b)** Contours of surface adsorbed CH(s)
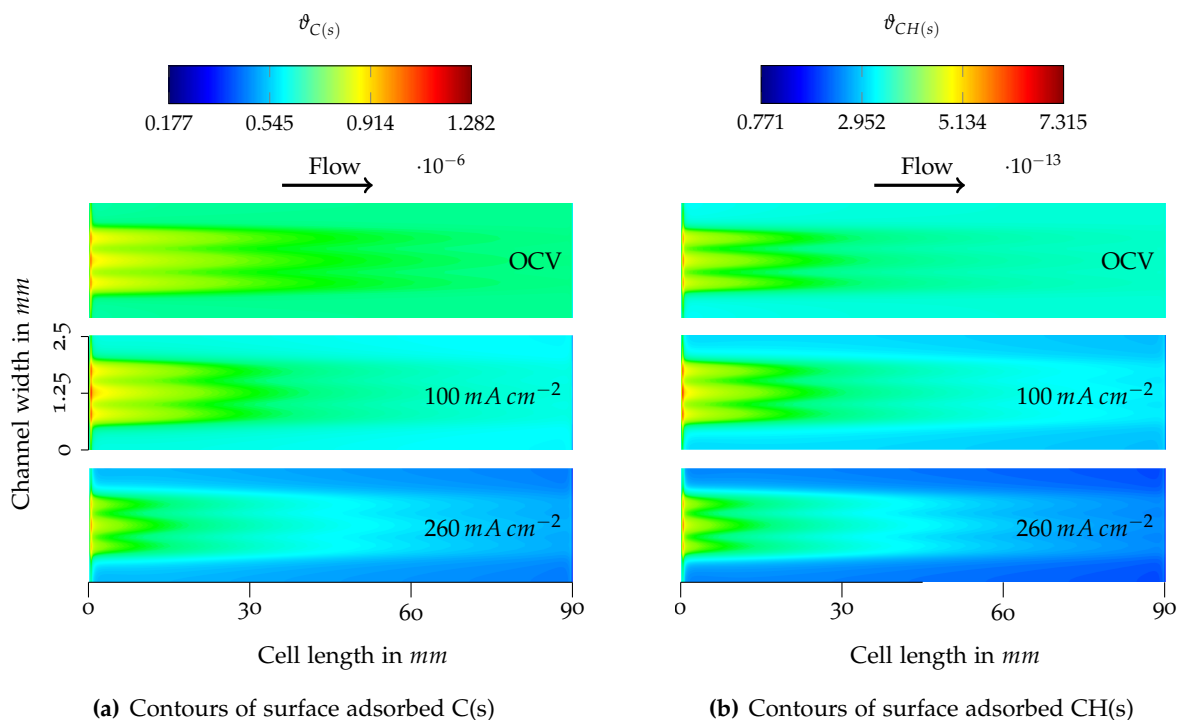
Figure 3.23.: Surface coverages for adsorbed $C(s)$ and $CH(s)$ on the anode at varying cell loads during internal reforming of diesel reformate at $800\,°C$ [41]

The contours of surface-adsorbed elementary carbon $C(s)$ are shown in Figure 3.23(a). Surface coverage is highest at the cell inlet, with local peaks resulting from the thin current collectors applied to the anodic surface. These thin wires can best be seen in the schematic of the

generated mesh in Figure 3.16(c). At OCV, carbon surface coverage is more homogeneously distributed and higher in magnitude than compared to the average $(100\,mA\,cm^{-2})$ and maximum $(260\,mA\,cm^{-2})$ cell load. The elevated oxygen ion transport through the electrolyte, which results from the increased loading of the cell, provokes higher conversion rates of adsorbed species, and thus leads to decreased carbon surface coverage.

A precursor of elementary surface adsorbed carbon is $CH(s)$, as shown by Yurkiv [87]. Thus, contours of surface-adsorbed $CH(s)$ are shown in Figure 3.23(b). As a direct precursor of $C(s)$, its general distribution across the surface is almost identical throughout the depicted load range. As indicated by the applied magnitude scale, surface coverage of $CH(s)$ is only a fraction of elementary carbon. This shows that significantly more elementary carbon is accumulated at the catalytic active areas (nickel) than $CH(s)$.

(a) Contours of surface adsorbed CH4(s), CH3(s) and CH2(s) at OCV

(b) Contours of surface adsorbed CH4(s), CH3(s) and CH2(s) at $260\,mA\,cm^{-2}$
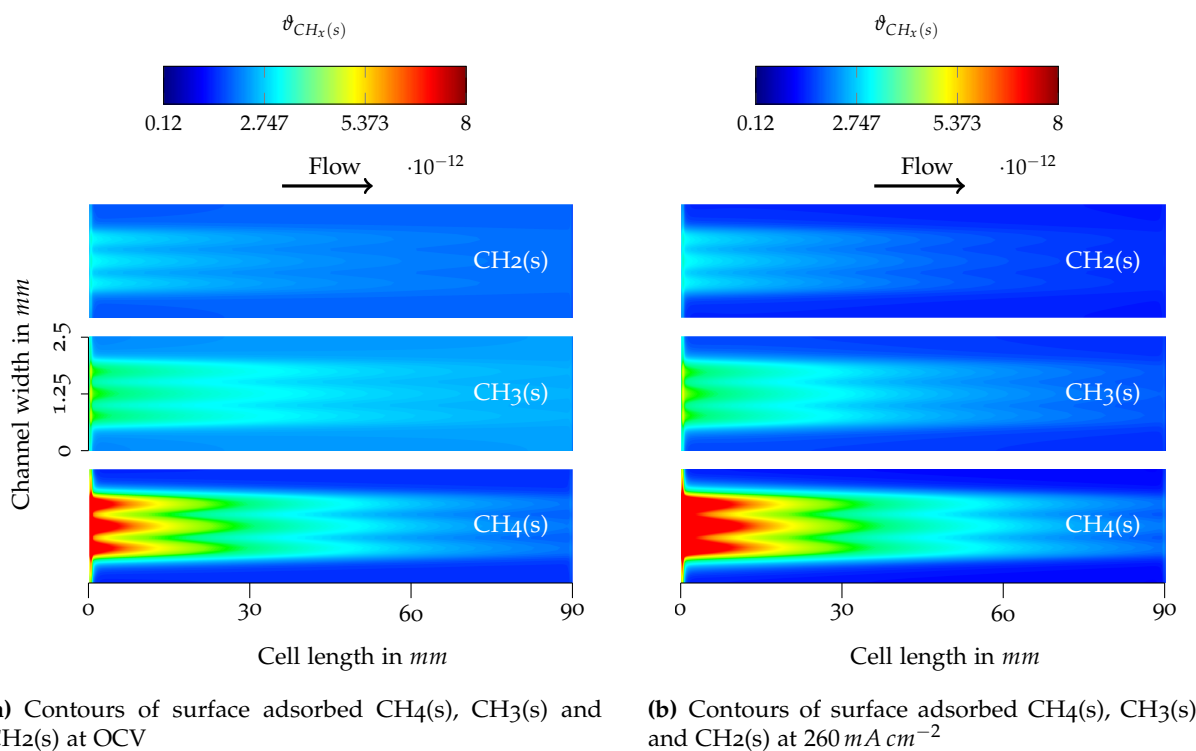
Figure 3.24.: Surface coverages for adsorbed $CH_x(s)$ on the anode surface at varying cell loads during internal reforming of diesel reformate at $800\,°C$ [41]

In Figures 3.24(a) and 3.24(b), a comparison of the decomposition steps of methane on the anodic surface at OCV and maximum cell load $(260\,mA\,cm^{-2})$ is shown. At open circuit voltage, the amount of adsorbed methane is more concentrated at the cells' inlet compared to maximum cell load. Under load, methane surface coverage is more pronounced within the first $20\,mm$ of the cell. As can be seen by the contours of intermediates $CH_3(s)$ and $CH_2(s)$, rising cell load promotes conversion rates, and, therefore, the surface coverage of these species is higher at OCV, which results in the coverages shown in Figure 3.23(b), and subsequently, to the carbon surface coverage depicted in Figure 3.23(a).

Figures 3.25 and 3.26 show the averaged surface coverages of major adsorbed hydrocarbon

species for the entire temperature range between 750 and 850 °C and between OCV and maximum cell load ($260\,mA\,cm^{-2}$) along the anode substrate centre. Different line styles indicate diverse temperature levels, markers represent different cell loads, and different colours depict different surface-adsorbed species. Figure 3.25(a) shows the area-averaged surface coverage trend of elementary carbon on active nickel sites along the centre of the cell (cf. schematic in Figure 3.21(a)). It's possible to see that the amount of adsorbed carbon species peaks within the first five millimetres of the anode substrate, regardless of the temperature level. With increasing cell length, the number of adsorbed molecules decreases. It is noticeable that for 750 °C, minimum surface coverage of elementary carbon is calculated for OCV, whereas maximum coverage was calculated for a medium cell load of $100\,mA\,cm^{-2}$. Surface coverages at the highest cell load ($260\,mA\,cm^{-2}$) are arranged between these two extrema.

(a) Surface coverage of $C(s)$

(b) Surface coverage of $CH(s)$
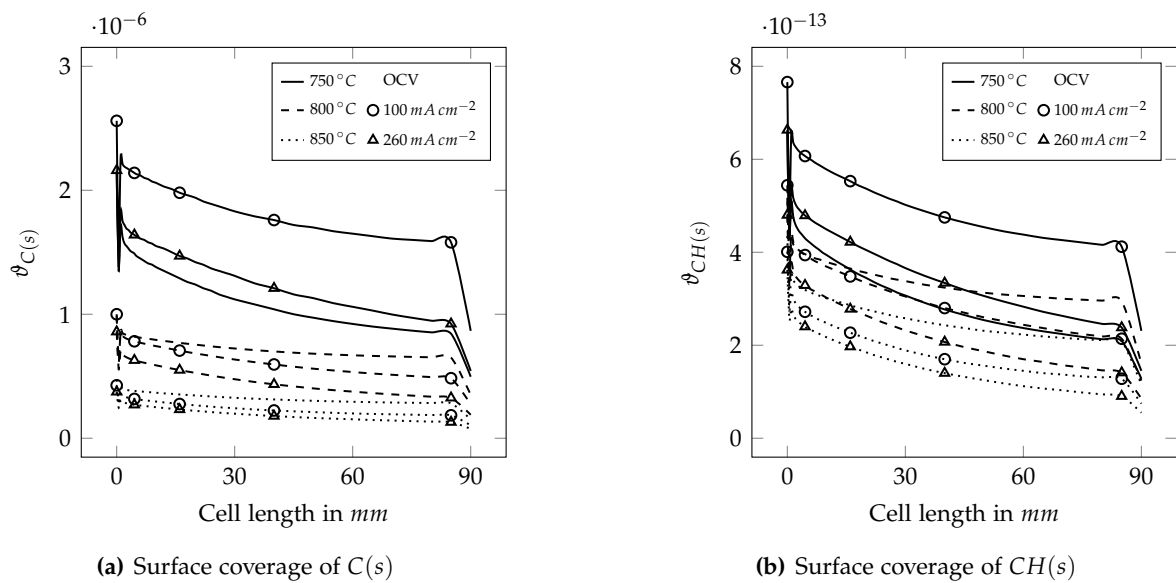
Figure 3.25.: Surface coverage trends of adsorbed $C(s)$ and $CH(s)$ at 750 °C, 800 °C and 850 °C along a line at the anode center [41]

This result disagrees with results in literature ([79], [81]), and can be attributed to the isothermal boundary condition. The simulation results show that at this decreased temperature, species coverages are maximized at medium cell load, and chemical reaction kinetics are lowered. The current drawn from the cell ($100\,mA\,cm^{-2}$) increases the electrochemical oxidation rates, which subsequently causes maximum species carbon and precursor species at this temperature. At elevated temperature levels (dashed lines: 800 °C, dotted lines: 850 °C), the magnitudes of adsorbed molecules drops to a third and a sixth of the peak values at 750 °C. The influence of the cell load changes noticeably. The maximum coverages were calculated for OCV, and decrease with rising cell load. The simulation results for elevated temperatures agree with the findings of the above mentioned literature. These simulations showed that at different temperature levels and cell loads, carbon formation is possible at the anode inlet zone.

A direct precursor species of elementary carbon is $CH(s)$. The simulated surface coverages of this species are plotted in Figure 3.25(b). The trend of this species is analogous to that described

for elementary carbon. Significant differences can be seen in the magnitude of the adsorbed molecules. Different temperature levels show the same behaviour as for elementary carbon species.

(a) Surface coverage of $CH_2(s)$ and $CH_3(s)$

(b) Surface coverage of $CH_4(s)$
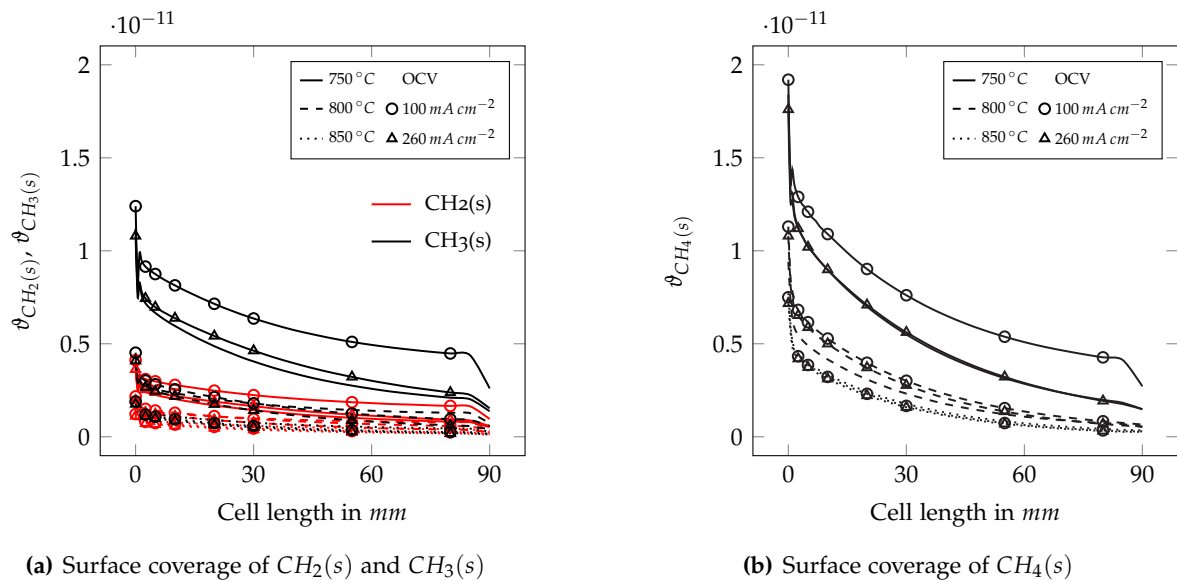
Figure 3.26.: Surface coverage trends of adsorbed $CH_2(s)$, $CH_3(s)$ and $CH_4(s)$ at $750\,^{\circ}C$, $800\,^{\circ}C$ and $850\,^{\circ}C$ along a line at the anode centre [41]

Figure 3.26(a) shows the reaction pathway from surface adsorbed methyl (CH_3) to methylene (CH_2) for the examined temperature range and cell loads. The highest surface coverages were again calculated for the lowest temperature level. As the temperature rises, the magnitude of surface-adsorbed species decreases in a manner similar to that described for Figures 3.25(a) and 3.25(b). In Figure 3.26(b), the trend of adsorbed methane to the catalytic active nickel sites is shown. Methane is the major hydrocarbon species adsorbed to the surface. The simulation shows that for $750\,^{\circ}C$, species coverages are maximized at medium cell loads. At this temperature, chemical reaction kinetics are lowered. If the applied cell current increases, so too does the electrochemical oxidation, which results in the maximum coverages at this temperature level at a medium current density of $100\,mA\,cm^{-2}$. This could represent a critical operating point for a low-temperature operation.

In a study by Janardhanan et al. [88], surface coverages of elementary carbon were calculated using the detailed heterogeneous reforming mechanism presented above. Higher methane volume fractions ($0.4\,mol\,mol^{-1}$) were used, leading to slightly higher surface coverages. Thus, the calculated results are plausible.

It is notable that the calculated carbon coverages $C(s)$ are only a precursor to amorphous or fibrous carbon, which can be found in physical experiments related to coking. A method for classifying these carbon coverages in terms of type and deposited moles of carbon per time will be presented and discussed in Chapter 4.

The surface coverages of water and its dissociation products ($OH(s)$ and $O(s)$) are shown

in Figures 3.27 and 3.28. In Figure 3.27(a), surface-adsorbed water $H_2O(s)$ dominates at the lowest temperature level of $750\,^{\circ}C$ at OCV. Minimum coverages were calculated for $850\,^{\circ}C$ at OCV. In this figure, it's possible to see that as the cell length increases, the anode surface coverage rises for all of the investigated cases. The surface coverages of hydroxyl- and oxygen radicals are depicted in Figures 3.27(b) and 3.28(a). With rising temperatures and cell loads, the coverages increase. For $750\,^{\circ}C$, maximum coverages were again calculated at OCV. The magnitude of all adsorbed species shows that most of the catalytically-active surface is covered by oxygen and water. The contour plot of surface adsorbed $O(s)$ in Figure 3.28(b) shows the local inhomogeneity of the adsorbed species. It can be seen that, at the inlet, coverages are low. In this region, major reforming steps take place. At the cell outlet, surface coverage increases, since most of the reforming steps have already been completed by this point.

(a) Surface coverage of $H_2O(s)$

(b) Surface coverage of $OH(s)$
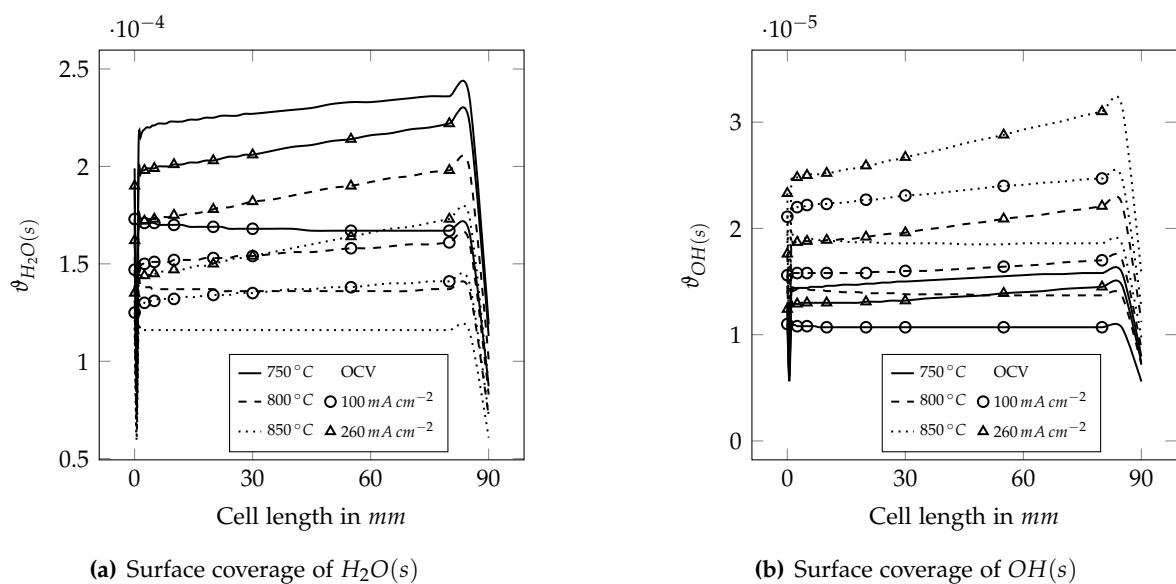
Figure 3.27.: Surface coverages of $H_2O(s)$ and $OH(s)$ at $750\,^{\circ}C$, $800\,^{\circ}C$ and $850\,^{\circ}C$ along a line at the anode center [41]

This data provides complete and detailed information of the gas phase and the surface-adsorbed species. It can subsequently be used to identify the critical operating points and conditions of large planar SOFCs. Since both the experimental and numerical data for gas phase reactions are in very good agreement, it possible to assume that the simulated local profiles of surface adsorbed species coincide with the species adsorption profiles induced by the experiments. Moreover, the calculated and experimentally-determined results for the hydrocarbon fuel mixture were also in general agreement with the outcomes of many studies on methane-fuelled SOFCs (cf. Refs. [8, 44, 73–75, 82–84, 88]).

3.4.12. Discussion of Yurkiv's Modelling Approach

As was briefly mentioned in Section 3.4.11, Yurkiv presented a novel approach to modelling and simulating carbon depositions in his study [87] that was based on the detailed heterogeneous

(a) Surface coverage of $O(s)$

(b) Contours of surface adsorbed $O(s)$ at $800\,°C$ and $260\,mA\,cm^{-2}$
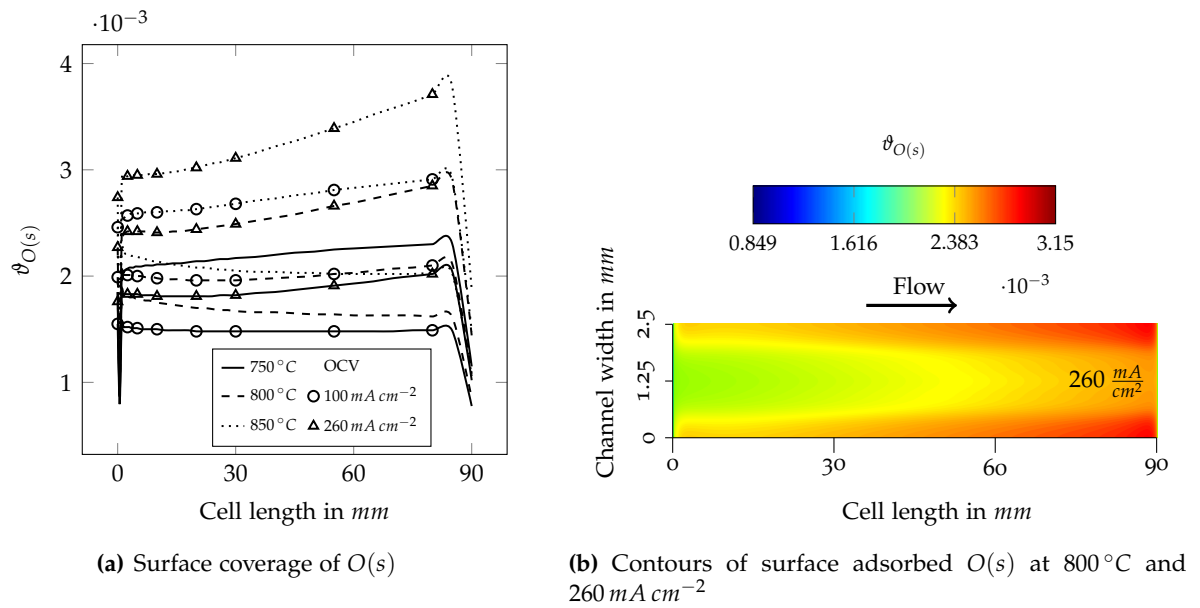
Figure 3.28.: $O(s)$ surface coverage trends and contour plot [41]

reaction mechanism, shown in Table 3.8 and in [74, 75]. He considered the formation of two types of solid carbon that can be observed on the nickel surface during SOFC operation. He modelled the formation of a film type carbon as a new phase, based on the carbon coverages $C(s)$. This carbon film hindered the catalytic and electrocatalytic reactions of the cell. Moreover, he modelled the formation of a second phase, pyrolytic carbon, which grows on top of the carbon film. This pyrolytic carbon was similar to soot, and blocked the pores of the cell, resulting in an increased flow resistance of the gases through the pores. Thus, this type of carbon increased the mass transport losses, leading to elevated concentration overpotentials.

Yurkiv's simulations were based on a $2D$ model of a planar SOFC, and were carried out on their in-house software package, DENIS. The extended detailed mechanism created by Yurkiv [87], as well as his proposed modelling approach, were applied to the model developed in this thesis, based on the software package ANSYS Fluent.

However, despite the extensive and thorough analysis of ways to implement this simulation approach in the ANSYS Fluent environment, the attempts failed, and Yurkiv's numerical results Yurkiv [87] could not be reproduced. This was attributed to the nature of the proposed reactions. The formation of a solid phase, based on the elementary carbon coverages $\vartheta_{C(s)}$ as well as its subsequent build-up of a secondary solid phase cannot be modelled in ANSYS Fluent in cooperation with the SOFC add-on module and the laminar-finite rate based chemistry interactions. Moreover, the solid-solid reactions mentioned (agglomeration of film to pyrolytic carbon) cannot be modelled in ANSYS Fluent. However, Yurkiv's proposed kinetics for this solid-solid interaction could not be found anywhere else in literature. The implementation of such a carbon build-up mechanism in the powerful ANSYS Fluent framework would make it possible to carry out the spatially- and temporally-resolved analysis of two different carbonaceous solid phases within the porosity of a high temperature solid oxide fuel cell. This

would constitute a major contribution to the scientific community.

Nevertheless, Yurkiv's modelling approach Yurkiv [87] could not be successfully applied to our 3*D* model of an entire SOFC single cell, the local and time-dependent species adsorption profiles of carbonaceous, hydrogenated and oxygenated species that occur during internal reforming of diesel reformates were scrutinized. These profiles were used to identify possible carbon formations, and even other degradation effects within the cell, such as nickel re-oxidation.

3.4.13. Summary of Internal Reforming Kinetics and Carbon Modelling Approaches

The present chapter has presented the numerical investigations of different modelling approaches for carbon formation pathways within SOFC anode structures fuelled with a hydrocarbon fuel mixture that represents diesel reformate. Global homogeneous reaction mechanisms, based on the evaluation of carbon formation activities, provided indicators of the thermodynamic equilibrium of the formation pathway under consideration. The kinetics of these global carbon formation reactions were not taken into account due to a lack of data in literature.

The simulation results were validated by experimental data for an anode supported SOFC single cell, and the reforming reactions were analysed by investigating the conversion rates of methane. The different approaches to global reaction kinetics that were investigated showed a pronounced deviation from the predicted conversion rates. Two approaches (**H2** and **H4**, see Table 3.6) completely failed to predict the occurring methane steam reforming and water-gas shift reaction. The kinetics approaches **H1** and, in particular, **H3** delivered results that, to a large extent, coincide with the experimental measurements. However, the only way to describe carbon formation based on global kinetics is to introduce carbon formation activities. The determination of possible carbon deposition based on formation activities has to be questioned, since cell degradation under slightly-elevated methane partial pressures was more pronounced than the changes that occurred under carbon monoxide. Moreover, the calculated carbon formation activities indicated the exact opposite behaviour: They showed that carbon formation due to carbon monoxide is much more likely than due to methane. Thus, carbon formation activities are an indicator of formation pathways, but cannot be used as the basis for future scrutiny of carbon removal strategies. These formation activities will be investigated in further detail in Chapter 4, and their applicability will be reviewed.

A cell's electrochemical performance is dependent on the partial pressures of electrochemically convertible constituents, such as hydrogen and carbon monoxide. An incorrect internal reforming rate of methane thus delivers imprecise H_2 and CO partial pressures, and leads to incorrect predictions of cell performance. Therefore, the chemical and electrochemical interaction in SOFCs is crucial. This highlights the importance of investigating each element scrutinized in this chapter, so as to be able to create the most precise and detailed simulation model. In spite of taking a number of global kinetic reaction approaches, their applicability has to be

specifically reviewed for each individual application, e.g., anode catalyst type and amount of catalyst material (in terms of electrode thickness). This finding constitutes an important finding of this thesis.

In a final step, a detailed heterogeneous reaction mechanism was applied in order to scrutinize the gas - solid interaction of the catalytic reforming process within the porous anode substrate. The best fit between experiment and simulation was achieved by means of this detailed heterogeneous reaction mechanism. Only this detailed mechanism made it possible to reliably investigate and evaluate the anodic structures vulnerable to carbon deposition in terms of kinetics. This thesis has shown that elementary carbon is permanently adsorbed to the catalytic active nickel sites during internal reforming in the porous anode. This important outcome of this work needs to be highlighted. These carbon coverages are only a precursor to the carbon that forms during SOFC experiments or during technical applications. A method to link the calculated surface coverages to actual carbon formation rates will be presented in Chapter 4. This mechanism further provides the option to investigate a multitude of surface-adsorbed species, and will thus be used to scrutinize the total surface coverage during the internal reforming of various fuels. In the following sections, major degradation sources, such as carbon formation and nickel re-oxidation, will be investigated.

4

Identification of Major Carbon Precursors

Diesel reformates are usually gas mixtures containing different carbonaceous precursors. The use of a representative diesel reformate was thoroughly analysed in Chapter 3. However, it is very difficult to identify and isolate one particular carbon formation pathway when using such a diesel reformate mixture in a SOFC. Thus, in this chapter, the number of unknown variables was reduced to a minimum by applying basic fuel mixtures.

The literature on the use of carbon containing fuels in SOFCs states that there are two main carbon precursors which have to be taken into account: methane and carbon monoxide. This chapter aims to identify the major carbon formation pathway by means of the detailed simulation model developed for this work. Therefore, equilibrium calculations and kinetics based simulation approaches are used to investigate critical operating conditions. The coking propensities of methane, carbon monoxide, and an equimolar mixture of both the aforementioned constituents are examined during internal reforming under varying S/C ratio in SOFC anodes at OCV. As seen in Chapter 3, the investigation of carbon formation activities for selected reaction pathways (e.g. methane cracking or the Boudouard reaction) can deliver conflicting results. Thus, in this Chapter, $0D$ equilibrium calculations and transient CFD simulations were carried out to identify major carbon precursors and their pathways. The carbon formation activity calculations and the kinetics-based simulations are compared in order to gain deep insight into the strengths and weaknesses of both approaches. Local and temporal surface coverage distributions of adsorbed elementary carbon are used to address regions in danger of short- and long-term degradation caused by carbon deposition.

4.1. Introduction[1]

One of the major advantages of SOFCs is the direct internal reforming of light hydrocarbons, such as methane, in the anode. This electrode is most commonly made from a highly porous metal-ceramic composite, usually nickel and YSZ. Nickel catalyses the reforming reaction of methane, thus it is possible to directly feed methane into the fuel cell's anode. One of the biggest challenges of directly feeding hydrocarbon fuels into SOFCs is the performance degradation that is brought about by the solid, elemental carbon that forms in the porous anodic structure [69, 70]. The dissociation reactions of alkane-based fuels were discussed in Section 3.4 in reactions (3.2), (3.3), (3.5) and (3.6). Carbon depositions within the porous anode can cause pore blocking, thereby inhibiting mass transfer to and from the catalytically and/or electro-catalytically active sites. Further, reforming reactions can be prevented by breaking or by blocking the TPB [68].

4.1.1. Hydrocarbon Fuels

Light hydrocarbons can be utilized by SOFCs in a temperature range between $600\,^{\circ}C$ and $1,000\,^{\circ}C$. Thus, different fuels and fuel compositions can lead to minor through to severe damage to the cell.

Methane is the simplest and most stable gaseous hydrocarbon used in SOFCs. It is reformed to carbon monoxide and hydrogen, which implies the possibility of carbon formation. Because of its frequent use, methane has been intensively studied as a fuel, both experimentally and numerically, by many researchers over a long period of time [7, 22, 23, 31, 58, 72–74, 78–81, 84, 86, 90–96]. The work of these researchers and the results of these publications are described below (see Section 4.1.2 and 4.1.3).

4.1.2. Material Properties of Carbon from Carbon Monoxide and Methane

Different carbonaceous fuels provoke the formation of diverse forms of carbon. Carbon formed through the dissociative reactions of carbon monoxide and CO/H_2 feeds is different from carbon decomposed from methane. Alzate-Restrepo and Hill [97] investigated carbon formation on electrolyte-supported button cells fed with CO and blends of CO and H_2. Their experiments (conducted at $800\,^{\circ}C$) determined that polarization has a positive protection effect, rejecting carbon deposition; i.e. less carbon was formed under a finite current than at OCV. An interesting outcome of this study was that CO led to either minimal carbon deposits at OCV and none at all under polarization. They also showed that the carbon formed was not hydrogenated, and that the amount of carbon deposited under CO and blends of CO and H_2 was higher by an order of magnitude, compared to the experiments conducted on methane (cf. [79]). Peak carbon

---

[1]Segments of this section were published in the *Journal of Fuel Cell Science and Technology* under the title "Carbon Deposition Simulation in Porous SOFC Anodes: A Detailed Numerical Analysis of Major Carbon Precursors" [89].

formation was observed with a CO/H_2 mixture of 3/1 on a molar basis. Snoeck, Froment, and Fowles [98] and T. Chen et al. [99] have experimentally shown that carbon monoxide and methane fuel feeds lead to different forms of carbon on the anode. Operation with carbon monoxide led to encapsulating carbon, whereas filamentous carbon deposits form during methane operation.

4.1.3. Carbon Formation: Experimental Investigations, Equilibrium Considerations and Reforming Kinetics

Ni-YSZ anodes and their outstanding reforming activities have attracted a lot of scientific attention. This has led to comprehensive investigations of their deactivation and carbon formation propensies [44, 78–84, 97]. Thermodynamic data for carbon deposited in SOFC anodes differs greatly in literature. It is often assumed that the carbon formed is similar to C(gr) [100, 101]. However, McIntosh and Gorte [92] showed that two primary pathways to carbon formation occur in SOFC anodes: the first, homogeneously formed soot consisting of polycyclic aromatic hydrocarbons (PAH), and the second, CNF that grow heterogeneously on the catalyst surface. They determined that the thermodynamic properties of this carbon differ from those of graphite. This is of major importance for gas composition calculations, as it leads to different results, as shown in [102]. Besides general operating conditions, such as pressure or current density, the extent of carbon formation in typical SOFC operating temperature ranges greatly depends on the S/C ratio. Depending on temperature and pressure, absolute S/C values can be calculated based on equilibrium considerations. It is important to know the fuel compositions in thermodynamic equilibrium for an initial, $0D$-assessment of carbon formation. Equilibrium, however, implies that dissociation kinetics are sufficiently fast, which is only a satisfactory assumption for a first guess. In their studies, Sasaki et al. [100, 101] and Lee et al. [102] showed the equilibrium compositions of different possible anode gases, as well as carbon formation boundaries dependent on the operating temperature or the thermodynamic properties of the precipitated carbon.

A more detailed numerical representation of carbon formation can be obtained with $2D-$ and $3D$-numerical simulations, such as CFD simulations. Different approaches, of increasing levels of sophistication, have been used in literature to describe the coking of the anode. The internal reforming of methane (steam reforming, dry reforming, as well as autothermal oxidation) and the water-gas shift reaction (CO utilization) has been studied in detail on Ni-YSZ catalysts. Many research groups [7, 8, 22, 23, 72–75] have developed and applied different numerical approaches that describe the reaction kinetics involved therein. These studies have developed homogeneous global reaction expressions [7, 22, 23, 72, 73] as well as very detailed heterogeneous catalytic reaction mechanisms [8, 74, 75]. Steam reforming and water-gas shift reactions have mostly been described and modelled by two or three reaction steps in global homogeneous reaction mechanisms, as seen in the studies of [44, 73, 82–84, 103].. Therein, only gas phase reactions are taken into account. These mechanisms are not able to describe the

detailed reaction paths and precipitation of elementary carbon species In these cases, carbon formation propensity is mainly calculated by evaluating the thermodynamic equilibrium of the methane-cracking reaction (see reaction (3.3)) or the Boudouard reaction (reaction (3.5)). This approach delivers values for the possibility of carbon forming in vulnerable regions of the anode.

As was demonstrated in Chapter 3 and [42], this detailed numerical model facilitates understanding of the complex superimposed transport processes within high-temperature solid oxide fuel cells. Moreover, it is able to reveal regions of SOFC anodes in danger of carbon deposition. Janardhanan et al. [93] also utilized this detailed mechanism to predict the reforming performance of a SOFC and showed that precise the calculation of surface carbon is essential for an accurate prediction of a cell's OCV at low S/C ratios.

As discussed in Section 3.4.12, Yurkiv [87] numerically predicted the formation of film and pyrolytic carbon layers on the catalytic active sites of a porous anode structure by means of the detailed reaction mechanism of [74]. Noticeable amounts of both modelled types of carbon were deposited and grew during operation on synthetic reformate. Furthermore, the performance deterioration of the cell was shown and validated with data from literature. As noted, this novel approach incorporates the formation of a solid carbon phase and the phase change from film carbon to pyrolytic carbon by agglomeration reactions. However, the CFD software used in this thesis is not able to predict the reaction rates of solid species or solid-solid interactions, as they are introduced in [87]. The numerical results of Yurkiv's study are impressive, but could not be reproduced with the CFD software applied in this thesis.

4.2. Analysis of Carbon Formation Pathways[2]

In this section, mixtures of methane and steam, carbon monoxide and steam, and equimolar mixtures of methane/carbon monoxide with steam will be investigated for their propensity to form carbon in porous SOFC anodes.

4.2.1. Thermodynamic Equilibrium of Fuels

Thermodynamic equilibrium calculations were conducted with the software HSC Chemistry 6.00 [104], incorporating a comprehensive thermochemical database. The equilibrium of a gas mixture was derived by minimizing the Gibbs free energy of formation. For the calculations, species and radicals consisting of the elements carbon, hydrogen and oxygen, were considered with a maximum carbon number of unity. All of the calculations were conducted for a fuel gas mixture normalized to 1 mol of carbon, in the temperature range of 100 to $1,000\,°C$ with an increment of $10\,K$. Carbon formation for gas mixtures was investigated by varying the steam-

---

[2]Segments of this section were published in the *Journal of Fuel Cell Science and Technology* under the title "Carbon Deposition Simulation in Porous SOFC Anodes: A Detailed Numerical Analysis of Major Carbon Precursors" [89].

to-carbon ratio from 0.5 to 2 with a step size of 0.5 using both thermodynamic properties of graphite and CNF, as per Ref. [102]. Since solid carbon precipitates during the dissociation process, the calculation results are displayed as amounts of products rather than molar fractions or concentrations.

4.2.2. Detailed Numerical Simulations

The transient carbon deposition simulations were conducted for temperatures of 600, 800 and $1,000\,^{\circ}C$, which are typical SOFC operating temperatures that mark lower and upper temperature boundaries. Gas mixtures similar to the equilibrium calculations were investigated. Many studies use global chemical reactions to describe internal reforming inside the porous anode structure (e.g. the global methane-steam reforming reaction, reaction (2.40), or the water-gas shift reaction, reaction (2.41)) with kinetics of **H1**, **H2** or **H3**, as shown in Table 3.6 and thoroughly scrutinized in Chapter 3.

As indicated in the introduction to this chapter, this strongly limits the possibility of characterizing carbon formation and deposition. The most commonly used possibility when using global reforming kinetics is to define carbon formation activities. These activities are given in Eqs. (3.10) - (3.12) in Table 3.9, and the corresponding discussions were presented in Sections 3.4.5 and 3.4.10. However, these activities were found to merely provide guide values for carbon formation when using diesel reformates. Thus, in the coming sections, they are investigated for methane and carbon monoxide fuels, and their applicability is questioned. Since they only represent a numerical value that describes the deviation from thermodynamic equilibrium, their utilization and validity is analysed herein, but their continuing usage for subsequent carbon removal simulations is precluded.

Detailed heterogeneous reaction mechanisms for methane reforming over nickel based catalysts offer the potential to directly calculate the amount of elementary carbon adsorbed at the catalytic active sites of the porous anode. The mechanism (as presented in Table 3.8) implemented in the simulation model is thus used as a powerful basis. Carbon deposition is evaluated by means of spatial and temporal surface-site coverage distributions of carbon $\vartheta_{C(s)}$. These values are then compared to carbon formation activities to evaluate their validity and accordance.

4.2.3. Computational Domain and Numerical Setup

The simulations in Section 3.2 showed that the ceramic single cell housing has both strengths and weaknesses when it comes to flow, species, temperature, and current density distribution. The profiles that occurred are assumed to be symmetrical normal to the central axis of the cell (see Figure 3.4(a) for a schematic of this axis position), which seems to be a good approximation. However, the near-wall regions are subject to inhomogeneities brought about by the anode and cathode sides' unequal distribution of flow channels . Nevertheless, most of the cell is

almost evenly supplied with fuel, and thus, the further simplification of the $3D$ simulation model is reasonable. A cross-section along the central axis of the cell indicated in Figure 3.4(a) was applied in order to create a $2D$ model that represents the majority of the cell's active area. This was done to further decrease the computational cost of the simulations, and to make it possible to conduct a multitude of different simulations. The simplified two-dimensional flow channel model of the anode-supported SOFC single cell model, presented in Chapter 3, was used to numerically evaluate the reaction kinetics of carbon deposition, and to identify major carbon precursors. The computational grid consists of approx. $1,400$ quad-cells with a maximum aspect ratio and a skewness of 18 and 0, respectively. The channel geometry and its dimensions are shown in Figure 4.1. The anode substrate thickness ($0.5\,mm$) was modelled according to measured data.

A $5-mm$ inlet zone was used before the substrate, in order to develop a flow profile inside the channel. Moreover, in Chapter 3, highest gradients of all reacting species, current densities and overpotentials, were shown to occur near the zone of the inlet section of the cell. As can be seen in all of the Figures in Chapter 3, the first third of the cell (0 - 30 mm) is subject to these gradients. Thus, only these first 30 mm were geometrically resolved, discretized, and scrutinized. This placed the primary focus on the main reforming zone, where degradation is most likely to occur.
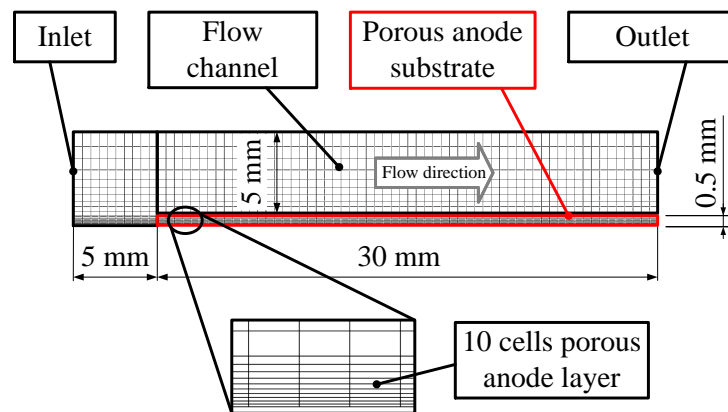
Figure 4.1.: Schematic of the $2D$-flow channel and the computational grid (not to scale) [89]

The numerical settings described in Section 3.2.2 were applied for the simulations in this chapter, but slight modifications were performed. A double precision pressure-based coupled solver was used instead of a segregated solver for the transient simulations. Carbon formation was investigated under open circuit condition (OCV), thus no electrochemical reactions occurred. This represents the worst case operating conditions of a high-temperature SOFC, since no water is formed by electrochemical reactions. This leads to minimal steam to carbon (S/C) ratios. Chemical species diffusion was again modelled using the Stefan-Maxwell model in order to delineate the details of molecular transport processes. All of the species transport equations involved are solved directly within the CFD code using a laminar finite-rate model. The solid material properties of the porous anode substrate are given in Table 4.1.

All of the transport equations involved were geometrically discretized by second order upwind

Table 4.1.: Porous Ni-YSZ anode substrate properties

Parameter	Value	Unit
Anode properties		
Thickness	0.5	mm
Density ρ	$3,030$	$kg\,m^{-3}$
Specific heat capacity $C_{mp,i}$	595.1	$J\,kg^{-1}\,K^{-1}$
Thermal conductivity λ	6.23	$W\,m^{-1}\,K^{-1}$
Porosity ε	0.3	-
Tortuosity τ	3	-

schemes. Temporal discretization was done by means of a first order scheme. Convergence of each time step was determined when residuals of continuity and momentum fell below 10^{-5} and those of species and energy fell below 10^{-7}. Convergence of the final, steady solution was monitored by means of constant surface coverage and outlet species composition, temperature, and outlet velocity. These approaches and assumptions are typical in the field of SOFC simulations, with many validated results, e.g. in [31, 38, 40–42, 44, 86, 87, 93].

4.3. Carbon Precursor Identification

In this section, the major carbon precursors will be identified by means of thermodynamic equilibrium calculations and detailed analyses of the developed CFD.

4.3.1. Thermodynamic Equilibrium of Fuels

Thermodynamic equilibrium calculations are often used as a basis for fuel cell systems in order to identify critical and safe operating conditions. Thus, in this section, 0D- equilibrium composition calculations of typical carbon containing fuels (CH_4/H_2O, CO/H_2O and $CH_4/CO/H_2O$) utilized in high temperature fuel cells were conducted. Furthermore, the difference between modelling precipitated elementary carbon as graphite (C(gr)) and as carbon nanofibers (CNF), as described by Sasaki and Teraoka [100] and Lee, Hanna, and Ghoniem [102], was investigated. The differences between these two carbon types were considered in the equilibrium calculations with differing thermodynamic properties. For graphite, the material properties tabulated in [104] for standard conditions were used. Data for standard enthalpy H^0_{CNF} and entropy of formation S^0_{CNF} for CNF were used based on Ref. [102]. H^0_{CNF} was set to $54.46\,kJ\,mol^{-1}$ and S^0_{CNF} was set to $68.90\,J\,mol^{-1}\,K^{-1}$. The trends of Gibbs free enthalpy of reaction for graphite and carbon nanofibers are shown for the interested reader in Appendix A.1.

Figure 4.2 plots the molar amount of components as a function of temperature at thermodynamic equilibrium for different fuels in a mixture with steam. It is based upon a S/C ratio of 0.5 normalized to 1 mol carbon. It's possible to see from Figure 4.2(a) and 4.2(b), that, for CH_4/H_2O mixtures, elementary carbon (solid and dashed red line) will precipitate above approx. $400\,°C$ for both graphite and CNF. Gas phase composition is similar in both cases, but
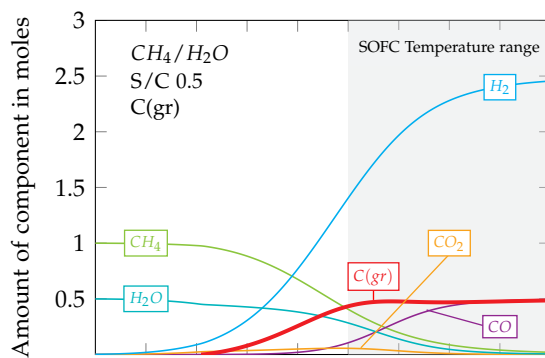
(a) Gaseous species: CH_4/H_2O at S/C 0.5. Solid phase: graphite C(gr)
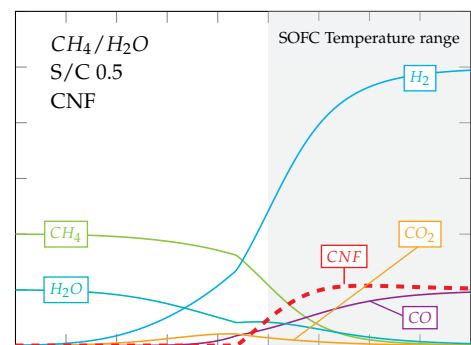
(b) Gaseous species: CH_4/H_2O at S/C 0.5. Solid phase: Carbon nano fibres CNF
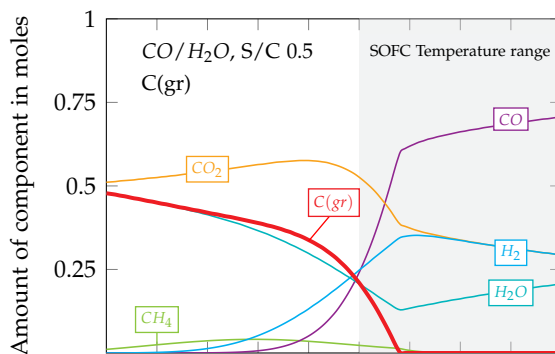
(c) Gaseous species: CO/H_2O at S/C 0.5. Solid phase: graphite C(gr)
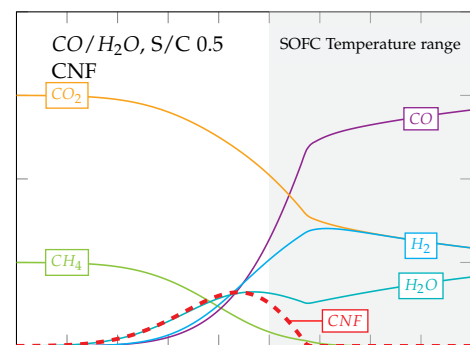
(d) Gaseous species: CO/H_2O at S/C 0.5. Solid phase: Carbon nano fibres CNF
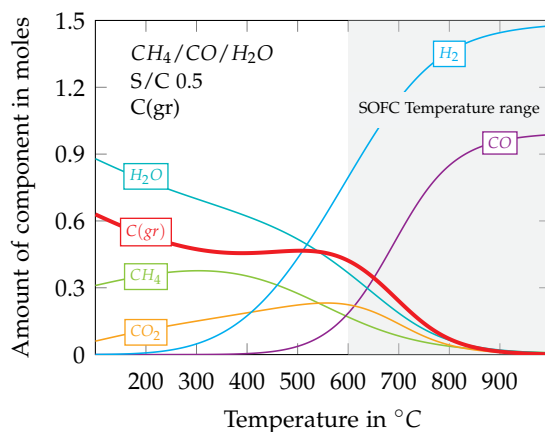
(e) Gaseous species: $CH_4/CO/H_2O$ at S/C 0.5. Solid phase: graphite C(gr)
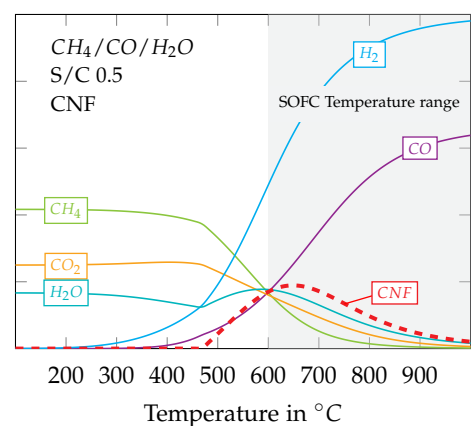
(f) Gaseous species: $CH_4/CO/H_2O$ at S/C 0.5. Solid phase: Carbon nano fibres CNF

Figure 4.2.: Thermodynamic equilibrium calculations for different carbon containing fuel feeds and two different forms of elementary carbon [89]

the equilibrium shifts towards products (based on the methane steam reforming and water-gas shift reaction) at higher temperatures for CNF compared to graphite. Out of 1 mol CH_4, almost 0.5 moles of graphite are formed at 700 °C and approx. 0.6 moles CNF at 750 °C.

Equilibrium calculations for CO/H_2O blends show considerable differences when comparing graphite and CNF (cf. Figure 4.2(c) and Figure 4.2(d)). Graphite will theoretically be built from CO at temperatures between 100 °C and 700 °C. 1 mol CO forms almost 0.5 moles of graphite at 100 °C, whereas no CNF is built until approx. 250 °C. Maximum CNF will form at 550 °C with a magnitude of 0.16 moles.

As shown in Figure 4.2(e) and Figure 4.2(f), equimolar mixtures of $CH_4/CO/H_2O$ at a S/C ratio of 0.5 show similar results. Elementary carbon can be formed as C(gr) over the entire temperature range, with peak values of 0.63 moles at 100 °C. Carbon nanofibers will form above temperatures of 480 °C with maximum amounts below 0.3 moles.

In conclusion, thermodynamic equilibrium cannot realistically be reached at temperatures below 200 °C. Thus, the data depicted at these temperatures in Figure 4.2 denotes theoretical values, but it is very unlikely that these compositions would occur in technical applications. This statement applies to all equilibrium calculation results in this chapter.

4.3.2. Carbon from Different Fuels

In this section, the formation of carbon as a function of temperature, species and S/C ratio is investigated. Furthermore, the differences between modelling it as graphite or CNF are discussed. Carbon as graphite is plotted as solid lines, whereas carbon nanofibers are plotted as dashed lines. Three fundamentally diverse fuel mixtures were used: methane/steam, carbon monoxide/steam and methane/carbon monoxide/steam mixtures (equimolar amounts of methane and carbon monoxide). Moreover, the amount of steam was varied, to get a steam-to-carbon (S/C) ratio of 0.5, 1, 1.5 and 2 for all of these mixtures. Each colour refers to a corresponding gas mixture: red graphs denote carbon from methane/steam mixtures, green graphs represent carbon from CO/steam mixtures, and blue graphs show carbon from equimolar mixtures of $CH4/CO$/steam. In Figures 4.3 and 4.4, only the trend of solid carbon is shown. The corresponding gas phase compositions, as plotted in Figure 4.2, are omitted so as to set the focus on possible carbon formation.

Varying the S/C ratio for the investigated fuels significantly influenced carbon formation at equilibrium. The diagram for a S/C ratio of 0.5 (cf. Figure 4.3(a), as depicted alongside gaseous species in Figure 4.2) shows that, for temperatures below 600 °C, carbon is mainly formed from CO and blends of CH_4/CO. For temperatures above 600 °C, carbon formation is highest due to CH_4/H_2O mixtures. Graphite can be formed from $CH_4/CO/H_2O$ mixtures throughout the entire temperature range. CNF formation is distinctly different from graphite precipitation. Below approx. 480 °C, no CNF is formed. In addition to their different temperature limits, the magnitude of moles of carbon formed is also different for graphite. Less carbon precipitates at
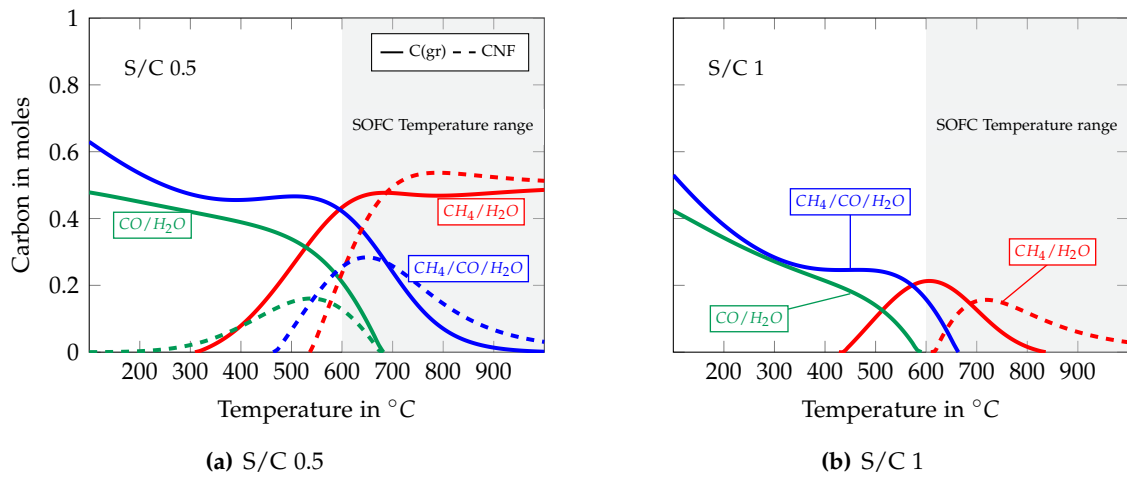
Figure 4.3.: Carbon formation from methane/steam, carbon monoxide/steam and equimolar methane/carbon monoxide/steam mixtures with varying S/C ratio [89]

a constant temperature level except for CH_4/H_2O mixtures. For temperatures above $700\,°C$, more CNF is formed than graphite. With rising S/C ratios, the magnitude of carbon formed decreases. Graphite is still formed for all three fuel mixtures at S/C 1, as can be seen from Figure 4.3(b). Alongside this decrease in magnitude, the temperature range narrows as well. Above $820\,°C$, no graphite is formed, independent of the fuel. Carbon nanofibers can only be formed from CH_4/H_2O mixtures, with a drop to about a third of its maximum at S/C 0.5.
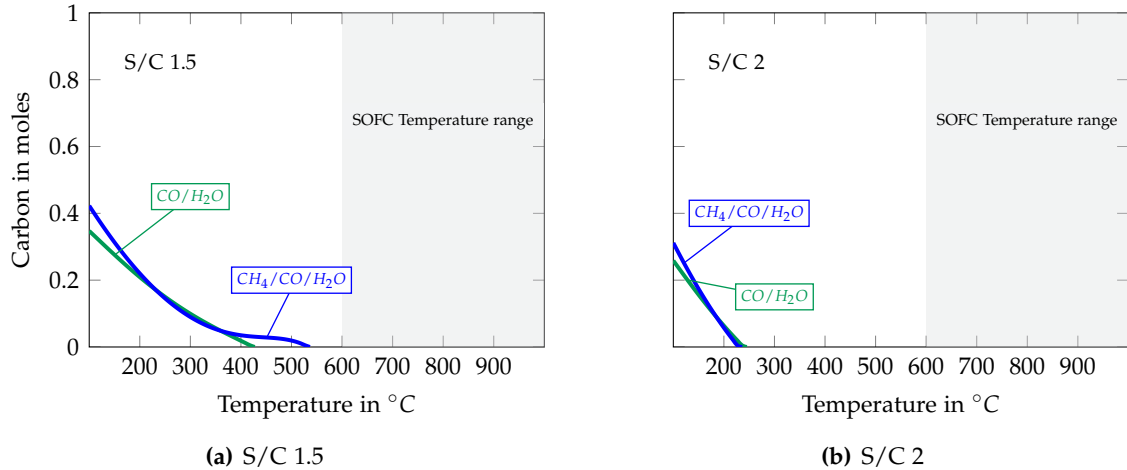
Figure 4.4.: Carbon formation from methane/steam, carbon monoxide/steam and equimolar methane/carbon monoxide/steam mixtures with varying S/C ratio [89]

For steam-to-carbon ratios of 1.5 and 2 (see Figure 4.4(a) and Figure 4.4(b)), the amount of carbon formed decreases furthermore. Methane does not form any type of elementary carbon in these cases. CO and mixtures of CH_4/CO show possible carbon formation up to $530\,°C$ and $230\,°C$ at S/C ratios of 1.5 and 2, respectively. This is critical for the start-up and shut down of SOFC systems. Below $600\,°C$, thermodynamic equilibrium in real (SOFC) applications can hardly be reached due to the lack of sufficient reaction kinetics and residence time.

4.3.3. Carbon Formation Boundaries for Different Fuels

The equilibrium calculations conducted were completed by identifying the carbon boundaries for the three different carbon containing fuels as a function of temperature, type of carbon formed, and S/C ratio. Again, the basis for the calculation of these formation boundaries were fuels normalized to 1 mol of carbon (either methane, carbon monoxide, or equal amounts of methane and carbon monoxide).
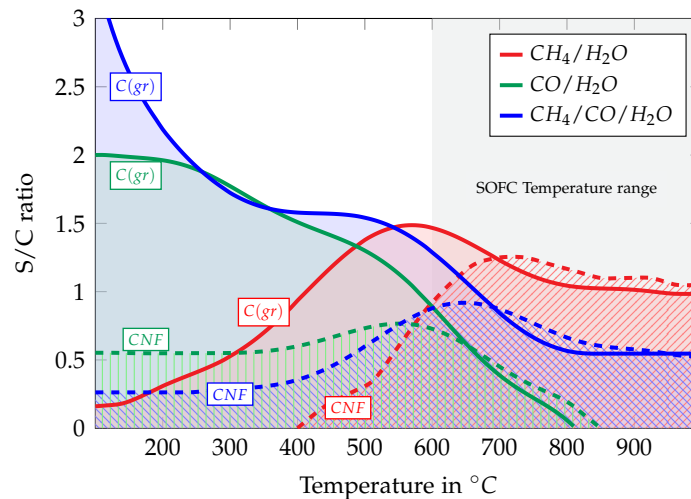
Figure 4.5.: Carbon boundaries for different carbon containing fuels [89]

Figure 4.5 shows the minimum S/C ratios necessary to inhibit carbon formation. Steam-to-carbon ratios below the calculated boundary curves (coloured area) lead to carbon formation when the system is in thermodynamic equilibrium. Solid lines and the corresponding area underneath them again represent carbon formed as graphite, whereas dashed lines and hatched areas denote carbon as carbon nanofibers. The significance of the graph colours is the same as those of Figures 4.3 and 4.4. When comparing the minimum S/C ratios for CH_4/H_2O mixtures, it can be seen that graphite is formed over the entire temperature range. S/C ratios of 0.16 at $100\,^{\circ}C$ and 0.984 at $1,000\,^{\circ}C$ were calculated. The maximum steam required to inhibit coking was calculated to be 1.49 at $570\,^{\circ}C$. Carbon nanofibers can precipitate from methane above temperatures of $400\,^{\circ}C$. Above $700\,^{\circ}C$ to a maximum temperature of $1,000\,^{\circ}C$, more steam is needed to prevent carbon formation compared to graphite.

According to the Boudouard equilibrium, elementary carbon formed from carbon monoxide is more prominent at lower temperatures. Starting from S/C 2 at $100\,^{\circ}C$, the amount of steam required in order to prevent coking decreases steadily for graphite until $800\,^{\circ}C$, above which no carbon can be formed from CO. CNF formation from CO is less likely to occur, and operating conditions with significantly lower S/C ratios can be used. A maximum ratio of 0.766 at $550\,^{\circ}C$ was calculated. Nanofibers are formed at temperatures up to $850\,^{\circ}C$.

The equimolar combination of both of the carbon containing fuels of this preliminary investigation delivers an interesting result. For graphite, the S/C ratio peaks at $100\,^{\circ}C$ to 3.4, then

decreases significantly and plateaus at 1.6 between $400\,°C$ and $500\,°C$, decreasing further until $800\,°C$, where it reaches its minimum value of 0.55. The calculations for carbon nanofibers show distinctly different results. Below temperatures of $300\,°C$ very low S/C ratios of 0.26 lead to carbon formation. As the temperature rises, the risk of carbon formation increases, and thus the minimum S/C ratio to prevent coking rises to 0.92 at $650\,°C$. A further temperature increase decreases the coking limit to 0.52 at $1,000\,°C$.

Carbon formation as a result of using the investigated fuels is thermodynamically possible within the temperature range relevant for SOFCs, between $600\,°C$ and $1,000\,°C$. Figure 4.5 shows that methane is the most prominent carbon precursor. S/C ratios of up to 1.5 were calculated, which are required to suppress carbon formation. For carbon monoxide and equimolar mixtures of CH_4 and CO, the coking propensity is significantly lower. Above $850\,°C$, no type of elementary carbon can be formed from CO, whereas for mixtures of CH_4/CO the ratio of carbon containing fuel to steam can be up to 1.92 at $1,000\,°C$. In other words, this means that methane and carbon monoxide can be used as a fuel in SOFCs without the risk of carbon formation when a S/C ratio ≥ 1.5 can be established throughout the entire operation.

4.3.4. CFD Simulations with Detailed Reaction Kinetics

As initially stated, chemical equilibrium calculations can be used to identify the thermodynamic boundaries for carbon formation in chemically reactive systems. In many applications, the residence time of reacting species or the reaction rates at intermediate temperatures are too low to reach chemical equilibrium. Thus, kinetic approaches have to be considered that describe the chemical reactions that occur. The results within Chapter 3 have shown that the detailed heterogeneous reaction mechanism (see Table 3.8) best fits the experimental data. Thus, this mechanism was also used for the $2D$ simulations in this chapter. Again, it is important to note that only the first third of the cell is scrutinized, since this is where the highest gradients occur, which makes it particularly susceptible to degradation phenomena.

4.3.5. Steady State Simulation Results to Evaluate Major Carbon Precursors

Transient CFD simulations were conducted to cover reaction limitations by kinetics (see Section 4.2.2 for the numerical setup). Furthermore, three different fuel mixtures are analysed by means of the detailed CFD model. Methane, carbon monoxide, and equimolar mixtures of both species were investigated as fuels, with water-vapour in a broad S/C range from 0.5 to 2, with increments of 0.5. The simulations were conducted at three typical ASC SOFC temperature levels: $600\,°C$, $800\,°C$ and $1,000\,°C$. As in Chapter 3, the volumetric flow rate of 2.4 SLPM was used for these simulations. A corresponding fuel mass flow rate was computed from this volumetric flow rate for the $2D$ model.

(a) Surface carbon $C(s)$ from CH_4/H_2O mixtures

(b) Surface carbon $C(s)$ from CO/H_2O mixtures

(c) Surface carbon $C(s)$ from equimolar $CH_4/CO/H_2O$ mixtures
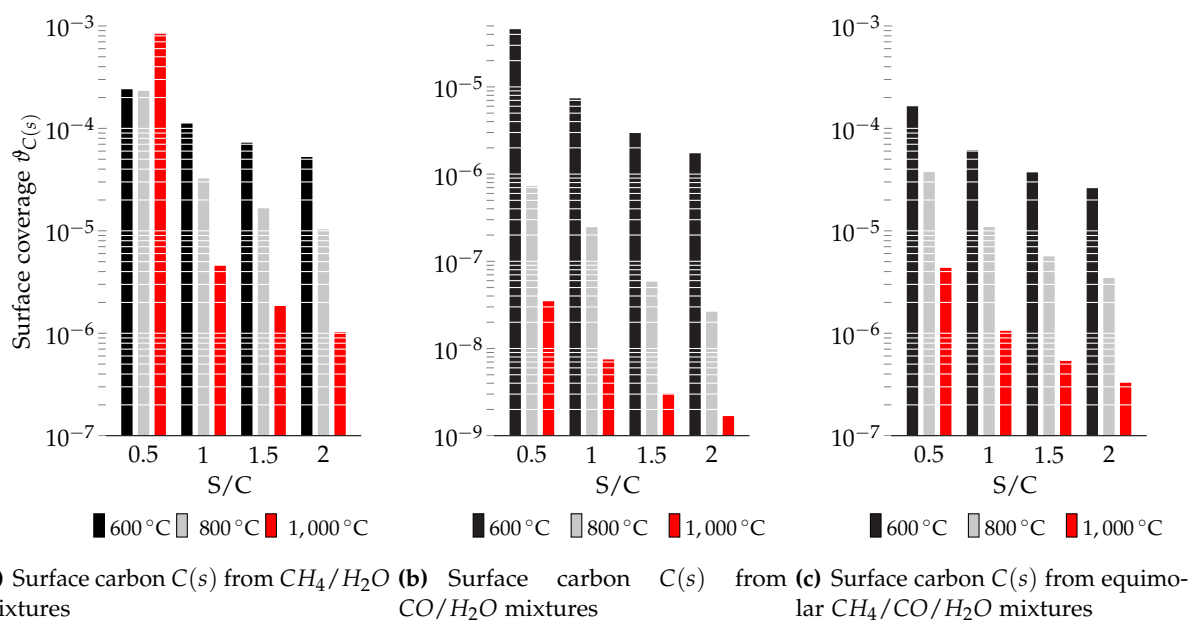
Figure 4.6.: Major carbon precursors due to different species, S/C ratios and temperatures at steady state [89]

In order to identify major carbon precursors and critical operating conditions, steady-state results of all transient simulations were analysed. This was done to investigate possible long-term degradation of the anode substrate. Steady states of the conducted simulations were determined by monitoring the overall surface coverage of adsorbed elementary carbon $\vartheta_{C(s)}$, substrate temperature, mass flow, and outlet gas phase composition (C(s) denotes an elementary carbon atom chemically adsorbed at a catalyst site). The constant values-over-time of aforementioned parameters indicated a steady-state solution. Figure 4.6 shows the maximum surface coverages of elementary surface adsorbed carbon $\vartheta_{C(s)}$ at the catalytically active Ni-centres.

Figure 4.6(a) shows the simulation results of CH_4 mixtures for the investigated S/C- and temperature ranges. For steam-to-carbon ratios between 1 and 2, a temperature increase (different colours) implies a significant decrease in the amount of adsorbed carbon. Surface coverage decreases from 1.5 decades at S/C 1 up to almost 2 decades at S/C 2 for rising temperature levels. An interesting result occurred for S/C 0.5. Absolute coverage is highest at this steam-to-carbon ratio. Increasing the temperature from $600\,°C$ to $800\,°C$ causes a slight decrease in the amount of adsorbed carbon atoms, while a further increase to $1,000\,°C$ results in a noticeable rise from 2.32×10^{-4} to 8.4×10^{-4}. This can be attributed to the increased kinetics of the methane reforming reaction and the methane cracking reaction. These overall, global reactions were modelled by several more detailed reaction steps (cf. Table 3.8). The global reactions can be used to interpret the resulting outcomes, but the exact reaction pathways used in this work are more complex, and are incorporated within the mechanism.

Surface coverages $\vartheta_{C(s)}$ from carbon monoxide are shown in Figure 4.6(b). Similar to the results described for methane, an increase in the amount of steam alongside a temperature increase, results in a decrease in the chemically adsorbed carbon atoms at the porous catalyst surface.

The magnitude of the most critical case (S/C 0.5 at 600 °C) is about one decade lower compared to methane. It can generally be seen that the coverages are significantly lower and the absolute amount of adsorbed species differs to a higher extent.

When using equimolar CH_4/CO blends as fuel (Figure 4.6(c)), the magnitudes of surface coverages resemble the results shown for methane. The peak at S/C 0.5 and 1,000 °C cannot be seen. The amount of adsorbed carbon is slightly decreased compared to methane.

From this analysis, it can be seen that methane and equimolar blends of CH_4/CO deliver the highest amounts of adsorbed carbon. Carbon formation from carbon monoxide plays either no, or only a subordinate role. A detailed analysis of the critical operating conditions identified can be carried out by applying the approach of global carbon formation activities $\alpha_{(3.2)-(3.6)}$ or by investigating the local surface carbon coverage trend.

The detailed CFD simulation results of surface carbon coverages $\vartheta_{C(s)}$ can be linked to the thermodynamic equilibrium calculations to determine the amount of graphite or CNF that forms while using such fuel mixtures. It is important to ensure that the reaction is equilibrated or at least near equilibrium within the porous anode. When this is confirmed, the formation or deposition rate of graphite and CNF can be evaluated by comparing the molar fuel flow to the cell with the amount of mol C(gr) or CNF formed at the particular temperature in thermodynamic equilibrium. Thus, a carbon formation rate can be calculated from the surface coverage profiles.

Carbon Formation Activity and Surface Coverage of C(s)

As was described in Section 4.2.2, there are two different approaches to identifying possible carbon formation in literature. Carbon formation activity can be defined for a corresponding dissociation reaction (cf. reactions (3.3), (3.5) and (3.6) in Section 3.4), which is an equilibrium based approach. Based on the partial pressures of the reactions' products and reactants, their deviation from equilibrium can be calculated. If this formation activity $\alpha_{(i)}$ is greater than unity, carbon can precipitate.

In Figures 4.7, 4.8, and 4.9 the most significant averaged carbon formation activities are shown. $\alpha_{(3.3)}$ denotes the formation activity due to the methane cracking reaction. $\alpha_{(3.5)}$ and $\alpha_{(3.6)}$ represent the formation activity caused by the Boudouard reaction (reaction (3.5)) and the carbon monoxide reduction reaction (reaction (3.6)), respectively. The trends of both the last-mentioned formation activities resemble each other for all of the investigated cases. Thus, for ease of better interpretation and clarity, only $\alpha_{(3.5)}$ is depicted.

Figure 4.7 shows the averaged formation activities for methane/steam and equimolar CH_4/CO /steam mixtures at 600 °C along the substrate length. At the beginning of the porous catalyst, partial pressures of methane predominate in comparison to hydrogen, since the reforming reaction of methane has not yet produced any products. Thus, the formation activity $\alpha_{(3.3)}$

(a) $\alpha_{(3.3)}$ for CH_4/H_2O mixtures

(b) $\alpha_{(3.3)}$ for equimolar $CH_4/CO/H_2O$ mixtures
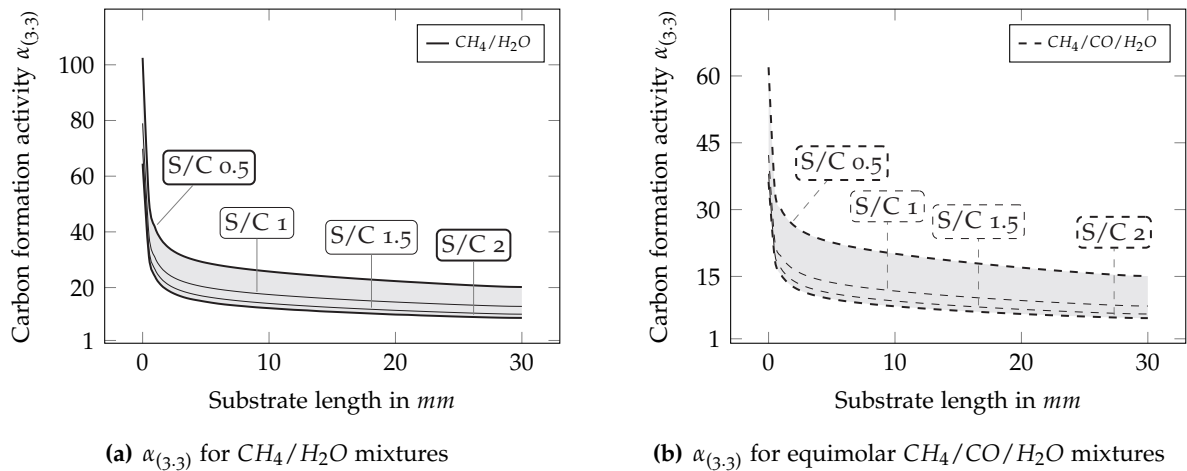
Figure 4.7.: Carbon formation activities $\alpha_{(3.3)}$ for methane/steam and methane/carbon monoxide/steam mixtures (S/C 0.5 - 2) at 600 °C [89]

peaks at the beginning of the substrate. With increasing substrate length the formation activity decreases due to the ongoing process. Throughout the whole cell length $\alpha_{(3.3)}$ stays distinctly above unity. The influence of an increase of the S/C ratio on the formation activity can clearly be seen in Figures 4.7(a) and 4.7(b). Low amounts of steam (S/C 0.5) hinder the methane reforming reaction, which results in exaggerated formation activities $\alpha_{(3.3)}$. At the inlet region, this fact is especially pronounced, which results in peak values in the range of 100 and 60 for methane/steam and equimolar methane/carbon monoxide/steam mixtures, respectively. An increase in the amount of steam to S/C 2 thus naturally decreases the carbon activities to a relative minimum. Calculated values for S/C 1 and 1.5 are also inserted to clarify the non-linear behaviour. An increment from S/C 0.5 to 1 decreases $\alpha_{(3.3)}$ by $\approx$ 30%. The formation activities for methane/steam mixtures at a given S/C ratio reside above those for methane/carbon monoxide/steam mixtures.

(a) $\alpha_{(3.5)}$ for CH_4/H_2O and equimolar $CH_4/CO/H_2O$ mixtures

(b) $\alpha_{(3.5)}$ for CO/H_2O
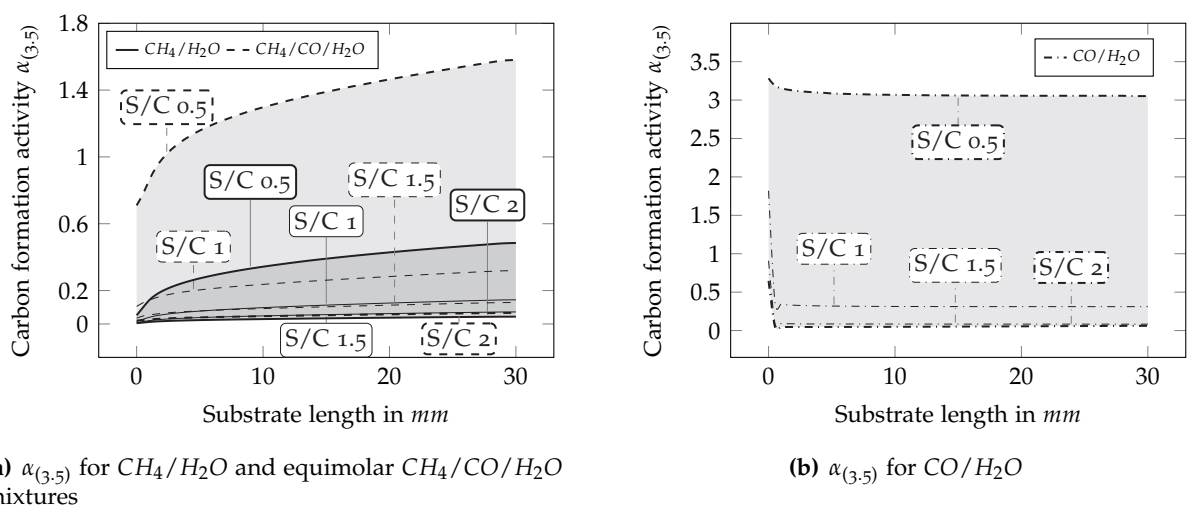
Figure 4.8.: Carbon formation activities $\alpha_{(3.5)}$ for methane/steam, carbon monoxide/steam and methane/carbon monoxide/steam mixtures (S/C 0.5 - 2) at 600 °C [89]

Carbon formation activities brought about by the Boudouard reaction are shown in Figure 4.8.

Carbon formation activity is highest ($\alpha_{(3.5),max} = 3.3$) for carbon monoxide/steam mixtures at a S/C ratio of 0.5 (cf. Figure 4.8(b)). The trend of this activity resembles the description given for Figure 4.7. For a steam-to-carbon ratio greater than 0.5, the formation activities decline drastically and fall below unity within the first millimetre of the substrate. For equimolar methane/carbon monoxide/steam mixtures (dashed lines in Figure 4.8(a)) only a S/C ratio of 0.5 delivered formation activities above unity. In this case, the first two millimetres of the substrate are not in danger of coking since the formation activity is lower than unity in this region. With increasing substrate length, $\alpha_{(3.5)}$ steadily increases, which runs contrary to the trend predicted for $\alpha_{(3.3)}$. Higher water vapour amounts lead to low carbon formation activities $\alpha_{(3.5)}$, significantly below the threshold value of unity mentioned. Since carbon monoxide is a product of the methane steam reforming reaction, carbon precipitation due to carbon monoxide can also be evaluated for methane/steam mixtures (the solid lines in Figure 4.8(a)). Formation activities reach their maximum values of 0.49 at S/C 0.5. Thus, no carbon formation will occur due to the Boudouard reaction for CH_4 mixtures. An increase of the amount of steam led to formation activities in the range of 0 over the entire substrate length.

(a) $\alpha_{(3.3)}$ for CH_4/H_2O at $800\,°C$ **(b)** $\alpha_{(3.3)}$ for equimolar $CH_4/CO/H_2O$ at $1,000\,°C$
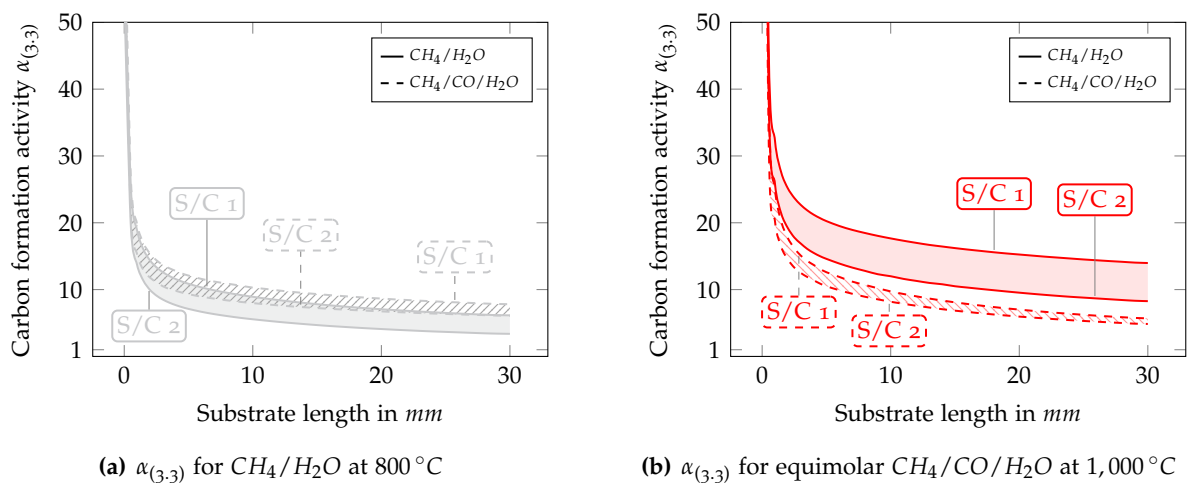
Figure 4.9.: Carbon formation activities $\alpha_{(3.3)}$ for methane/steam and carbon monoxide/steam mixtures (S/C 1 - 2) at $800\,°C$ and $1,000\,°C$ [89]

In Figure 4.9, calculated formation activities $\alpha_{(3.3)}$ for elevated temperatures of $800\,°C$ and $1,000\,°C$ and methane/steam as well as equimolar CH_4/CO/steam mixtures are shown. At these elevated temperatures, formation activities due to carbon monoxide dissociation were calculated to be negligible. The general trend is analogous to that of Figure 4.7, except for a lowered magnitude of the calculated values. Formation activities again peak at the beginning of the substrate and monotonously decrease with increasing substrate length. Figures 4.7 and 4.8 showed that carbon formation at S/C ratios of 0.5 is always possible due to its main decomposition route. Thus, in Figure 4.9 only mixtures with S/C ratios > 0.5 are shown. This is done in order to illustrate that even for high water amounts carbon formation activities greater than unity occur. Maximum values were calculated for methane/steam mixtures at operating temperatures of $1,000\,°C$ (cf. Figure 4.9(b)) whereas minimum formation activities were calculated at $800\,°C$, as shown in Figure 4.9(a). The hatched area depicts data

for CH_4/CO/steam mixtures. Minimum and maximum values form a narrow band for both temperature levels, which intersect with increasing substrate length.

A huge advantage of the detailed heterogeneous reaction mechanism used in this work is that permanently surface-adsorbed species and their according spatial distribution can be simulated. The results of previously identified, very critical operating conditions ($600\,^{\circ}C$, CH_4 and CH_4/CO mixtures) are shown in Figure 4.10. The averaged surface coverages depicted in this figure denote the amount of catalytically active Ni-centres permanently covered with elementary carbon. These results are fundamentally different from previous carbon formation activities, since these activities merely denote the deviation from equilibrium for different dissociation reactions. Surface coverages $\vartheta_{C(s)}$ represent elementary carbon atoms chemically adsorbed to the surface.

(a) CH_4/H_2O mixtures   **(b)** Equi-molar $CH_4/CO/H_2O$ mixtures
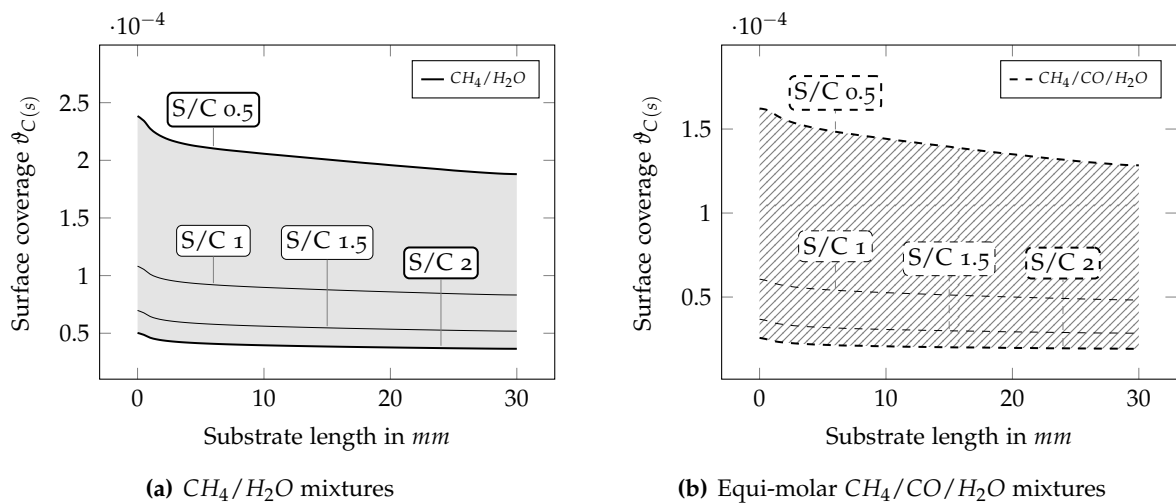
Figure 4.10.: Steady state averaged carbon surface coverages $\vartheta_{C(s)}$ at $600\,^{\circ}C$ and S/C $0.5 - 2$ [89]

Maximum values were again calculated for a minimum steam-to-carbon ration of 0.5 for both methane/steam (Figure 4.10(a)) and CH_4/CO/steam (Figure 4.10(b)) mixtures. The reaction rates of the reforming process are highest at the substrate inlet. Thus, maximum surface coverages occur in this region. Coverages decline towards the end of the porous substrate. Increasing the amount of water vapour lowers the number of adsorbed carbon atoms. The absolute minimum coverages at this temperature level were identified to occur at S/C 2 for CH_4/CO/steam mixtures. The trends of surface coverages shown in Figure 4.10 correlate with those of carbon formation activities shown in Figure 4.7 and 4.8. The thermodynamic equilibrium assumptions were confirmed by the actual surface coverages of elementary carbon atoms. The highest coverages were calculated at the beginning of the substrate. Formation activities were highest in this region as well. The detailed mechanism made it possible to identify the fact that higher carbon surface coverages occur when using methane/steam mixtures compared to the usage of equimolar methane/carbon monoxide/steam mixtures. This can best be compared for a particular S/C ratio between Figure 4.10(a) and 4.10(b). The general trends are similar, but the carbon coverage magnitude is decreased for $CH4/CO$/steam mixtures.
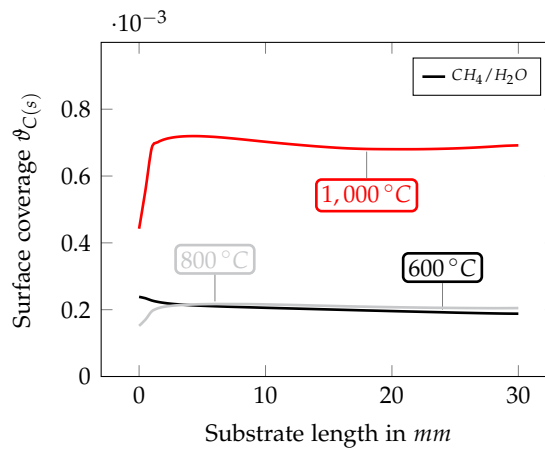
Figure 4.11.: C(s) for methane/steam mixtures (S/C 0.5) between $600\,^\circ C$ and $1{,}000\,^\circ C$

Figure 4.11 shows the spatial coverage distribution of the three most critical operating temperatures, as identified in Figure 4.6(a). The trend of $600\,^\circ C$ was described beforehand. A temperature increase to $800\,^\circ C$ has only minor effects on the amount of surface-adsorbed carbon. At the beginning of the substrate local surface coverages are lower compared to $600\,^\circ C$. With increasing length, more carbon is adsorbed, and slightly higher values were calculated. For $1{,}000\,^\circ C$, significantly more carbon is permanently adsorbed to the active surface; surface coverage is more than three times higher compared to $600\,^\circ C$ and $800\,^\circ C$. It must be noted that for the maximum temperature, surface coverage increases dramatically within the first two millimetres of the substrate. This can be attributed to increased reaction and reforming kinetics at these elevated temperatures. Coverages in the range of 7×10^{-4} were calculated for the remaining length.
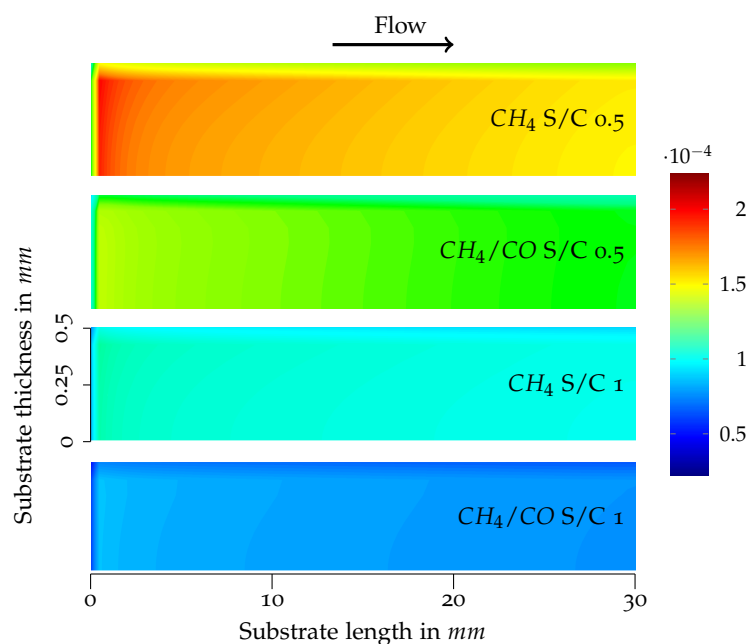
Figure 4.12.: Steady state carbon surface coverage contours of $C(s)$ at $600\,^\circ C$ [89]

Figure 4.12 shows the carbon surface coverage contour plots of the porous anode substrate

at different operating conditions at $600\,°C$. In this figure, only the porous anode substrate is shown and magnified. The actual dimensions are given in the plot ($0.5\,mm$ substrate thickness and $30\,mm$ substrate length, which is equivalent to the first third of the cell). The flow channel is neglected, since the focus is set to the catalytically-active area. Both the spatial distribution with increasing substrate length and the substrate thickness can clearly be seen. Moreover, it is evident that the highest carbon coverages occur at the front of the substrate, where the highest reforming rates occur. The top surface shows the lowest coverages for all depicted cases. Here, adsorbed species are quickly desorbed due to low transport limitations. The surface coverage increase with increasing substrate thickness can thus be attributed to the transport limitation. This plot makes it possible to establish a good connection between the calculated coverage distribution and the thickness-averaged data shown in Figure 4.10.

4.3.6. Transient Simulation Results

As initially stated, all of the simulations conducted were performed on a transient timescale. This was done in order to identify time-dependent carbon agglomeration in the porous anode structure when introducing carbon containing fuels to the system. Transient simulation results for the entire temperature range between $600\,°C$ and $1,000\,°C$ are shown in Figures 4.13, 4.15, and 4.16. The carbon surface coverages $\vartheta_{C(s)}$ depicted in these figures are averaged values of the entire porous structure. As shown in previous figures, the surface coverage is evaluated for methane/steam and CH_4/CO/steam mixtures at a S/C ratio range of $0.5 - 2$.

(a) Methane/steam mixtures

(b) Equi-molar Methane/carbon monoxide/steam mixtures
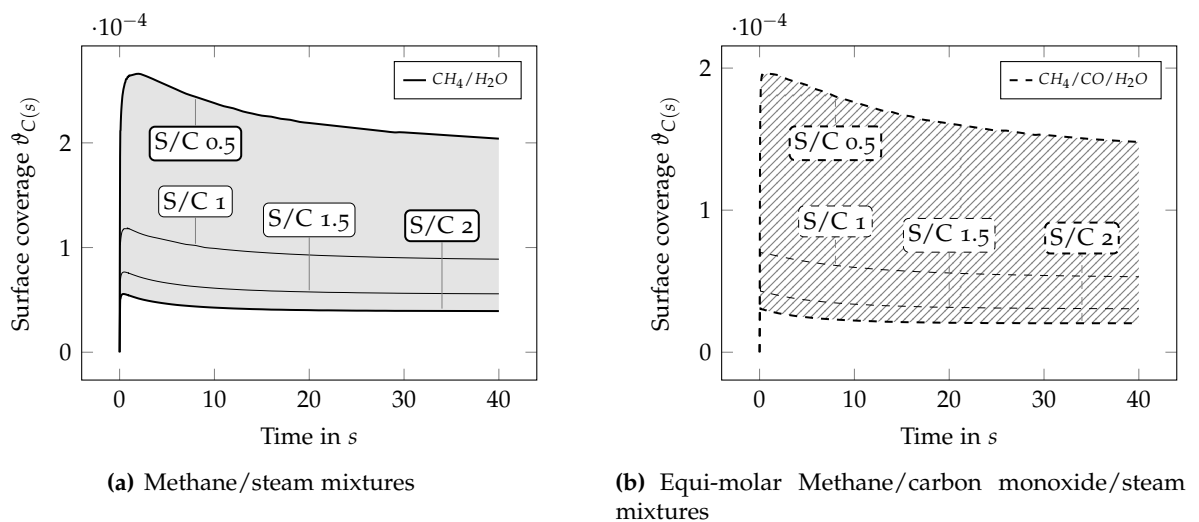
Figure 4.13.: Transient surface coverages of C(s) at $600\,°C$ and S/C $0.5 - 2$ [89]

In Figure 4.13, temporal carbon coverages caused by methane/steam (cf. Figure 4.13(a)) and CH_4/CO/steam mixtures (cf. Figure 4.13(b)) during internal reforming at $600\,°C$ are depicted. The highest coverages were calculated for both fuel mixtures at S/C ratios of 0.5. The surface coverages can clearly be seen to increase significantly within the first two seconds until they reach a maximum value of 2.66×10^{-4} for methane/steam. Moreover, the

maximum surface coverages for equimolar methane/carbon monoxide/steam mixtures were calculated to 1.96×10^{-4}. With increasing time, the average surface coverages reduced and asymptotically tended towards a steady state condition (coverages after $40\,s$). Increasing the S/C ratio, decreased the overall amount of carbon adsorbed. The general shape of the evolving carbon was similar for all investigated cases, but the magnitude was decreased.
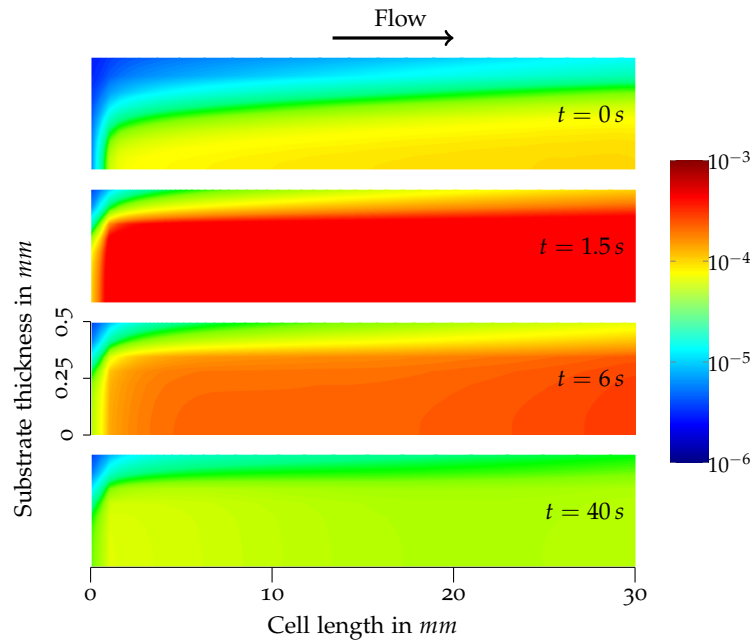
Figure 4.14.: Transient surface coverage contours of $C(s)$ at $1,000\,^{\circ}C$ for a methane/steam mixture at S/C 0.5 [89]

The peak at the beginning can be attributed to the development of the reforming process. Initially, the catalytically-active centres are occupied with a certain amount of carbon, which inhomogeneously grows from the back of the substrate to the front (cf. Figure 4.14 for a more graphic illustration of the process).The reforming rates are highest at the beginning of the substrate (top left corner). Here, the least amount of carbon is adsorbed, since it is regenerated immediately by the water vapour coming to the substrate through the feed stream. Once, steady state is reached ($t = 40\,s$), the final methane conversion rates are established and constant amounts of carbon monoxide and hydrogen are produced. This leads to a more uniform, yet slightly inhomogeneous coverage distribution along the substrate.

Simulation results for 800 and $1,000\,^{\circ}C$ are shown in Figures 4.15 and 4.16, respectively. As in previous figures, the data for $800\,^{\circ}C$ is shown as grey plots while the red plots represent the simulation results for $1,000\,^{\circ}C$. A filled area denotes methane/steam mixtures (cf. 4.15(a) and 4.16(b)) whereas a hatched area represents CH_4/CO/steam mixtures (Figures 4.15(b) and 4.16(b)) with varying S/C ratios. The highest coverages at $800\,^{\circ}C$ were again calculated for a methane/steam mixture at a S/C ratio of 0.5. Peak values of 3.1×10^{-4} were found to occur at $t = 4\,s$. The general temporal carbon coverage evolution profile resembled the trends described for Figure 4.13. A logarithmic scale is used for the axis of ordinates. Thus, the difference between the minimum and maximum coverages is more pronounced than at $600\,^{\circ}C$. Carbon coverages resulting from CH_4/CO/steam mixtures (Figure 4.15(b)) reach a maximum value

of 1/8 of the methane/steam mixture at a corresponding S/C ratio. Increasing the amount of water vapour at this elevated temperature level has a major impact on the absolute amount of adsorbed species. An increment of water lowers the coverage drastically.

(a) Methane/steam mixtures

(b) Equi-molar Methane/carbon monoxide/steam mixtures
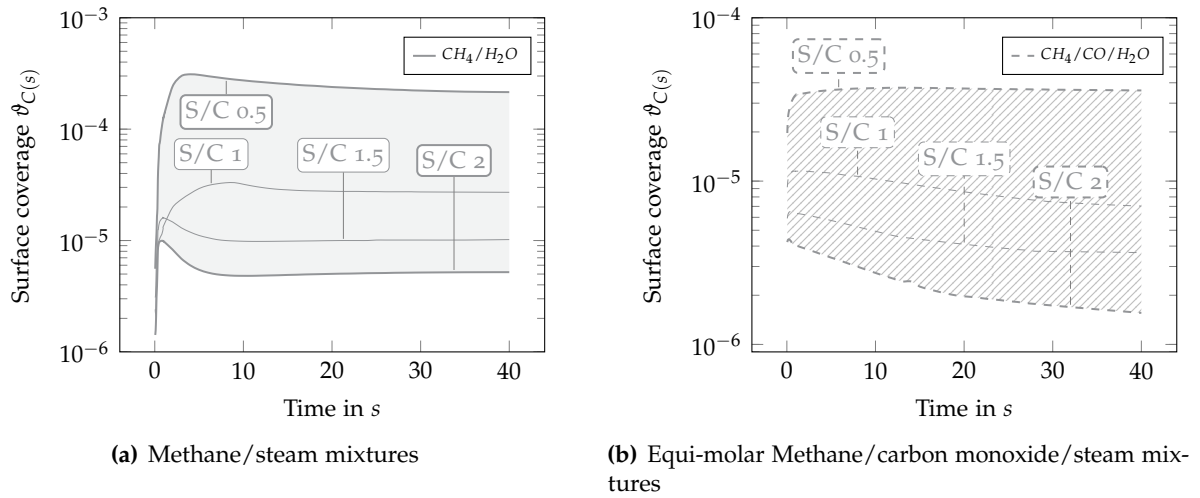
Figure 4.15.: Transient surface coverages of C(s) at $800\,^{\circ}C$ and S/C $0.5 - 2$ [89]

As shown in Figure 4.6(a), the highest steady state surface coverages were calculated for methane at a S/C ratio of 0.5 at $1{,}000\,^{\circ}C$. The temporal evolution of the coverage profile confirms this outcome, as can be seen in Figure 4.16(a). Similar to the cases described above, the average surface coverage rapidly increases at the beginning of the process until it reaches a sharp maximum of 1.17×10^{-3} at $t = 1.5\,s$. This peak can be attributed to an elevated amount of carbon containing gas (e.g. methane) at the porous structure, similar to the one that occurs at $600\,^{\circ}C$ and $800\,^{\circ}C$, before the reforming process has started. With increasing time, methane conversion takes place. The carbon containing reforming products (carbon monoxide) cause significantly lower coverages than methane (cf. Figure 4.16(b), as was shown in Figures 4.6(a) and 4.6(b). This leads to a decrease in the overall carbon surface coverage. In steady state, an average coverage of 7.2×10^{-4} was calculated. Introducing carbon monoxide to the fuel stream as a further agent drastically lowers the surface coverage (cf. $CH4/CO/H_2O$ at S/C 0.5) by several orders of magnitude. Absolute coverages are lowest at the maximum temperature for a $CH4/CO$ mixture with an corresponding steam-to-carbon ratio of 2.

4.4. Discussion

In this chapter, different numerical approaches to identifying carbon formation and the corresponding carbon precursors in porous SOFC anodes were investigated. Thermodynamic equilibrium calculations were performed for two different types of carbon. Depending on the carbon type (graphite C(gr) or carbon nano fibers CNF), distinctly different equilibrium compositions and total amounts of carbon will form. For methane/steam mixtures, S/C ratios significantly higher than unity are necessary to inhibit coking in temperature ranges suitable

(a) Methane/steam mixtures

(b) Equi-molar Methane/carbon monoxide/steam mixtures
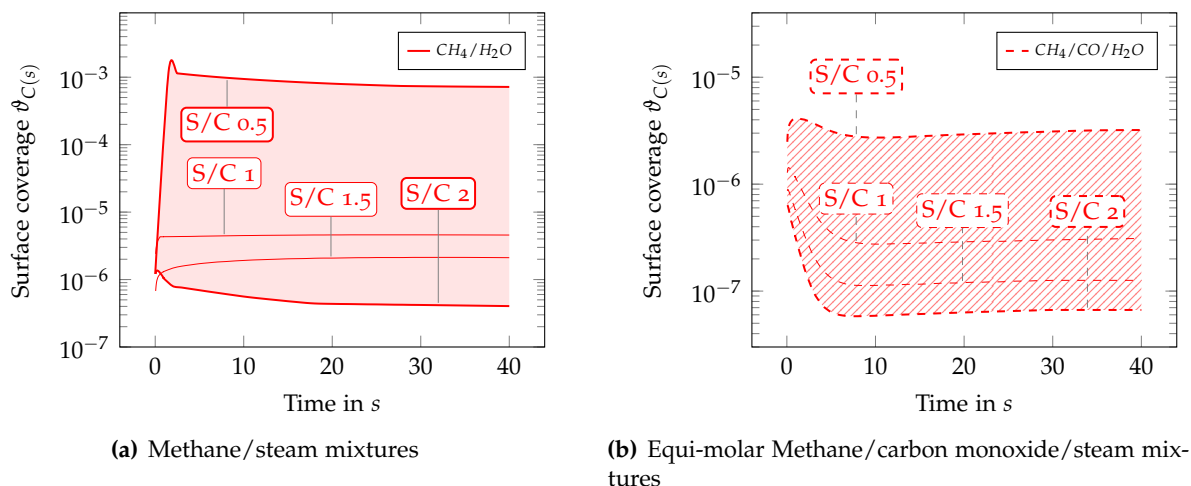
Figure 4.16.: Transient surface coverages of C(s) at $1,000\,^{\circ}C$ and S/C $0.5 - 2$ [89]

for SOFC applications. Mixtures of $CH_4/CO/H_2O$ and CO/H_2O can be utilized with S/C ratios below unity without the risk of carbon formation. Start-up and shut down can be critical for SOFC systems, since the system has to be heated up, and low temperatures can occur. Equilibrium calculations revealed that for temperatures below $600\,^{\circ}C$, steam to carbon ratios significantly higher than unity are required to avoid coking of the SOFC anode. The magnitude strongly depends on the gas composition, but it was shown found that carbon is most unlikely to be formed from methane/steam mixtures. Carbon monoxide/steam and equimolar mixtures of methane and carbon monoxide and steam are more likely to form elementary carbon, since an increased amount of steam is needed to avoid coking.

Thermodynamic equilibrium presumes sufficiently fast (reforming) reaction kinetics and adequate residence time. This assumption has to be checked and evaluated in for practical SOFC system applications. However, the application of detailed kinetics is a logical improvement in the level of sophistication of reaction modelling. By means of the detailed heterogeneous reaction mechanism used in this thesis, it was possible to directly calculate the spatial and temporal distribution of chemically adsorbed elementary carbon at the reacting porous substrate surface. CH_4/H_2O and equimolar mixtures of CH_4 and CO with steam were identified as causing the highest carbon surface coverages between $600\,^{\circ}C$ and $1,000\,^{\circ}C$. Methane/steam mixtures caused the highest surface coverages, making $CH_4/CO/H_2O$ mixtures the second most important carbonaceous fuel.

Pure carbon monoxide and steam mixtures played a subordinate role. This can be attributed to the reaction rates of the involved dissociation steps. It can be seen from kinetic data (cf. reaction mechanism in Table 3.8) that the desorption rates of hydrogenation reactions of surface-adsorbed carbon are almost two magnitudes lower than those of reactions of surface-adsorbed oxygen and elementary carbon. This results in elevated carbon coverages due to hydrogenated species, such as methane and its radicals. Oxygen reaction rates are higher, leading to low carbon coverages caused by carbon monoxide.

An equimolar fuel mixture of CH_4 and CO with steam led to average reaction rates of both described phenomena. This resulted in carbon coverages below the maximum caused by methane/steam and above the minimum brought about by carbon monoxide/steam mixtures. These results coincide with the experimental findings of [79] and [97].

Scrutiny of the spatial carbon distribution in the final steady state showed that most of the carbon is adsorbed within the first 5 to $10\,mm$ of the substrate. Surface coverage decreased with increasing substrate length. This can be attributed to the reforming reactions that occur, which are highest at the substrate beginning. Increasing the amount of steam within the system significantly decreased the total amount of adsorbed carbon atoms, which makes a S/C ratio of 0.5 the most critical operating parameter throughout the investigated temperature range.

Comparing the carbon surface coverage results with the simplest way of identifying possible carbon formation (formation activities α_i) reveals that this equilibrium approach for the dissociation reactions can be used as a reasonable indicator of carbon formation. Both approaches indicated that the first few millimetres of the substrate are in particular danger of coking. Nonetheless, these formation activities merely describe the deviation from thermodynamic equilibrium of some dissociation reactions under explicit investigation. This deviation indicates possible carbon formation, but does not give an absolute value of formed carbon. The detailed reaction mechanism used in this work made it possible to directly calculate the number of carbon atoms adsorbed to the surface, making it a much more valuable and more significant simulation approach.

This surface site coverage can be connected with the equilibrium calculations, as presented in Section 4.3.2, to obtain a carbon formation or deposition rate. Equilibrium has to be fulfilled within the reacting porous substrate zone. When this requirement is fulfilled, local and temporal carbon formation rates due to graphite (C(gr)) or carbon nano fibers (CNF) can be determined. As was shown in Figure 4.3(a), at $800\,°C$, $0.47\,mol$ C(gr) will form from $1\,mol$ of methane at a S/C of 0.5. A volumetric fuel flow of $2.4\,SLPM$ at a S/C of 0.5 for an equilibrated reaction thus results in a C(gr) formation rate of $5.12 \times 10^{-4}\,mol_{C(gr)}/s$. This approach can be universally applied for reacting systems at equilibrium.

Temporal analysis revealed that carbon surface coverage differs greatly between the start of the feed gas supply and the steady state condition. Throughout the entire temperature range, steam-to-carbon ratios and the most significant carbon precursors (methane/steam and equimolar mixtures of $CH_4/CO/H_2O$), carbon surface coverage peaked within the first 10 seconds until the final steady state condition was reached. Another interesting outcome is that, with increasing operating temperatures, the number of adsorbed carbon atoms at the surface increased significantly for a minimum S/C ratio of 0.5. A simultaneous increase of steam in the system showed an obviously non-linear carbon surface coverage decrease. Thus, minimum and maximum surface coverages differed in many orders of magnitude at $800\,°C$ and $1,000\,°C$. For a SOFC during load operation it is to be expected that coking propensity decreases in comparison to an artificial S/C increase, since water is formed under load operation.

As described in Sections 4.3.4 to 4.3.6, it is impossible to avoid permanent chemisorption of elementary carbon at the catalytic active sites, regardless of the amount of water vapour added to the system. Elementary carbon is a precursor of the further formation of e.g. C(gr) or CNF. As shown by Mermelstein et al. [47], Sumi et al. [105] and Subotić et al. [106, 107], medium carbon surface coverage can lead to the enhanced performance of a SOFC due to an increase in electrical conductivity caused by a thin layer of carbon. For practical SOFC operation, it is recommended to use a S/C ratio sufficiently high to avoid equilibrium formation of C(gr) or CNF as indicated in Figure 4.5. The ratio of carbon formed to the gaseous carbon precursor fed to the system can be severe if the temperature and species dependent S/C ratio falls below a certain threshold. This can lead to irreversible cell degradation and, in the long-term, to the total failure of the cell.

5

Internal Reforming of Synthetic Reformates

The high operating temperatures of SOFCs allow them to utilize a broad range of fuels. Diesel reformate (the main fuel mixture used in this thesis), natural gas, biogas, gas from biomass gasification, and any pre-reformed liquid hydrocarbon are fuel mixtures that contain methane, carbon monoxide, carbon dioxide, hydrogen, water vapour and, depending on the gasification/reforming strategy, nitrogen. Reformates are of special interest to SOFC applications, thanks to their ability to (1) internally reform methane and short-chained hydrocarbons; (2) electrochemically utilize carbon monoxide, which is a major advantage over low temperature fuel cells; and (3) produce high quality heat that can be utilized in further downstream processes. When using these gas mixtures as fuels for SOFCs, impurities such as sulphur, hydrogen chlorides, and particulate matter must be removed. As shown in Chapter 4, degradation can occur as a result of any carbon precursor in the aforementioned fuel mixtures. These carbon precursors are methane and carbon monoxide, and they form carbon deposits with different morphologies. This thesis has shown that methane is the most prominent gaseous carbon precursor in the SOFC operating temperature range. However, superimposed degradation phenomena can occur when fuel mixtures are used, which contain different carbon precursors.

The internal reforming of these hydrocarbons includes the risk that carbon deposits will form at the anode surface, which then block the chemically-and electrochemically-active nickel particles. This leads to increased charge transfer resistance and rapid cell performance deterioration. The addition of large amounts of steam can prevent the formation of carbon deposits, but also dilutes the fuel, which lowers the achievable power output [2, 3]. Thus, in order to achieve a reasonable electrical power output, low - and, in steady state operation, fixed - steam-to-carbon ratios are used, which can trigger carbon formation on the porous anode. These carbon deposits limit the lifetime of the SOFC. A detailed analysis of the reforming catalyst's surface condition during internal reforming can provide detailed insight into the processes involved, and helps researchers identify the sources of degradation. Thus, in this chapter, the influence of different synthetic reformates on the catalytic active nickel surface during internal reforming conditions is investigated in detail.

In this chapter, diverse carbon-containing gas mixtures with critical steam-to-carbon ratios (S/C ratio below unity, which can exist at open circuit condition or during the start-up and shutdown of SOFC systems) are used to scrutinize the spatial species adsorption distribution. In addition to changes in the S/C ratio, the carbon precursor ratio is also varied, that is, the methane-to-carbon monoxide ratio. This ratio is of high significance, as the individual importance of each carbon precursor was highlighted in Chapter 4. The propensity of methane and carbon monoxide, as constituents of a fuel mixture, to precipitate carbon deposits is thus investigated.

State-of-the-art global gas phase classification methods are employed at surface-level to investigate the ratios of locally adsorbed species: e.g. elementary carbon, oxygen, or carbon precursors such as carbon monoxide, methane or hydrocarbon radicals. A global, gas phase S/C ratio is generally used during practical applications, and in almost every scientific study, to evaluate the propensity to form coke or to calculate the equilibrium composition of a gas mixture during internal reforming.

The current chapter introduces global gas phase S/C ratios to surface level ($H_2O(s)/C(s)$) in order to investigate the conditions of the porous anode substrate. The adsorbed state of a species is indicated by $X(s)$. Furthermore, different ratios will be investigated, including the oxygen and hydroxyl-radical ratio $O(s)/C(s)$, the oxygen and elementary carbon ratio $O(s)/C(s)$ and the ratio of elementary carbon compared to the total number of adsorbed species. This is done to provide a more detailed view inside the cell, and to create a sophisticated understanding of the ramifications of internal reforming of hydrocarbons.

5.1. Carbonaceous Mixtures and Their Impact on the Catalyst[1]

Chapter 3 provided a broad and general introduction to the topic of carbon formation during the usage of carbonaceous fuels. The general formation pathways (methane cracking reaction and Boudouard reaction) were presented, and a multitude of global homogeneous were scrutinized in addition to a detailed heterogeneous reaction mechanism used to numerically describe the reforming reactions that occurred.

In Chapter 4, the main gaseous carbon precursor was investigated. It was found that, in the typical SOFC operating temperature range, methane is the most prominent carbon precursor. Thus, precise S/C ratios need to be maintained throughout the entire cell operation time to avoid coking of the cell. The previous chapter examined the presence of single carbonaceous components in a mixture with steam. However, future SOFC applications need to compete with existing, conventional technologies that utilize fossil fuels. When diesel is used in SOFCs, it needs to be pre-reformed in order to get a gaseous hydrocarbon fuel mixture, mainly consisting of methane, carbon monoxide, carbon dioxide, hydrogen, water vapour, and nitrogen. Such fuel mixtures need to be investigated in order to determine any possible interactions of the

---

[1]Segments of this section were published in the *Journal of The Electrochemical Society* under the title "Numerical SOFC Anode Catalyst Occupation Study: Internal Reforming of Carbonaceous Fuel Mixtures" [108].

constituents, and to identify possible differences between operation with methane/steam and carbon monoxide/steam mixtures.

In their study, Subotić et al. [106] showed that an increase of the methane molar fraction in a synthetic diesel reformate had a major impact on the performance degradation rate of a SOFC cell. They investigated three different synthetic diesel reformates with increasing amounts of methane, and showed that an increase from 0.023 to 0.14 $mol\,mol^{-1}$ drastically reduced the time that was needed to provoke a specific performance degradation.

Carbon formation was detected on the nickel catalyst and over the entire YSZ surface. Moreover, they found that with increasing amounts of methane in the reformate mixture, carbon nanofibers formed, which delaminated the anode from the electrolyte, leading to irreversible cell degradation. A further interesting outcome of this study was that low methane amounts in the fuel feed resulted in the formation of amorphous carbon, which crushed the YSZ particles and deposited them on the nickel particles. Thus, the catalytically-active area was reduced, and the cell performance was degraded in an additional irreversible way.

Mermelstein et al. [47] investigated the impact of tars formed during biomass gasification, on the performance and durability of SOFC anodes. They found that the tar can be partially oxidized under load condition. Cell degradation was minimized as the cell load was increased towards the identified threshold current density. Ni/GDC anodes suffered less degradation than Ni/YSZ anodes. This indicates that not only the catalyst has an influence on the carbon-formation propensity but also the oxygen ion conductor.

Other than carbon formation, the degradation of the electrocatalyst also plays an important role in the cell's performance. This phenomenon is generally referred to as nickel re-oxidation. Significant degradation and even total cell failure can occur if nickel is re-oxidized during high-temperature operation. In their study, Ettler et al. [109] summarized the failure modes of single cells and stack cassettes as well as the corresponding deformation characteristics. Nickel re-oxidation can induce cracks in the electrolyte, leading to the mechanical destruction of the cell. Anode-supported cells are in particular danger of critical cell malfunction brought about by nickel re-oxidation, due to the high amount of nickel that is incorporated in their mechanically-supporting anode layer.

Nickel oxidation is, to a certain extent, reversible, but after re-oxidation, the anode structure does not regain the initial structure of the pre-reduced anode. Repeated re-oxidation cycles cause bulk expansion, and thus lead to the mechanical damage of the cell [110]. Performance degradation is caused by a microstructural change (accompanied by a volumetric change) from elementary nickel to nickel oxide. This volumetric change leads to mechanical stresses that can crack the thin electrolyte, denoting the end of a cell's lifetime.

The choice to investigate the local amount and distribution of adsorbed oxygen, carbon, hydrogen, and a multitude of other species, during the internal reforming of synthetic diesel reformates was made based on the findings of the previous chapters as well as the literature presented above. These adsorbed species will be investigated in order to identify critical

operating conditions and vulnerable regions at risk from degradation. Nickel re-oxidation potentials will be identified, and a detailed analysis of carbonaceous species in the porous anode will be carried out.

5.2. Model Description[2]

The numerical used to carry out the simulations in this chapter is the same as that presented in Chapter 4. The operating temperature was set to $800\,°C$, which is a typical value for an anode-supported cell. A detailed heterogeneous reaction mechanism for the internal reforming of methane on the catalytically-active sites of the porous anode structure was used, as in Table 3.8 and in [75]. The surface adsorbed species incorporated in this section are: $Ni(s)$, $H_2O(s)$, $H(s)$, $OH(s)$, $O(s)$, $CO(s)$, $CO_2(s)$, $CH_4(s)$, $CH_3(s)$, $CH_2(s)$, $CH(s)$, $C(s)$ and $HCO(s)$. In this chapter, the surface composition analysis is done by means of steady state simulations, covering diesel reformates with a wide steam-to-carbon ratio of 0.3 to 0.84. This range was chosen so as to identify regions where carbon formation occurs. The importance of the carbon precursor (either methane or carbon monoxide) on the amount of carbon adsorbed to the surface was highlighted in the previous chapter. Thus, along with the variation of the steam-to-carbon ratio, the methane-to-carbon-monoxide (CH_4/CO) ratio is also varied, to identify the impact of each constituent in a fuel mixture on the carbon-formation propensity. This ratio was varied between 0 and 1.75. A detailed description of the boundary conditions is provided in Section 5.2.2.

5.2.1. Computational Domain and Numerical Setup

The computational grid used in this chapter is shown in Figure 5.1. Ideal, symmetrical flow conditions were presumed, since this assumption is applicable for the entire cell, except the near-wall regions. It was thus reasonable to simplify the entire $3D$-domain of a complete single cell to a $2D$-domain. The model represents the first third of the anode-supported SOFC installed in our test bench at the IWT. The previous chapter established that it is here that the highest reaction and species gradients occur, which is the main cause for this simplification. The domain thus has a geometrically active length of $30\,mm$. The porous fuel electrode thickness is $0.5\,mm$, the same as in all of the previously-conducted simulations. Heterogeneous reforming reactions were modelled to occur within this porous fuel electrode, as it was shown in Chapter 4. This makes it possible to carry out a spatially-resolved simulation that predicts the distribution of all of the surface-adsorbed species involved. An extended outlet zone was added to the $2D$ model to avoid a backflow from the domain's outlet. The mesh consisted of approx. $1,400$ quad-cells with a maximum aspect ratio and skewness of 30 and 0.1, respectively. An independence check of the grid was conducted, to make sure that the simulated temporal and spatial species

---

[2]Segments of this section were published in the *Journal of The Electrochemical Society* under the title "Numerical SOFC Anode Catalyst Occupation Study: Internal Reforming of Carbonaceous Fuel Mixtures" [108].

distributions were independent of the size of the computational grid, the type of cells, and the geometric discretization method.
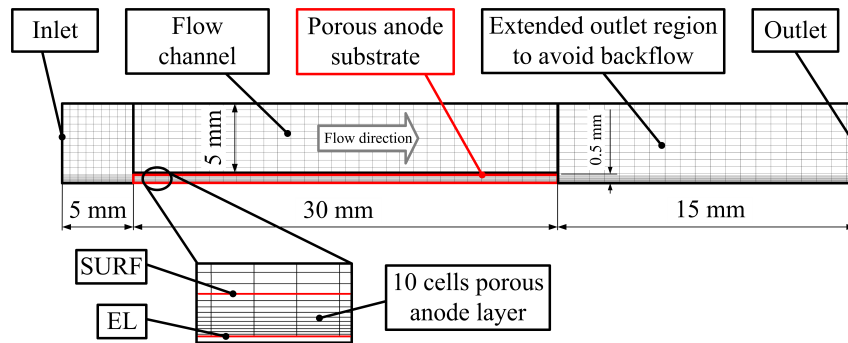
Figure 5.1.: Schematic of the 2*D*-flow channel and the computational grid (not to scale) [108]

The numerical settings described in Section 4.2.3 were used. However, for the sake of readability, the most important settings are also displayed below. The steady-state simulations were carried out using a double precision pressure-based (coupled) solver. The operating temperature was set to $800\,°C$, and a laminar flow model was used. The critical operating conditions for internal reforming occur during open circuit condition, since no water is formed. This leads to minimal steam-to-carbon ratios, thus making it possible to exclude an electrochemistry sub-model from the numerical model.

Multicomponent species diffusion is modelled using the Stefan-Maxwell model equations in order to describe molecular transport processes. A laminar finite-rate approach was used to predict the Arrhenius-type reaction rates. The adsorption and desorption rates of heterogeneous reactions are governed by both chemical kinetics and diffusion to and from the surface. The fuel mixtures were modelled as incompressible ideal gases. Ni-YSZ anode properties were set as constant for the corresponding temperature (see Table 4.1). Geometrical and temporal discretization were conducted by second-order and first-order upwind schemes, respectively. Convergence was determined when residuals fell below a threshold value (10^{-5} for continuity and momentum, 10^{-7} for species), and when species outlet compositions, surface coverages, temperature, and outlet velocity remained constant.

5.2.2. Boundary Conditions

As mentioned above, the operating temperature of the SOFC single cell was set to $800\,°C$, a typical value for an anode-supported type cell. The fuel electrode was fed with six different gas mixtures, as shown in Table 5.1.

These mixtures represent any kind of reformate or carbon-containing fuel mixture. The molar amount of methane was varied for different cases, while the amounts of hydrogen, carbon dioxide, water vapour, and carbon monoxide were held constant. Supplementary nitrogen was also added. This chapter will highlight the influence of varying the S/C ratio, as well as the methane-to-carbon monoxide ratio, on the catalyst's condition. Varying the molar methane

amounts makes it possible to investigate scenarios with differing carbon precursors, e.g., from a high amount of methane and highest CH_4/CO ratio at S/C 0.3 to pure CO as carbon precursor at S/C 0.83. The upper limit (S/C 0.83) was defined based on the reformate composition in [111], but in the absence of methane. This represents a carbon precursor loading due to carbon monoxide only. A S/C ratio of 0.71 was used as a reference case, since the experimental and numerical investigations for this mixture were carried out and extensively validated in Chapter 3 and in [111]. The lower limit (S/C 0.3) was set on the basis of the reformate composition used for the fast coking of the cell in Ref. [112] (**DR20.3**). The fuel mixture with S/C 0.41 was defined as an equimolar mixture of methane and carbon monoxide ($CH_4/CO = 1$).

Table 5.1.: Diesel reformate compositions

Species	Value	Unit
Constant species		
H_2	0.154	$mol\ mol^{-1}$
CO_2	0.098	$mol\ mol^{-1}$
H_2O	0.113	$mol\ mol^{-1}$
CO	0.137	$mol\ mol^{-1}$
N_2	supplementary	$mol\ mol^{-1}$
S/C 0.3		
CH_4	0.24	$mol\ mol^{-1}$
CH_4/CO	1.75	$mol\ mol^{-1}$
S/C 0.41		
CH_4	0.137	$mol\ mol^{-1}$
CH_4/CO	1	$mol\ mol^{-1}$
S/C 0.447		
CH_4	0.1158	$mol\ mol^{-1}$
CH_4/CO	0.845	$mol\ mol^{-1}$
S/C 0.5		
CH_4	0.089	$mol\ mol^{-1}$
CH_4/CO	0.65	$mol\ mol^{-1}$
S/C 0.71		
CH_4	0.0225	$mol\ mol^{-1}$
CH_4/CO	0.16	$mol\ mol^{-1}$
S/C 0.83		
CH_4	0	$mol\ mol^{-1}$
CH_4/CO	0	$mol\ mol^{-1}$

By means of thermodynamic equilibrium calculations, it was determined that for the prevalent boundary conditions, a steam-to-carbon ratio of 0.447 (CH_4/CO ratio 0.845) is necessary to inhibit carbon formation due to graphite and carbon nanofibers (cf. Lee et al. [102]). The results of this case will thus be used as a threshold or boundary for carbon formation. S/C 0.5 was added as an extra sampling point. It is important to investigate these different fuel composition variations since it was shown by [79, 89, 97] that different carbonaceous species (methane / carbon monoxide) provoke differing coking scenarios on the fuel electrode. The fuel mass flow of the reference case (S/C 0.71) was calculated on the basis of a volumetric fuel flow

of $\dot{V} = 2.4\,SLPM$, as described in the previous chapters. Based on this, a reference carbon precursor mass flow was calculated. This carbon precursor mass flow was set to be the sum of methane and carbon monoxide mass flows. In order to ensure a constant supply of carbon for all of the investigated cases, this carbon precursor mass flow was set to be constant. This meant that with varying fuel compositions, the overall fuel mass flow varied. This was done in order to ensure similar carbon loading scenarios for all cases during internal reforming in order to identify the critical parameters (besides the S/C ratio) for the safe operation of SOFCs.

5.3. Catalyst Occupation During Internal Reforming of Carbonaceous Mixtures[3]

5.3.1. Overall Adsorbed Species

The species distributions at the catalytically-active sites and their coverages are scrutinized below. The averaged amounts of adsorbed species for all investigated cases are shown in Figures 5.2 and 5.3. The species are ordered by the total amounts that occurred during the internal reforming process. It can be seen in 5.2(a) that numerous surface sites are unoccupied (denoted by empty $Ni(s)$ sites). As the S/C ratio increases, the amount of adsorbed carbon monoxide $CO(s)$ and hydrogen $H(s)$ decreases. Although the mass flow of carbon precursors (methane and carbon monoxide) was held constant, the highest surface coverages of $CO(s)$ occur at the highest CH_4/CO (lowest S/C) ratio. $CO(s)$ surface coverages ranged from 0.43 (for S/C 0.3) and 0.35 (for S/C 0.83). Hydrogen surface coverage amounted to 0.17 and 0.14 for the lowest and highest S/C ratios, respectively.

(a) Major adsorbed species

(b) Adsorbed $O(s)$, $OH(s)$ and $H_2O(s)$
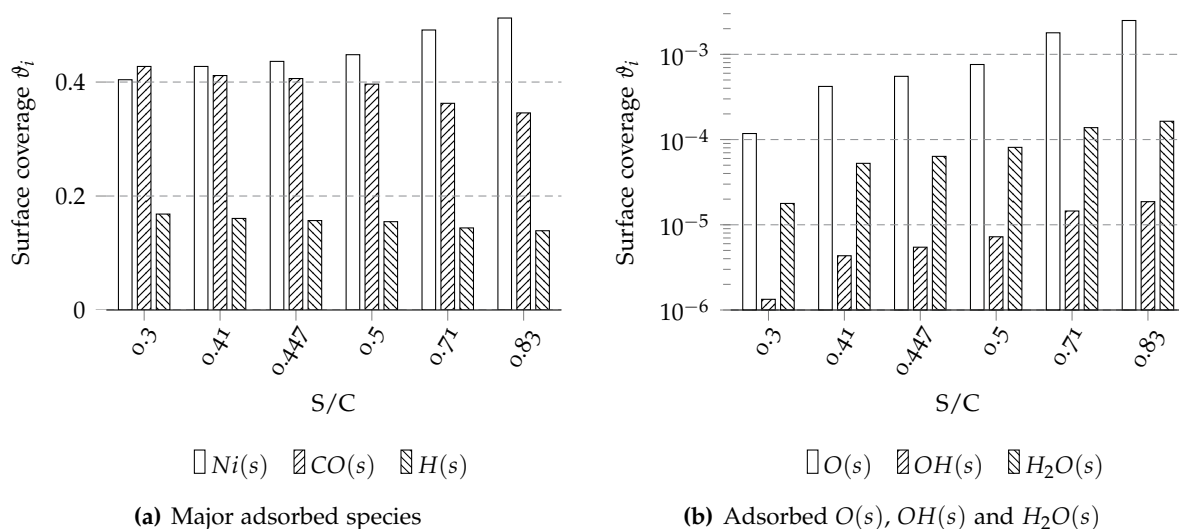
Figure 5.2.: Average adsorbed major species amounts for the investigated cases [108]

---

[3]Segments of this section were published in the *Journal of The Electrochemical Society* under the title "Numerical SOFC Anode Catalyst Occupation Study: Internal Reforming of Carbonaceous Fuel Mixtures" [108].

Notably, the second highest surface coverages occurred for $O(s)$, $OH(s)$ and $H_2O(s)$ (see Figure 5.2(b)). Increasing amounts of steam within the fuel feed led to increased oxygenated species surface site coverages. Adsorbed oxygen atoms $O(s)$ covered 0.25 % of the catalytically-active nickel sites at maximum S/C ratio. This indicates that elevated S/C ratios can be a potential cause of nickel re-oxidation. Nickel re-oxidation can occur if the amount of adsorbed oxygen exceeds the amount of adsorbed hydrogen. In the majority of cases, re-oxidation will not occur, but this model allows the potential for its occurrence to be evaluated. The surface coverages of $OH(s)$ radicals were two orders of magnitude below those of oxygen; adsorbed water molecules $H_2O(s)$ were calculated to be below $O(s)$ coverages by approx. one order of magnitude.

(a) Adsorbed $C(s)$ and $CO_2(s)$

(b) Adsorbed hydrocarbons
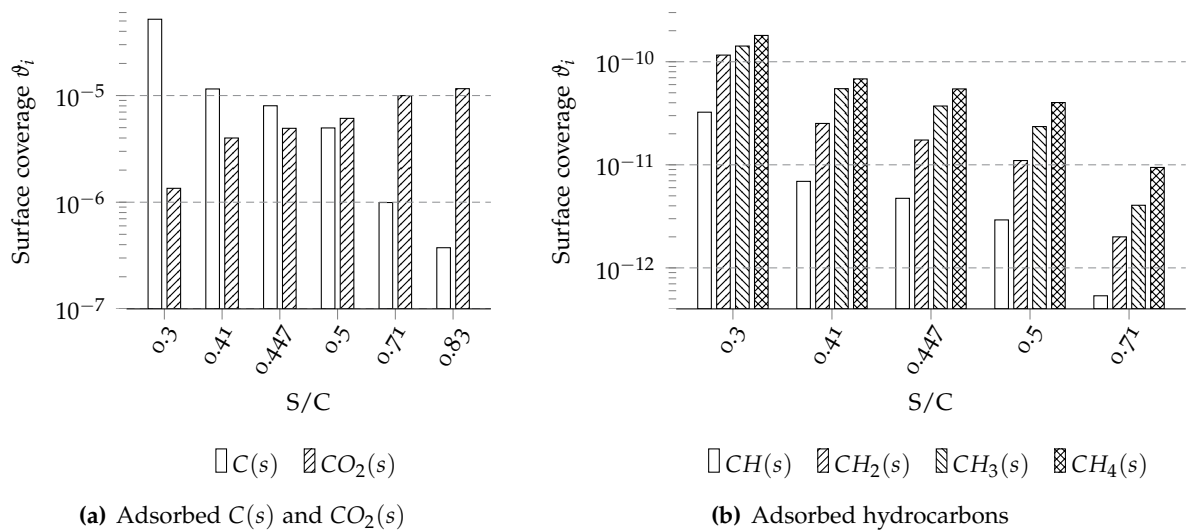
Figure 5.3.: Average adsorbed species minor amounts for the investigated cases [108]

Adsorbed elementary carbon and carbon dioxide are depicted in Figure 5.3(a). An inverse trend can be seen between these species as the S/C ratio increases. As expected, highest carbon coverages were calculated for S/C 0.3 to 5.2×10^{-5}, due to insufficient supply of water vapour. It is possible to see that the correlation between S/C ratio and the amount of adsorbed carbon is strongly non-linear. An increase from S/C 0.3 to S/C 0.83 results in a decrease of adsorbed elementary carbon of almost 1.5 orders of magnitude. HCO coverages were neglected, since they were approximately 1×10^{-11}.

At this point, it is important to note that the carbon coverages calculated can be interpreted as precursors of graphite, carbon nanofibers, and filamentous or pyrolytic carbon. This coverage should not be confused with carbon found after experimental carbon formation investigations. Based on the works of Lee et al. [102] and on the findings of Chapter 4, thermodynamic equilibrium calculations determined that carbon formation is thermodynamically inhibited above a S/C ratio of 0.447 ($CH_4/CO = 0.845$) for the present gas mixture compositions.

The heterogeneous reforming reactions at the catalytic surface deviate from equilibrium by two percent at most. Thus, thermodynamic boundaries can be applied to the present case. The carbon surface coverages for S/C 0.447 therefore delineate the boundary of no carbon formation. Coverages above this threshold value of $\vartheta_{C(s)} = 8 \times 10^{-6}$ denote that graphite or CNF can form.

Below this S/C ratio, no permanent coking of the catalyst will occur, while coverages above this threshold value indicate that carbon will form. This is an important finding of this thesis, and the applied methodology can be used to connect thermodynamic equilibrium calculations and this detailed surface occupation analysis to determine carbon formation rates which will occur during experimental investigations of such reformate mixtures. This eliminates the need to employ hardly understood carbon formation kinetics in the simulations.

The amounts of adsorbed hydrocarbons are shown in Figure 5.3(b). Since no hydrocarbon is included in S/C 0.83, this set of columns was excluded from this figure. A strongly non-linear trend can be seen between the gas phase methane-to-carbon monoxide ratio and the surface adsorbed hydrocarbon species. A stepwise decrease in the amount of adsorbed species from $CH_4(s)$ to $CH(s)$ can be seen over the entire S/C ratio zone. For the case of S/C 0.3, one can observe that, although $0.24\,mol\,mol^{-1}$ methane is included in the fuel stream, the total amount of adsorbed species is negligible. The magnitude of adsorbed hydrocarbons is in the range of 10^{-10} to 10^{-12}, which is several orders below that of elementary carbon and carbon dioxide.

Figures 5.2 and 5.3 provide an initial overview of the general catalyst site condition. During internal reforming of both methane-containing (S/C 0.3, highest methane amounts) and methane-free (only carbon monoxide as carbon precursor, S/C 0.83) reformates, most of the catalytically-active sites are covered by adsorbed carbon monoxide $CO(s)$ and elementary hydrogen $H(s)$. Adsorbed methane $CH_4(s)$ is more or less negligible. These adsorbed species can be electrochemically converted. Thus, not only hydrogen electrochemistry is of high importance for SOFCs, but also their ability to electrochemically convert carbon monoxide to carbon dioxide. Oxygenated species and hydrogenated species indicate that the risk for nickel re-oxidation has to be taken into account when fuelling SOFCs with high S/C ratios.

The threshold value for carbon formation based on the elementary carbon surface coverage was also identified. This value is $\vartheta_{C(s)} = 8 \times 10^{-6}$ for the prevalent boundary conditions. Carbon coverages above this value lead to coking of the catalyst; lower amounts of adsorbed carbon can effectively be desorbed or recombined, so that no coking will occur.

5.3.2. Local Species Coverages

In order to provide a more detailed understanding of the surface composition, local and spatial species coverages for S/C 0.3 are depicted in Figures 5.4 and 5.5. As in Figures 5.2 and 5.3, the species are plotted in descending order of their catalyst surface occupation. The trends shown in Figures 5.4 and 5.5 represent the minimum and maximum coverages through the substrate thickness of $0.5\,mm$ for the first third ($\hat{=} 30\,mm$) of an entire SOFC cell. Markers were added to each figure to indicate the corresponding adjacent surface or fluid zone. The electrolyte-anode interface (EL) denotes the interface between the anode substrate and the electrolyte. The surface of the anode substrate is marked as the anode-flow channel interface (SURF). These two notations are given in a detail-view in Figure 5.1. The surface-average coverage is plotted as a

dashed line for all corresponding species. It should be noted that the surface average is in clear divergence from the arithmetical average, which is an important outcome. This shows that the species distribution is inhomogeneous, indicating that, throughout the substrate thickness, there are regions with a higher potential to cause failure modes than others. Furthermore, arrows were inserted to emphasize the increase in the substrate thickness, starting from the electrolyte.
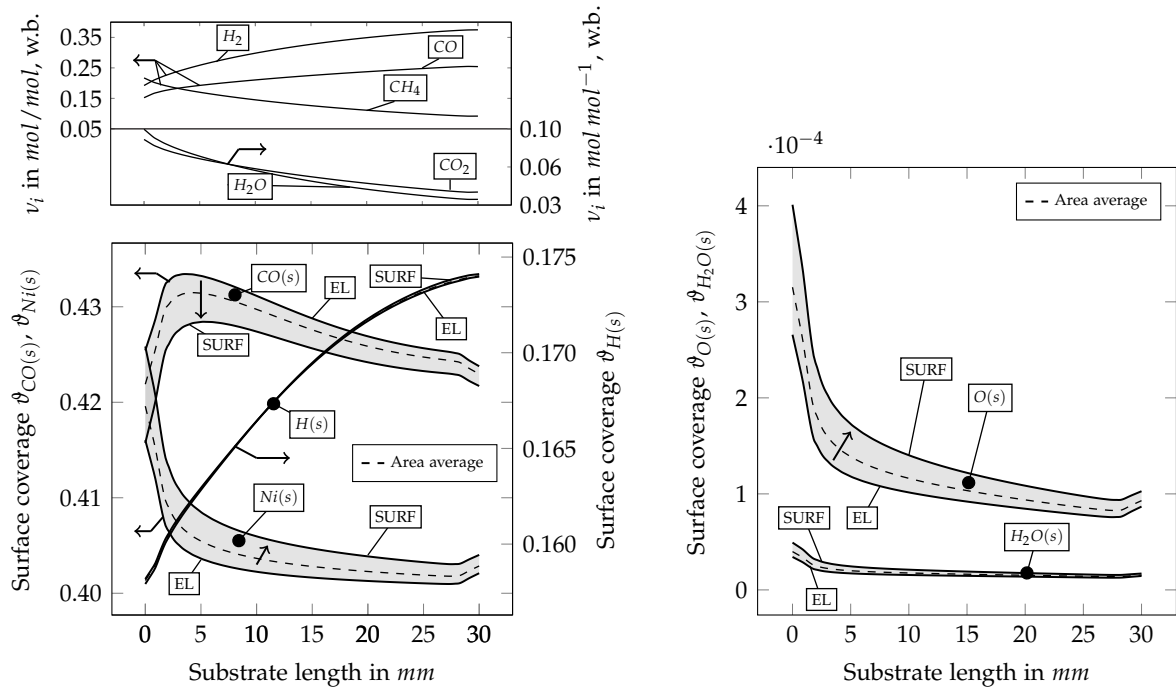
(a) Average molar gas composition in flow channel (cf. Scheme in Figure 5.1) (top) and surface adsorbed species $Ni(s)$, $CO(s)$ and $H(s)$ (bottom)

(b) $O(s)$ and $H_2O(s)$

Figure 5.4.: Local coverage trends of major adsorbed species for S/C 0.3 at 800 °C along the channel length [108]

Figure 5.4(a) is divided into two subfigures. The top figure gives the average molar gas composition in the flow channel during internal reforming in the porous anode substrate. This makes it easier to visualize the reforming process and its results on the catalyst. The fuel mass flow is in a range that excess fuel mixes with reformed gas at the outlet, as is the case at our test bench at the IWT. The reaction in the substrate itself is at equilibrium, which was determined by comparing equilibrium conversion rates with the conversion rates within the porous structure. Methane, water vapour, and carbon dioxide decrease, whereas hydrogen and carbon monoxide are produced. Since carbon monoxide decreases, it is possible to conclude that, in this specific case, the overall equilibrium of the water-gas shift reaction (although it is not modelled as a gas phase reaction per se, but rather a more detailed surface level [75]) tends towards the reactants side. The overall reforming process is the cause of all subsequent results. As can be seen in the bottom figure, the free nickel sites $Ni(s)$ decline as the substrate length increases. This means that the overall number of adsorbed species increases towards the end of the substrate, indicating that there are highly active zones at its front (possible fast degradation) and regions for at risk of long-term degradation at the end of the substrate.

The trend of adsorbed carbon monoxide $CO(s)$ is almost inverse to that of free nickel sites. A steep increase in the first three millimetres of the anode substrate is followed by a steady decrease towards the end of the substrate. The slight discontinuities at the end of the substrate (for all shown cases) can be attributed to computational errors of the second-order upwind discretization scheme. The highest amounts of adsorbed CO were simulated to occur at the anode-electrolyte interface. A decrease towards the anodic surface (SURF) can be seen throughout the entire substrate length. Almost 43 % of the catalytically active surface is covered by adsorbed carbon monoxide. It can thus be concluded that adsorbed carbon monoxide $CO(s)$ is a central precursor for both the elementary carbon that is deposited, as well as for gaseous carbon dioxide that is emitted as a reaction product. The second highest coverages were calculated for hydrogen. As can be seen in Figure 5.4(a), it is adsorbed uniformly through the substrate thickness. Due to the fact that no electrochemical conversion occurs, the amount of adsorbed hydrogen increases along the substrate length. From 15.75 % to almost 17.5 % of the catalyst surface is occupied by hydrogen.

The surface site coverage distribution of oxygen and water vapour is shown in Figure 5.4(b). As in Figure 5.2, absolute coverages are in the range of 1×10^{-4}. Although oxygen was not included as a discrete species in the gas phase, the third highest surface coverages were simulated as a result of its central role as an intermediate species during internal reforming. Coverages are highest at the beginning of the substrate and sharply decrease during the first $5\,mm$ of the substrate. This identifies regions with high catalytic activity and high reaction rates. Towards increasing substrate length, coverages further slightly decrease. Here too, the surface average coverage diverges from the arithmetical average. This again indicates that coverage change through the substrate is not linear, and that only a thin layer on top has high oxygen coverage, while most of the substrate has lower oxygen coverages. The lowest coverages occur on the EL interface, with a continuous increase through the substrate thickness.

The trend of $OH(s)$ species distribution is similar to that of $O(s)$, but its absolute values decrease by two orders of magnitude. It was thus excluded from this figure. The amount of adsorbed water vapour $H_2O(s)$ are approx. nine times lower than those of $O(s)$. Aside from this decrease, the general descriptions made for the trend of adsorbed oxygen also apply here. This figure shows that reactive oxygen species are more available than product species (water), indicating that high gas phase S/C ratios can indicate a high risk of nickel oxidation, since it was shown in Figure 5.2(b) that a slight increase of the S/C ratio leads to a steep increase in the amount of available oxygen at the surface. The oxygen can then react with nickel to form nickel oxide, which can cause a mechanical failure.

Figure 5.5(a) presents an interesting simulation result, showing the coverages of adsorbed elementary carbon $C(s)$ and carbon dioxide $CO_2(s)$. The highest amounts of both elementary carbon and carbon dioxide were calculated to occur within the first $5\,mm$ of the substrate. Carbon shows a pronounced peak at 5.61×10^{-5}, followed by a sharp decrease towards the end of the substrate. Furthermore, the position of local maximum coverages change along the substrate length. Within the first 8 millimetres, the most carbon is found at the anode-electrolyte

interface (EL). Past this point, the highest amounts of carbon appeared at the surface of the anode substrate SURF. Elementary carbon coverages are approx. one order of magnitude below those of oxygen.

(a) $C(s)$ and $CO_2(s)$

(b) $CH_4(s)$, $CH_3(s)$, $CH_2(s)$ and $CH(s)$
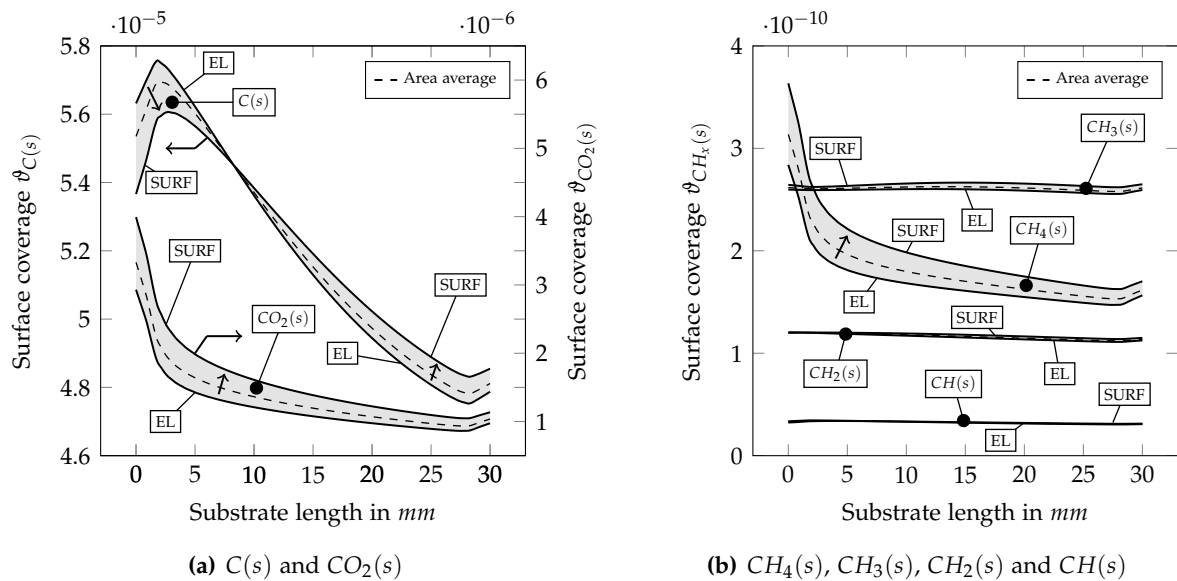
Figure 5.5.: Local coverage trends of minor adsorbed species for S/C 0.3 at 800 °C along the channel length [108]

As described in Section 5.3.1, this reaction only deviates from equilibrium by two percent. Thus, the calculated elementary surface coverages can be linked to a carbon formation rate (graphite (C(gr)) or CNF) from thermodynamic equilibrium. The thermodynamic equilibrium calculations in Figure 5.6 show that S/C 0.3, 0.21 *mol* CNF and 0.12 *mol* graphite form from diesel reformate at 800 °C. This equilibrium calculation was done based on the fuel composition as given in 5.1 for S/C 0.3, normalized to 1 mol of carbon precursor. These precursors are methane and carbon monoxide. Supplementary material on the thermodynamic equilibrium calculation results for the other five remaining fuel mixtures (S/C 0.41 - 0.83, cf. Table 5.1) can be found in Appendices A.2 and A.3. Connecting these results to the mass flow conditions of the CFD simulations for the entire cell, we find that 2.6×10^{-6} *mol/s* CNF and 1.46×10^{-6} *mol/s* graphite form. This leads to severe damage of the cell and blocks its pores, thus inhibiting correct cell functioning. Moreover, the carbon surface coverages of $\approx 5 \times 10^{-5}$ can be attributed to these carbon formation rates.

The trend descriptions for carbon dioxide coverages are the same as those of oxygen coverages, except that they are lowered by one order of magnitude. Adsorbed hydrocarbon species trends are depicted in Figure 5.5(b). Their amounts are in the range of 0.3 to 3.6×10^{-10}. With a decreasing number of hydrogen bonds, the surface coverage decreases. Furthermore, the difference through the substrate thickness similarly decreases. This shows that these species are uniformly adsorbed throughout the substrate thickness. From the front to the back of the substrate length, amounts decrease steadily
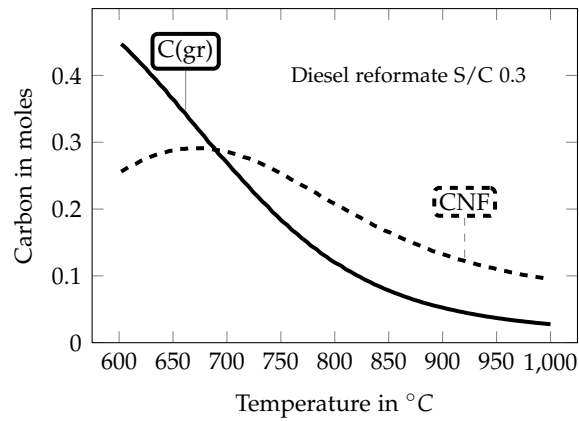
Figure 5.6.: Equilibrium carbon formation from diesel reformate S/C 0.3 in a typical SOFC temperature range, normalized to 1 mol of carbon precursor

5.3.3. Surface Specific Relations

As mentioned in the introduction to this section, gas phase steam-to-carbon ratios are generally used during practical applications, and, specifically, in almost every scientific study that evaluates propensity to form coke or to calculate the equilibrium composition of a gas mixture during internal reforming. In this work, global gas phase S/C ratios are introduced at surface level in order to investigate the conditions of the porous anode substrate. Furthermore, different ratios ($O(s)/H(s)$, $O(s)/C(s)$, $C(s)/(1 - Ni(s))$) that can be used to identify oxidation potentials and the ratio of elementary carbon compared to the total number of adsorbed species are investigated. Since the carbon formation boundary was identified to be at a S/C of 0.447, elementary $C(s)$ coverages above the threshold value of 8×10^{-6} lead to carbon formation, as mentioned previously. Figures 5.7 and 5.8 show the characteristic surface ratios for this limit case.

(a) Surface $H_2O(s)/C(s)$ (S/C) ratio

(b) Surface $O(s)/H(s)$ ratio
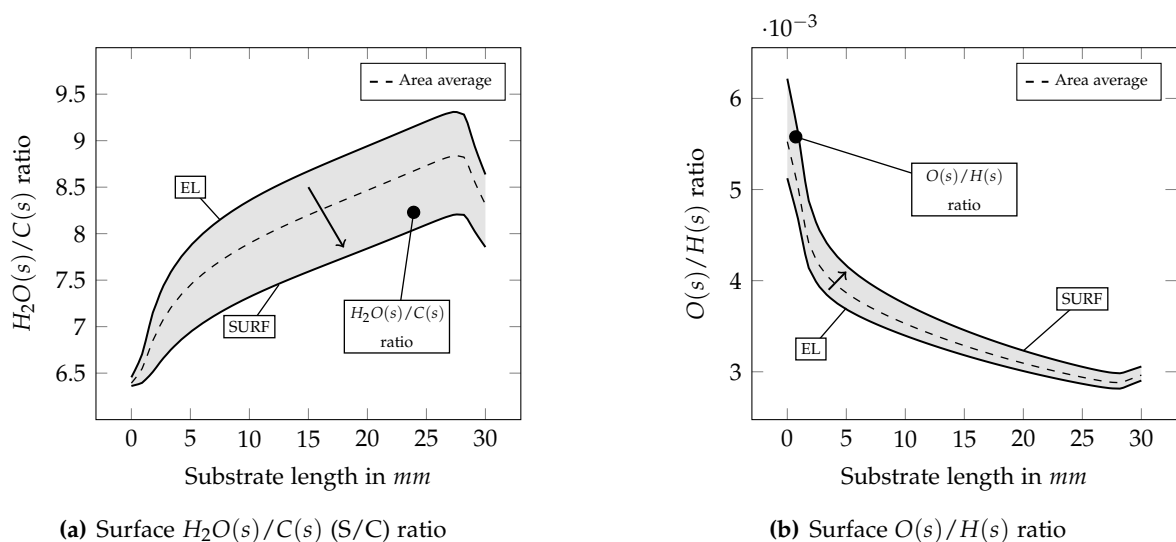
Figure 5.7.: $H_2O(s)/C(s)$ and $O(s)/H(s)$ surface ratios for S/C 0.447 at 800 °C along the channel length [108]

The local, surface specific steam to carbon ratio ($H_2O(s)/C(s)$) is introduced in Figure 5.7(a).

Similar to the global gas phase steam-to-carbon ratio, this specific ratio gives information about the local amounts of adsorbed water vapour and elementary carbon at the catalytically-active nickel sites. This ratio steadily increases along the porous substrate. At the inlet of the substrate, ratios of approximately 6.4 were calculated, and coverage differences between the electrolyte EL and anode surface SURF were small. With increasing substrate length, the difference between these two surfaces increased, with maximum coverages at the electrolyte. It is possible to conclude that zones near the surface have a higher carbon loading, whereas zones in the vicinity of the electrolyte are at less risk of coking. This can lead to pore blocking at the anode surface, thus inhibiting mass transport to the active centres. This outcome demonstrates the power and versatility of the CFD model, since such local and temporal evaluations are impossible to conduct by means of in-situ or in-operando experiments. The drop at the end of the substrate can be attributed to flow distribution within the flow channel. A direct interpretation of this ratio is nontrivial, but from thermodynamic calculations, it can be concluded that local ratios below these threshold values ($H_2O(s)/C(s) = 6 \div 10$), as shown in Figure 5.7(a), can be attributed to coking. Above these local values, no coking can occur.

The ratio of adsorbed elementary oxygen and hydrogen was investigated in Figure 5.7(b). This ratio can be taken into account to identify possible nickel oxidation potentials. At this specific boundary condition, no oxidation will occur, since the level is approximately $3 \div 6 \times 10^{-3}$. When this ratio becomes greater than unity, nickel oxidation can occur, since the amount of available oxygen is higher than the amount of hydrogen, leading to possible oxidation. The literature does not provide experimental verification for the surface ratio of $O(s)/H(s)$ and local nickel oxidation. Thus, this statement is a hypothesis and needs to be investigated further.

However, it is possible to see that, in the inlet region of the substrate, this ratio has a maximum with a steady decrease towards the end of the substrate. Due to high reforming rates at the substrate inlet, the highest surface occupations were simulated to occur in this region. Due to the recombination of oxygen and carbon monoxide to CO_2, the amount of locally-adsorbed oxygen decreases, which leads to the trend depicted. This profile therefore identifies the inlet zone (with the applied boundary conditions) as being most at risk of nickel oxidation. Nevertheless, a detailed analysis of nickel oxidation, as well as its corresponding threshold values and ratios, needs to be carried out so as to be able to definitively assign these ratios to nickel oxidation.

The oxygen to carbon ratio (in combination with the surface steam-to-carbon ratio) can further be used as an important indicator in SOFC applications for the purpose of locating degradation sources, such as nickel re-oxidation and coking, or to identify whether coking or re-oxidation is most probable. Figure 5.8(a) shows that, on average, approx. 70 times more elementary oxygen atoms $O(s)$ are adsorbed at the catalyst than elementary carbon. This indicates that adsorbed oxygen plays a central role in internal reforming. As stated above in the context of the surface steam-to-carbon ratio, values below these threshold values will lead to coking of the anode. Oxygen outweighs carbon at the electrolyte, whereas lower ratios were calculated to occur on

the anode surface. This identifies zones where either coking or re-oxidation are most likely to occur first.

(a) Surface $O(s)/C(s)$ ratio

(b) Surface $C(s)/(1-Ni(s))$ ratio
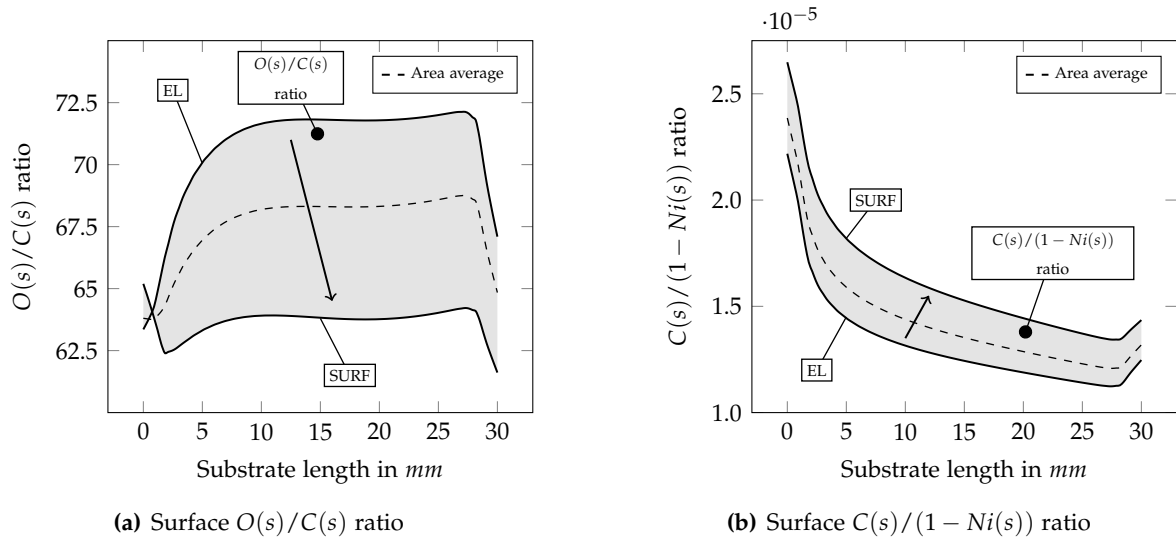
Figure 5.8.: $O(s)/C(s)$ and $C(s)/(1-Ni(s))$ surface ratios for S/C 0.447 at 800 °C along the channel length [108]

A ratio that indicates the amount of elementary carbon compared to the total number of adsorbed species is shown in Figure 5.8(b). A steady decrease was calculated with increasing substrate length. The maximum carbon ratio amounts to 2.5×10^{-5}. The highest surface coverages occurred on the anode surface, as mentioned above. This profile identifies the inlet region as zone with the highest risk of coking, since the lowest surface steam-to-carbon ratios and the highest reforming reaction rates occur here.

The introduction of these surface-specific ratios constitutes a novel method that can be used to identify the coking or nickel re-oxidation potential of SOFC anodes during internal reforming, using a detailed heterogeneous reaction mechanism. Both the profiles and their magnitudes can be used to assign different degradation sources to regions within the anode substrate. In the case shown in Figures 5.7 and 5.8, the local threshold values for carbon-free operation using a carbon-containing fuel mixture were: $(H_2O(s)/C(s))$ in the range of 6 to 10, $O(s)/H(s)$ in the range of 3×10^{-3} to 6×10^{-3}, $O(s)/C(s)$ in the range of 60 to 75 and $C(s)/(1-Ni(s))$ from 1×10^{-5} to 2.5×10^{-5}. In the main reforming zone (the first $5\,mm$ of the substrate), peak coverages occur, which can cause severe cell damage. These ratios can be calculated for different SOFC operation modes to identify critical operating conditions, and can thus be used to develop highly optimized cell designs. Furthermore, safe cell and stack operations can be established by inhibiting coking or re-oxidation.

In order to highlight the capabilities of the spatially-resolved numerical model, contour plots of the previously mentioned surface-specific coverage ratios are depicted in Figure 5.9. Here, the spatial distribution of the relationships for the gas mixture S/C 0.3 of the transient simulation, evaluated at steady state, can be seen. In this visualization, red to blue colours represent high to low values, respectively. The specific $H_2O(s)/C(s)$ ratio is plotted in the top part of this

figure. It can be seen that the highest values occur at the top corner of the substrate. With increasing substrate length and thickness, the ratio decreases. All oxygenated species ratios ($H_2O(s)/C(s)$, $O(s)/H(s)$ and $O(s)/C(s)$)) demonstrate this behaviour. Maxima of all depicted ratios within this figure can be seen to occur within the first five millimetres of the substrate.
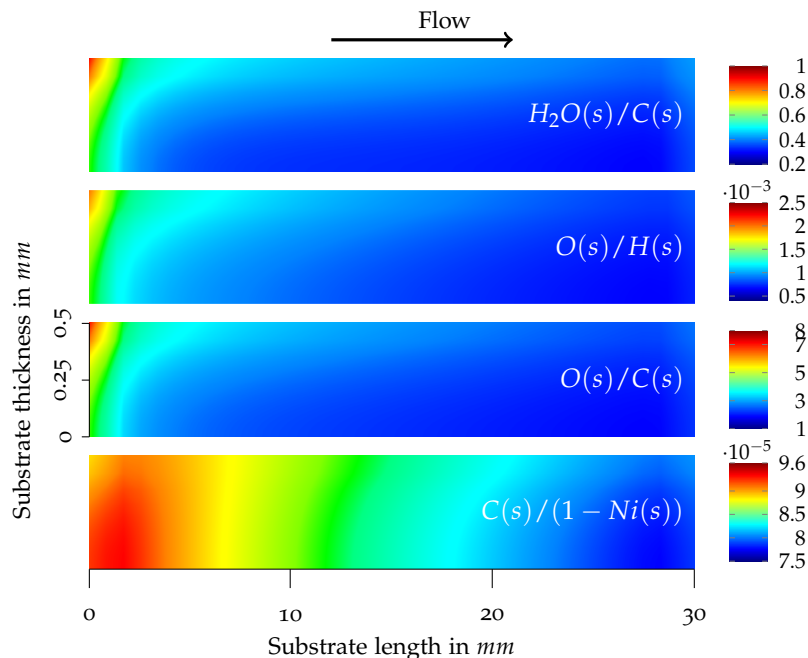
Figure 5.9.: Contours of surface coverage ratios for S/C 0.3 at 800 °C at the porous substrate [108]

For the $C(s)/(1-Ni(s))$ ratio, the highest coverages of elementary carbon occur at the substrate-electrolyte interface at the prevalent gas phase S/C ratio of 0.3. This finding is another original contribution provided by this thesis, and, therefore, showcases the power of numerical simulation. This finding indicates that it highly important to investigate every operating point in order to reveal possible degradation sources. Carbon formation does not only occur on the substrate surface, but also within the porosity of the catalytically-active electrode. With increasing substrate length, a steady decrease in the amount of this ratio can be seen.

5.3.4. Relative Surface Ratios for the Entire S/C Range

As a conclusion, a comparison of all previously defined surface-specific ratios for the entire global steam-to-carbon range is shown in Figures 5.10 and 5.11. The results shown in these figures are related to the outcomes of the case for S/C 0.447 (see Table 5.1) in Figures 5.7 and 5.8, which was defined as the carbon-free boundary reference. Thus, Figures 5.10 and 5.11 contain information about the deviation of surface-specific relations in comparison to this reference.

At this point it is worth repeating that the carbon precursor mass flow of the fuel feed stream was kept constant for all cases. A variation of the steam-to-carbon ratio was induced by

changing the molar methane amounts. This means that S/C 0.3 represents a high CH_4/CO ratio whereas a fuel feed with a S/C ratio of 0.83 denotes a methane-free reformate composition. The boundary conditions can be reviewed in Section 5.2.2, and the diesel reformate compositions are provided in Table 5.1.

(a) Specific surface $H_2O(s)/C(s)$ ratios

(b) Specific surface $O(s)/H(s)$ ratios
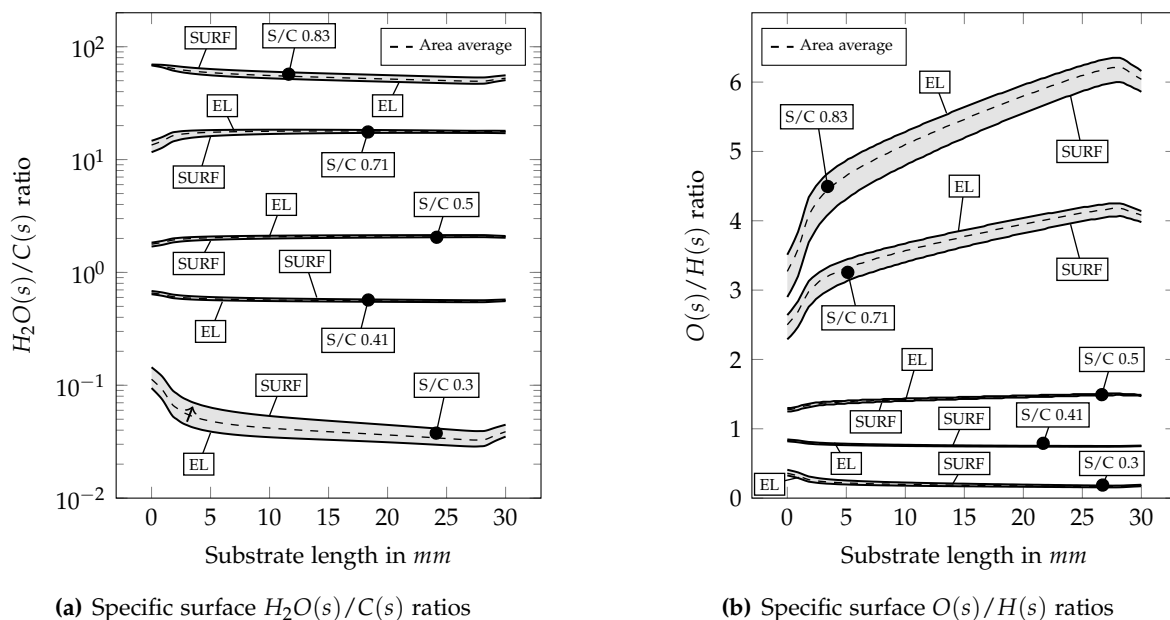
Figure 5.10.: Specific $H_2O(s)/C(s)$ and $O(s)/H(s)$ surface ratios for gas phase S/C 0.3 ÷ 0.83 (related to S/C 0.447) [108]

The local $H_2O(s)/C(s)$ coverage ratio comparison in Figure 5.10(a) shows that with a slight increase of the global S/C ratio (e.g. from S/C 0.3 to 0.41) the overall $H_2O(s)/C(s)$ coverage ratio rises tremendously, by one order of magnitude. A further increment of the S/C ratio up to 0.83 shows an increase by a factor of approximately 80. This shows the tremendous impact of gas phase S/C variation on the behaviour of surface species. The reference case was set to be S/C 0.447. Thus, ratios below unity can occur. The absolute overall coverages can be seen in Figures 5.2 and 5.3. The maximum and minimum values are again marked with either EL or SURF to indicate the spatial distribution.

Figures 5.10(b) and 5.11(a) show a similar dependence on the global S/C ratio variation for $O(s)/H(s)$ and $O(s)/C(s)$, respectively. An increase of the gas phase S/C ratio led to a rise in the appropriate surface-specific relation. The variation of $O(s)/H(s)$ is less strongly pronounced. An increment of the S/C ratio causes a rise of surface-specific relations by 6.5 times at most. This ratio would have to increase by several orders of magnitude for there to be the potential for nickel re-oxidation. Carbon coverages show a strong inverse dependence on gas phase S/C ratios (cf. Figure 5.3); consequently, there is a significant increase in the $O(s)/C(s)$ ratio of several orders of magnitude.

The inverse behaviour of adsorbed carbon and global S/C ratio can be attributed to the rise of water vapour availability for the reforming process. If the amount of adsorbed water vapour is sufficient to recombine with high amounts of adsorbed elementary carbon, $C(s)$ decreases.

(a) Specific surface $O(s)/C(s)$ ratios **(b)** Specific surface $C(s)/(1-Ni(s))$ ratios
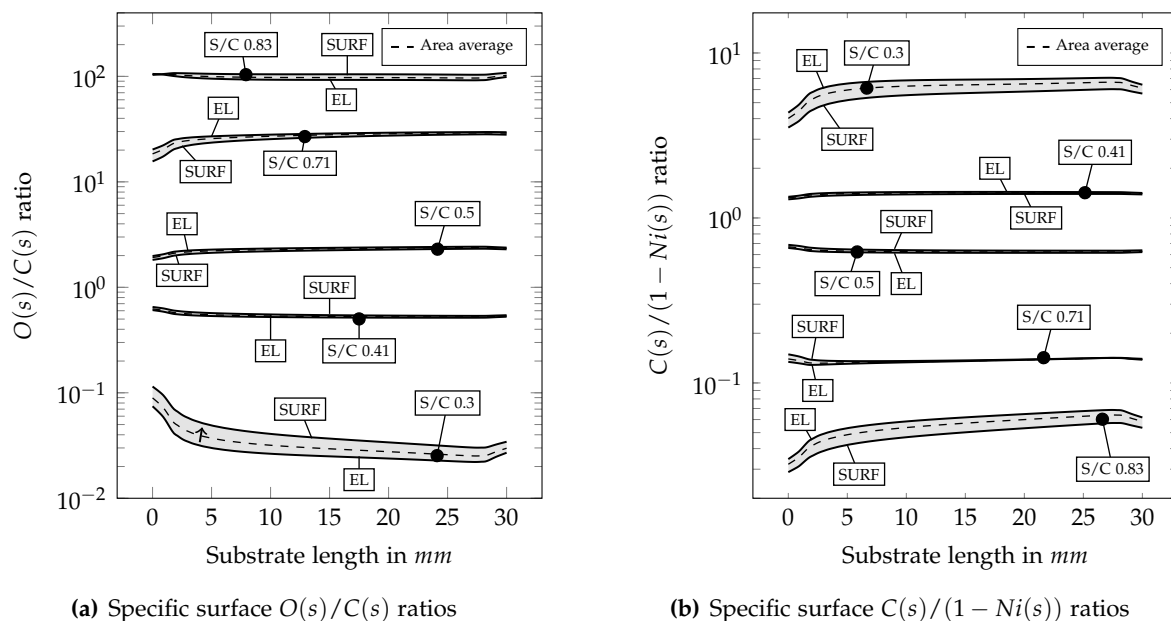
Figure 5.11.: Specific $O(s)/C(s)$ and $C(s)/(1-Ni(s))$ surface ratios for gas phase S/C $0.3 \div 0.83$ (related to S/C 0.447) [108]

Otherwise, the inverse behaviour can be noted, thus leading to low coverages of permanently adsorbed carbon for gas phase S/C ratios above 0.447. Figure 5.11(b) depicts the absolute coverages of carbon compared to all of the active sites. An increase from S/C 0.3 to 0.83 results in a decrease of absolute carbon coverages of about two orders of magnitude. Again, these elementary carbon coverages are precursors to the formation of graphite or carbon nanofibers. Reaction kinetics for their build-up and depletion need to be applied in order to numerically describe the coking of the anode, as can be seen in the experiments.

5.4. Summary of This Chapter[4]

This chapter investigated the impact of the internal reforming of different fuel mixture compositions on the catalytically-active sites within a porous nickel-based anode substrate. A detailed heterogeneous reaction mechanism was used to describe the gas-surface interactions that occur, and to evaluate the spatial distributions of adsorbed species. This made it possible to provide a significantly more detailed analysis of the local and time-dependent processes that occur.

The highest surface coverages that occur during the internal reforming of such gas mixtures were found to be caused by adsorbed carbon monoxide and hydrogen. Oxygenated species were found to cause the second highest site occupations, but their surface coverages are lower by two to three orders of magnitude. Carbonaceous species are the third highest, while adsorbed hydrocarbons occupy the least amount of anode substrate surface. Again, there are several orders of magnitude between these species coverages. It was further shown that the highest

---

[4]Segments of this section were published in the *Journal of The Electrochemical Society* under the title "Numerical SOFC Anode Catalyst Occupation Study: Internal Reforming of Carbonaceous Fuel Mixtures" [108].

gradients of all adsorbed species occur within the first five to ten millimetres of the anodic substrate. This indicates that the highest conversion rates are prevalent in this region. Thus, the inlet is especially susceptible to cell degradation caused by carbon deposition or nickel re-oxidation, depending on the gas phase boundary conditions.

Furthermore, surface related ratios, such as a surface steam-to-carbon ratio ($H_2O(s)/C(s)$), a surface oxygen-to-carbon ratio $O(s)/C(s)$, a surface oxygen-to-hydrogen $O(s)/H(s)$ ratio or the ratio of surface carbon to the total amount of adsorbed species ($C(s)/(1 - Ni(s))$) were introduced. By means of these ratios, it is possible to analyse potential sources of degradation. High amounts of adsorbed water vapour or oxygen at the inlet region indicate, on the one hand, that high reforming rates are prevalent, but also that there is the potential for the re-oxidation of nickel in this area. If the amount of adsorbed oxygen exceeds the amount of adsorbed hydrogen, nickel re-oxidation can occur. The majority of boundary conditions and gas mixtures do not provoke re-oxidation, but the method presented within this chapter can be used to analyse the coking propensity of nickel-based anodes, which will be done in the following chapter.

By means of the $C(s)/(1 - Ni(s))$ ratio, it is possible to analyse carbon formations. It is important to note that the simulated elementary carbon occupations are only precursors of carbon (graphite or carbon nanofibers) that form during real coking experiments. A threshold gas phase S/C ratio of 0.447 was determined, based on thermodynamic equilibrium calculations for the fuel mixture, above which the formation of both graphite and carbon nanofibers was inhibited. This detailed analysis showed that the reforming reactions are near equilibrium (deviations of 2% at most). The equilibrium calculations could thus be used as limits for detailed CFD simulations. Fuel mixtures with a gas phase S/C ratio below the threshold of 0.447 do cause the coking of the anode. The corresponding carbon surface coverages therefore delineate values where coking will occur. These values were calculated and spatially-depicted for a gas phase S/C of 0.3.

In conclusion, the ratios introduced elsewhere in this thesis were compared to the entire boundary condition matrix. Variation of the gas phase CH_4/CO ratio (which correlates to a change in S/C ratio) was found to have a great influence on the surface site coverage and on the specific relationships. Despite a constant carbon precursor mass flow (either methane or carbon monoxide), the absolute and relative coverages calculated differed significantly. The influence of the corresponding carbon precursor can clearly be seen in Figures 5.3. High amounts of methane (S/C 0.3) resulted in the highest carbon coverages, leading to the lowest carbon-related ratios. High amounts of carbon monoxide in the fuel feed, on the other hand (S/C 0.83), resulted in the lowest elementary carbon surface occupations. This was accompanied by the highest coverages of oxygenated and hydrogenated species. This dependency is reflected by the variation of the specific surface ratios change of several orders of magnitude. A method for identifying nickel oxidation was also presented within this chapter, which will be considered in more detail in Chapter 6. The simulation results of this chapter will further be used as base cases for carbon removal simulations with different removal strategies in the next chapter.

6

Effective Carbon Removal Strategies

This chapter presents four different strategies for the removal of elementary carbon deposited within the porous anodic structure of a single fuel cell. The strategies are based on the reverse reaction pathway of the main carbon formation reactions, as presented and discussed in earlier chapters. Gas mixtures are introduced to the fuel cell's anode flow channel to reduce the carbon depositions at OCV. Furthermore, a promising electrochemical method is presented. A removal strategy is evaluated at the catalytic active sites inside the porous anode structure. Therefore, surface environments that oxidise or reduce the catalyst indicate the effectiveness and suitability of a particular removal strategy.

When carbon formation occurs, the lifetime of a cell is critically reduced. In order to achieve reasonable cell, stack, and system lifetimes, it is of utmost importance to use effective and protective carbon removal strategies to restore initial cell performance. Thus, it is important to find and investigate strategies and methods that quickly and effectively remove deposited carbon and preserve the cell's performance.

One method for removing these deposits is to introduce a gaseous reducing or oxidizing agent to the anodic flow channel of a fuel cell. There are several gaseous agents and mixtures that appear to be suitable for this purpose. Kirtley et al. [113] proposed carbon removal methods based on the oxidation of carbon deposits and the reverse Boudouard reaction. They employed in-situ vibrational Raman spectroscopy to investigate the carbon removal rates of water vapour, carbon dioxide, and oxygen. In their study, water vapour showed the highest carbon removal rates, followed by oxygen and carbon dioxide. They explicitly mentioned the fact that all of these strategies oxidize the nickel catalyst, but O_2 acted most aggressively, by drastically decreasing the open circuit voltage OCV.

Nickel re-oxidation is of particular interest when oxygen is used as the removal agent for carbon deposits. Nickel easily forms NiO in the presence of an oxidizing agent at elevated temperatures. This results in a microstructural change (accompanied by a volumetric change), inducing cracks in the electrolyte, and leading to the mechanical destruction of the cell [114]. Several RedOx cycles show the deformation of SOFC single cells and stack cassettes on a macroscopic level [109]. Significant changes in the microstructural morphology were observed

by Brus et al. [115] after fuel starvation, leading to RedOx cycles of the anode. They found that tortuosity increased and a substantial loss in the connectivity of nickel particles was evident. This was attributed to the expansion and contraction of nickel particles during re-oxidation. Furthermore, oxidized nickel particles were found in the vicinity of the anode-electrolyte interface.

Snoeck, Froment, and Fowles [98] used CO_2, H_2, and steam to remove carbon deposits from steam reforming catalysts (not complete fuel cells) at $550\,°C$. They showed that the carbon removal rates differed between the three strategies, and that they depended on the carbon formation pathway (either through methane dissociation or Boudouard reaction).

Takenaka et al. [116] showed that CO_2 is a suitable agent for the removal of carbon from these catalysts. Methane decomposition was tested and, subsequently, the carbon deposits were removed with CO_2 at $650\,°C$. They showed that the deposited carbon nanofibers had a nickel particle at each end, which is indicative of nickel dusting. The fibres were not completely removed after a single carbon removal cycle, but had decreased in length and size. They found that 95% of the catalytic reforming activity can be restored by means of their carbon removal strategy. It was thus shown that CO_2 is a suitable removal agent for carbon deposits on nickel catalysts. Nonetheless, it is important to note that a loss of catalytic active area was proven and has to be accounted for when adapting this method to complete SOFC cells. Further, the electrochemical performance of SOFC cells strongly depends on the amount of vacant three-phase boundaries. Nickel acts as a catalyst for both the reforming reactions and the electrochemical reactions. High catalytic performance does not ensure high electro-catalytic activity. When nickel particles are detached from the YSZ-lattice, the chemical reforming performance is still existent, but the electrochemical performance is drastically decreased due to the loss of active TPB sites.

Subotić et al. [111, 112] showed that both dry and humidified hydrogen feeds can be used to effectively remove carbon deposits from the fuel electrode. In their studies, carbon depositions that occurred during the operation of a modified synthetic diesel reformate were identified by means of electrochemical impedance spectroscopy, gas analysis, and microstructural analysis. These deposits were subsequently gasified with humidified and dry hydrogen. Cell performance in low and medium current densities was restored using humidified hydrogen. Dry hydrogen had to be fed to the cell after $24\,h$ of exposure to humidified hydrogen to restore cell performance in the high current density region. Partial nickel oxidation occurred during the carbon deposition process. The application of humidified hydrogen removed the deposited carbon from the pores and nickel sites, but did not reduce the oxidized nickel particles. Therefore, to completely restore catalytic activity, dry hydrogen had to be fed to re-reduce the partially oxidized nickel. After all of the active three-phase boundaries had been restored, high performance was once again achieved.

A literature review has shown that there are removal and regeneration strategies for carbon deposits on nickel based catalysts. Nevertheless, their application and suitability for SOFCs

has to be verified. One very important issue that has to be addressed is the fact that not only do carbon deposits need to be successfully removed from the anode surface, but the cell performance also needs to be restored. In this chapter, the SOFC catalyst surface composition during carbon removal is investigated in detail. Thus, the local and temporal amounts and distribution of adsorbed species at the catalytically active sites during the removal process are scrutinized. The strategies are based on:

1. the reverse carbon monoxide reduction reaction and the reverse methane dissociation reaction,
2. the regeneration of carbon through the reverse Boudouard reaction,
3. the reverse Boudouard reaction and the carbon oxidation reaction due to oxygen in the fuel, and
4. cell polarization to accelerate the hydrogen based strategy.

Research has revealed that the effluent gas composition measurement is not a sufficient method to determine the completeness of the carbon removal process. The outlet gas composition reaches a stationary state after several seconds. The detailed numerical analysis and experimental investigations at the IWT test rig showed that the removal process takes at least 10 times longer than it is indicated by the measurable off-gas compositions.

6.1. Basis of the Carbon Removal Simulations[1]

The simulations within this chapter are based on the investigations and findings of Chapter 5. Thus, the steady state surface site coverage profiles that formed during the internal reforming of synthetic diesel reformate 'S/C 0.3' are used as the basis for the experiments described in this chapter . This case contains a porous anode exposed to crucial carbon deposits. The ramifications of the four different gaseous carbon regeneration strategies are analysed by means of the detailed heterogeneous reaction mechanism, given in [74] and presented in Chapter 3. The simulations were conducted at a typical SOFC operating temperature of $800\,^{\circ}C$ and at intermediate temperature levels down to $400\,^{\circ}C$ with an increment of $100\,K$.

As mentioned, four main strategies were investigated in terms of their carbon removal effectiveness: (1) mixtures of hydrogen and steam; (2) carbon dioxide; (3) carbon dioxide and oxygen; and (4) cell under $40\,mA\,cm^{-2}$ load during operation on dry hydrogen. This chapter will provide detailed information about the surface site occupation during the different regeneration strategies and will also identify critical operating times in order to regain optimum catalyst performance. Strategies (1 - 3) were applied at open circuit condition, whereas the cell was put under load operation for strategy (4).

---

[1]Segments of this section were published in the *International Journal of Hydrogen Energy* under the title "CFD-Simulation of Effective Carbon Gasification Strategies From High Temperature SOFC Ni-YSZ Cermet Anodes" [117].

As was shown by Subotić et al. [111], strategy (1) can be used to effectively remove carbon deposits and restore cell performance, by supplying the anode with humidified hydrogen. Furthermore, carbon dioxide can be used as a carbon removal agent, as shown by [98, 106, 113, 116]. Subotić et al. [106] showed experimentally that although carbon monoxide was measured as a gaseous product of the reverse Boudouard reaction during the regeneration process, cell performance had decreased once the removal process with CO_2 was finished. This indicates that carbon can be gasified by CO_2, but that it has detrimental effects on the cell performance. Permanent performance degradation was determined over the entire load range and in regions of high current density in particular.

The thoroughly validated CFD model created in Chapter 3 was used for the simulations. The model makes it possible to simulate the amount, spatial and temporal distribution of surface adsorbed species. These are $Ni(s)$, $H_2O(s)$, $H(s)$, $OH(s)$, $O(s)$, $CO(s)$, $CO_2(s)$, $CH_4(s)$, $CH_3(s)$, $CH_2(s)$, $CH(s)$, $C(s)$, and $HCO(s)$. Herein, (s) denotes the adsorbed state of a constituent. As was shown in Chapter 5, $CO(s)$, $H(s)$ and $O(s)$ are the most important surface species during the internal reforming of light hydrocarbons and reformates. Thus, the main surface site occupations of these major species provide us with information about the overall chemical surface conditions. Surface coverages of $C(s)$ represent the amount of present carbon precursors that cause performance degradation. It is important to note that $C(s)$ merely denotes a precursor of carbon found in experiments, such as graphite (C(gr)) or carbon nanofibers (CNF).

6.1.1. Computational Domain and Numerical Setup

The numerical model used in this chapter was discussed and presented in Chapter 5. In order to efficiently investigate the temporal evolution of the adsorbed species during the removal process, it uses a two-dimensional simplification of the first third of an anode-supported SOFC. This first third correlates to a length of $30 \, mm$ for the anode substrate. The geometrical discretization, dimensions, and supplementary information are shown in Figure 5.1. The mesh characteristics remain unchanged, and are described in Section 5.2.1. The chemical reforming process is catalysed by the nickel incorporated within the porous anode structure. Thus, the chemical reactions were set to occur within this porosity, meaning that the spatial and temporal allocation of all involved surface species is possible.

Carbon removal is a time-dependent process. Thus, transient simulations were carried out using a double precision pressure-based coupled solver. Second-order upwind schemes were applied for the geometrical discretization. Temporal discretization was conducted by a first order upwind scheme. The remaining numerical setup options were kept the same as presented in Chapter 5. Species composition, temperature, mass flow and velocity were monitored at the anode outlet. The simulation was determined to be convergent when the time-dependent outlet monitor data remained constant, and when the residuals of the continuity and momentum equation fell below 10^{-4}, and those of all species and the energy equation fell below 10^{-7}.

6.1.2. Carbon Formation Boundary Case for Regeneration Simulations

These carbon removal simulations are based on the spatial steady-state results of the surface occupation during internal reforming of carbonaceous fuel mixtures, as described in Chapter 5. The synthetic reformate with a S/C ratio of 0.3 (see Table 5.1 in Section 5.2.2) led to the highest $C(s)$ site coverages, and thus provokes the highest carbon formation rates. It was therefore chosen as the basis for the removal simulations in this chapter.

Table 6.1.: Carbon formation base case 'S/C 0.3'

Species	Value	Unit
H_2	0.154	$mol\,mol^{-1}$
CO_2	0.098	$mol\,mol^{-1}$
H_2O	0.113	$mol\,mol^{-1}$
CO	0.137	$mol\,mol^{-1}$
CH_4	0.24	$mol\,mol^{-1}$
N_2	0.258	$mol\,mol^{-1}$
T	800	$°C$
$\dot{V}$	2.4	SLPM
S/C	0.3	
CH_4/CO	1.75	

Chapter 5 showed that, apart from the S/C ratio, the methane-to-carbon monoxide (CH_4/CO) ratio of diesel reformates has a significant influence on the carbon mono layer build-up. High amounts of methane, in combination with low amounts of steam (high CH_4/CO ratio and low S/C ratio), induce the critical operating condition of the fuel cell's anode. Severe carbon deposits can form, which cause performance degradation. This was shown experimentally by Subotić et al. [106, 111, 112] in their studies. Furthermore, the adsorbed carbon monoxide plays a central role during internal reforming, regardless of whether it is incorporated in the fuel feed or not. Chapters 5 and 6 discussed the fact that $CO(s)$ is the main intermediate species during the internal reforming of both pure (methane/steam) fuels and reformates. The detailed analysis in these chapters revealed that $CO(s)$ occupies high amounts of the catalyst surface during internal reforming. The elementary carbon $C(s)$ and carbon monoxide $CO(s)$ coverages were determined to cause severe carbon formation rates (graphite and/or carbon nanofibers).

The fuel mixture in Table 6.1 (S/C 0.3) at an operating temperature of $800°C$ and at OCV was used to create the initial species surface coverages that occur during internal reforming of a synthetic diesel reformate. The previous chapter demonstrated that carbon formation under reformate operation occurs when the CH_4/CO ratio used is above 0.845 (all mixture constituents in Tables 6.1 and 5.1 remain constant except methane and supplementary nitrogen). Thus, a fuel mixture with a CH_4/CO ratio of 1.75 (S/C 0.3) was chosen to induce severe carbon formations. The corresponding elementary carbon surface coverages $C(s)$ thus represent an anode exposed to severe carbon deposits. These coverages were then used for all further regeneration simulations.

(a) Major adsorbed species in the porous substrate   **(b)** Minor adsorbed species in the porous substrate
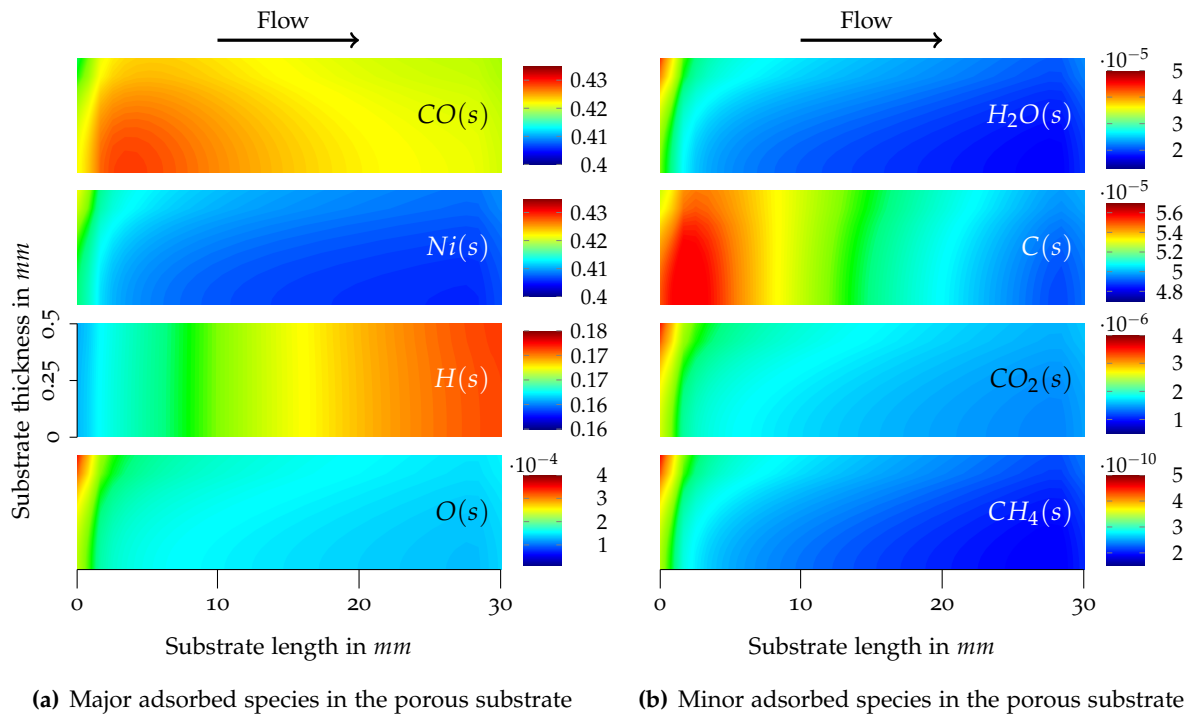
Figure 6.1.: Contours of local surface species coverages after internal reforming of the base case (S/C 0.3 at 800 °C) at steady state [117]

Figure 6.1 shows the surface site coverage contours and Figure 6.2 shows gaseous species of the fuel mixture (dry base) of the base case within the porosity of the anodic substrate. In Figures 6.1(a) and 6.1(b), only the substrate is magnified. The representation of the anode substrate is not to scale. Its vertical and horizontal dimensions were distorted in order to make it easier to interpret the results. The flow channel is neglected, since the focus is set on the surface occupation of the catalyst. The flow direction in the adjacent flow channel is indicated by the arrow at the top of the figure. It can clearly be seen that the main reforming zone is located within the first 5 to 10 mm of the substrate, since high changes and gradients of all adsorbed species occur there.

The highest occupations occurred while using adsorbed carbon monoxide $CO(s)$ (cf. Figure 6.1(a)). Unoccupied nickel sites are between 0.4 to 0.435. Hydrogen $H(s)$ and oxygen $O(s)$ complete the list of major adsorbed species. Water vapour $H_2O(s)$ coverages and elementary carbon $C(s)$ coverages are one order of magnitude below $O(s)$, at approximately 2 to 6×10^{-5} (cf. Figure 6.1(b)).

It is possible to see that the highest carbon coverages occur within the first 10 mm of the substrate. Furthermore, it is evident that they reach their maximum at the bottom of the substrate, which corresponds to the anode-electrolyte interface. This is highlighted here because most scientific studies propose that carbon forms mainly at the anode surface, which means that this is an original contribution by this thesis. Carbon dioxide coverages $CO_2(s)$ and methane coverages $CH_4(s)$ are several orders of magnitude below those of $CO(s)$, $H(s)$, and $O(s)$. These are the steady-state spatially fixed coverages within the fuel electrode for this fuel supply.
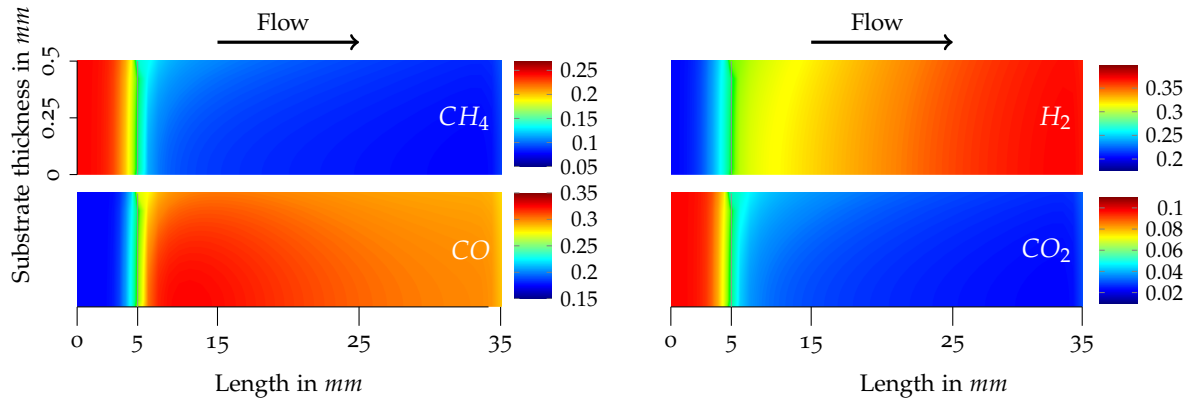
(a) Mol fractions of gaseous reforming educts in porous substrate, d.b.

(b) Mol fractions of gaseous reforming products in porous substrate, d.b.

Figure 6.2.: Contours of gaseous species (d.b.) in the porous anode after internal reforming of the base case (S/C 0.3 at 800 °C) at steady state [117]

In Figures 6.2(a) and 6.2(b), the trends of the fuel mixture (d.b.) during internal reforming in the porous substrate and the 5 mm inlet region in front of the substrate (see Figure 5.1 for a schematic view of this inlet region) are shown. This inlet region was added to ensure that a laminar flow profile developed before the substrate, as occurs in the real 3D geometry (see Chapter 3). The beginning of the substrate is indicated with a vertical line at 5 mm. Methane is reformed to hydrogen, carbon monoxide, and carbon dioxide. High conversion rates lead to high species gradients in the substrate. The methane conversion rate of our CFD model was 82.3 %. Experimentally-determined conversion rates of 84.3 % were measured at OCV and 800 °C at our experimental test setup (see [111] and [42]). The model slightly underestimates the methane conversion by about 2 %. Nevertheless, this reflects the high correlation between the simulation model and the experiments. The base case shown in Figures 6.1 and 6.2 makes it easier to visualize the surface site occupation condition as well as the gaseous species trend in the porous structure during the internal reforming of a fuel mixture under carbon formation condition.

6.1.3. Carbon Removal Strategies

As stated, four different carbon removal strategies were investigated. Based on the main carbon formation reactions (3.3) - (3.7), regeneration strategies adapted from their reverse reaction paths were formulated.

The first approach was to combine the reverse carbon monoxide reduction reaction and the reverse methane dissociation reaction. This was done by introducing a humidified hydrogen/nitrogen mixture at the inlet, as was applied in [111, 112]. Moreover, water vapour dependency was investigated by varying the amount of water added to the mixture. Therefore, two different mixtures, **R1** and **R2** (see Table 6.2), were used. These hydrogen-based mixtures were applied at OCV.

Table 6.2.: Carbon removal mixtures and boundary conditions

Species	Value	Unit	Species	Value	Unit
R1 @ OCV, w.b.			**R2** @ OCV, w.b.		
H_2	0.45	$mol\,mol^{-1}$	H_2	0.45	$mol\,mol^{-1}$
H_2O	0.11	$mol\,mol^{-1}$	H_2O	0.20	$mol\,mol^{-1}$
$\dot{V}$	2.4	SLPM	$\dot{V}$	2.4	SLPM
B @ OCV, d.b.			**E** (load case, d.b.)		
CO_2	0.25	$mol\,mol^{-1}$	i	40	$mA\,cm^{-2}$
$\dot{V}$	2.4	SLPM	H_2	0.45	$mol\,mol^{-1}$
			$\dot{V}$	2.4	SLPM
R3 @ OCV, d.b.			**R3H** @ OCV, w.b.		
CO_2	0.189	$mol\,mol^{-1}$	CO_2	0.189	$mol\,mol^{-1}$
O_2	0.02	$mol\,mol^{-1}$	O_2	0.02	$mol\,mol^{-1}$
			H_2O	0.11	$mol\,mol^{-1}$
R4 @ OCV, d.b.			**R5** @ OCV, d.b.		
CO_2	0.0945	$mol\,mol^{-1}$	CO_2	0.04725	$mol\,mol^{-1}$
O_2	0.01	$mol\,mol^{-1}$	O_2	0.005	$mol\,mol^{-1}$
$\dot{V}$	0.4	SLPM	$\dot{V}$	0.4	SLPM
	Temperature	$400-800$	$°C$		
	Increment	100	K		
	N_2	supp.	$mol\,mol^{-1}$		

The second approach was based on the reverse Boudouard reaction, by supplying the fuel channel with a mixture of CO_2 and N_2, again at OCV. This approach is often used and postulated as an effective method for removing carbon deposits from porous SOFC anodes, as in [98, 113, 116] and in [106]. The method is indicated as **B**.

As a third method, a combination of the reverse Boudouard reaction and the carbon oxidation reaction was investigated with the cell at open circuit condition. Three mixtures (**R3** - **R5**) were used to examine the impact of carbon dioxide and oxygen as a carbon removal agent, as shown in Table 6.2. Furthermore, steam was added to mixture **R3** in order to examine the effect of steam on the sensitivity of the process (**R3H**).

Finally, the cell was operated under load, inducing a specific oxygen flux from the cathode through the electrolyte to the anode. This oxygen flux was set to correspond to a current density of $40\,mA\,cm^{-2}$. Dry hydrogen and nitrogen were fed to the flow channel, to act as fuel and reducing agent, respectively. This method makes it possible to directly interact with carbonaceous species at the incorporated nickel sites, and is indicated as **E** in Table 6.2.

The base operating temperature was set to $800\,°C$. Furthermore, all removal strategies were scrutinized in a temperature range between 400 and $800°C$ with an increment of $100\,K$. All walls were set to be isothermal, as it is the case in the electrically-heated high temperature furnace at the test rig at the IWT. This made it possible to analyse the temperature dependency of the reactions and processes that occur during carbon removal.

The mass flow rates of the removal strategies were based on volumetric flow rates of $2.4\,SLPM$

for the hydrogen-based methods (**R1** and **R2**), the reverse Boudouard-method (**B**), and the electrochemical method (**E**). This was done in order to represent the flow conditions of real SOFC applications. Kirtley et al. [113] showed that gaseous oxygen can lead to rapid oxidation of the Ni-YSZ cermet anode. In order to avoid this fast oxidation process, the mass flow rates of **R3** - **R5** were lowered based on a volumetric flow rate of $0.4\,SLPM$. All boundary data for these carbon regeneration simulations is summarized in Table 6.2.

6.2. Application of Carbon Removal Methods[2]

As described, a synthetic diesel reformate with S/C 0.3 (mixture composition see Table 6.1) was used as a base case for all subsequent carbon removal simulations. The fluid domain and porous anode substrate domain were rendered inert with nitrogen (according to the measurements at our test rig) prior to the application of any carbon removal agents. Thus, only the surface adsorbed species and their corresponding profiles, shown in Figure 6.1, remained as boundary surface coverage conditions within the porous anode structure. With suitable methods, these permanent surface adsorbed species can be regenerated to volatile gaseous products. In case of the total removal of all surface species, the coverage of $Ni(s)$ sums up to unity, and all other species sum up to zero. Species that can cause degradation are twofold: elementary, reactive carbonaceous species and oxygenated species. Thus, surface coverage trends within the porosity of elementary carbon $C(s)$ and carbon monoxide $CO(s)$ need to be decreased. Furthermore, adsorbed oxygen $O(s)$ can oxidise the nickel catalyst, which implies that it is necessary to monitor and control the amount of oxygen at the catalytic active sites. This thesis has found that coverages in the range of 5×10^{-10} (equal to that of $CH_4(s)$ at initial conditions) are very small and can thus be neglected. Therefore, a regeneration cycle was defined as successful when the average surface coverage of elementary carbon $C(s)$ fell below that of the initial coverage of $CH_4(s)$ (below this threshold value of 5×10^{-10}). When carbon coverages fell below this threshold value, the anodic substrate was determined to be free from the carbonaceous precursors that can cause deposits. Once this threshold was reached, the regeneration strategy was deemed to be successful, and the substrate was then able to be supplied with fuel and put back into normal SOFC operation.

6.2.1. Humidified Hydrogen/Nitrogen Mixtures R1 and R2

In this section, the results of removal method **R1** and **R2** are discussed. As described above, humidified hydrogen is fed to the computational domain through the inlet. Figure 6.3 shows the time dependent trends of the average outlet gas composition during the application of these two methods.

---

[2]Segments of this section were published in the *International Journal of Hydrogen Energy* under the title "CFD-Simulation of Effective Carbon Gasification Strategies From High Temperature SOFC Ni-YSZ Cermet Anodes" [117].

First of all, it is possible to see that within the first 15 seconds, desorption of the major adsorbed species occurs. *CO* and *CO$_2$* are the noticeable and, especially experimentally, measurable gaseous products. Weakly bound, physically adsorbed species desorb at the beginning of the process, while chemically adsorbed species are more strongly bound to the surface. Thus, the desorption of chemisorbed species takes place after all physically bound species have been desorbed. At 600 °C (cf. Figure 6.3(c)) and below, the amount of *CO* and *CO$_2$* that gasifies falls below measurable values of gas analysers. Temperatures below 600 °C were thus excluded from Figure 6.3. Increasing temperature promotes the desorption of physically bound *CO(s)*, due to increased energy levels. After 8 seconds, measurable volatile components were desorbed at all temperature levels investigated. The peak molar methane amounts after this point in time were simulated to be in the range of $2 \times 10^{-5} mol \, mol^{-1}$ and are thus not measurable. The reaction rates of reaction (3.2) for this removal strategy are low and almost non-existent.

(a) 800 °C

(b) 700 °C

(c) 600 °C
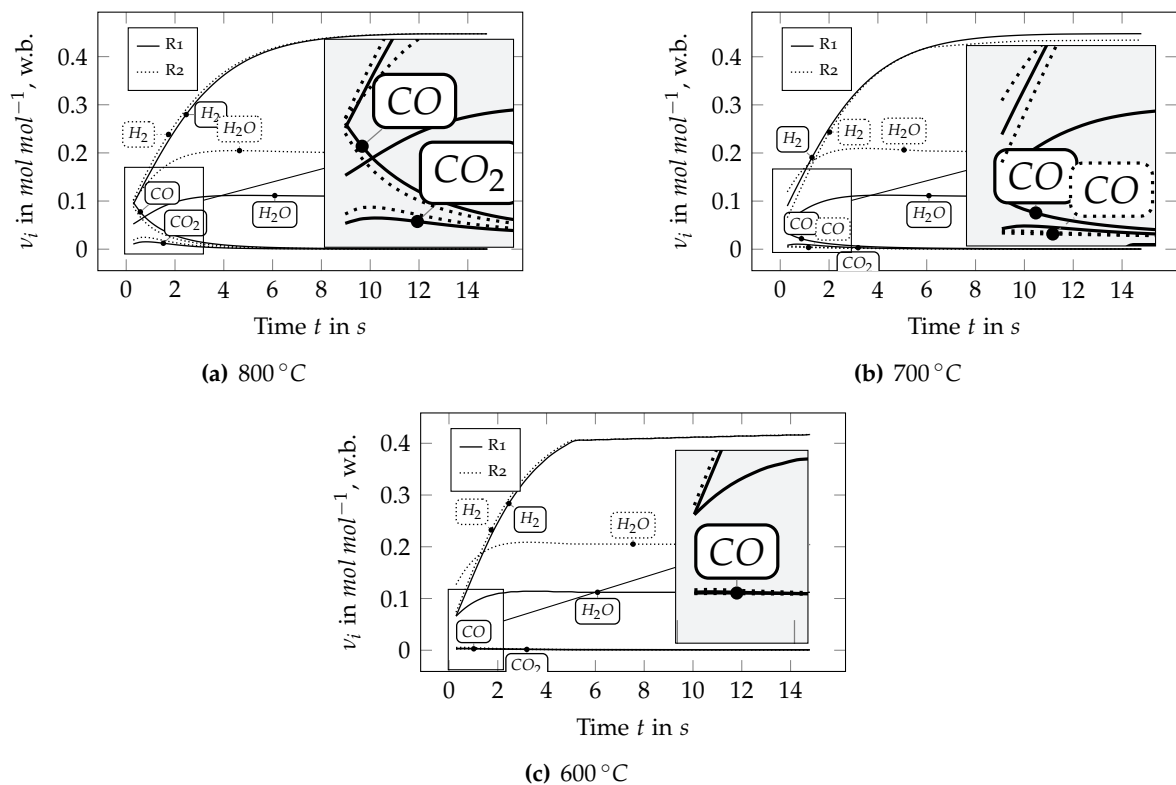
Figure 6.3.: Outlet gas composition for **R1** and **R2** [117]

There are only marginal differences between removal strategies **R1** and **R2**. A slight difference can be seen at 800 °C (Figure 6.3(a)) within the first 4 seconds: an incremental increase of the amount of water vapour in the removal agent results in the formation of more *CO$_2$* and less *CO*. This can be attributed to increased reaction rates of the water-gas shift reaction, shifting the equilibrium towards the product side, which can also be seen through the slightly increased *H$_2$* amounts compared to strategy **R1**.

Analysis of these volatile species, which can also be experimentally measured, indicate that the regeneration process is finished within this short period of time. A detailed investigation of all involved surface adsorbed species indicated that the removal process was not yet completed,

since the defined threshold value for elementary carbon $C(s)$ had not been reached. The experimental findings of Subotić et al. [106] showed that gas analysis of volatile species can be conducted during such regeneration approaches. However, electrochemical impedance spectroscopy and polarization curve measurements showed that the successful application of a regeneration approach takes much more time than is indicated by the volatiles measured with a gas analyser. The regeneration processes are diffusion-dominated, and the reaction rates between solid and gas phases are low, so that the entire regeneration process takes much longer than can be deduced from a gas analyser's measurement reading. Thus, in the next step, a detailed analysis of the occurring surface reactions was conducted and the surface site occupation was examined in detail. The results are shown in Figures 6.4, 6.5 and 6.6.

(a) R1 @ OCV   **(b) R2 @ OCV**
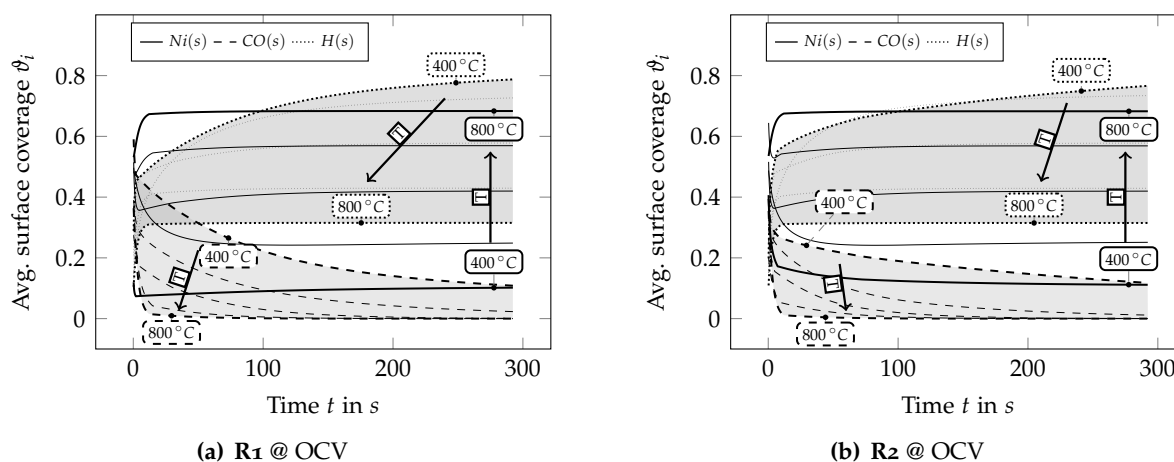
Figure 6.4.: Major adsorbed species surface coverages for strategies **R1** and **R2** [117]

The detailed heterogeneous reaction mechanism [74] (see Table 3.8) facilitates to scrutinize all surface adsorbed species during internal reforming as well as the removal process. Figure 6.4 shows the temporal profiles of the most important adsorbed species during the removal process. Figures 6.4(a) and 6.6(a) represent the temporal evolution for the strategy **R1**, whereas the profiles for R2 are depicted in 6.4(b) and 6.6(b). Every adsorbed species was allocated to a line style and a certain filling to highlight the corresponding region. The inserted arrows indicate the direction of increasing temperature. Every non-temperature-marked line corresponds to a $100\,K$ increase in temperature (starting at $400\,°C$).

As already shown in Figure 6.3(a), carbon monoxide desorbs quickly within the first 8 seconds after the application of the removal agent at $800\,°C$. The temporal evolution of adsorbed carbon monoxide $CO(s)$ underlines this in Figure 6.4(a). Lowering the temperature drastically slows this $CO(s)$ desorption process. In addition, higher amounts of hydrogen $H(s)$ adsorb with this temperature decrease. Surface coverage of $H(s)$ after $300\,s$ ranges between 0.32 at $800\,°C$ and 0.8 at $400\,°C$. The amount of vacant nickel sites $Ni(s)$ rises with a temperature increase.

The temporal profiles of adsorbed oxygen $O(s)$, hydroxyl $OH(s)$, water vapour $H_2O(s)$ and elementary carbon $C(s)$ for strategy **R1** are plotted on a logarithmic scale in Figures 6.5(a) and 6.6(a). The temporal profiles of adsorbed water vapour $H_2O(s)$ and hydroxyl radicals

$OH(s)$ for strategies **R1** are plotted on a logarithmic scale in Figure 6.5(a). With a temperature increase from 400 to 800 °C, the amount of adsorbed $H_2O(s)$ decreases from $\vartheta_{H_2O(s)} = 2 \times 10^{-3}$ by almost one order of magnitude to $\vartheta_{H_2O(s)} = 2 \times 10^{-4}$ during the entire regeneration process. Hydroxyl radicals $OH(s)$, on the other hand, increase by almost two orders of magnitude $\vartheta_{OH(s)} = 2 \times 10^{-7}$ to $\vartheta_{OH(s)} = 2 \times 10^{-5}$.

(a) R1 @ OCV **(b) R2 @ OCV**
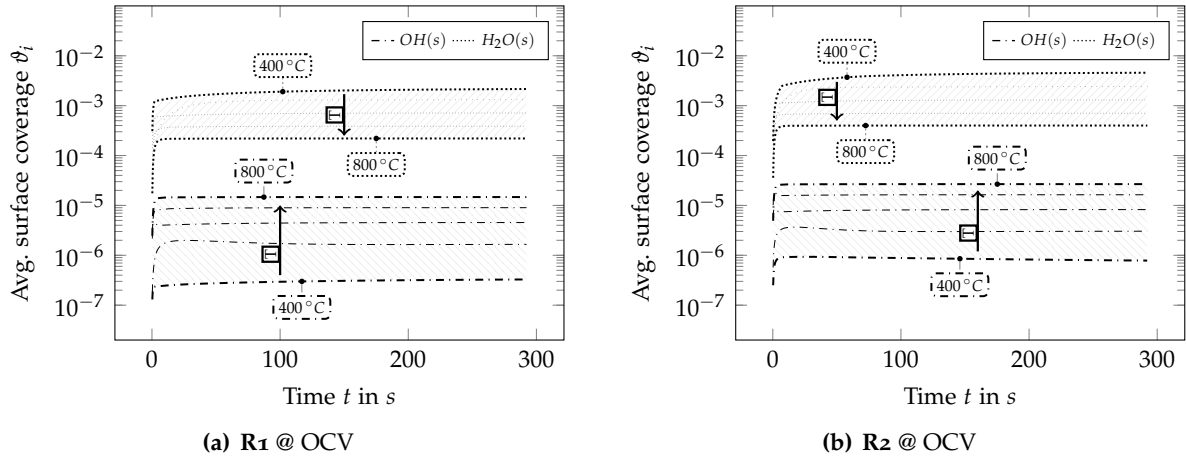
Figure 6.5.: $OH(s)$ and $H_2O(s)$ surface coverages for strategies **R1** and **R2**

For slightly elevated water vapour molar fractions in the carbon removal agent (strategy **R2**), in Figure 6.5(b) it is possible to see that all species coverages are increased by a factor of 2. This indicates the linear dependence of the surface adsorbed $H_2O(s)$ and $OH(s)$ species and the molar amount of water vapour in the gaseous carbon removal mixture. Except for this change, no differences in the time-dependent trends can be seen.

As mentioned, the threshold value of adsorbed carbon $C(s)$ was set to 5×10^{-10} to indicate that a removal strategy had been deemed successful; this is marked red in Figures 6.6(a) and 6.6(b). The corresponding time it took the carbon coverages to decrease below this threshold value will henceforth be referred to as the carbon regeneration time t_r. Figure 6.6(a) provides crucial information about the direct precursors of degradation phenomena, such as carbon formation/removal or nickel oxidation. Re-oxidation of the catalytic active nickel sites is possible when the amount of locally adsorbed oxygen $O(s)$ exceeds the amount of adsorbed hydrogen $H(s)$ (compare Figures 6.4(a) with 6.6(a) for removal strategy **R1** and Figures 6.4(b) with 6.6(b) for removal strategy **R2**). Nickel re-oxidation is thus possible when the $O(s)/H(s)$ ratio exceeds unity. For strategies **R1** and **R2**, this is not the case at any point in time during the carbon removal procedure. The carbon regeneration times increase non-linearly with a temperature decrease. At 800 °C $t_r = 103\,s$, at 700 °C $t_r = 175\,s$, at 600 °C $t_r = 300\,s$, at 500 °C $t_r > 1260\,s$, and at 400 °C $t_r > 6400\,s$.

An increment in the amount of water vapour added to the removal agent (see Figures for **R2**: 6.4(b) and 6.6(b)) shows higher temporal species coverage gradients, which accelerate the removal process. The regeneration times t_r decrease to 70, 157, 253 s, $t_r > 1260\,s$, and $t_r > 6400\,s$ at 800, 700, 600, 500, and 400 °C, respectively. The elevated amount of water vapour in the feed

stream only has a marginal effect on the amount of oxygenated and hydrogenated species at the surface (compare dashed, dash-dotted and dotted graphs in Figures 6.6(a) and 6.6(b).

(a) R1 @ OCV

(b) R2 @ OCV
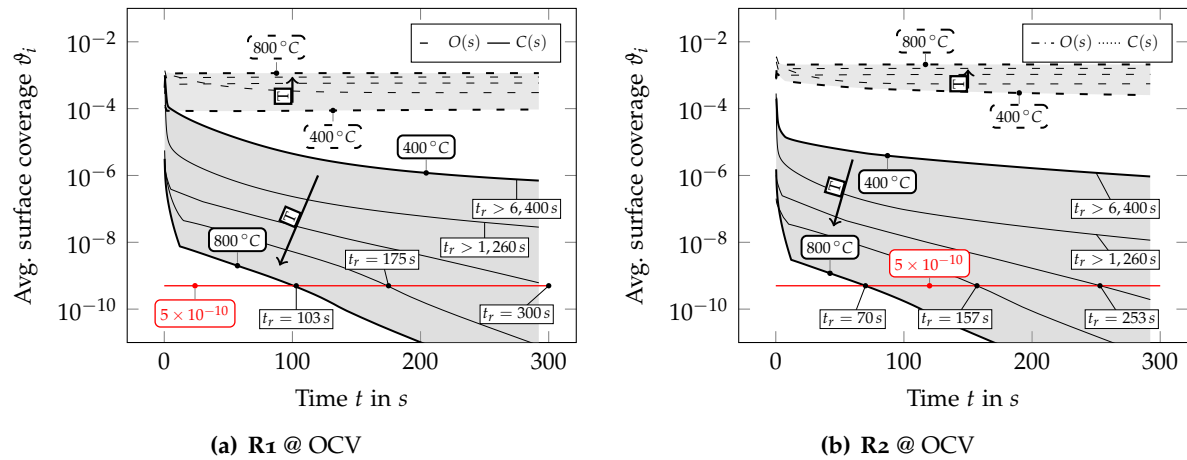
Figure 6.6.: $O(s)$ and $C(s)$ surface coverages for strategies **R1** and **R2**

The strategy **R1** was applied to a SOFC single cell in [111] at an operating temperature of $800\,°C$. The cell was operated on a synthetic diesel reformate, as seen in Table 6.1, but with a lower methane amount ($0.023\,mol\,mol^{-1}$, S/C 0.71). Figure 6.7 shows the polarization curves of the non-degraded cell, the cell after carbon deposition, and after the application of removal strategy **R1**. Carbon formation led to an increase in ohmic resistance, resulting in performance degradation in elevated current density regions. This indicates the build-up of a non-conductive layer. After performance degradation was detected, the cell was supplied with gas mixture **R1** for $24\,h$. It can be seen that, in high current density regions ($220\,mA\,cm^{-2}$), the initial performance was restored. This confirms that the deposited carbon was removed. Furthermore, the electrochemical activity of the cell was increased, which resulted in lowered activation losses in the low current density region. This can be attributed to two different effects: (1) additional cell activation aroused by the hydrogen feed; and (2) a conductivity increase caused by small amounts of carbon particles being linked with nickel, which was described in [47, 105, 112].
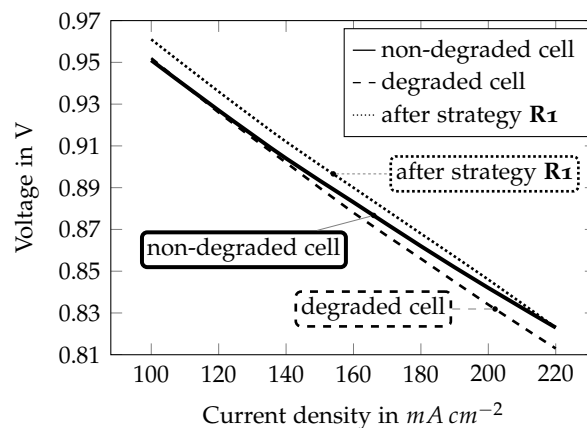
Figure 6.7.: Polarization curves: initial performance of a new cell, performance after carbon formation, and after application of strategy **R1** [111]

The numerical results of strategy **R1** were experimentally proven, since original cell performance was restored. A slightly different base case was used in the experimental study in [111], but the performance degradation of a planar SOFC single cell was detected and the application of strategy **R1** re-established the cell performance. Thus, the applicability and validity of these hydrogen-based strategies were validated, and the detailed surface site coverage analysis made it easier to understand the underlying reaction mechanisms that occur.

In summary, **R1** and **R2** are suitable high-temperature methods for carbon removal due to the fact that it is not possible for nickel re-oxidation to occur, and adsorbed carbon $C(s)$ can be removed in a controlled manner in a reasonable period of time. Temperatures below the typical operating temperatures of anode-supported SOFCs (below $800\,°C$) prolong the regeneration time and do not contribute any additional safety benefits. Thus, decreasing the temperature does not have a positive effect on this strategy. The detailed heterogeneous reaction mechanism helped identify the fact that the carbon removal process is not complete after a few seconds, as can interpreted from Figure 6.3.

The successful removal of adsorbed carbon takes at least $70\,s$ for **R2** at $800\,°C$ (cf. Figure 6.6(b)), which cannot be seen from the outlet gas composition in Figure 6.3. These outlet gas compositions can easily be measured in practical applications by a gas analyser, but can also be falsely interpreted by these short measurable desorption times, as shown in Figure 6.3. The complete desorption process lasts distinctly longer than can be measured by a gas analyser.

It was experimentally shown in Figure 6.7 and in [111, 112] that this method is suitable for practical application, and that it makes it possible to restore the cell performance after severe carbon depositions have been detected. Therefore, this method is a significant contribution to the scientific community. Nevertheless, the time scales of the experimental investigations ($24\,h$ for total carbon removal) differ greatly from the regeneration times calculated here. This can be attributed to two main facts: First, solid carbon was formed during the experiments, which blocks pores and covers the catalytically active sites. In this numerical simulation, carbon is used in its adsorbed state, which can only be treated as a precursor to solid amorphous or fibrous carbon. The numerical representation of carbon does not incorporate the decomposition of a solid material to reactive precursors and adsorbed species. It is assumed that the decomposition of solid carbon into an adsorbed state is the rate limiting step, and thus significantly prolongs the regeneration time. Secondly, a small single cell ($30 \times 30\,mm^2$) was used in this numerical simulation in order to investigate only the first third of the cell, and to speed up simulation times. Large cells ($90 \times 90\,mm^2$) were used in the experiments to demonstrate the practicability of the strategy for industrial applications. This also influences the regeneration time. Nonetheless, the numerical results show that a complete carbon removal process takes much longer than it is indicated by the gaseous desorption products. The experiments showed that the removal of a solid carbonaceous deposit and its transformation into an adsorbed species with subsequent desorption takes several hours, after which the initial cell performance is restored. Thus, the simulation provides a good representation of the general temporal trend of carbon removal strategies, but the absolute time scales need to be connected via experiments.

6.2.2. Carbon Removal by Reverse Boudouard Reaction B

Several studies in the literature use CO_2 to remove carbon deposits from packed bed nickel catalysts [98, 116] and to remove deposits from Ni-YSZ cermet anodes [113]. Kirtley et al. [113] claim that these carbon formations can be gasified by CO_2 but, at a certain point in time during the removal process, oxidation of the anode occurs. Figures 6.8 and 6.9 show the surface species coverage composition of the porous anode structure exposed to strategy **B** (mol fraction $CO_2 = 0.25\, mol\, mol^{-1}$) in the temperature range 800 to 600 °C.
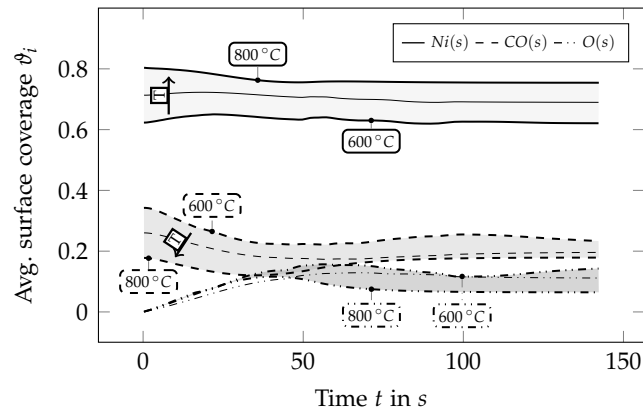
Figure 6.8.: Major adsorbed species for strategy **B** [117]

As identified by Kirtley et al. [113] using in-situ vibrational Raman spectroscopy, elementary oxygen $O(s)$ is found at the surface during the process (see Figure 6.8), which decomposes from CO_2 on the surface. The $O(s)/H(s)$ ratio exceeds unity after $4\,s$. This leads to the potential for oxidation, and can be directly linked to the findings of Kirtley et al. A temperature decrease from 800 to 600 °C has negative effects on the method, and elevated oxygen coverages were identified at 600 °C in comparison to 800 °C. This can be attributed to the Boudouard equilibrium. Thus, it is possible to conclude that the oxidation potential rises with decreasing operating temperatures.
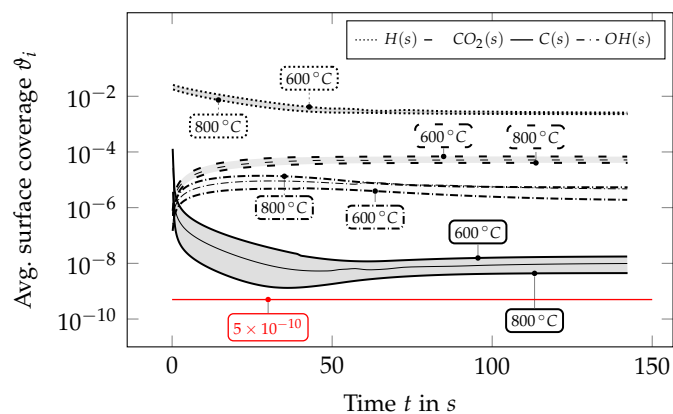
Figure 6.9.: Oxygenated and carbonaceous adsorbed species for strategy **B** [117]

Furthermore, the carbon coverages in Figure 6.9 remain above the threshold limit of 5×10^{-10} during the removal process. High amounts of adsorbed carbon monoxide exist on the surface

during the process, and no significant reduction in these coverages can be noted. What was noted for the temperature dependency of adsorbed oxygen is also true for adsorbed carbon monoxide.

These findings indicate that carbon dioxide can be theoretically used as an agent for carbon removal, but that it also poses a twofold risk: First, local parts of the catalyst can be oxidized by the adsorbed oxygen even when the oxidation potential is lower than that of **R3** - **R5**, which will be discussed below. Second, elementary carbon $C(s)$ and carbon monoxide coverages $CO(s)$ still exist after the application of the removal agent, and a complete removal of all adsorbed species is not possible.

These numerical results substantiate the experimental findings in [106], wherein the carbon dioxide-assisted removal of carbon deposits was proven, but the electrical and electrochemical performance of the cell was not restored. The cell performance decreased after each carbon dioxide removal cycle, indicating a reduction of catalytic active sites, and leading to further degradation. This numerical scrutiny provides a detailed analysis of the surface conditions during this removal strategy, and identifies adsorbed oxygen from decomposed CO_2 as a further source of degradation.

6.2.3. Oxygen Enriched Mixtures R3 - R5

Oxygen-enriched mixtures were also investigated as possible carbon removal agents, and are depicted in Figures 6.10 - 6.14.

(a) $800\,°C$ **(b)** $600\,°C$
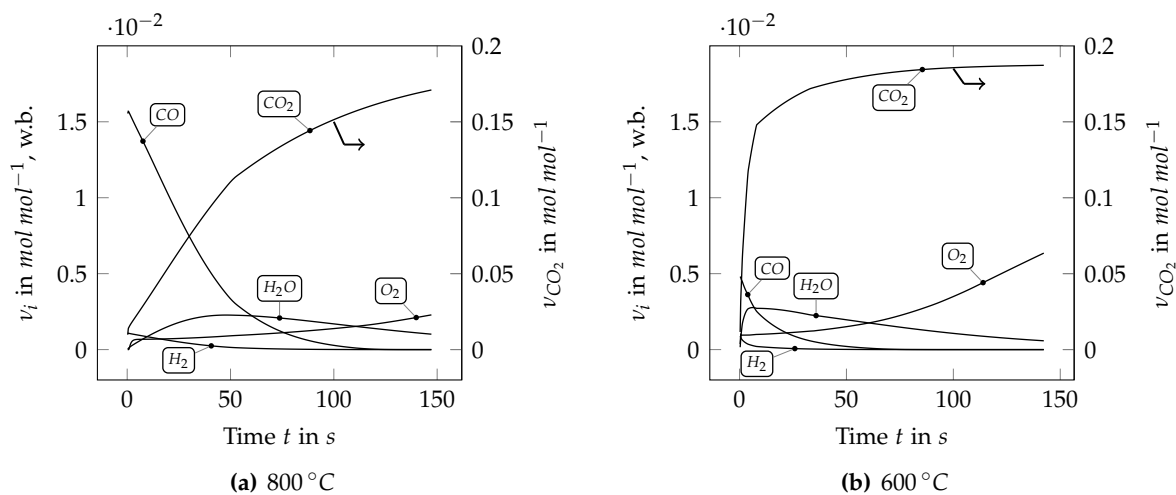
Figure 6.10.: Outlet gas composition for **R3** at two distinct operating temperatures [117]

The right axis of ordinates in Figures 6.10 and 6.11 refers to carbon dioxide. Figure 6.10 shows the temporal outlet gas composition for **R3** (see Table 6.2) at 800 and $600\,°C$. Simulation results for all oxygen-enriched removal strategies are only displayed in this temperature range, due to numerical convergence problems below $600\,°C$. Gaseous CO and H_2 is lowered by an order of magnitude compared to **R1** and **R2** (compared to Figure 6.3). This can be attributed to a

lack of H_2O in the fuel feed, which triggers the carbon monoxide reduction reaction. Lowering the temperature decreases the carbon monoxide desorption rates. In addition to CO, also H_2 and H_2O are desorption products. H_2O and H_2 desorb faster at lower temperatures (cf. Figures 6.10(a) and 6.10(b)).

For both temperature levels, it is possible to see that, after $150\,s$, O_2 is still being utilized (outlet amount is different from inlet amount), whereas CO_2 has almost reached its inlet composition value. Thus, oxygen still adsorbs at the catalyst. It was calculated that this adsorption process is finished for strategy **R3** after $330\,s$ and $400\,s$ at $800\,°C$ and $600\,°C$, respectively. At this point in time, the outlet gas composition was equal to the inlet composition and denoted the end of the regeneration process in terms of experimentally detectable gas components. However, a detailed analysis of the surface site coverage trend will also be conducted, through which these experimentally measurable time durations will be compared with those of the detailed heterogeneous simulation results.

(a) $800\,°C$ **(b)** $600\,°C$
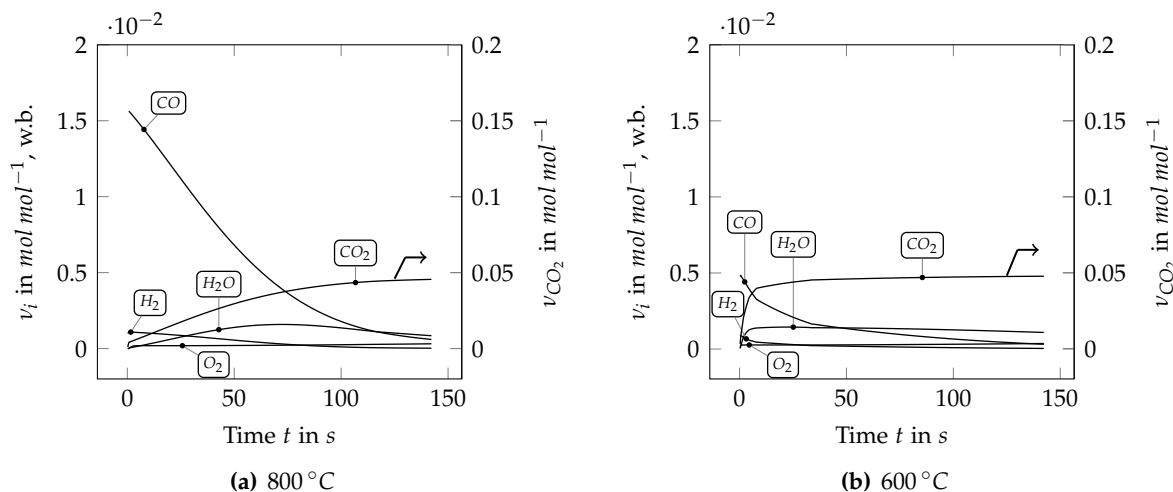
Figure 6.11.: Outlet gas composition for **R5** at two distinct operating temperatures [117]

The outlet gas composition for strategy **R5** is shown in Figure 6.11. **R5** contains a fourth of the O_2 and CO_2 of **R3**; **R4** only the half of **R3** (cf. Table 6.2). The results of **R4** were between those of **R3** and **R5** and are thus excluded from the figures. The outlet species trends of **R5** exhibit similar behaviour to those of **R3**, but the decreased O_2 and CO_2 amounts in the inlet feed lower the reaction rates, and thus increase the desorption time. This can be seen at the two plotted temperatures for all volatile species (cf. Figures 6.10 and 6.11). The average surface coverages in Figures 6.12, 6.13 and 6.14 clearly deviate from those of strategies **R1** and **R2**.

For **R3** (Figures 6.12(a), 6.13(a) and 6.14(a)), oxygen in the inlet feed quickly adsorbs at the active nickel sites, and thus reduces the availability of vacant sites. The trend of $O(s)$ in Figure 6.13(a) exhibits strong progressive behaviour. At $800\,°C$ it takes only $150\,s$ until $100\,\%$ of the catalytic active area is occupied by oxygen. All other adsorbed species are desorbed during this adsorption process, as can be seen in Figure 6.12(a). Lowering the operating temperature leads to even higher rates of oxygen adsorption, which is caused by CO_2 decomposition, as

discussed in Section 6.2.2. Decreasing the temperature thus worsens the effectiveness of this strategy.

(a) R3 @ OCV   **(b) R5 @ OCV**
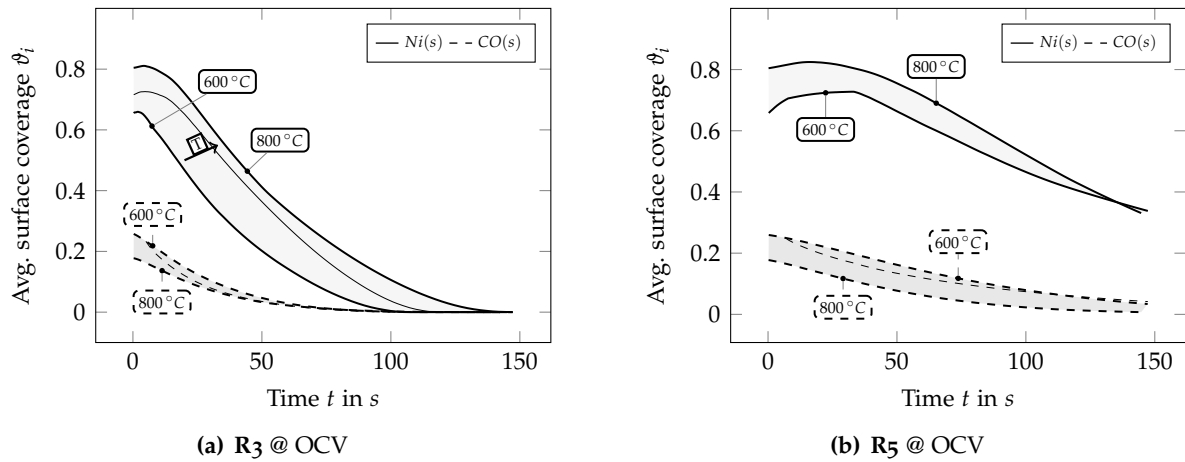
Figure 6.12.: $Ni(s)$ and $CO(s)$ surface coverages for **R3** and **R5** [117]

It is possible to note that the $O(s)/H(s)$ ratio exceeds unity after 5.5 seconds. This point of time is critical for the catalyst, since the amount of oxidative species exceeds the amount of reducing species. Severe nickel re-oxidation is a likely consequence. Nickel oxidation is reversible, but if the electrolyte cracks during this procedure, it constitutes a fatal cell malfunction.

Elementary carbon coverages $C(s)$ in Figure 6.14(a) show that the regeneration times t_r are 45 and $46\,s$ at 600 and $800\,°C$, respectively. This indicates that this strategy would allow short removal cycles. At t_r, 50 to 70 % of the catalytic area was already occupied by oxygen, which suggests the massive re-oxidation potential of the catalyst.

(a) R3 @ OCV   **(b) R5 @ OCV**
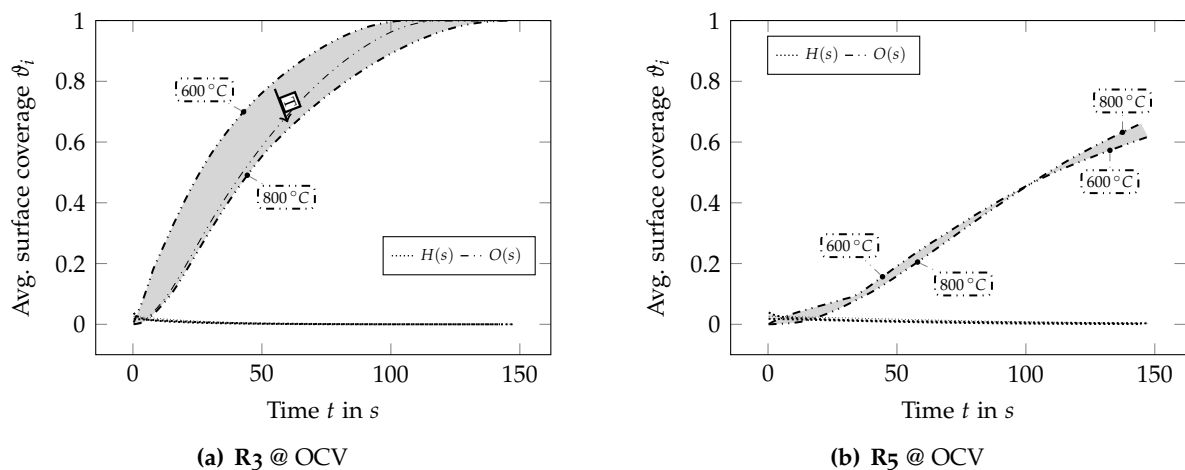
Figure 6.13.: $H(s)$ and $O(s)$ surface coverages for **R3** and **R5** [117]

One possibility to avoid the rapid oxidation of the anode would be to lower the amount of oxygen added to the inlet feed. This was done for strategy **R5** (mol fraction $O_2 = 0.005\,mol\,mol^{-1}$, see Table 6.2). Figures 6.12(b), 6.13(b) and 6.14(b) show the temporal trend of all adsorbed species for method **R5**. As intended, the adsorption rates of oxygen $O(s)$ decreased, as is shown

in Figure 6.13(b). At $150\,s$, only $62\,\%$ of the catalytic active area was occupied by elementary oxygen $O(s)$, compared to $100\,\%$ when strategy **R3** was applied.

(a) R3 @ OCV   **(b) R5 @ OCV**
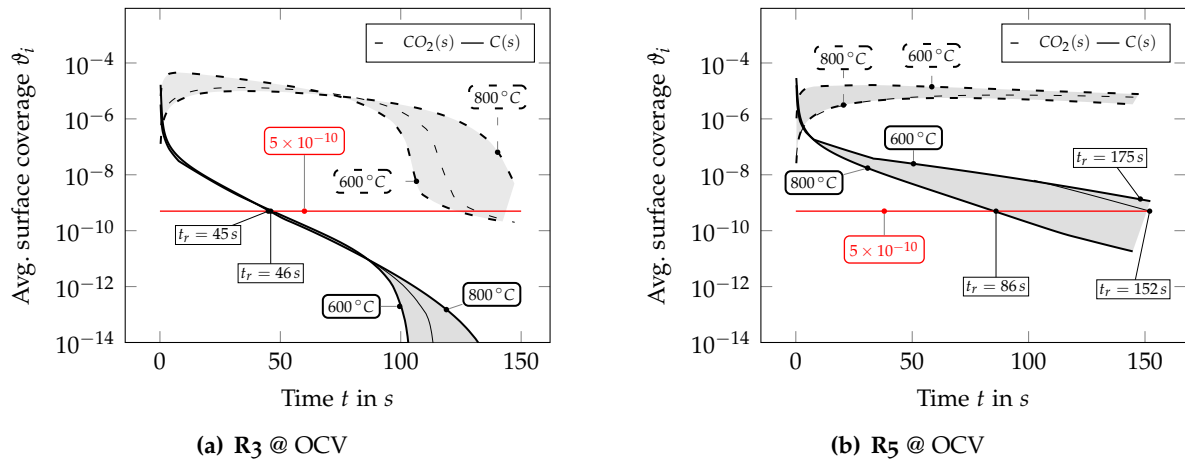
Figure 6.14.: $CO_2(s)$ and $C(s)$ surface coverages for **R3** and **R5** [117]

Furthermore, the gradients of all other species coverages are lowered. Thus, it takes longer for the $O(s)/H(s)$ ratio to exceed unity ($16\,s$). Figure 6.14(b) shows that the regeneration time increases considerably. It is also possible to see that a temperature decrease results in an increase of time t_r, in contrast to **R3**. This can be attributed to the decreased oxygen adsorption rates brought about by lower thermal and mass diffusion forces. Figures 6.10 and 6.12 - 6.14 show that oxygen-enriched strategies **R3** - **R5** can be used to remove elementary carbon coverages. Nonetheless, they pose a huge risk of oxidizing the fuel electrode, a fact that was investigated in a post-mortem microstructural analysis.

Figure 6.15 shows SEM images of the anodic substrate of an anode-supported SOFC single cell, before and after exposure to removal strategy **R3** for $300\,s$. The investigated Ni-YSZ anode-supported cell had a geometrically active area of $90 \times 90\,mm^2$. Detailed information about cell type, dimensions, and properties can be found in [107, 111, 112].
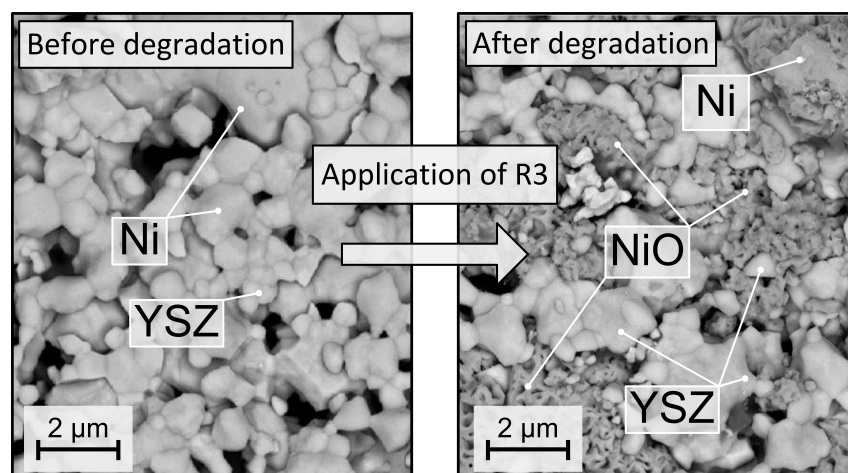
Figure 6.15.: SEM-analysis of the anode before (left) and after (right) exposure to strategy **R3** [117]

The micrographs clearly delineate the microstructure of the anode before degradation (left

image) and the tremendous effects of the exposure to strategy **R3** (right image). It can clearly be seen that the nickel particles were oxidized, which led to a structural change, through which porous nickel oxide (NiO) was formed. Furthermore, the application of removal agent **R3** detached YSZ and nickel particles, which led to a decrease in active three-phase boundaries and thus resulted in a distinct performance degradation. The post-mortem microstructural analysis emphasizes the validity of the simulation model, since it showed that severe oxidation takes place when the anode is supplied with a constant feed of removal strategy **R3**. This directly correlates with the findings shown in Figures 6.12 - 6.14.

In a further numerical approach, water vapour was added to removal mixture **R3** in order to dampen the high oxygen adsorption rates. Thus, $0.11 \, mol \, mol^{-1} \, H_2O$ were added in **R3H** (cf. Table 6.2). It showed that the regeneration time can be increased, but oxygen is still adsorbed at the nickel sites. Water vapour dampens the oxidation process, since it was shown in [89, 108] that water vapour decomposes to adsorbed hydrogen and oxygen at stoichiometric ratios. Nevertheless, complete oxygen surface occupation was not prevented by the addition of water vapour.

The practical application of these oxygen-enriched methods would require an advanced removal agent control strategy as well as sophisticated equipment to monitor for performance degradation. In order to bypass the total oxidation of the nickel catalyst, short, interrupted pulses of an oxygen-lean fuel mixture as represented by **R3** - **R5**, could be used to remove carbon deposits. Cell performance and cell impedance would have to be monitored continuously in order to quickly identify performance deterioration or severe nickel oxidation. These requirements imply the need for extensive research in this field. Furthermore, advanced on-line cell performance and impedance monitoring equipment would be required to use oxygen-enriched removal strategies as simple removal methods.

6.2.4. Electrochemical Method E

As mentioned in the description of the simulation model, a further strategy was introduced to remove carbon deposits from the fuel electrode.
The cell was fed with dry hydrogen and was put into fuel cell operation. This caused an oxygen ion flux O^{2-} from the cathode to the anode. Severe carbon depositions can significantly reduce the cell performance when the cell is put under load condition, so that the cell voltage would drop significantly below $0.7 \, V$. A molar flux of oxygen ions equivalent to an area averaged current density of $40 \, mA \, cm^{-2}$ was used for this method, since this load can be delivered by cells even after serious degradation. This current density was chosen to establish a regeneration environment that enables carbon removal in a safe and controlled manner.

Figure 6.16 shows the averaged current density trend along the cell length, and a contour plot of the current density distribution of an entire $90 \times 90 \, mm^2$ SOFC single cell. These trends depend on the findings of Chapter 3, and Figure 3.9(a) in particular. The local current densities were

found to be highest at the inlet of the cell, due to the boundary conditions of the experimental setup, and steadily decrease towards the cell outlet.
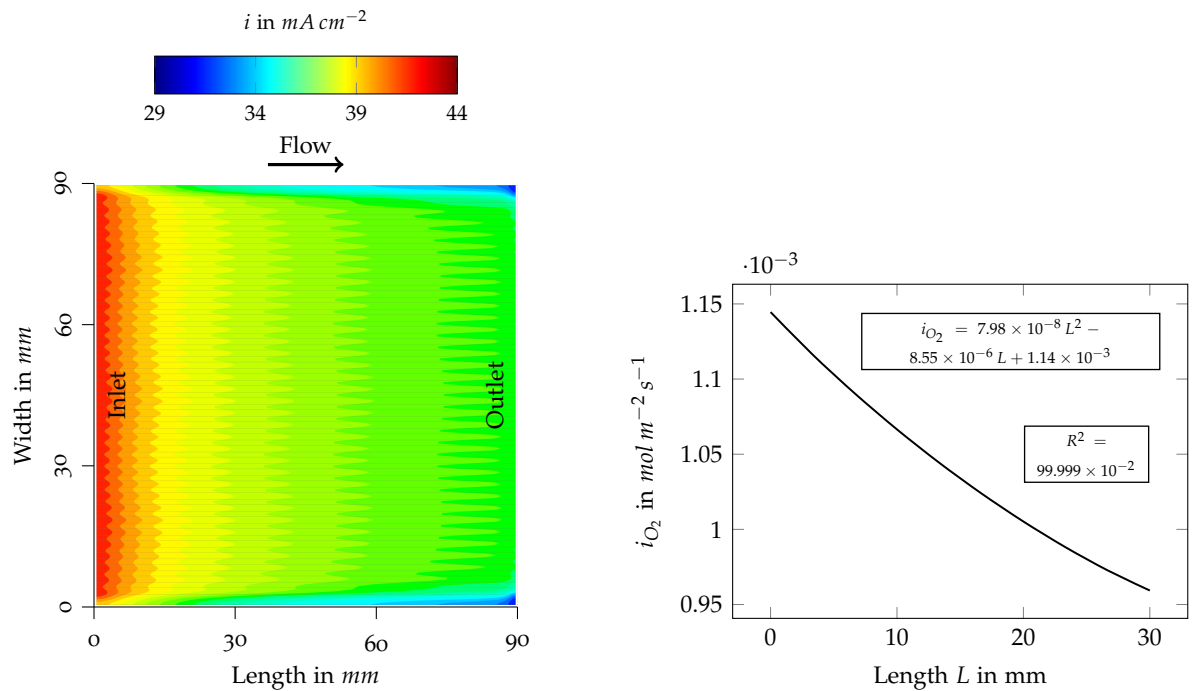
(a) Contours of current density i distribution (average: $40\,mA\,cm^{-2}$) of a complete $90 \times 90\,mm^2$ cell at $800\,°C$

(b) Average oxygen flux through the electrolyte, corresponds to an average of $40\,mA\,cm^{-2}$ [117]

Figure 6.16.: Oxygen molar flux profile and current density distribution

The cell was operated in co-flow condition, which provoked the local current density distribution of a cell operated at an overall current density of $40\,mA\,cm^{-2}$. This current density distribution during the dry hydrogen fuel feed (cf. Table 6.2) is shown in Figure 6.16(a). The co-flow condition of fuel and oxidant, as well as the current collector layout, led to this spatial current density distribution. The highest current densities occurred at the inlet region of the cell, and then steadily decreased towards the outlet of the cell. The averaged local current densities were found to almost perfectly obey a second order polynomial behaviour. This area-averaged local current density trend and the resulting oxygen ion flux (or rather oxygen molar flux) is plotted in Figure 6.16(b). Since no additional electrochemistry model was used in these $2D$ simulations, the actual resulting oxygen ion flux was transferred into an oxygen molar flux through the electrolyte boundary face to the porous anode. This oxygen molar flux profile was then defined as a boundary condition at the electrolyte interface EL (cf. Figure 4.1 for the dimensions and position) in the CFD code, by means of a user-defined function.

Highest current densities occurred at the inlet region of the cell, which steadily decreased towards the outlet of the cell. It was found that the averaged local current densities almost perfectly obey a second order polynomial behavior. This area-averaged local current density trend, or rather the resulting oxygen ion flux (or rather oxygen molar flux) is plotted in Figure 6.16(b). Since no additional electrochemistry model was used in these $2D$ simulations, the actual resulting oxygen ion flux was transferred into an oxygen molar flux through the

electrolyte boundary face to the porous anode. This oxygen molar flux profile was then defined as a boundary condition at the electrolyte interface EL (cf. Figure 4.1 for the dimensions and position) in the CFD code by means of a user-defined function.
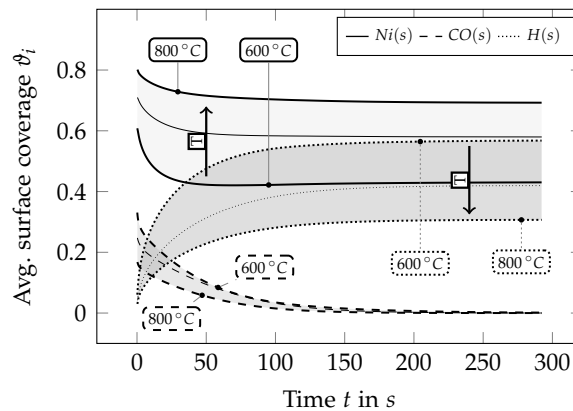
Figure 6.17.: Major adsorbed species for strategy **E** [117]

The results of method **E** are shown in Figures 6.17 and 6.18. A high number of vacant nickel sites $Ni(s)$ are present, and adsorbed hydrogen $H(s)$ was found to occupy high amounts of the active surface (see Figure 6.17). The amount of adsorbed carbon monoxide $CO(s)$ steadily decreased due to the applied carbon removal strategy. A temperature decrease to $600\,^\circ C$ resulted in higher hydrogen occupations, which is beneficial for the substrate, since it creates a reducing environment. Furthermore, this method provoked the surface sites to be only occupied by hydrogen $H(s)$, and the major part of the catalyst to be unoccupied (free nickel $Ni(s)$ sites).

The amount of adsorbed oxygen $O(s)$ is far below of that of hydrogen for all temperatures, resulting in $O(s)/H(s)$ ratios far below unity (compare Figures 6.17 and 6.18). This eliminates the risk of nickel re-oxidation. Figure 6.18 further shows that due to the oxygen molar flux from the electrolyte to the anode, a constant amount of adsorbed $O(s)$ ($\vartheta_{O(s)} = 5.4 \times 10^{-4}$ is established during the carbon removal process. This is equal to the amount of oxygen that is available at the electrocatalytically active TPB.
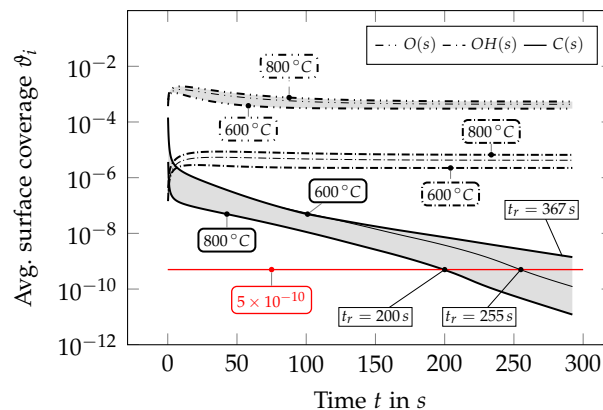
Figure 6.18.: $O(s)$, $OH(s)$ and $C(s)$ surface coverages for strategy **E** [117]

The time-dependent trend of elementary carbon $C(s)$ coverages in Figure 6.18 indicates that within the first 10 seconds after the application of the carbon removal strategy, high carbon removal rates occur. This can be attributed to the fact that a high amount of carbonaceous species is adsorbed at the anode-electrolyte interface EL (cf. Figures 5.1 for a schematic description of this interface). Figure 6.1 shows the spatial distribution of adsorbed species at the beginning of the carbon removal process. This is worth highlighting at this point for the sake of a better understanding.

After the first ten seconds, carbon was steadily removed, which is indicated by the almost constant slope of the graphs. The time-dependent trends described are independent of the operating temperature, whereas the removal gradients show a pronounced temperature dependence. The regeneration times t_r were calculated to be $t_r = 200$, 255 and $367\,s$ for 800, 700 and $600\,°C$, respectively. Higher current densities may shorten the removal process but they also conduct more oxygen to the anode, which can trigger partial nickel oxidation at very high fuel utilizations. While these regeneration times are higher than those of the other strategies, this strategy also makes it possible to entirely desorb both elementary carbon coverages $C(s)$ and carbon monoxide coverages $CO(s)$ without provoking additional degradation sources.

(a) Spatial $C(s)$ coverages from start to $25\,s$ (b) Spatial $C(s)$ coverages from 50 to $200\,s$
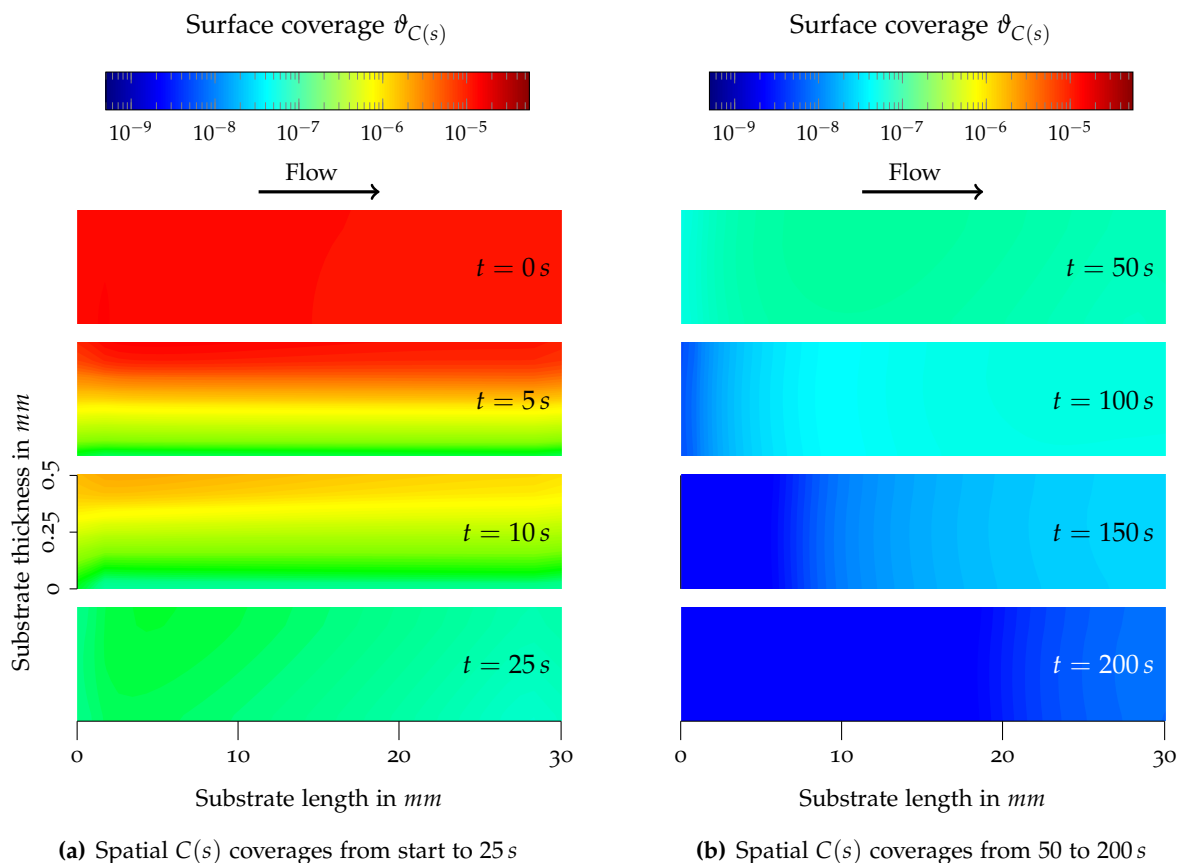
Figure 6.19.: Contours of time-dependent $C(s)$ surface coverages evolution during carbon removal with strategy **E** at $800\,°C$

Figure 6.19 shows elementary carbon $C(s)$ coverage trends at eight specific time steps during the carbon removal process with strategy **E**. The colour coding of these contours was done

for a species coverage range of 5×10^{-10} to 5.6×10^{-5}. Thus, a logarithmic scale was used to cover this big range. In these contour plots, only the anode substrate is magnified, since the main focus of this thesis is on the catalyst occupation. The dimensions are not to scale, and the thickness of the substrate was magnified by a bigger factor than the length.

Figure 6.19(a) depicts the process of initial fuel supply and the application of the oxygen molar flux. The $C(s)$ contours look different from the base case in Figure 6.1 at the start ($t = 0\,s$), but this is only due to the logarithmic colour code scaling. After $5\,s$, the effects of the carbon removal process become visible. The elementary carbon coverages are regenerated from the anode-electrolyte interface EL (bottom of each contour plot) due to the application of the oxygen molar flux from this interface.

It is possible to see that after $10\,s$, the carbon removal process has advanced, and a slight gradient from top to bottom and front to back of the substrate occurs. This is an interesting outcome of these simulations, and highlights the power of the transient, spatially resolved simulation model. The dry hydrogen in the fuel feed does not directly regenerate the adsorbed carbon, but water vapour has to be formed beforehand, which can then further remove the carbon deposits. This is the reason behind this inclined species coverage trend, contrary to the main flow direction of the fuel support. This plot also clarifies the high carbon removal rates at the beginning of the process. The oxygen molar flux from the electrolyte surface regenerates the locally high amount of species coverages at this interface. These local coverages can better be seen in Figure 6.1. Thus, the high $C(s)$ gradients, as shown in Figure 6.18, can be attributed to the local desorption of carbon at the front of the substrate.

After this point in time (see the contour plot at $25\,s$ in Figure 6.19(a) and plots in Figure 6.19(b)), the carbon coverages steadily decreased. The coverages were then regenerated from the front to the back of the substrate, and a slight superposition of the oxygen molar flux from the anode-electrolyte surface can be seen (cf. Figure 6.19(b) at $150\,s$). The successful carbon removal process was finished after $200\,s$, when the species coverages of $C(s)$ across the entire anode substrate fell below the threshold value of 5×10^{-10}.

All of the simulation results presented in this section show that the removal by strategy **E** is both a promising and successful process to remove the carbon deposits that occur during the internal reforming of diesel reformates. It was also shown that this strategy is slower than **R1** and **R2**, but it also eliminates the need to humidify the fuel. Thus, this strategy is able to successfully, effectively, and permanently remove carbonaceous deposits from the fuel electrode of a solid oxide fuel cell. The experimental investigations have shown that strategies **R1**, **R2** and **E** are able to remove carbon deposits, prevent nickel re-oxidation, and restore the cell performance of planar anode supported single cells.

6.3. Summary of Suitable Carbon Removal Methods[3]

This chapter has investigated the impact of different carbon removal strategies on the catalytically active sites of a Ni-YSZ cermet anode as well as their ability to successfully remove carbon from a porous nickel-based anode substrate. The detailed heterogeneous reaction mechanism used to scrutinize gas-surface interactions was used to evaluate the spatial and temporal distribution of adsorbed species. This made it possible to have a significantly higher level of detail in the analysis of the processes that occur.

The profiles of steady-state surface site occupation during the internal reforming of a synthetic diesel reformate mixture with a S/C of 0.3 were used as a base case for the carbon removal simulations. The computational domain was inertised with nitrogen before the gaseous mixtures were introduced to the flow channel, according to the experimental procedure. Four different removal strategies were applied: Hydrogen/water vapour, carbon dioxide, carbon dioxide/oxygen, and putting the cell under load condition when fed with hydrogen.

The first methods, hydrogen/water vapour mixtures **R1** and **R2**, were able to successfully minimize the elementary adsorbed carbon $C(s)$ within time spans that are acceptable for practical applications. Carbon monoxide coverages decreased comparably to those of $C(s)$. From this point of view, it is a suitable method for the removal of carbon deposits. However, it was shown by [111], that the underlying mechanism for the removal of amorphous or fibrous carbon is complex. Thus, with this method, the total removal of solid carbon can take up to $44\,h$ in experiments. The time scale differences between the experimental and numerical findings can be addressed: Carbon is modelled to occur in adsorbed state. The formation of a second, solid carbon phase is not taken into account due to the poorly understood reaction kinetics and discrepancies in the numerical handling of these separate phases and their interactions. It is particularly important to note that the build-up of a solid phase influences the number of catalytically active sites, the porosity, as well as the tortuosity. All of these interactions are, as yet, poorly understood and were thus neglected. Nevertheless, the coverage trends can be used to gain a better understanding of the surface site occupations during the removal process. Furthermore, degradation sources can be identified and linked to actual cell performance losses during the application of various carbon removal strategies.

Carbon dioxide is not suitable as a gaseous agent for practical uses. This analysis has shown that both elementary carbon coverages and carbon monoxide coverages cannot be decreased below the defined threshold value using a supply of CO_2. Oxygen coverages occur as a result of CO2 surface decomposition reactions. Thus, the $O(s)/H(s)$-ratio exceeds unity at a certain point in time (few minutes). Nickel re-oxidation is possible, as stated in [98, 113, 116]. The practical application of this removal method is thus questionable.

---

[3]Segments of this section were published in the *International Journal of Hydrogen Energy* under the title "CFD-Simulation of Effective Carbon Gasification Strategies From High Temperature SOFC Ni-YSZ Cermet Anodes" [117].

The third method presented here, carbon dioxide/oxygen-based removal mixtures **R3** - **R5**, achieved very high carbon removal rate, thus, resulting in low regeneration times. Unfortunately, despite these high carbon removal rates, oxygen adsorbs at the catalyst, occupying 100% of the catalytically active sites in a short period of time. This is critical since, within seconds, the $O(s)/H(s)$ ratio exceeds unity, making the re-oxidation potential of the nickel catalyst extremely high. If this ratio exceeds unity at any local position within the porous media during the application of these carbon removal methods, the cell is at a particularly high risk of suffering serious degradation. Thus, on the one hand, this method is very fast, but on the other, it also poses an enormous risk of degradation. The application of this method would require fast and reliable real-time performance monitoring equipment in order to quickly react to any deterioration in cell performance. This could pose a problem for the practicability of this method.

For the last approach, the cell was put under load condition and fed with dry hydrogen. An oxygen molar flux equivalent to an average current density of $40\,mA\,cm^{-2}$ was used to provide product water vapour to remove the carbon. Using this method, both elementary carbon coverages $C(s)$ and carbon monoxide coverages $CO(s)$ can be effectively minimized in a controlled manner. Furthermore, this method made it possible to maintain a $O(s)/H(s)$ ratio below unity. The hydrogen supply creates a reducing environment in the porous anode, in which the risk of nickel oxidation identified for other methods is eliminated. Regeneration times using this method are higher than the other methods presented, but are still acceptable for practical applications. Strategies **R1**, **R2** and **E** constitute novel methods of carbon removal which are presented to the literature for the purpose of removing carbon coverage and simultaneously protecting the catalyst from the severe consequences of irreversible electrolyte cracking brought about by massive nickel re-oxidation.

It can thus be concluded that two of the four carbon removal strategies can be used to prolong the lifetimes of single cells and stacks in practical applications. On the one hand, humidified hydrogen puts the catalyst in a safe, reducing environment, while the carbon coverages are decreased in a controlled manner. On the other hand, the novel electrochemical approach utilizes oxygen ions and product water, which are conducted through the electrolyte. This method eliminates the transport limitation of the gaseous agent into the porous structures. It is thus both a promising and novel carbon removal strategy that can easily be applied in technical applications.

7
Conclusions

This thesis aimed to find answers to the following initial research questions: Is a commercial CFD software able to predict the chemical and electrochemical performance of a SOFC single cell? And, is it possible to model performance degradation effects? In the effort to help SOFC technology overcome an important hurdle on its path to successful commercialization, these are important questions. The occurrence of degradation phenomena, such as carbon formation, during the internal reforming of hydrocarbon fuels, in addition to nickel re-oxidation brought about by any carbon removal procedures, are still major issues of SOFCs. These degradation effects limit the lifetimes of cells, stacks, and entire SOFC systems. Successful measures to both identify and quantify degradation effects and to restore the initial cell performance will eventually help SOFC technology overcome one of its last hurdles.

SOFCs are highly fuel flexible devices able to utilize hydrocarbons. This thesis paid particular attention to the use of diesel reformates as a fuel supply, which brings with it the risk of carbon formation within the cell. When carbon precipitates, it forms at the nickel catalyst within the porous electrodes at temperatures between $600 - 1,000\,°C$. Thus, the experimental determination of local- and time-dependent carbon formation effects in large planar cells can only be accomplished with high experimental and monetary effort. Numerical models to simulate the performance of solid oxide fuel cells are time- and cost-saving alternatives to explore this topic. However, the modelling and simulation of carbon formation is a demanding task. SOFC literature lacks a detailed model that is able to predict this carbon deposition process both spatially and on a time-dependent scale. Therefore, a detailed simulation model was developed in this thesis that is able to predict carbon formations and serve as a base model for further scrutiny of carbon removal strategies.

In combination with a SOFC sub-module, the commercial CFD software, ANSYS Fluent, was used as a framework to generate a flexible $3D$ simulation model. This model is able to predict the electrochemical performance of both electrolyte and anode-supported planar $100 \times 100\,mm^2$ cells. In addition to these particular types, the performance of circular, tubular, and button cells can also be simulated with the flexible model generated. All of the simulations conducted for this thesis were based on experiments that were performed at an in-house high temperature test bench for large, planar SOFCs at the Institute of Thermal Engineering at Graz University

of Technology. The experimental results were critically examined for their physical correctness and were then applied in order to validate the simulation model.

In a first step, the electrochemical performance of a cell was characterized by polarization curves for both conventional and alternative fuels in a typical SOFC temperature range. All relevant aspects of the SOFC model, such as the solver and sub-model settings, boundary conditions, and material data were thoroughly scrutinized, and their impact on the simulation result and its accuracy was analysed. High accordance was established between the experimental and numerical results. This ensured the correct modelling of all superimposed transport phenomena that occur within a fuel cell. As was shown, the model was able to predict the electrochemical performances of both electrolyte and anode-supported cells for hydrogen and synthetic diesel reformate feeds with high accuracy. The average relative deviations between the experiment and the simulation were $+1.17\%$ for an ASC-SOFC fed with humidified hydrogen and $+0.8\%$ for a ESC-SOFC fed with synthetic diesel reformate. These results highlight both the high accuracy and the flexibility of the $3D$-simulation model created for this thesis. This initial validation of the simulation results provided the evidence that the simulation model provided a resilient and reliable foundation for further, more detailed, and more sophisticated simulations.

In a second step, simulations of the internal reforming performance of ASC-SOFC and ESC-SOFC single cells fed with various diesel reformates were investigated. In literature, simulation models propose two different major numerical approaches for the internal reforming of light hydrocarbons: global homogeneous and detailed heterogeneous mechanisms. Both of these approaches were implemented in the simulation model, and a multitude of kinetics approaches that are presented in literature were analysed. This analysis revealed that both of the fundamentally diverse mechanisms can be used to predict the internal reforming performance. Nevertheless, the first approach with global homogeneous mechanisms lacks the essential option of being used for further simulations carbon formation. This is due to the fact that only the evaluation of carbon formation activities is possible. These activities act as indicators of any reactions' deviation from thermodynamic equilibrium. This deviation is the only way in which this approach can be used as basis for the evaluation of carbon formations. The requirements that the simulation model be able to predict the amount, location, and point in time of carbon formation occurrence can therefore not be met simply by means of these carbon formation activities.

The second possibility to describe the internal reforming reactions of light hydrocarbons is to use a detailed heterogeneous reaction mechanism. Herein, the occurring gas phase - solid interactions of the heterogeneous reforming process are depicted in a more detailed manner. The mechanism used in this thesis makes it possible to investigate thirteen different surface-adsorbed species, including elementary carbon. The steady-state and transient simulations conducted showed that elementary carbon is consistently present during the internal reforming of diesel reformate to the catalytic active nickel sites in the porous anode. The simulations showed that carbon precipitates almost uniformly across the anode surface when the cell is reforming during open circuit conditions. This spatial surface coverage changed when the cell

was put under load operation. More elementary carbon is deposited at the inlet region of the cell, which makes it especially vulnerable to degradation. This is an important result that will help cell manufacturers better adapt the local microstructure of cells to specific applications. Moreover, the simulations revealed that lower temperatures favour carbon formation during the internal reforming of diesel reformate. Besides elementary carbon, the hydrogenated and oxygenated species profiles that occur during internal reforming can be evaluated by means of the detailed mechanism implemented. The generated base model, which can predict the electrochemical performance of a cell, in combination with the heterogeneous mechanism to describe spatial species coverages within the porous anode structure, represent powerful simulation tools. It was thus used as a base model for further scrutiny of major carbon precursors, to identify surface coverage conditions during internal reforming of synthetic reformates, and for the application of effective carbon removal strategies.

In a third step, the simulation model was used to address the main carbon formation route of carbonaceous species in mixtures with steam. This was done on a detailed, elementary basis as a consequence of the previous findings. The application of detailed kinetics for the reforming reactions that occur is thus a logical improvement in the level of sophistication of reaction modelling. Methane was identified as the major carbon precursor in the typical SOFC temperature range between $600 - 1,000\,°C$. Carbon monoxide, on the other hand, was shown to play only a subordinate role. These results agree with the experimental findings of [79] and [97], where they also found that methane led to more carbon deposits than carbon monoxide. Thermodynamic equilibrium calculations were used to analyse whether graphite or carbon nanofibers (CNF) would form. Thus, the detailed simulation model and the thermodynamic equilibrium calculations were linked. The surface coverages were attributed to a carbon formation rate of graphite and CNF.
A transient analysis revealed that carbon surface coverage differs greatly between the start of gas supply and the steady state condition. For a mixture of methane and steam, carbon surface coverage peaked within the first 10 seconds and then subsequently decreased to a lower steady state coverage. This was shown for the entire temperature range and a broad range of steam-to-carbon ratios. This analysis showed that the start of fuel supply is a critical operating point for a SOFC. Furthermore, it was found that a single increment of steam, added to the fuel supply, decreases the amount of deposited carbon tremendously. The steam-to-carbon ratio is thus a crucial value for a SOFC, which must be kept constant to avoid carbon formation, and has to be monitored carefully. This is a crucial outcome of this thesis and a highlight of the research conducted herein.

Methane was found to be the main cause of carbon formation, as the single carbonaceous constituent in a mixture with steam. The ultimate goal of SOFC technology is be able to compete with other technologies on the market. Thus, they must be usable with commercially available fuels. Various diesel reformate compositions therefore needed to be scrutinized as SOFC fuels for their propensity to build carbon deposits. This analysis showed that the highest surface coverages during internal reforming of such gas mixtures were caused by adsorbed

carbon monoxide and hydrogen. Carbonaceous species were third highest after oxygenated species. The simulations again revealed that highest gradients of all adsorbed species occur within the first five to ten millimetres of the cell. The inlet section is thus especially susceptible to performance degradation during the use of reformates. The methane to carbon monoxide ratio was further detected to be a critical value during the utilization of reformates. However, a constant carbon precursor mass flow (either methane/steam or carbon monoxide/steam mixtures) resulted in significantly different carbon coverages during the internal reforming of these carbonaceous mixtures. High amounts of methane resulted in the highest carbon coverages. On the other hand, elevated amounts of carbon monoxide in the fuel feed resulted in the lowest elementary carbon surface occupations. This was accompanied by the highest coverages of oxygenated and hydrogenated species. Thermodynamic equilibrium calculations were again used to connect the detailed numerical results to carbon formation rates. For the investigated reformate compositions, below a S/C ratio of 0.447 carbon formation will occur. For a S/C of 0.3, a carbon formation rate of $2.6 \times 10^{-6} \, mol/s$ CNF and $1.46 \times 10^{-6} \, mol/s$ graphite was identified.

A literature review revealed that possible gasification strategies for carbon deposits already exist for nickel-based catalysts. Nevertheless, their application and suitability for SOFCs had to be verified. Not only do the carbon deposits need to be efficiently and successfully removed, but the cell performance also needs to be restored and returned to its initial state. This is of major importance to the future commercialization of SOFC technology, and, therefore, in a last step, four fundamentally diverse carbon removal strategies were developed and subsequently scrutinized in the temperature range of $400 - 800\,°C$ to restore cell performance. Both the impact of these carbon removal strategies on the catalytically active sites as well as their ability to successfully remove carbon were investigated. These removal strategies were applied to the cells after permanent performance degradation caused by carbon deposits had been detected. The four carbon removal strategies developed were: (1) hydrogen/water vapour, (2) carbon dioxide, (3) carbon dioxide/oxygen, and (4) carbon removal with dry hydrogen during load operation. These strategies were applied to a degraded cell, and their impact on the catalytic surface was thoroughly analysed.

CO_2, and a mixture of CO_2 and O_2 exhibited high carbon-removal rates. Nevertheless, these methods are not suitable for practical use since nickel re-oxidation occurs when they are introduced to the cell, and cell performance deteriorated upon their application. This cell performance deterioration was experimentally linked to nickel re-oxidation by SEM micrographs. These showed that CO_2 and O_2 oxidized the nickel catalyst to NiO, which led to a decrease in electrochemically active three-phase boundary sites, ultimately resulting in cell performance deterioration. Moreover, more severe nickel re-oxidation led to high tensile stresses, which led to the mechanical failure of the cells. The detailed simulation model made it possible to analyse the temporal evolution of surface adsorbed oxygen. The entire active catalyst area was occupied by oxygen after these strategies were applied.

The mixture of carbon dioxide and oxygen shows promise to be used as a possible carbon

removal strategy in a technical application, if the fast and reliable real-time monitoring of the cell performance can be achieved. One possibility for the application of this method would be to use it in an intermittent pulse mode, in which the cell would be supplied with a short pulse of this gas mixture and then the cell performance response would be analysed. Nevertheless, such an application requires a more detailed analysis and could be the subject of later research activities.

Humidified hydrogen and dry hydrogen under load operation were also demonstrated to be successful and realizable carbon removal strategies. They enabled a safe and efficient process by creating a reducing surface condition. This means that more hydrogen was adsorbed to the surface across the entire cell than oxygenated species. Thus, nickel re-oxidation was effectively avoided. Carbon removal rates were lower compared to oxygen and carbon dioxide based methods. However, adsorbed carbon was removed, and the initial cell performance was repeatedly and effectively restored. The lifetime of cells and stacks can thus be successfully prolonged.

In conclusion, with regard to the initial research question: Yes, a commercial CFD software can be used to predict the performance of different types of high temperature solid oxide fuel cells. Reproducible results were achieved for hydrogen and for synthetic diesel reformate fuel feeds. The numerical model developed, in connection with a SOFC module, made it possible to predict the performance trends of electrolyte- and anode-supported cells. The model is particularly suited to the use of reformates, and not only is the internal reforming of light hydrocarbons possible, but correct cell performances can also be predicted. Internal reforming rates could be accurately predicted due to the application of a detailed heterogeneous reaction mechanism, which made it possible to simulate the local and time-dependent distribution of permanently adsorbed species. Degradation effects were also successfully simulated. Carbon formation during internal reforming was thoroughly analysed, and the spatial and temporal occurrence of carbon deposits was highlighted. Moreover, the simulation model made it possible to develop, identify and analyse effective carbon removal strategies that would also restore cell performance. The model made it possible to scrutinize degradation mechanisms that occur on a detailed surface level, which had not yet been done in the literature. The causes of the carbon formation phenomena investigated, as well as the effects of the removal strategies developed were identified. The contents of this thesis have provided a thorough overview of the processes that occur within SOFCs. All of its simulation results were validated by experimental data gained at the high temperature SOFC test rig at the Institute of Thermal Engineering at Graz University of Technology. High accordance between the experimental and simulation results were achieved, which adds additional value to the results of this thesis. These results will ultimately lead to the prolongation of the lifetime of large, planar SOFCs, and thus contribute to their eventual commercial breakthrough.

A

Thermodynamic Equilibrium Compositions

A.1. Thermodynamic Data of Graphite and Carbon Nano Fibers
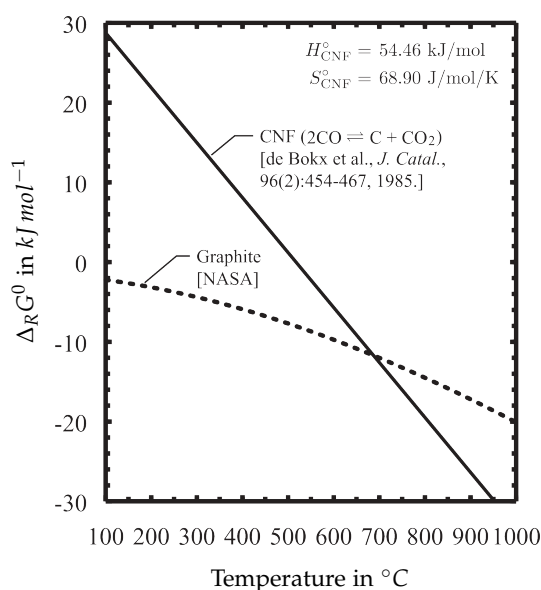
Figure A.1.: Gibbs free energy of carbon nano fibers CNF and graphite C(gr) [102]

Figure A.1 shows the temperature dependent thermodynamic data of carbon nano fibers CNF and graphite C(gr) in the temperature range of 100 to $1,000\,°C$, which were used for all equilibrium investigations in this thesis.

A.2. Synthetic Diesel Reformate Equilibria: Gaseous Compositions

This appendix provides the thermodynamic equilibria of the gaseous species of the synthetic diesel reformates used and scrutinized in Chapter 5. The mixture composition can be reviewed in Table 5.1, Section 5.2.2. The data presented can be used to gain a better understanding of the reformates' temperature dependence and their corresponding equilibrium composition. The fuel mixtures were normalized to $1\,mol$ of carbon precursors (sum of methane and carbon monoxide), in order to represent comparable results for different fuel compositions. This procedure was also described in Chapter 5.

(a) S/C 0.3
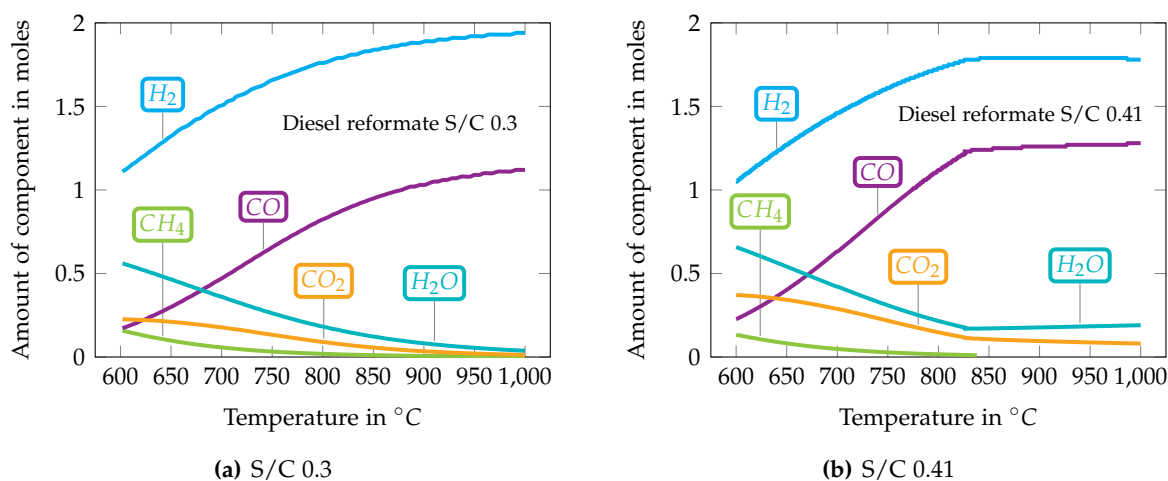
(b) S/C 0.41

Figure A.2.: Equilibrium composition of diesel reformates S/C 0.3 and S/C 0.41 at temperatures of $600 - 1,000\,^\circ C$

(a) S/C 0.447

(b) S/C 0.5
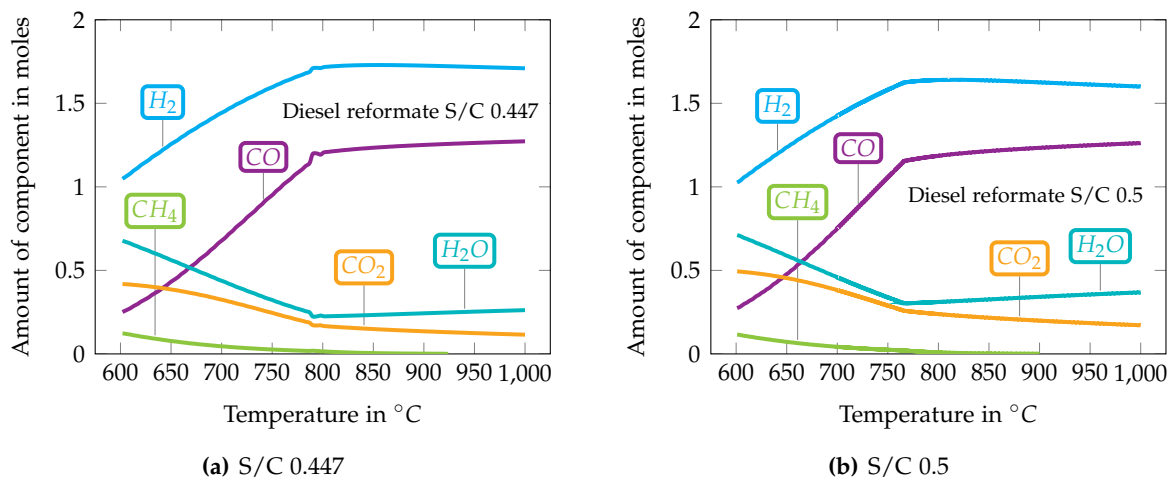
Figure A.3.: Equilibrium composition of diesel reformates S/C 0.447 and S/C 0.5 at temperatures of $600 - 1,000\,^\circ C$
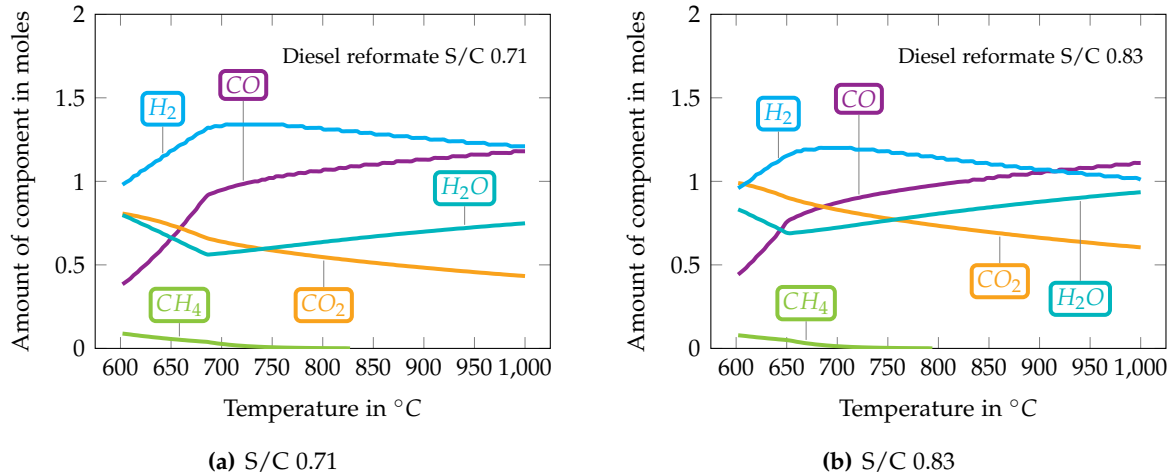
(a) S/C 0.71

(b) S/C 0.83

Figure A.4.: Equilibrium composition of diesel reformates S/C 0.71 and S/C 0.83 at temperatures of $600 - 1,000\,°C$

A.3. Synthetic Diesel Reformate Equilibria: Solid Compositions

In this appendix, thermodynamic equilibria of the solid species formed from synthetic diesel reformates (see Chapter 5) are provided as supplementary material. The mixture composition can be reviewed in Table 5.1, in Section 5.2.2. These equilibrium compositions, or rather, the amount of formed carbon (both graphite (C(gr)) and carbon nanofibers (CNF)) can be used to link the simulation results of the detailed CFD model to carbon formation rates. The fuel mixture was normalized to $1\,mol$ of carbon precursors (sum of methane and carbon monoxide), in order to present comparable results for different fuel compositions.
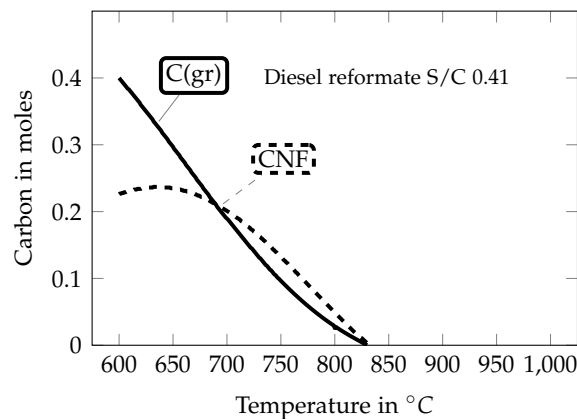
Figure A.5.: Equilibrium carbon formation from diesel reformate S/C 0.41

(a) S/C 0.447

(b) S/C 0.5
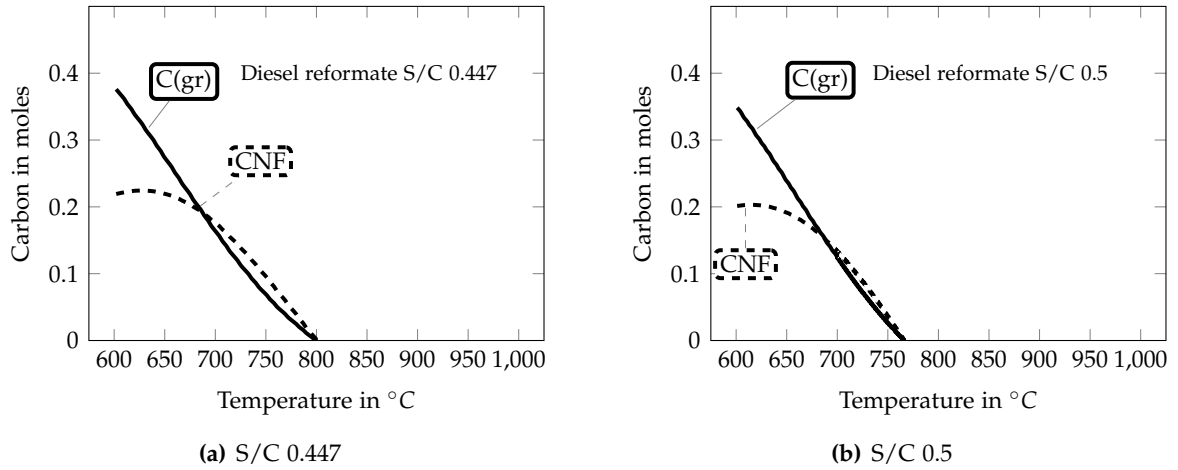
Figure A.6.: Equilibrium carbon formation from diesel reformate S/C 0.447 and S/C 0.5
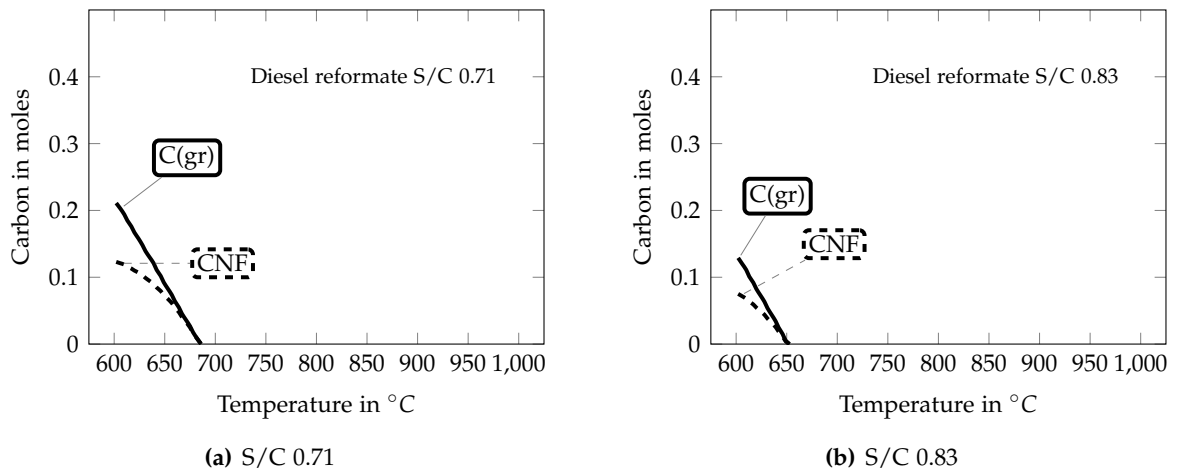
(a) S/C 0.71

(b) S/C 0.83

Figure A.7.: Equilibrium carbon formation from diesel reformate S/C 0.71 and S/C 0.83

Bibliography

[1] EG & G Technical Services, Inc. Fuel Cell Handbook. 7th ed. Morgantown, West Virginia: U.S. Department of Energy, 2004.

[2] R. O'Hayre, S.-W. Cha, W. Colella, et al. Fuel Cell Fundamentals. Wiley, 2009. 576 pp.

[3] J. Maček, B. Novosel, and M. Marinšek. Ni–YSZ SOFC anodes - Minimization of carbon deposition. *Journal of the European Ceramic Society*, **27** (2) (2007): 487–491.

[4] C. H. Cheng, Y. W. Chang, and C. W. Hong. Multiscale Parametric Studies on the Transport Phenomenon of a Solid Oxide Fuel Cell. *Journal of Fuel Cell Science and Technology*, **2** (4) (2005): 219–225.

[5] C. Frayret, A. Villesuzanne, M. Pouchard, et al. Density functional theory calculations on microscopic aspects of oxygen diffusion in ceria-based materials. *International Journal of Quantum Chemistry*, **101** (6) (2005): 826–839.

[6] N. Autissier, D. Larrain, J. Van herle, et al. CFD simulation tool for solid oxide fuel cells. *Journal of Power Sources*, **131** (1) (2004): 313–319.

[7] K. Ahmed and K. Foger. Kinetics of internal steam reforming of methane on Ni/YSZ-based anodes for solid oxide fuel cells. *Catalysis Today*, **63** (2) (2000): 479–487.

[8] H. Zhu, R. J. Kee, V. M. Janardhanan, et al. Modeling Elementary Heterogeneous Chemistry and Electrochemistry in Solid-Oxide Fuel Cells. *Journal of The Electrochemical Society*, **152** (12) (2005): A2427–A2440.

[9] S. H. Chan, H. K. Ho, and Y. Tian. Multi-level modeling of SOFC–gas turbine hybrid system. *International Journal of Hydrogen Energy*, **28** (8) (2003): 889–900.

[10] K. Kendall. "1 - Introduction to SOFCs." In: *High-Temperature Solid Oxide Fuel Cells for the 21st Century (Second Edition)*. Boston: Academic Press, 2016, 1–24.

[11] W. Winkler. "3 - Thermodynamics A2 - Kendall, Kevin." In: *High-Temperature Solid Oxide Fuel Cells for the 21st Century (Second Edition)*. Ed. by M. Kendall. Boston: Academic Press, 2016, 51–83.

[12] S. B. Adler. "Sources of cell and electrode polarisation losses in SOFCs." In: *High-Temperature Solid Oxide Fuel Cells for the 21st Century (Second Edition)*. Ed. by M. Kendall. Boston: Academic Press, 2016, 357–381.

[13] H. Zhu and R. J. Kee. A general mathematical model for analyzing the performance of fuel-cell membrane-electrode assemblies. *Journal of Power Sources*, **117** (1) (2003): 61–74.

[14]   S. H. Chan, K. A. Khor, and Z. T. Xia. A complete polarization model of a solid oxide fuel cell and its sensitivity to the change of cell component thickness. *Journal of Power Sources*, **93** (1) (2001): 130–140.

[15]   M. Ni, M. K. H. Leung, and D. Y. C. Leung. Parametric study of solid oxide fuel cell performance. *Energy Conversion and Management*, **48** (5) (2007): 1525–1535.

[16]   X. Deng and A. Petric. Geometrical modeling of the triple-phase-boundary in solid oxide fuel cells. *Journal of Power Sources*, **140** (2) (2005): 297–303.

[17]   E. Hernández-Pacheco, D. Singh, P. N. Hutton, et al. A macro-level model for determining the performance characteristics of solid oxide fuel cells. *Journal of Power Sources*, **138** (1) (2004): 174–186.

[18]   R. Suwanwarangkul, E. Croiset, M. W. Fowler, et al. Performance comparison of Fick's, dusty-gas and Stefan–Maxwell models to predict the concentration overpotential of a SOFC anode. *Journal of Power Sources*, **122** (1) (2003): 9–18.

[19]   Y. Jiang and A. V. Virkar. Fuel Composition and Diluent Effect on Gas Transport and Performance of Anode-Supported SOFCs. *Journal of The Electrochemical Society*, **150** (7) (2003): A942–A951.

[20]   Y. Fu, Y. Jiang, S. Poizeau, et al. Multicomponent Gas Diffusion in Porous Electrodes. *Journal of The Electrochemical Society*, **162** (6) (2015): F613–F621.

[21]   J.-W. Kim, A. V. Virkar, K.-Z. Fung, et al. Polarization Effects in Intermediate Temperature, Anode-Supported Solid Oxide Fuel Cells. *Journal of The Electrochemical Society*, **146** (1) (1999): 69–78.

[22]   J. Xu and G. F. Froment. Methane steam reforming, methanation and water-gas shift: I. Intrinsic kinetics. *AIChE Journal*, **35** (1) (1989): 88–96.

[23]   K. Hou and R. Hughes. The kinetics of methane steam reforming over a Ni/a-Al2O catalyst. *Chemical Engineering Journal*, **82** (1) (2001): 311–328.

[24]   F. Joos. Technische Verbrennung. Springer Berlin Heidelberg New York, 2006. 907 pp.

[25]   ANSYS Inc. ANSYS FLUENT User's Guide V14.0. Canonsburg, PA, 2011.

[26]   J. H. Ferziger and M. Peric. Computational Methods for Fluid Dynamics. 3rd ed. Springer Berlin Heidelberg New York, 2002. 426 pp.

[27]   ANSYS Inc. ANSYS FLUENT Fuel Cell Modules Manual. Canonsburg, PA, 2011.

[28]   S. Kakac, A. Pramuanjaroenkij, and X. Zhou. A review of numerical modeling of solid oxide fuel cells. *International Journal of Hydrogen Energy*, **32** (7) (2007): 761–786.

[29]   V. A. Danilov and M. O. Tade. A CFD-based model of a planar SOFC for anode flow field design. *International Journal of Hydrogen Energy*, **34** (21) (2009): 8998–9006.

[30]   H. Djamel, A. Hafsia, Z. Bariza, et al. Thermal field in SOFC fed by hydrogen: Inlet gases temperature effect. *International Journal of Hydrogen Energy*, **38** (20) (2013): 8575–8583.

[31] D. Sanchez, R. Chacartegui, A. Munoz, et al. On the effect of methane internal reforming modelling in solid oxide fuel cells. *International Journal of Hydrogen Energy*, **33** (7) (2008): 1834–1844.

[32] S. Hosseini, K. Ahmed, and M. Tade. CFD model of a methane fuelled single cell SOFC stack for analysing the combined effects of macro/micro structural parameters. *Journal of Power Sources*, **234** (2013): 180–196.

[33] B. Shaffer and J. Brouwer. Dynamic Model for Understanding Spatial Temperature and Species Distributions in Internal-Reforming Solid Oxide Fuel Cells. *Transactions of the ASME-U-Journal of Fuel Cell Science and Technology*, **9** (4) (2012): 041012.

[34] D. McLarty, J. Brouwer, and S. Samuelsen. A spatially resolved physical model for transient system analysis of high temperature fuel cells. *International Journal of Hydrogen Energy*, **38** (19) (2013): 7935–7946.

[35] V. Lawlor, K. Klein, C. Hochenauer, et al. Experimental and Numerical Study of Various MT-SOFC Flow Manifold Techniques: Single MT-SOFC Analysis. *Journal of Fuel Cell Science and Technology*, **10** (1) (2013): 011003–011003.

[36] M. Andersson, H. Paradis, J. Yuan, et al. Modeling Analysis of Different Renewable Fuels in an Anode Supported SOFC. *Journal of Fuel Cell Science and Technology*, **8** (3) (2011): 031013–031013.

[37] M. Andersson, J. Yuan, and B. Sundn. SOFC modeling considering electrochemical reactions at the active three phase boundaries. *International Journal of Heat and Mass Transfer*, **55** (4) (2012): 773–788.

[38] O. Razbani, M. Assadi, and M. Andersson. Three dimensional CFD modeling and experimental validation of an electrolyte supported solid oxide fuel cell fed with methane-free biogas. *International Journal of Hydrogen Energy*, **38** (24) (2013).

[39] L. Fan, E. Dimitriou, M. J. B. M. Pourquie, et al. Prediction of the performance of a solid oxide fuel cell fuelled with biosyngas: Influence of different steam-reforming reaction kinetic parameters. *International Journal of Hydrogen Energy*. European Fuel Cell 2011 **38** (1) (2013): 510–524.

[40] C. Schluckner, V. Subotić, V. Lawlor, et al. Three-dimensional numerical and experimental investigation of an industrial-sized SOFC fueled by diesel reformat - Part I: Creation of a base model for further carbon deposition modeling. *International Journal of Hydrogen Energy*, **39** (33) (2014): 19102–19118.

[41] C. Schluckner, V. Subotić, V. Lawlor, et al. Three-dimensional numerical and experimental investigation of an industrial-sized SOFC fueled by diesel reformat - Part II: Detailed reforming chemistry and carbon deposition analysis. *International Journal of Hydrogen Energy*, **40** (34) (2015): 10943–10959.

[42] V. Subotić, C. Schluckner, and C. Hochenauer. An experimental and numerical study of performance of large planar ESC-SOFCs and experimental investigation of carbon depositions. *Journal of the Energy Institute*, **89** (1) (2016): 121–137.

[43] M. Brandner, M. Bram, J. Froitzheim, et al. Electrically Conductive Diffusion barrier layers for Metal-Supported SOFC. *Solid State Ionics*. Solid State Ionics 16: Proceedings of the 16th International Conference on Solid State Ionics (SSI-16), Part II **179** (27) (2008): 1501–1504.

[44] E. Vakouftsi, G. Marnellos, C. Athanasiou, et al. CFD modeling of a biogas fuelled SOFC. *Solid State Ionics*, **192** (1) (2011): 458–463.

[45] J. Kuhn and O. Kesler. Carbon deposition thresholds on nickel-based solid oxide fuel cell anodes I. Fuel utilization. *Journal of Power Sources*, **277** (2015): 443–454.

[46] Y. M. Barzi, A. Raoufi, and H. Lari. Performance analysis of a SOFC button cell using a CFD model. *International Journal of Hydrogen Energy*, **35** (17) (2010): 9468–9478.

[47] J. Mermelstein, M. Millan, and N. Brandon. The impact of steam and current density on carbon formation from biomass gasification tar on Ni/YSZ, and Ni/CGO solid oxide fuel cell anodes. *Journal of Power Sources*, **195** (6) (2010): 1657–1666.

[48] S. A. Klein. EES - engineering equation solver - User Manual. Vol. Academic Professional V9.433-3D. F-Chart Software, 2013.

[49] G. Wang, Y. Yang, H. Zhang, et al. 3-D model of thermo-fluid and electrochemical for planar SOFC. *Journal of Power Sources*, **167** (2) (2007): 398–405.

[50] K. Tseronis, I. Bonis, I. K. Kookos, et al. Parametric and transient analysis of non-isothermal, planar solid oxide fuel cells. *International Journal of Hydrogen Energy*. 11th China Hydrogen Energy Conference **37** (1) (2012): 530–547.

[51] M. Suzuki, N. Shikazono, K. Fukagata, et al. Numerical analysis of coupled transport and reaction phenomena in an anode-supported flat-tube solid oxide fuel cell. *Journal of Power Sources*, **180** (1) (2008): 29–40.

[52] M. M. Hussain, X. Li, and I. Dincer. Mathematical modeling of planar solid oxide fuel cells. *Journal of Power Sources*, **161** (2) (2006): 1012–1022.

[53] F. P. Incropera, D. P. DeWitt, T. L. Bergman, et al. Principles of Heat and Mass Transfer. 7th ed. Hoboken, NJ: John Wiley & Sons Singapore Pte Ltd., 2013.

[54] N. P. Frank. "Umsetzung von Kohlenwasserstoffen in SOFCs." PhD thesis. München, Techn. Univ., Diss., 2010, 2009.

[55] J. Bae, S. Lim, H. Jee, et al. Small stack performance of intermediate temperature-operating solid oxide fuel cells using stainless steel interconnects and anode-supported single cell. *Journal of Power Sources*, **172** (1) (2007): 100–107.

[56] I. Kang, Y. Kang, S. Yoon, et al. The operating characteristics of solid oxide fuel cells driven by diesel autothermal reformate. *International Journal of Hydrogen Energy*, **33** (21) (2008): 6298–6307.

[57] B. Emonts, L. Blum, T. Grube, et al. "Technical Advancement of Fuel-Cell Research and Development." In: *Fuel Cell Science and Engineering*. Ed. by D. Stolten and B. Emonts. Wiley-VCH Verlag GmbH & Co. KGaA, 2012, 1–42.

[58] E. Achenbach and E. Riensche. Methane steam reforming kinetics for solid oxide fuel cells. *Journal of Power Sources*, **52** (2) (1994): 283–288.

[59] F. Bustamante, R. M. Enick, R. P. Killmeyer, et al. Uncatalyzed and wall-catalyzed forward water-gas shift reaction kinetics. *AIChE Journal*, **51** (5) (2005): 1440–1454.

[60] V. Lawlor, C. Hochenauer, D. Meissner, et al. The Use of a High Temperature Wind Tunnel for MT-SOFC Testing - Part II: Use of Computational Fluid Dynamics Software in Order to Study Previous Measurements. *Journal of Fuel Cell Science and Technology*, **8** (6) (2011): 061019–061019.

[61] A. Singh, S. Singh, S. Ganguly, et al. Steam reforming of methane and methanol in simulated macro & micro-scale membrane reactors: Selective separation of hydrogen for optimum conversion. *Journal of Natural Gas Science and Engineering*, **18** (2014): 286–295.

[62] N. Park, M. Park, S. Baek, et al. Modeling and optimization of the mixed reforming of methane: Maximizing CO2 utilization for non-equilibrated reaction. *Fuel*, **115** (2014): 357–365.

[63] W. Chen, M. Lin, T. Jiang, et al. Modeling and simulation of hydrogen generation from high-temperature and low-temperature water gas shift reactions. *International Journal of Hydrogen Energy*, **33** (22) (2008): 6644–6656.

[64] C. Odabasi, M. Gunay, and R. Yildirim. Knowledge extraction for water gas shift reaction over noble metal catalysts from publications in the literature between 2002 and 2012. *International Journal of Hydrogen Energy*, **39** (11) (2014): 5733–5746.

[65] J. Park, S. Lee, C. Lee, et al. Single-stage temperature-controllable water gas shift reactor with catalytic nickel plates. *Journal of Power Sources*, **247** (2014): 280–285.

[66] C. Callaghan. "Kinetics and catalysis of the water-gas-shift reaction: A microkinetic and graph theoretic approach." PhD thesis. Worcester Polytechnic Institute, 2006.

[67] V. Lawlor, C. Hochenauer, A. Mariani, et al. Scrutiny of MT-SOFC Stack Manifolding Design Using CFD. *The Open Fuel Cells Journal*, (5) (2012): 1–13.

[68] V. Lawlor. Review of the micro-tubular solid oxide fuel cell (Part II: Cell design issues and reserach activities). *Journal of Power Sources*, **240** (2013): 421–441.

[69] D. Singh, E. Hernández-Pacheco, P. N. Hutton, et al. Carbon deposition in an SOFC fueled by tar-laden biomass gas: a thermodynamic analysis. *Journal of Power Sources*, **142** (1) (2005): 194–199.

[70] D. Chen, R. Lodeng, A. Anundskas, et al. Deactivation during carbon dioxide reforming of methane over Ni catalyst: microkinetic analysis. *Chemical Engineering Science*, **56** (4) (2001): 1371–1379.

[71] C. M. Chun and T. A. Ramanarayanan. Mechanism and Control of Carbon Deposition on High Temperature Alloys. *Journal of The Electrochemical Society*, **154** (9) (2007): C465–C471.

[72] W. Lehnert, J. Meusinger, and F. Thom. Modelling of gas transport phenomena in SOFC anodes. *Journal of Power Sources*, **87** (1) (2000): 57–63.

[73] J.-M. Klein, Y. Bultel, S. Georges, et al. Modeling of a SOFC fuelled by methane: From direct internal reforming to gradual internal reforming. *Chemical Engineering Science*, **62** (6) (2007): 1636–1649.

[74] E. S. Hecht, G. K. Gupta, H. Zhu, et al. Methane reforming kinetics within a Ni-YSZ SOFC anode support. *Applied Catalysis A: General*, **295** (1) (2005): 40–51.

[75] L. Maier, B. Schädel, K. Herrera Delgado, et al. Steam Reforming of Methane Over Nickel: Development of a Multi-Step Surface Reaction Mechanism. *Topics in Catalysis*, **54** (13) (2011): 845–858.

[76] M. Cimenti and J. M. Hill. Direct Utilization of Liquid Fuels in SOFC for Portable Applications: Challenges for the Selection of Alternative Anodes. *Energies*, **2** (2) (2009): 377–410.

[77] K. Kendall, M. Slinn, and J. Preece. Formulating liquid ethers for microtubular SOFCs. *Journal of Power Sources*. Selected papers presented at the Ninth Grove Fuel Cell Symposium Ninth Grove Fuel Cell Symposium **157** (2) (2006): 750–753.

[78] C. M. Finnerty, N. J. Coe, R. H. Cunningham, et al. Carbon formation on and deactivation of nickel-based/zirconia anodes in solid oxide fuel cells running on methane. *Catalysis Today*, **46** (2) (1998): 137–145.

[79] V. Alzate-Restrepo and J. M. Hill. Effect of anodic polarization on carbon deposition on Ni/YSZ anodes exposed to methane. *Applied Catalysis A: General*, **342** (1) (2008): 49–55.

[80] K. Girona, J. Laurencin, J. Fouletier, et al. Carbon deposition in CH_4/CO_2 operated SOFC: Simulation and experimentation studies. *Journal of Power Sources*, **210** (2012): 381–391.

[81] J.-H. Koh, Y.-S. Yoo, J.-W. Park, et al. Carbon deposition and cell performance of Ni-YSZ anode support SOFC with methane fuel. *Solid State Ionics*, **149** (3) (2002): 157–166.

[82] Y. Wang, F. Yoshiba, M. Kawase, et al. Performance and effective kinetic models of methane steam reforming over Ni/YSZ anode of planar SOFC. *International Journal of Hydrogen Energy*, **34** (9) (2009): 3885–3893.

[83] J. Yu, Y. Wang, and S. Weng. Numerical Analysis of the Possibility of Carbon Formation in Planar SOFC Fueled With Syngas. *Journal of Fuel Cell Science and Technology*, **9** (2) (2012): 021011–021011.

[84] J.-M. Klein, M. Pons, P. Ozil, et al. Modeling of a Solid Oxide Fuel Cell Fueled by Methane: Analysis of Carbon Deposition. *Journal of Fuel Cell Science and Technology*, **4** (4) (2006): 425–434.

[85] C. H. Bartholomew. Carbon Deposition in Steam Reforming and Methanation. *Catalysis Reviews*, **24** (1) (1982): 67–112.

[86] K. Nikooyeh, A. A. Jeje, and J. M. Hill. 3D modeling of anode-supported planar SOFC with internal reforming of methane. *Journal of Power Sources*, **171** (2) (2007): 601–609.

[87] V. Yurkiv. Reformate-operated SOFC anode performance and degradation considering solid carbon formation: A modeling and simulation study. *Electrochimica Acta*, **143** (2014): 114–128.

[88] V. M. Janardhanan, V. Heuveline, and O. Deutschmann. Performance analysis of a SOFC under direct internal reforming conditions. *Journal of Power Sources*, **172** (1) (2007): 296–307.

[89] C. Schluckner, V. Subotić, V. Lawlor, et al. Carbon Deposition Simulation in Porous SOFC Anodes: A Detailed Numerical Analysis of Major Carbon Precursors. *Journal of Fuel Cell Science and Technology*, **12** (5) (2015): 051007–051007.

[90] J. R. Rostrup-Nielsen. Equilibria of decomposition reactions of carbon monoxide and methane over nickel catalysts. *Journal of Catalysis*, **27** (3) (1972): 343–356.

[91] J.-H. Koh, B.-S. Kang, H. C. Lim, et al. Thermodynamic Analysis of Carbon Deposition and Electrochemical Oxidation of Methane for SOFC Anodes. *Electrochemical and Solid-State Letters*, **4** (2) (2001): A12–A15.

[92] S. McIntosh and R. J. Gorte. Direct Hydrocarbon Solid Oxide Fuel Cells. *Chemical Reviews*, **104** (10) (2004): 4845–4866.

[93] M. Janardhanan and O. Deutschmann. CFD analysis of a solid oxide fuel cell with internal reforming: Coupled interactions of transport, heterogeneous catalysis and electrochemical processes. *Journal of Power Sources*, **162** (2) (2006): 1192–1202.

[94] K. Nikooyeh, R. Clemmer, V. Alzate-Restrepo, et al. Effect of hydrogen on carbon formation on Ni/YSZ composites exposed to methane. *Applied Catalysis A: General*, **347** (1) (2008): 106–111.

[95] E. Ivers-Tiffée, H. Timmermann, A. Leonide, et al. Methane reforming kinetics, carbon deposition, and redox durability of Ni/8 yttria-stabilized zirconia (YSZ) anodes. Hoboken, N.J: Wiley-Blackwell, 2009.

[96] V. Eveloy. Anode Fuel and Steam Recycling for Internal Methane Reforming SOFCs: Analysis of Carbon Deposition. *Journal of Fuel Cell Science and Technology*, **8** (1) (2011): 011006.

[97] V. Alzate-Restrepo and J. M. Hill. Carbon deposition on Ni/YSZ anodes exposed to CO/H_2 feeds. *Journal of Power Sources*, **195** (5) (2010): 1344–1351.

[98] J.-W. Snoeck, G. F. Froment, and M. Fowles. Steam/CO_2 Reforming of Methane. Carbon Filament Formation by the Boudouard Reaction and Gasification by CO_2, by H_2, and by Steam: Kinetic Study. *Industrial & Engineering Chemistry Research*, **41** (17) (2002): 4252–4265.

[99] T. Chen, W. G. Wang, H. Miao, et al. Evaluation of carbon deposition behavior on the nickel/yttrium-stabilized zirconia anode-supported fuel cell fueled with simulated syngas. *Journal of Power Sources*, **196** (5) (2011): 2461–2468.

[100] K. Sasaki and Y. Teraoka. Equilibria in Fuel Cell Gases. *Journal of The Electrochemical Society*, **150** (7) (2003): A878.

[101] K. Sasaki and Y. Teraoka. Equilibria in Fuel Cell Gases. *Journal of The Electrochemical Society*, **150** (7) (2003): A885.

[102] W. Y. Lee, J. Hanna, and A. F. Ghoniem. On the Predictions of Carbon Deposition on the Nickel Anode of a SOFC and Its Impact on Open-Circuit Conditions. *Journal of The Electrochemical Society*, **160** (2) (2013): F94–F105.

[103] J.-M. Klein, S. Georges, and Y. Bultel. Modeling of a SOFC Fueled by Methane: Anode Barrier to Allow Gradual Internal Reforming Without Coking. *Journal of The Electrochemical Society*, **155** (4) (2008): B333.

[104] O. R. Oy. HSC Chemistry 6.0. Finland, 1974.

[105] H. Sumi, K. Ukai, Y. Mizutani, et al. Performance of nickel–scandia-stabilized zirconia cermet anodes for SOFCs in 3% H2O–CH4. *Solid State Ionics*. Solid State Ionics Dokiya Memorial Special Issue **174** (1) (2004): 151–156.

[106] V. Subotić, C. Schluckner, B. Stöckl, et al. Strategy for Carbon Gasification from Porous Ni-YSZ Anodes of Industrial-Sized ASC-SOFCs and Effects of Carbon Growth. *Journal of The Electrochemical Society*, **163** (14) (2016): F1515–F1522.

[107] V. Subotić, C. Schluckner, J. Strasser, et al. In-situ electrochemical characterization methods for industrial-sized planar solid oxide fuel cells Part I: Methodology, qualification and detection of carbon deposition. *Electrochimica Acta*, **207** (2016): 224–236.

[108] C. Schluckner, V. Subotić, V. Lawlor, et al. Numerical SOFC Anode Catalyst Occupation Study: Internal Reforming of Carbonaceous Fuel Mixtures. *Journal of The Electrochemical Society*, **163** (7) (2016): F761–F770.

[109] M. Ettler, H. Timmermann, J. Malzbender, et al. Durability of Ni anodes during reoxidation cycles. *Journal of Power Sources*, **195** (17) (2010): 5452–5467.

[110] Y. Zhang, B. Liu, B. Tu, et al. Understanding of redox behavior of Ni–YSZ cermets. *Solid State Ionics*, **180** (36) (2009): 1580–1586.

[111] V. Subotić, C. Schluckner, J. Mathe, et al. Anode regeneration following carbon depositions in an industrial-sized anode supported solid oxide fuel cell operating on synthetic diesel reformate. *Journal of Power Sources*, **295** (2015): 55–66.

[112] V. Subotić, C. Schluckner, H. Schroettner, et al. Analysis of possibilities for carbon removal from porous anode of solid oxide fuel cells after different failure modes. *Journal of Power Sources*, **302** (2016): 378–386.

[113] J. Kirtley, A. Singh, D. Halat, et al. In Situ Raman Studies of Carbon Removal from High Temperature Ni–YSZ Cermet Anodes by Gas Phase Reforming Agents. *The Journal of Physical Chemistry C*, **117** (49) (2013): 25908–25916.

[114] T. Klemenso, C. Chung, P. H. Larsen, et al. The Mechanism Behind Redox Instability of Anodes in High-Temperature SOFCs. *Journal of The Electrochemical Society*, **152** (11) (2005): A2186.

[115] G. Brus, K. Miyoshi, H. Iwai, et al. Change of an anode's microstructure morphology during the fuel starvation of an anode-supported solid oxide fuel cell. *International Journal of Hydrogen Energy*, **40** (21) (2015): 6927–6934.

[116] S. Takenaka, E. Kato, Y. Tomikubo, et al. Structural change of Ni species during the methane decomposition and the subsequent gasification of deposited carbon with CO_2 over supported Ni catalysts. *Journal of Catalysis*, **219** (1) (2003): 176–185.

[117] C. Schluckner, V. Subotić, V. Lawlor, et al. CFD-simulation of effective carbon gasification strategies from high temperature SOFC Ni-YSZ cermet anodes. *International Journal of Hydrogen Energy*, **42** (7) (2017): 4434–4448.